IHEP-CEPC-DR-2017-01

IHEP-AC-2017-01

CEPC-SPPC

Progress Report (2015 – 2016)

Accelerator

The CEPC-SPPC Study Group

April 2017

Contents

1 Introduction

1.1 Purpose of the Report

Since the publication of the CEPC-SPPC Preliminary Conceptual Design Report (Pre-CDR, the "*white report*") in March 2015 [1], significant progress has been made in the design of the accelerators. This report (the "*yellow report*") summarizes the progress during 2015-2016. Unlike the Pre-CDR, we do not have a comprehensive description of every aspect of the accelerator in this report. We focus on the option studies – baseline and alternative option proposals. This report has five chapters in addition to this introduction:

Chapter 2: CEPC Accelerator Physics
Chapter 3: CEPC Technical Systems
Chapter 4: CEPC Injectors
Chapter 5: SPPC
Chapter 6: R&D Program

1.2 Luminosity Goals

The principal luminosity goals of CEPC remain unchanged, namely, construction of a Higgs factory that will deliver 5 ab^{-1} and generate one million (10^6) Higgs particles in 10 years as shown in Table 1.1. In addition, CEPC will serve as a Super-Z factory that will deliver 2.5 ab^{-1} and generate 100 billion (10^{11}) Z particles or more in ~2 years as shown in Table 1.2.

Table 1.1: CEPC Parameters for a Higgs factory.

Parameter	**Design Goal**
Particles	*e+, e-*
Center of mass energy	240 GeV
Integrated luminosity (per IP per year)	250 fb^{-1}
No. of IPs	2
No. of Higgs (per year)	10^5

Table 1.2: CEPC Parameters for a Super-Z factory.

Parameter	**Design Goal**
Particles	*e+, e-*
Center of mass energy	91.2 GeV
Integrated luminosity (per IP per year)	600 fb^{-1}
No. of IPs	2
No. of Z's (per year)	5×10^{10}

1.3 Machine Layout

There are major changes from the Pre-CDR in the machine layout. The Pre-CDR had a single-ring design and a pretzel orbit to separate the e+ and e- beams in the arcs to avoid parasitic collisions. The single-ring design had the advantage of lower cost, a major design constraint when the study began in 2014. However, the pretzel scheme has a number of beam physics difficulties which pose machine operation challenges. Although CESR and LEP adopted this pretzel scheme successfully, it became clear that to reach the required luminosity of 2×10^{34} $cm^{-2}s^{-1}$, 100 times greater than LEP, using a pretzel orbit would be very difficult, and the commissioning time could take one or more years, which would delay valuable time for experiment data taking. Therefore, it was decided to pursue several alternative designs: a partial double ring (PDR), an advanced partial double ring (APDR) and a double ring (DR). These design options are presented in chapters 2 and 3.

The PDR design uses a bunch train structure, namely puts all the bunches close to each other as if it is a "macro" bunch. The two macro bunches, one each for electrons and positrons, circulating in the ring will only collide at the two interaction points (IPs) without parasitic collisions in the arcs. Therefore, a pretzel orbit is not needed. Furthermore, as there will be two rings near the IP, a crossing angle and the crab waist scheme can be utilized. This scheme has several important advantages: (1) for the same vertical beam-beam tune shift, the luminosity is higher; (2) the horizontal beam-beam tune shift is lower; (3) the overlapping area of the two colliding beams is shorter, therefore, longer bunch and larger $\beta(y)^*$ are allowed; (4) the required RF voltage is lower and the HOM loss is reduced (because of longer bunches). This scheme worked successfully at DAFNE and increased its luminosity by a factor of 4. On the other hand, a crossing angle makes the machine-detector interface (MDI) more complicated, which is arguably the most difficult and most complicated component in a high-energy collider such as the CEPC.

During the study of the PDR, it was found that the bunch train structure would lead to a serious beam loading problem in the superconducting RF (SRF) system. The SRF would need to operate in the pulsed mode instead of the CW mode, which would greatly reduce the RF efficiency. To overcome this problem, an advanced partial double ring (APDR) was considered. In this design, instead of one bunch train, there are four bunch trains for each beam. To avoid parasitic crossing in the arcs, there are 8 double ring sections instead of 2 as in the PDR. This design partially mitigates the beam loading problem because the bunches are distributed more evenly in the ring.

For both PDR and APDR, a price to pay is that for the same arc length (which determines the RF power), the machine circumference becomes larger due to the double ring sections.

We have also studied the double ring (DR) design, in which each beam circulates in its own ring as in the BEPC-II, PEP-II, DAFNE, KEKB and SuperKEKB colliders. This solves the parasitic crossing problem completely. Furthermore, it can also avoid the beam energy sawtooth problem by tapering the arc magnets.

The readers can find details of all these designs in the following chapters. However, it should be noted that after a careful comparison of the pros and cons of each design, it was decided in early 2017 that the CEPC baseline design will be a double ring, the

machine circumference will be increased to 100 km, and the synchrotron radiation power will be limited to 30 MW per beam.

1.4 Cost Consideration

Cost is a major factor when the baseline machine circumference is increased from 54 km to 100 km. During the Pre-CDR study, two cost estimates were made, one for 54 km, another for 100 km. In the Pre-CDR, our cost estimate for a 54 km, single ring machine was 25 billion Chinese Yuan, or about US$ 3.5 billion. For the new baseline of a 100 km, double-ring machine, the cost estimate is 40 billion Chinese Yuan, or about US$ 5.7 billion.

In this progress report, we will not detail the cost changes in each technical system but only summarize the factors that impact the cost:

A. From 54 km to 100 km:
    - When the luminosity is beam-beam limited (which is the case for CEPC), for the same luminosity and beam current, the synchrotron radiation power P_{SR} and energy loss per turn U are inversely proportional to the machine radius ρ. Therefore, when the machine size is increased from 54 km to 100 km, both P_{SR} and U will be reduced by half, resulting in large savings in the "big three" technical systems – superconducting RF (SRF), RF power source and cryogenics. These "big three" represent about half of the total accelerator cost.
    - The cost of other technical systems (magnets, power supplies, vacuum, instrumentation, control, mechanical, survey and alignment) is proportional to the machine size and, therefore, will be doubled.
    - The cost of civil construction will increase 50%.
    - The cost of the detectors will not change.
    - It should also be pointed out that for a 100 km machine, the operations cost will be significantly lower because less RF power is needed. In other words, the machine will be "greener."

B. From single-ring to double-ring:
    - The cost of the "big three" systems will not change.
    - The cost of other technical systems in the Collider will increase. But the change is not double since the magnet and beam pipe can be made smaller when each ring accommodates only one beam. These costs are increased by an estimated factor of 70%.
    - The cost of the Booster, Linac and particle sources will not change.
    - The cost of civil construction and detectors will not change.

1.5 R&D Planning

Major progress on CEPC during 2015-2016 was the establishment of a large-scale R&D program. This program is essential for preparing for construction of the CEPC, which is expected to begin in the early 2020's. The R&D details for each technical system are described in Ch. 6.

This program is partially sponsored by the Ministry of Science and Technology (MOST) in China. In 2016 MOST approved 36M Chinese Yuan (the equivalent of about US$ 5M) of R&D funding for 5 years. Another 40M (about US$ 6M) is expected in 2018.

The National Science Foundation of China (NSFC) approved 12M Chinese Yuan R&D funding for 4 years, and another 6M per year is expected.

The Chinese Academy of Sciences (CAS) will also provide significant R&D funding. The exact amount is currently under discussion.

The Beijing municipal government has approved the construction of a major SRF laboratory in Huairou in north suburban Beijing. This laboratory will have 4,500 m^2 (about 50,000 ft^2), similar to SRF laboratories at KEK, JLab, DESY and Fermilab. It will be equipped with cavity treatment facilities, clean rooms, vertical and horizontal test stands, an assembly station, etc. and will serve as a center for both initial technology R&D and pre-construction R&D. The laboratory will be completed in 3 years. These facilities will allow critical CEPC R&D projects to proceed effectively and timely.

With these funds, we expect a successful R&D program over the next ~5 years will place CEPC in a good position to begin construction in the early 2020's.

1.6 Landscape of Energy Frontier Lepton Colliders

Currently there are four high-energy lepton colliders being proposed – ILC, CLIC, FCC-ee and CEPC. While the study of ILC and CLIC started much earlier and is in more advanced stage, the study of FCC-ee and CEPC started in 2012 after the discovery of the Higgs boson but is catching up quickly.

Recently both ILC and CLIC changed their baseline design goal. The first stage of the ILC will be a 250 GeV center of mass energy linear collider, and the CLIC will have a center of mass energy of 380 GeV in the first stage. It is interesting to notice that the cost estimate for the new baselines of CEPC, ILC and CLIC is close to each other: CEPC at US$ 5.7B (equiv.) [2], ILC at US$ 5-6B (equiv.) [3] and CLIC at US$ 6.7B (equiv.) [4]. The FCC-ee has a cost estimate for the tunnel construction but which has not been made public yet.

For the schedule planning, both ILC and CEPC aim to start data taking by the end of next decade. But the CLIC and FCC-ee would be later – in the middle of 2030's because the LHC will keep running for the next 20 years.

Each of the four machines is technically challenging and financially costly. It is very important to build an effective collaboration among the four teams so that no matter which machine(s) will eventually be built, the valuable knowledge, experiences and technologies of each team can be shared and put to good use.

1.7 References

1. CEPC-SPPC Preliminary Conceptual Design Report, March 2016, IHEP-CEPC-DR-2016-01, http://cepc.ihep.ac.cn/preCDR/volume.html
2. Yifang Wang, presentation at the Institute for Advanced Study (IAS) High Energy Physics Conference 2017, Hong Kong University of Science and Technology (HKUST), Hong Kong, January 23-26, 2017, http://iasprogram.ust.hk/hep/2017/conf.html
3. Akira Yamamoto, ibid.
4. Philip Burrows, ibid.

2 CEPC – Accelerator Physics

2.1 Main Parameters

2.1.1 Parameter Tables

The CEPC main parameters using the crab waist scheme for collisions are listed in Tables 2.1.1 and 2.1.2. Table 2.1.1 is for a circumference of 61 km and Table 2.1.2 is for a circumference of 100 km. In both tables the comparison is made with the 54 km circumference of the Pre-CDR.

First, let's consider Table 2.1.1 and C = 61 km. As shown in the high luminosity column, we keep the same beam power as in the Pre-CDR (50 MW/beam) and obtain almost a 50% gain in luminosity. Alternately, as shown in the low power column, we can decrease the beam power from 50 MW to ~30 MW and have the same luminosity as in the Pre-CDR.

Now let's turn to Table 2.1.2 where C = 100 km. Based on a double ring scheme we can get higher Higgs luminosity (+170%) keeping the Pre-CDR beam power or by reducing the beam power to 19 MW keep the same luminosity. The requirement for energy acceptance was reduced from 2% to 1.5% by enlarging the ring to 100 km. The luminosity at the Z-pole is at the level of 10^{35} $cm^{-2}s^{-1}$.

Fig. 2.1.1 shows the maximum luminosity for a 100 km CEPC with the double ring scheme, calculated with the full SR power 50 MW per beam.

Fig. 2.1.2 shows the relationship between the CEPC Higgs luminosity and crossing angle with a 54 km circumference. It seems that 40 mrad is the best choice. Also, Fig. 2.1.3 shows the relationship between the CEPC luminosity and the circumference. It shows that larger ring give higher luminosity and at 100 km circumference, CEPC can get same luminosity as FCC-ee at the Higgs energy.

Table 2.1.1. 61 km CEPC crab waist parameters

	Pre-CDR	***H-high lumnosity.***	***H-low power***	***W***	***Z***
Number of IPs	2	2	2	2	2
Energy (GeV)	120	120	120	80	45.5
Circumference (km)	54	61	61	61	61
SR loss/turn (GeV)	3.1	2.96	2.96	0.58	0.061
Half crossing angle (mrad)	0	15	15	15	15
Piwinski angle	0	1.88	1.84	4.11	5.86
N_e/bunch (10^{11})	3.79	2.0	1.98	0.85	0.6
Bunch number	50	107	70	400	1100
Beam current (mA)	16.6	16.9	11.0	26.8	52.0
SR power /beam (MW)	51.7	50	32.5	15.7	3.2
Bending radius (km)	6.1	6.2	6.2	6.2	6.2
Momentum compaction (10^{-5})	3.4	1.48	1.48	1.48	3.1
β_{IP} x/y (m)	0.8/0.0012	0.272/0.0013	0.275 /0.0013	0.16/0.001	0.12/0.001
Emittance x/y (nm)	6.12/0.018	2.05/0.0062	2.05 /0.0062	0.93/0.003	0.87/0.0046
Transverse σ_{IP} (um)	69.97/0.15	23.7/0.09	23.7/0.09	12.2/0.056	10.2/0.068
ξ_x/IP	0.118	0.041	0.042	0.0145	0.0098
ξ_y/IP	0.083	0.11	0.11	0.084	0.073
V_{RF}(GV)	6.87	3.48	3.51	0.7	0.12
f_{RF} (MHz)	650	650	650	650	650
Nature σ_z (mm)	2.14	2.7	2.7	3.23	3.9
Total σ_z (mm)	2.65	2.95	2.9	3.35	4.0
HOM power/cavity (kw)	3.6	0.74	0.48	0.47	0.59
Energy spread (%)	0.13	0.13	0.13	0.087	0.05
Energy acceptance (%)	2	2	2		
Energy acceptance by RF (%)	6	2.3	2.4	1.3	1.1
n_γ	0.23	0.35	0.34	0.28	0.24
Life time due to beamstrahlung_cal (minute)	47	37	37		
F (hour glass)	0.68	0.82	0.82	0.89	0.92
L_{max}/IP (10^{34}cm^{-2}s^{-1})	2.04	3.1	2.01	3.5	3.44

Table 2.1.2. 100 km CEPC parameters for double-ring

	Pre-CDR	***H-high lumnosity.***	***H-low power***		***W***	***Z***	
Number of IPs	2	2	2	2	2	2	2
Energy (GeV)	120	120	120	120	80	45.5	45.5
ference (km)	54	100	100	100	100	100	100
SR loss/turn (GeV)	3.1	1.67	1.67	1.67	0.33	0.034	0.034
Half crossing angle (mrad)	0	15	15	15	15	15	15
Piwinski angle	0	2.5	2.5	2.5	3.57	5.69	5.69
N_e/bunch (10^{11})	3.79	1.12	1.12	1.12	1.05	0.46	0.46
Bunch number	50	555	333	211	1000	16666	65716
Beam current (mA)	16.6	29.97	17.98	11.4	50.6	367.7	1449.7
SR power /beam (MW)	51.7	**50**	**30**	**19**	16.7	12.7	50
Bending radius (km)	6.1	11	11	11	11	11	11
Momentum compaction (10^{-5})	3.4	0.96	0.96	0.96	3.1	3.3	3.3
β_{IP} x/y (m)	0.8/0.0012	0.3/0.00**1**	0.3/0.00**1**	0.3 /0.00**1**	0.1 /0.001	0.12/0.001	0.12/0.001
Emittance x/y (nm)	6.12/0.018	1.01/0.0031	1.01/0.0031	1.01/0.0031	2.68/0.008	0.93/0.0049	0.93/0.0049
Transverse σ_{IP} (um)	69.97/0.15	17.4/0.055	17.4/0.055	17.4/0.055	16.4/0.09	10.5/0.07	10.5/0.07
ξ_x/ξ_y/IP	0.118/0.083	0.029/0.083	0.029/0.083	0.029/0.083	0.0082/0.055	0.0075/0.054	0.0075/0.054
RF Phase (degree)	153.0	123.3	123.3	123.3	149	160.8	160.8
V_{RF}(GV)	6.87	**2.0**	**2.0**	**2.0**	**0.63**	**0.11**	**0.11**
f_{RF} (MHz) (harmonic)	650	650	650	650	650 (217800)	650 (217800)	
Nature σ_z (mm)	2.14	**2.72**	**2.72**	**2.72**	**3.8**	**3.93**	**3.93**
Total σ_z (mm)	2.65	2.9	2.9	2.9	3.9	4.0	4.0
HOM power/cavity (kw)	3.6 (5cell)	0.75(2cell)	0.45(2cell)	0.28(2cell)	1.0 (2cell)	1.6(1cell)	6.25(1cell)
Energy spread (%)	0.13	0.098	0.098	0.098	0.065	0.037	0.037
Energy acceptance (%)	2	1.5	1.5	1.5			
Energy acceptance by RF (%)	6	1.8	1.8	1.8	1.5	1.1	1.1
n_γ	0.23	0.26	0.26	0.26	0.26	0.18	0.18
Life time due to beamstrahlung_cal (minute)	47	52	52	52			
F (hour glass)	0.68	0.83	0.83	0.83	0.84	0.91	0.91
L_{max}/IP (10^{34}cm^{-2}s^{-1})	2.04	5.42	3.25	2.06	4.08	18.0	70.97

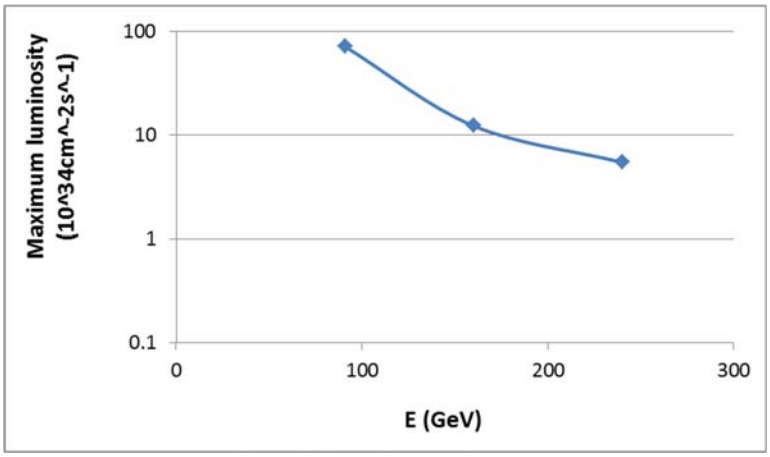

Fig. 2.1.1. 100km CEPC luminosity potential with 50MW/beam

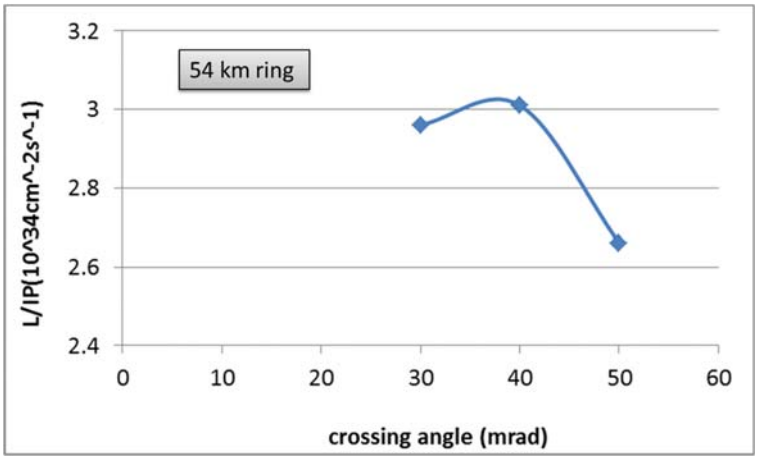

Fig. 2.1.2. CEPC Higgs luminosity vs. crossing angle with 54km circumference

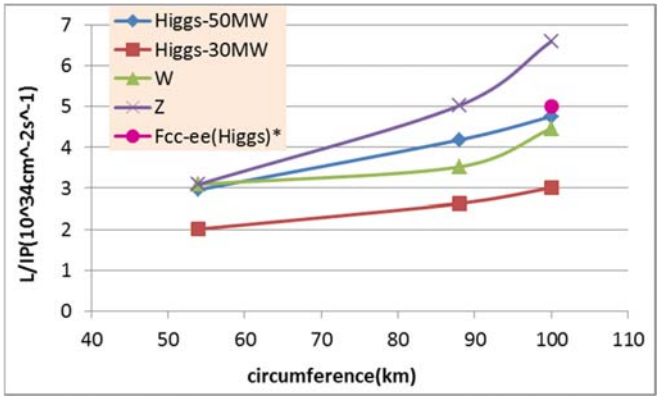

Fig. 2.1.3. CEPC luminosity vs. circumference

2.1.2 Calculation of Derived Parameters

Step 1: Beam-beam limit

In our method, the energy of the ring E_0, the bending radius of the main dipole magnets ρ, the synchrotron radiation power P_0 (machine technical constraint), the aspect ratio R and the IP number N_{IP} are known quantities. From these input parameters one first gets:

$$U_0 = 88.5\times10^3 \frac{E_0^4(GeV)}{\rho(m)} \tag{2.1.1}$$

$$I_b = \frac{eP_0}{U_0} \tag{2.1.2}$$

$$\delta_0 = \gamma\sqrt{\frac{C_q}{J_\varepsilon\rho}} \tag{2.1.3}$$

And the maximum beam-beam tune shift is [6]

$$\xi_y = \frac{2845}{2\pi}\sqrt{\frac{U_0}{2\gamma E_0 N_{IP}}}\times F_l \tag{2.1.4}$$

where F_l is the beam-beam limit (ξy) enhancement factor from the crab waist scheme. We assume it is 1.5 for the Higgs and 2.6 at the Z-pole.

Step 2: Luminosity

The luminosity of a circular collider is expressed by

$$L_0[cm^{-2}s^{-1}] = 2.17\times10^{34}(1+r)\xi_y\frac{eE_0(GeV)N_bN_e}{T_0(s)\beta_y^*(cm)} \tag{2.1.5}$$

According to eq. (2.1.4), (2.1.5) can be expressed by another way

$$L_0\left[cm^{-2}s^{-1}\right] = 0.7\times10^{34}(1+r)\frac{1}{\beta_y[cm]}\sqrt{\frac{E_0[GeV]I_b[mA]P_0[MW]}{\gamma N_{IP}}} \tag{2.1.6}$$

Step 3: Transverse beam size

V. I. Telnov pointed out that at energy-frontier e+e− storage ring colliders, beamstrahlung determines the beam lifetime through the emission of single photons in the tail of the beamstrahlung spectra. If we want to achieve a reasonable beamstrahlung-driven beam lifetime of at least 30 minutes, we need to confine the relation of the bunch population and the beam size as in eq. (2.1.7) [7, 8]

$$\frac{N_e}{\sigma_x\sigma_z} \le 0.1\eta\frac{\alpha}{3\gamma r_e^2} \tag{2.1.7}$$

Recalling the definition of the vertical beam-beam tune shift, for a flat beam, we obtain

$$\frac{N_e}{\sigma_x\sigma_y\sqrt{1+\Phi^2}} = \frac{2\pi\gamma}{r_e\beta_y}\xi_y \tag{2.1.8}$$

Combining eq. (2.1.7) with eq. (2.1.8), one has

$$\frac{N_e^2}{\sigma_x^2\sigma_y\sigma_z}=\frac{0.2\pi\eta\alpha\xi_y\sqrt{1+\Phi^2}}{3r_e^3\beta_y} \tag{2.1.9}$$

In order to control the additional energy spread from beamstrahlung, we introduce a constraint

$$\delta_{BS}=\frac{\delta_0}{A}\qquad (A\geq 3) \tag{2.1.10}$$

From eq. (2.1.10) and the definition of beamstrahlung energy spread, one finds

$$\frac{N_e^2}{\sigma_x\sigma_y\sigma_z}=\frac{3\delta_0}{2.6r_e^3\gamma rA} \tag{2.1.11}$$

So, according to eq. (2.1.9) and (2.1.11), we get

$$\sigma_x=\frac{5.77\delta_0\beta_y}{\pi\eta\alpha\xi_y\sqrt{1+\Phi^2}\gamma rA} \tag{2.1.12}$$

Given the coupling factor κ_ε (0.003 for example) and the aspect ratio r, one can calculate the vertical beam size/emittance and horizontal emittance/beta:

$$\begin{aligned}&\sigma_y=r\sigma_x, \qquad \varepsilon_y=\frac{\sigma_y^2}{\beta_y}\\ &\varepsilon_x=\frac{\varepsilon_y}{\kappa_\varepsilon}, \qquad \beta_x^*=\frac{\sigma_x^2}{\varepsilon_x}\end{aligned} \tag{2.1.13}$$

Assuming we use a 60 degree FODO cell for the arc, then we can get the bending angle per FODO cell knowing the horizontal emittance.

$$\varepsilon_x=\frac{C_q\gamma^2\varphi^3\left(1-\frac{3}{4}\sin^2\left(\frac{\mu}{2}\right)+\frac{1}{60}\sin^4\left(\frac{\mu}{2}\right)\right)}{8J_x\sin^3\left(\frac{\mu}{2}\right)\cos\left(\frac{\mu}{2}\right)} \qquad \rightarrow \quad \varphi \tag{2.1.14}$$

Furthermore, one can make an estimation of the momentum compaction factor.

$$\alpha_p=(\frac{\varphi}{2})^2(\frac{1}{sin^2\frac{\mu}{2}}-\frac{1}{12}) \tag{2.1.15}$$

Step 4: Crossing angle

From eq. (2.1.8) one gets

$$N_e=\frac{2\pi\gamma\xi_y\sqrt{1+\Phi^2}}{r_e\beta_y}\sigma_x\sigma_y \tag{2.1.16}$$

Then, having the bunch population from eq. (2.1.16), it's easy to get the bunch number

$$N_b=\frac{I_bT_0}{eN_e} \tag{2.1.17}$$

And also from eq. (2.1.7) one gets

$$\sigma_z=\frac{3\gamma r_e^2N_e}{0.1\eta\alpha\sigma_x} \tag{2.1.18}$$

The Piwinski angle is defined by:

$$\Phi = \frac{\sigma_z}{\sigma_x} tg\theta_h \tag{2.1.19}$$

Combining eq. (2.1.18) and eq. (2.1.19), one finds out the value of the half crossing angle for the partial double ring scheme.

$$\theta_h = Arctg\left(\frac{0.1\eta\alpha\sigma_x^2\Phi}{3\gamma r_e^2 N_e}\right) \tag{2.1.20}$$

Step 5: Hour glass effect

By the crab waist method, the overlap area of colliding bunches is much shorter than the bunch length. Here, we define a new parameter, effective bunch length as

$$\sigma_{zeff} = \frac{\sigma_x}{\sin\theta_h} \tag{2.1.21}$$

Then the hour glass effects can be evaluated by

$$F_h = \frac{\beta_y}{\sqrt{\pi}\sigma_{zeff}} \exp\left(\frac{\beta_y^2}{2\sigma_{zeff}^2}\right) K_0\left(\frac{\beta_y^2}{2\sigma_{zeff}^2}\right) \tag{2.1.22}$$

Finally, the real luminosity can be expressed as the product of peak luminosity L_0 and hour glass factor F_h.

$$L = L_0 F_h \tag{2.1.23}$$

Step 6: RF parameters

First, considering that the synchrotron radiation energy loss must be compensated by the RF cavities, one finds

$$U_0 = eV_{rf} \sin\phi_s \tag{2.1.24}$$

The natural bunch length is expressed by

$$\sigma_{z0} = \sigma_z \times \frac{A}{1+A} = \sqrt{-\frac{2\pi E_0 \alpha_p}{f_{rf} T_0 e V_{rf} \cos\phi_s}} \bar{R}\delta_0 \tag{2.1.25}$$

From eq. (24) and eq. (25), we can get the RF voltage V_{rf} and RF accelerating phase ϕs. Then we can calculate the energy acceptance for the RF system.

$$\eta_{RF} = \sqrt{\frac{2U_0}{\pi\alpha_p f_{rf} T_0 E_0}\left(\sqrt{q^2-1} - \arccos(\frac{1}{q})\right)} \quad \left(q = \frac{eV_{rf}}{U_0}\right) \tag{2.1.26}$$

Step 7: Beam life time and RF HOM power

As a final step, we check the beam lifetime due to radiative Bhabha scattering and the beam lifetime due to the beamstrahlung effect.

$$\tau_{bhabha} = \frac{I_b}{eLN_{IP}\sigma_{ee}f_0} \quad \left(\sigma_{ee} = 1.52\times10^{-25} cm^2\right) \tag{2.1.27}$$

$$\tau_{BS} = \frac{2\pi R}{c}\frac{\sqrt{6\pi}r_e\gamma e^{1.475u}}{0.057\alpha^2\eta\sigma_z} \text{[9]} \tag{2.1.28}$$

In addition, we need to check the HOM power per cavity.

$$P_{HOM} = k(\sigma_z)eN_e \cdot 2I_b \le 1kw \text{ [10]} \tag{2.1.29}$$

where the HOM loss factor is

$$k(\sigma_z) = \frac{1.8}{\sqrt{\sigma_z / 0.00265}} \quad V/pC \tag{2.1.30}$$

2.1.3 Crosscheck by Beam-Beam Simulations

We have carried out strong-strong simulations for the100 km CEPC parameters with full crab waist strength. We found large horizontal longitudinal oscillations with the parameters in Table 2.1.2, but we can suppress this kind of oscillation by changing the working point or reducing the β_x*. Fig. 2.1.4 gives an example for the high luminosity Higgs parameter with 100km circumference. The luminosity by simulation is close to the parameter table.

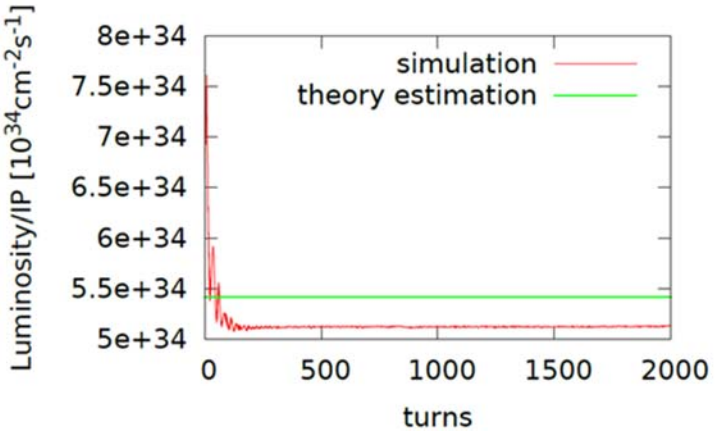

Fig. 2.1.4. Strong-strong simulation of the 100 km CEPC for the high luminosity Higgs parameter (beam lifetime: 400min)

2.2 Lattice

2.2.1 Considerations for Lattice Design

To achieve the desired Higgs factory luminosity, low emittance and low beta functions at the interaction points are required. A momentum acceptance as large as 2 % is also required to achieve a reasonable beam lifetime. In this section, the considerations for main ring lattice design will be presented. The requirements for the main ring lattice design are listed in Table2.2.1.

Table 2.2.1: Requirements for the main ring lattice design

Parameter	Symbol	Unit	Value
Luminosity per IP	L_{max}	10^{34} cm^{-2} s^{-1}	2.05
Main ring emittance	$\varepsilon_x/\varepsilon_y$	nm·rad	1.56 /0.0047
DA requirement from beam-beam (including errors and beam-beam effect)	DA_x/DA_y	σ	20 / 40 (dp/p=0) 5 / 10 (dp/p=±2%)

2.2.1.1 Arc Region

For the arc region, the FODO cell structure is chosen to provide a large dipole filling factor.

The aberration in lattices with different phase advances and sextupole configurations have been compared, and presented in Table2.2.2. For the interleaved sextupole scheme with $60°/60°$ phase advance, all the 3rd and 4th order resonance driving terms (RDT) except 2Qx −2Qy are cancelled out within one betatron unit, i.e. 6 cells. However, the tune shifts accumulate along the arc cells and reach a very large number around the whole ring. The negative tune shift pushes the tune of CEPC (0.08/0.22) to an integer resonance and thus limits the on-momentum dynamic aperture. To solve this problem, the non-interleaved sextupole scheme with $90°/90°$ phase advance was selected for the CEPC main ring arcs. In this scheme, all 3rd and 4th RDT due to sextupoles are cancelled, except for small 4Qx, 2Qx+2Qy, 4Qy, 2Qx-2Qy that are cancelled out within 5 cells. The tune shifts are very small thus the dynamic aperture for on-momentum particle is large. The dynamic aperture for off-momentum particles can be optimized with many families of sextupoles.

Table 2.2.2. Aberrations of different arc lattices

Sextupole scheme	Interleaved	Non-interleaved
60 ° /60°	n=6 All 3rd RDT due to sextupoles cancelled All 4th RDT except 2Qx-2Qy due to sextupoles cancelled dQ(Jx,Jy): accumalte to be large dQ(δ): small even with 2 families DA on momentum: easy to optimize DA off momentum: easy to optimize	-
90 ° /60 °	n=12 All 3rd RDT due to sextupoles cancelled All 4th RDT except 4Qx due to sextupoles cancelled dQ(Jx,Jy): accumalte to be large dQ(δ): small even with 2 families DA on momentum: easy to optimize DA off momentum: easy to optimize	-
90 ° /90 °	n=4 All 3rd RDT due to sextupoles cancelled 4th RDT except 4Qx, 2Qx+2Qy, 4Qy, 2Qx-2Qy due to sextupoles cancelled dQ(Jx,Jy): accumalte to be large dQ(δ): small even with 2 families DA on momentum: - DA off momentum: -	n=5 All 3rd RDT due to sextupoles cancelled 4th RDT except small 4Qx, 2Qx+2Qy, 4Qy, 2Qx-2Qy due to sextupoles cancelled dQ(Jx,Jy): small dQ(δ): correct with many families DA on momentum: easy to optimize DA off momentum: with many families to correct dQ(δ) and –I break down

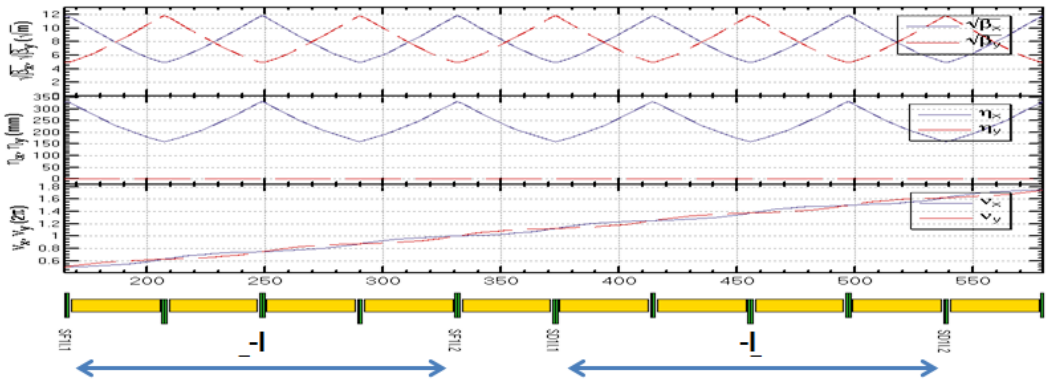

Figure 2.2.1: Sextupole configuration for the non-interleaved sextupole scheme with 90 ° /90° phase advance

If the emittance is fixed, the bending angle θ per dipole and cell number N_{cell} of the arc region are also fixed:

$$\varepsilon_x = \frac{FC_q\gamma^2\theta^3}{J_x}$$

$$F = \frac{1-\frac{3}{4}\sin^2\frac{\mu}{2}}{\sin^3\frac{\mu}{2}\cos\frac{\mu}{2}}$$

The chromaticity of ARC ξ is fixed, but the dispersion at sextupole D_x will increase with a longer cell length L:

$$\xi = -\frac{N_{cell}}{\pi}\tan\frac{\mu}{2}$$

$$D_x = \frac{L\theta(1\pm\frac{1}{2}\sin\frac{\mu}{2})}{4\sin^2\frac{\mu}{2}}$$

The nonlinearity generated by sextupole $K_2\beta$ will decrease with a longer cell length L:

$$K_2\beta \propto \frac{\xi}{D_x} \propto \frac{1}{L}$$

Thus, a larger ring will lead to a bigger dynamic aperture if the emittance is fixed. Fig. 2.2.2 shows the dynamic aperture when the arc region legnths are 55 km, 74 km and 93 km respectly. The emittance is fixed at 2 nm·rad.

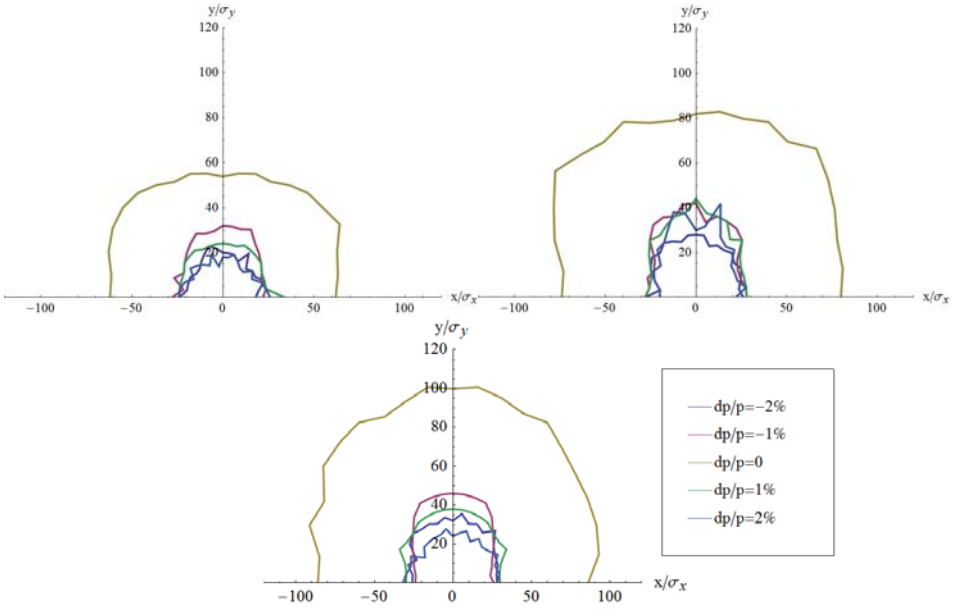

Figure 2.2.2: Dynamic aperture vs. arc region legnth (55 km, 74 km, 93 km).

2.2.1.2 Interaction Region

We have developed two interaction region (IR) designs as described below.

2.2.1.2.1 IR Design A

The CEPC interaction region (IR) was designed with modular sections [1–4] including the final transformer (FT), chromaticity correction for the vertical plane (CCY), chromaticity correction for the horizontal plane (CCX) and a matching transformation section (MT). To achieve a momentum acceptance as large as 2%, local correction of the large chromaticity from the final doublet (FD) is necessary. Two pairs of sextupoles separated with -I transportation are used to make the 1st order chromaticity correction. The optics of the IR starting from the interaction point (IP) are shown in Fig. 2.2.3.

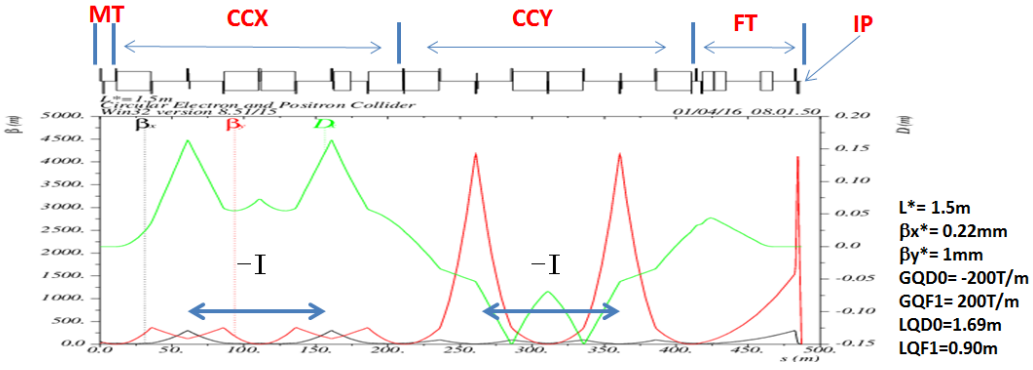

Figure 2.2.3: Interaction region lattice design.

To correct the tune shift due to finite length of main sextupoles, two pairs of weak sextupoles are installed next to the main ones [5]. To reduce the 2nd order chromaticity, the phases of sextupoles are carefully tuned. To reduce the 3rd order chromaticity, one

additional sextupole is installed at the 1st image point [1]. All the 3rd and 4th RDT due to sextupoles are almost cancelled. The break down of –I and high order dispersion can be optimized with an odd dispersion scheme or Brinkmann sextupoles. The latter method is applied for the CEPC dynamic aperture optimization.

2.2.1.2.2 IR Design B

The lattice design of FFS (betax=0.22m, betay=0.002m) for the CEPC double ring is shown in Fig. 2.2.4. The L^* is 1.5m and the strength of first quadrupole (twin aperture) is 200T/m. The critical energy of the FFS is controlled under 100keV within 560m and is under 200 keV within 630m. We need a pair of weak sextupoles to correct the nonlinearity of the length effect of the main sextupole pair in FFS. The strength of the weak sextupole pair is about -10% of the main sextupole pair.

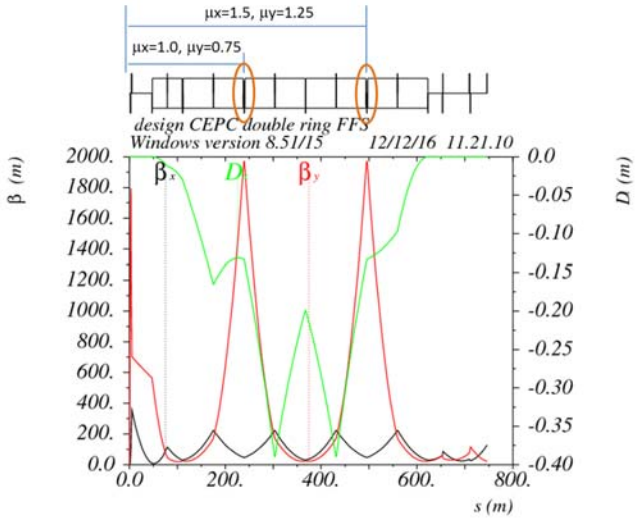

Fig. 2.2.4. **FFS optics for CEPC double ring.**

The crab sextupole should be placed on both sides of the IP in phase with the IP in the horizontal plane and at π/2 in the vertical plane. In this design, both FFS main sextupoles of the CCS-Y section can work as crab sextupoles. Still we need to check the DA of the whole ring to decide which IR design is better.

The crab sextupole strength should satisfy the following condition depending on the crossing angle and the beta functions at the IP and the sextupole locations:

$$K_2 L = \frac{1}{2\theta}\frac{1}{\beta_y^*\beta_y}\sqrt{\frac{\beta_x^*}{\beta_x}} = 0.57m^{-2}$$

$$K_2 = 1.9m^{-3}$$

2.2.2 Partial Double Ring (PDR) Lattice Design

In March 2015, we published the Preliminary Conceptual Design Report (Pre-CDR) for CEPC-SPPC [4]. In that report, we choose the single-ring scheme for CEPC. The synchrotron radiation power of CEPC is as high as 50 MW and its goal is to deliver a peak luminosity greater than 10^{34} cm^{-2} s^{-1} per IP [7,8]. The e^+e^- beams are in the same pipe, therefore requiring the adoption of a pretzel orbit. And this single-ring scheme is not

suitable as a high luminosity Z factory. As a solution to these problems we have considered a partial double ring (PDR) scheme [9, 10]. This scheme can get rid of the pretzel orbit and accommodate more bunches. We can get a higher luminosity with lower power and create a machine that is suitable to serve as a high luminosity Z factory. Meanwhile, there are also many challenges to overcome, including crossing angle and crab waist, electron cloud problem, and beam loading due to bunch train operation.

2.2.2.1 PDR Lattice Layout

We choose a double ring scheme for e^+e^- at IP1 and IP3. The total length of this part is about 3.2 km. The arcs of both side of IP1 and IP3 are kept the same as in the Pre-CDR single ring scheme. The other straight sections' lengths are also kept the same. Figure 2.2.5 is the layout of the CEPC partial double ring (PDR part and arc part) and the detail of the PDR part.

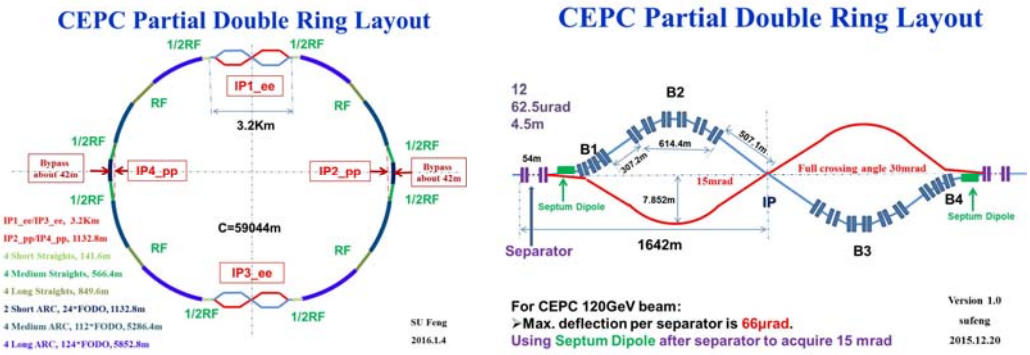

Figure 2.2.5. CEPC partial double ring layout (whole ring and PDR part).

The full crossing angle in the CEPC partial double ring scheme is 30 mrad. If we assume the final focus system (FFS) length is about 500 m, then the largest distance at the end of the FFS is about 7.5 m and between the two separated pipes is about 15 m. At the start of the double ring, we need to use an electrostatic separator to separate the electron and positron beams. We choose the electrostatic separator parameters from experience at LEP. The maximum operating field strength is 2 MV/m. The length of electrostatic separator is 4.5 m [11]. For beam energy 120 GeV, the maximum deflection per separator is about 66 urad. We choose 12 electrostatic separators to work together to obtain a deflection 0.75 mrad, each separator deflecting 62.5 urad. After those separators, we use a straight section to obtain a large separation between the two beams. After that we use a group of dipoles (B1) to obtain the other 14 mrad and suppress the dispersion to zero. To carry out the simulation of the separators using MAD we replace the separators with dipoles having the same length and deflection angle. The scheme is shown in Fig. 2.2.5. We use a group of dipoles to bend the beam, which are shown in that figure as B2. B3, B4 are the symmetrical to B2 and B1. Each group (for example B2) has 16 dipoles in 8 FODO cell and 8 half-strength dipoles in 2 dispersion suppressor sections, and each dipole bends the beam 1.5 mrad and a half-strength dipole bends the beam 0.75 mrad. This scheme can keep the dispersion 0 at the two sides of this bending section [12]. We use straight FODO instead of final focus system optics. The total length of this layout is about 3.2 km.

2.2.2.2 PDR Lattice without FFS

2.2.2.2.1 Orbit and Optics without FFS

We have designed the partial double ring lattice using MAD. Figure 2.2.6 shows the beta function and Figure 2.2.7 shows the orbit of the PDR part without the FFS.

2.2.2.2.2 Dynamic Aperture without FFS

Figure 2.2.8 is the dynamic aperture of the partial double ring lattice without the FFS. The on-momentum dynamic aperture is about 45 σ_x in horizontal plane and 780 σ_y in vertical plane. But for the off-momentum particles the dynamic aperture is only about 23σ_x in the horizontal plane for dp/p=1.5% and almost 0 for dp/p=2%.

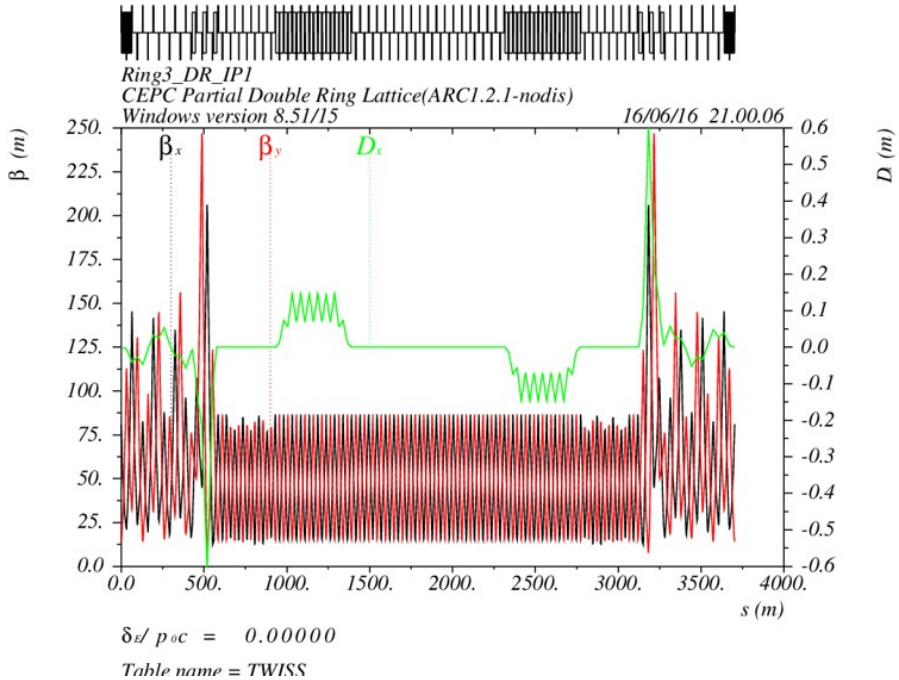

Figure 2.2.6. Beta function of the CEPC PDR part without FFS

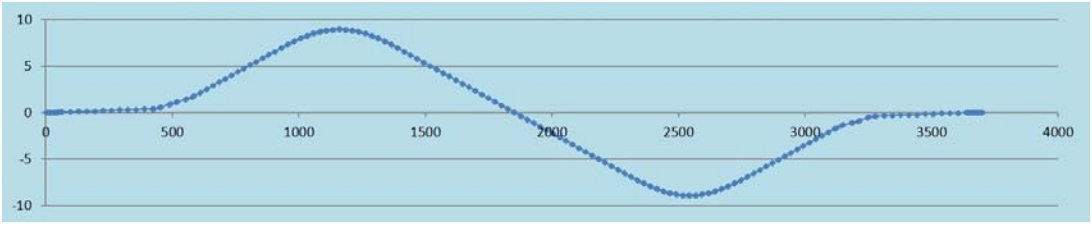

Figure 2.2.7: Orbit in the CEPC PDR part without FFS

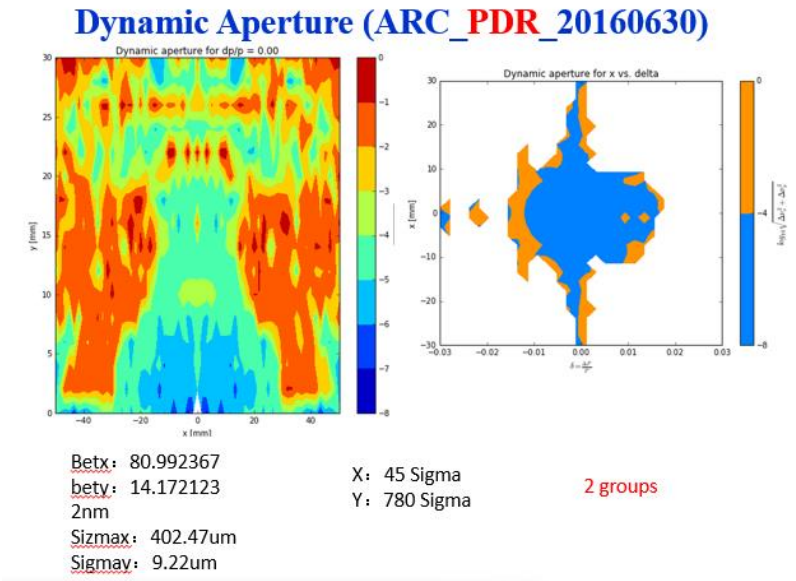

Figure 2.2.8. Dynamic aperture for the CEPC partial double ring lattice without FFS

2.2.2.3 PDR Lattice with FFS

2.2.2.3.1 Orbit and Optics with FFS

In this section, we insert the lattice of the FFS described in Sec. 2.2.1 into the partial double ring lattice. Figure 2.2.9 is the beta function, and Figure 2.2.10 is the orbit for the PDR lattice with FFS.

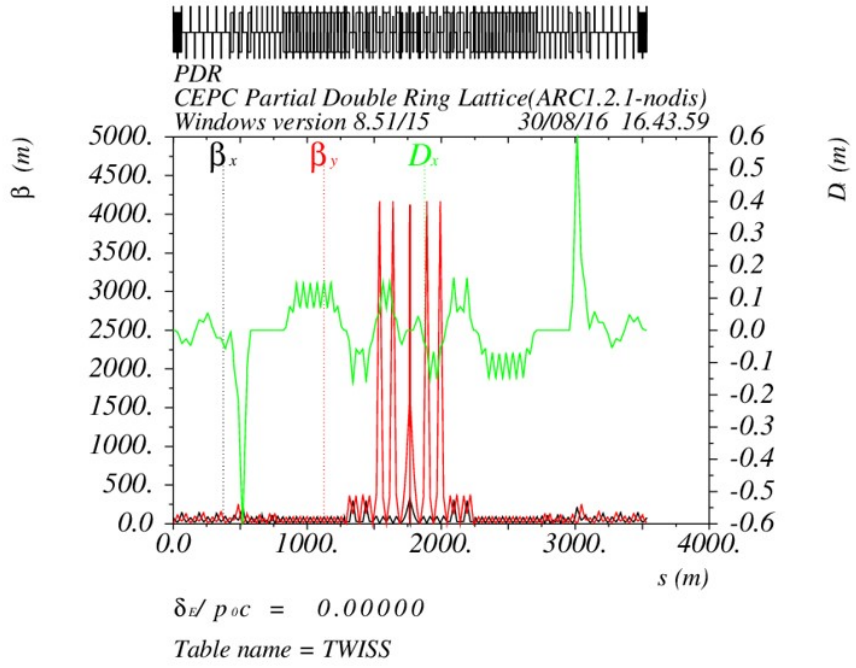

Figure 2.2.9: Beta function for the PDR lattice with FFS.

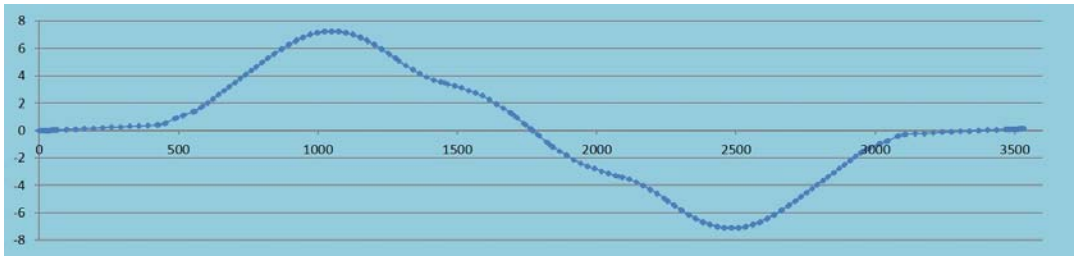

Figure 2.2.10. Orbit for the PDR lattice with FFS.

2.2.2.3.2 Dynamic Aperture with FFS

Figure 2.2.11 shows the dynamic aperture of the PDR lattice with FFS after it is optimized by the method called Multi-objective Optimization Genetic Algorithm (MOGA). We can see that the dynamic aperture becomes much better than before with only 2 groups of sextupoles. The on-momentum dynamic aperture is about 18 σ_x in the horizontal plane and 40 σ_y in the vertical plane. And the off-momentum particles dynamic aperture is much larger than before, about 10 σ_x horizontally for dp/p=1% and 4σ_x for dp/p=2%. In the vertical plane, the dynamic aperture is also much bigger than before.

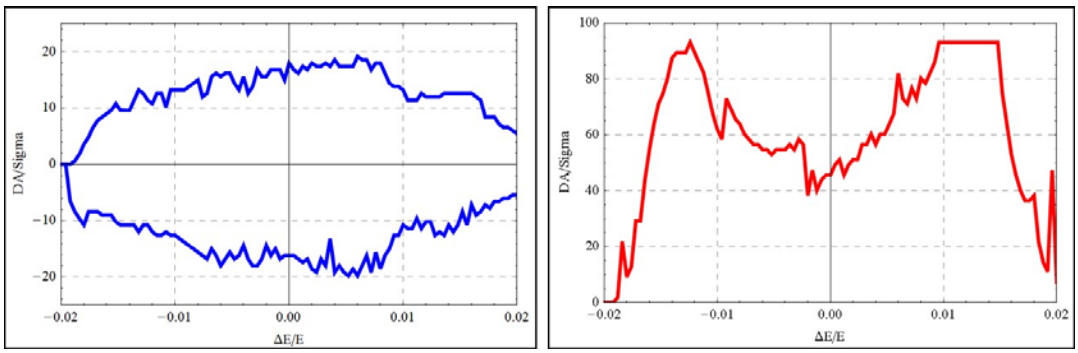

Figure 2.2.11. Dynamic aperture for the PDR lattice with FFS after optimization by MOGA.

2.2.3 Advanced Partial Double Ring (APDR) Lattice Design

The parameters are almost the same as with the PDR scheme. The beam loading and sawtooth effect is very serious in the partial double ring scheme. So we introduce the advanced partial double ring scheme with 8 PDR sections in the ring. Figure 2.2.12 is the layout. Figure 2.2.13 shows the optics for the APDR scheme and Figure 2.2.14 the dynamic aperture with 2 groups sextupoles keeping the first order dispersion a little larger than 0.

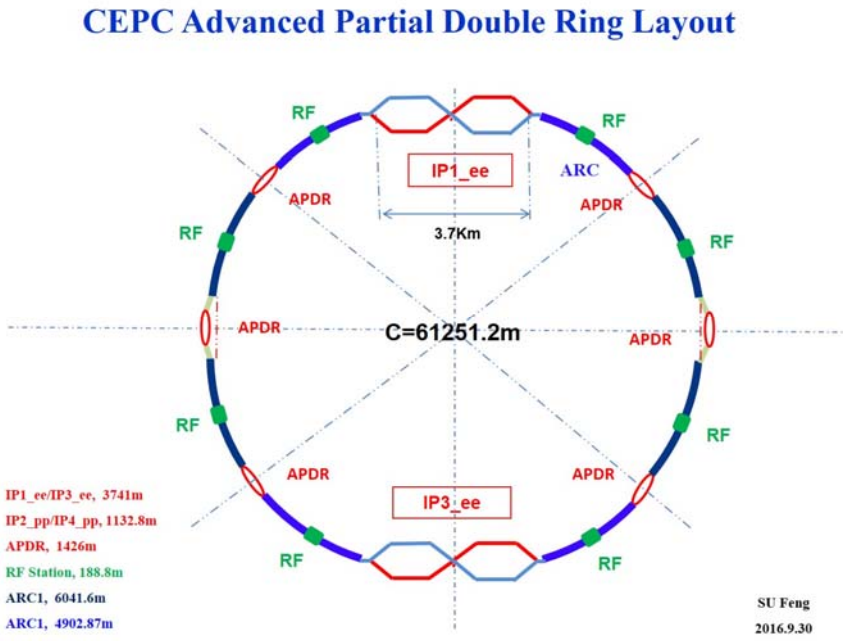

Figure 2.2.12. CEPC advanced partial double ring layout

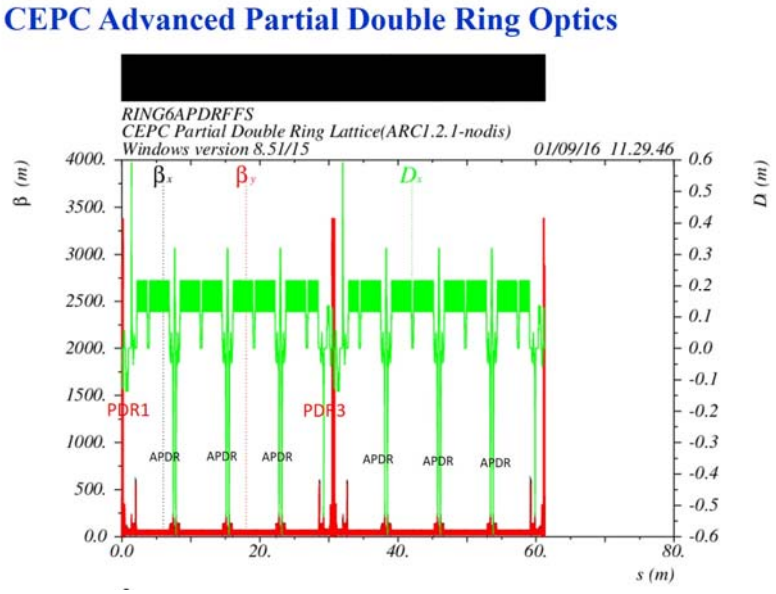

Figure 2.2.13: Optics of the CEPC advanced partial double ring scheme.

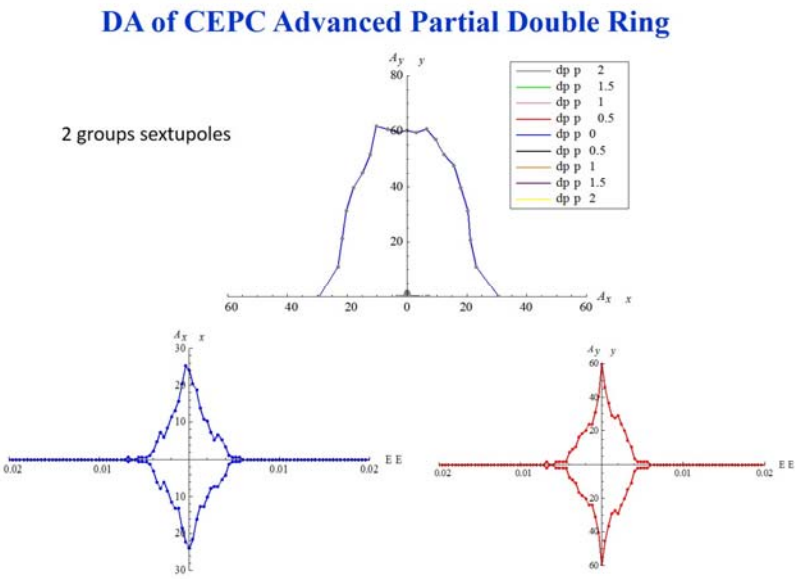

Figure 2.2.14. Dynamic aperture of the CEPC advanced partial double ring scheme.

2.2.4 Double Ring Lattice Design

A full double ring design of for CEPC has been considered. The parameters are kept almost the same as with the partial double ring scheme. Figure 2.2.15 is the layout and Figure 2.2.16 is the dynamic aperture for the double ring scheme with 2 groups of sextupoles keeping the first order dispersion a little larger than 0.

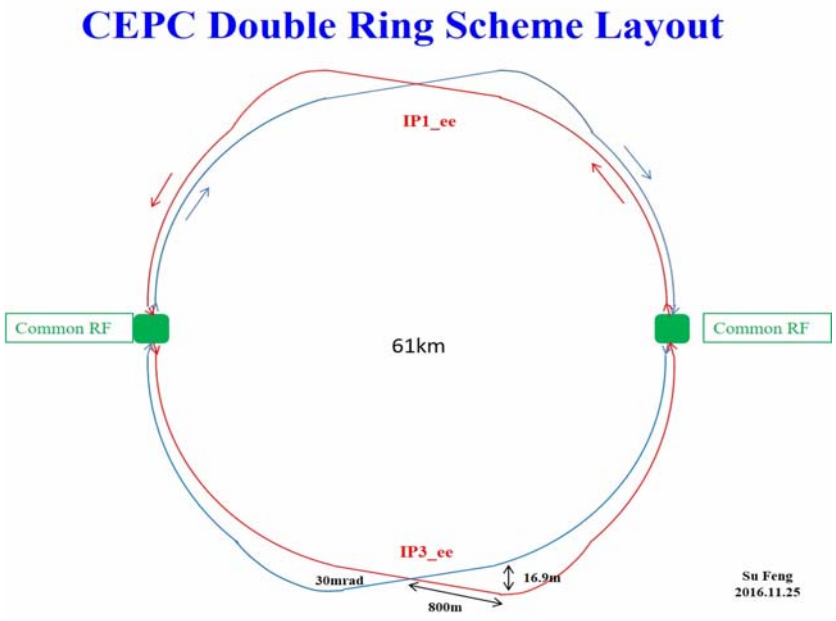

Figure 2.2.15: Layout of the CEPC double ring scheme.

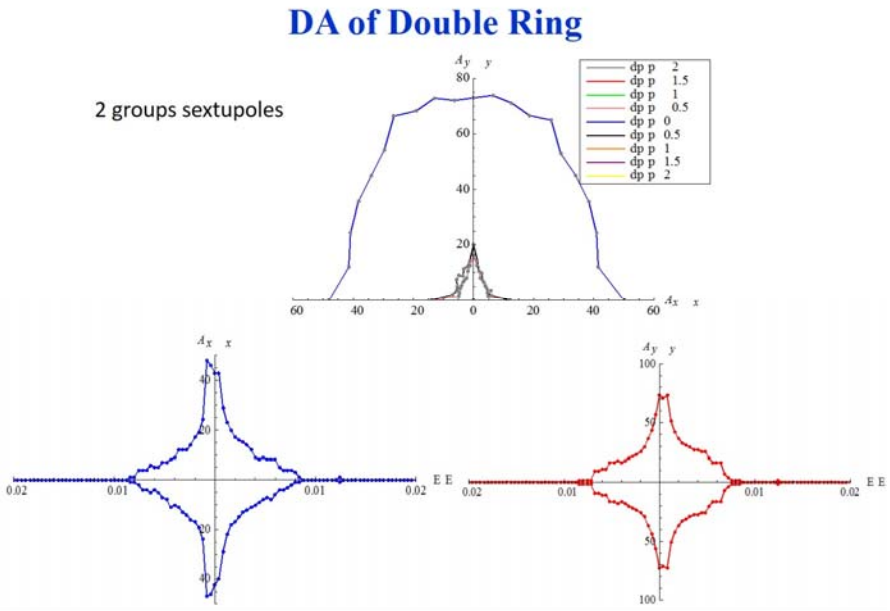

Figure 2.2.16. Dynamic aperture of the CEPC double ring scheme.

2.2.5 Summary

We have presented the details of the CEPC partial double ring lattice design and shown the dynamic aperture study and optimization. The first version of the CEPC partial double ring lattice has been done and the dynamic aperture needs further optimization. At this point in the design work the DA of CEPC with PDR without FFS has been improved, but the DA with FFS is not good enough. These results indicate that there still is lots of work to be done to optimize the design.

2.2.6 References

1. F. Zimmermann, HE-LHC \& VHE-LHC accelerator overview (injector chain and main parameter choices), Report of the Joint Snowmass-EuCARD/AccNet-HiLumi LHC meeting, Switzerland, 2013
2. F. Zimmermann, M. Benedikt, H. Burkhardt et al, FCC-ee Overview, in Proceedings of HF2014, edited by N. Zhao and V. R. Schaa, p.6-15
3. Layout and Performance, in LHC Design Report Volume 1, European Organization for Nuclear Research, 2004, p21-22.
4. The CEPC-SPPC Study Group, \textit{CEPC-SPPC: Pre-CDR, Volume II - accelerator} (March, 2015, IHEP-CEPC-DR-2015-01), p.28-35
5. J. Gao, Review of some important beam physics issues in electron positron collider designs, Modern Physics Letters A, Vol. 30, No. 11, p. 1530006, 2015.
6. F. Su et al., Method study of parameter choice for a circular proton-proton collider, Chinese Physics C, Vol. 40, No. 1, p. 017001, 2016.
7. D. Wang, J. Gao, \textit{etc.}, Optimization parameter design of a circular e+e- Higgs factory, \textit{Chinese Physics C}, vol. 37, no. 9, p. 97003-0970, 2013.
8. M. Xiao, J. Gao, \textit{etc.}, Study on CEPC performances with different collision energies and geometric layouts, \textit{Chinese Physics C}, vol. 40, no. 8, 2016.

9. J. Gao, ultra-low beta and crossing angle scheme in CEPC lattice design for high luminosity and low power, private note, \textit{IHEP-AC-LC-Note2013-012}, Jun. 2013.
10. M. Koratzinos, F. Zimmermann, Mitigating performance limitations of single beam-pipe circular e+e- colliders, in \textit{Proc. IPAC'15}, Richmond, VA, USA, May 2015, paper TUPTY058, pp. 260-261.
11. W. Kalbreier, \textit{etc.}, Layout, design and construction of the electrostatic separation system of the LEP e+e- collider, CERN, Geneva, Switzerland.
12. F. Su, J. Gao, \textit{etc.}, CEPC partial double ring lattice design and SPPC lattice design, IAS White Paper, submitted for publication, Apr. 2016.
13. F. Su, J. Gao et al, "SPPC Parameter Choice and Lattice Design", TUPMW001, Proceedings of IPAC2016.
14. F. Su, J. Gao et al, "CEPC Partial Double Ring Lattice Design", THPOR009, Proceedings of IPAC2016.

2.3 Beam Instability

2.3.1 Introduction

In CEPC, high beam current is required to achieve the design luminosity. Interaction of an intense charged particle beam with the vacuum chamber may lead to collective instabilities. These instabilities will induce beam quality degradation or beam loss, and finally restrict the luminosity of the machine. So the study of beam instability is essential in the design of a new machine. In this section, the impedance budget for the CEPC main ring is first given. Based on impedance studies, beam instabilities due to single bunch and multi bunch effects are estimated. Instabilities due to interaction of the electron beam with the residual (positive) ions and instabilities from positron beam interaction with the electron cloud are also investigated.

2.3.2 Impedance Threshold

The limitation on the longitudinal broadband impedance mainly comes from the microwave instability and bunch lengthening. Since longer bunch is beneficial in terms of Touschek lifetime and higher instability threshold, we are mainly concerned with the microwave instability, which can induce turbulent behavior on the longitudinal motion. The threshold of microwave instability can be estimated according to the Boussard or Keil-Schnell criteria [1, 2]

$$I_b^{th} = \frac{\sqrt{2\pi}\alpha_p \frac{E}{e}\sigma_{e0}^2\sigma_{l0}}{R\left|\frac{Z}{n}\right|_{eff}}, \qquad (2.3.1)$$

where α_p is the momentum compaction factor, E is the beam energy in eV, σ_{e0} is the rms energy spread, σ_{l0} is the rms bunch length in meters, and R is the radius of the storage ring, $|Z/n|_{eff}$ is the longitudinal effective impedance expressed as

$$\left(\frac{Z}{n}\right)_{eff} = \frac{\omega_0 \sum_{p=-\infty}^{\infty} \frac{Z_{\|0}(\omega_p)}{\omega_p} h_m(\omega_p)}{\sum_{p=-\infty}^{\infty} h_m(\omega_p)}, \tag{2.3.2}$$

where $\omega_p = \omega_0(pn_B + \mu + m\nu_s)$, μ is the coupled bunch mode number, m is the azimuthal mode number, $h_m(\omega) \propto |\tilde{\lambda}_m(\omega)|^2$ is the spectral density, $\tilde{\lambda}_m(\omega)$ is the Fourier transform of the line density, for Gaussian bunch, $h_m(\omega)$can be expressed as $(\omega\sigma_\tau)^{2m} e^{-\omega^2\sigma_\tau^2}$, with σ_τ the rms bunch length in time.

This implies that the limit on the longitudinal broadband impedance at design current is

$$|Z/n|_{eff} < 24\text{m}\Omega, \tag{2.3.3}$$

which suggests that broadband impedance should be well controlled.

The limitation on the transverse broadband impedance mainly comes from the transverse mode coupling instability, which occurs when the frequencies of two neighboring head tail modes approach each other. For Gaussian bunches, the threshold current can be expressed with the transverse kick factor [3]

$$I_b^{th} = \frac{2Q_s\omega_0 E/e}{\sum_j \beta_{y,j}\kappa_{y,j}}\Theta, \tag{2.3.4}$$

where Q_s is the synchrotron tune, ω_0 is the angular revolution frequency, $\Theta \approx 0.7$, $\beta_{y,j}$ is the betatron function at the j^{th} impedance element, $\kappa_{y,j}$ is the transverse kick factor defined in terms of the transverse impedance $Z_\perp(\omega)$ or wake potential $W_{\perp\lambda}(\tau)$

$$\kappa_y = \frac{1}{\pi}\int_0^\infty d\omega \,\text{Im}\, Z_\perp(\omega)h(\omega) = \int_{-\infty}^{\infty} d\tau W_{\perp\lambda}(\tau)\lambda(\tau). \tag{2.3.5}$$

For Gaussian bunch with rms $\sigma = \sigma_z/\beta c$,

$$\lambda = e^{-t^2/2\sigma^2}/(\sqrt{2\pi}\sigma), \quad h(\omega) = e^{-\omega^2\sigma^2}. \tag{2.3.6}$$

This gives the limit on the total transverse kick factor:

$$\kappa_{y,total} = \frac{1}{\beta_{y,ave}}\sum_j \beta_{y,j}\kappa_{y,j} < 68.9 \text{ kV/pC/m}. \tag{2.3.7}$$

The narrowband impedances are mainly contributed by cavity like structures. These impedances may induce coupled bunch instabilities in both the longitudinal and transverse planes. Considering n_B uniformly filled bunches, the growth rate in the longitudinal plane is [4]

$$\frac{1}{\tau_\|} = \frac{I_0\eta}{4\pi(E/e)\nu_s}\sum_{p=-\infty}^{\infty} \omega_p e^{-(\omega_p\sigma_\tau)^2}\,\text{Re}\, Z_0(\omega_p), \tag{2.3.8}$$

where $\omega_p = \omega_0(pn_B + \mu + \nu_s)$. The limitation on the shunt impedance of a HOM can be evaluated in a resonant condition when the resonance frequency overlaps the beam

spectrum line. The growth rate of the coupled bunch instability is less than the synchrotron radiation damping. This gives

$$\frac{f}{\mathrm{GHz}}\frac{\mathrm{Re}\,Z_{\parallel}}{\mathrm{k\Omega}}e^{-(2\pi f\sigma_\tau)^2} < 6.5. \tag{2.3.9}$$

In the transverse case, the growth rate can be written as [4]

$$\frac{1}{\tau_\perp} = -\frac{I_0 c}{4\pi\beta(E/e)\nu_\beta}\sum_{q=-\infty}^{\infty} e^{-(\omega_q-\xi\omega_0/\alpha_p)^2\sigma_\tau^2}\,\mathrm{Re}\,Z_\perp(\omega_q), \tag{2.3.10}$$

with $\omega_q = \omega_0(qn_B + \mu + \nu_\beta)$, and $\xi = d\nu_\beta/\delta p$. Similarly, we find that the threshold for the transverse narrowband impedance is

$$\frac{\mathrm{Re}\,Z_\perp}{\mathrm{M\Omega/m}}e^{-(2\pi f\sigma_\tau)^2} < 3.4. \tag{2.3.11}$$

2.3.3 Impedance Model

The impedance and wake are calculated with analytical formulas along with numerical simulations using ABCI [5] and CST [6]. The wake potentials and impedances are calculated with a bunch length of 4.1 mm. The vacuum components considered in the calculation includes resistive wall, RF cavities, flanges, bellows, BPMs and pumping ports. A more complete impedance model will be calculated as additional vacuum components are designed.

The wake contribution of different impedance objects at the nominal bunch length of 4.1mm are shown in Figure 2.3.1. Table 2.3.1 lists the impedance budget of the objects that have been considered, where $Z_\parallel/n$ is the longitudinal effective impedance, k_l is the loss factor, R and L are effective resistance and inductance of the components obtained by fitting the wake potential with the Bane's formula [7].

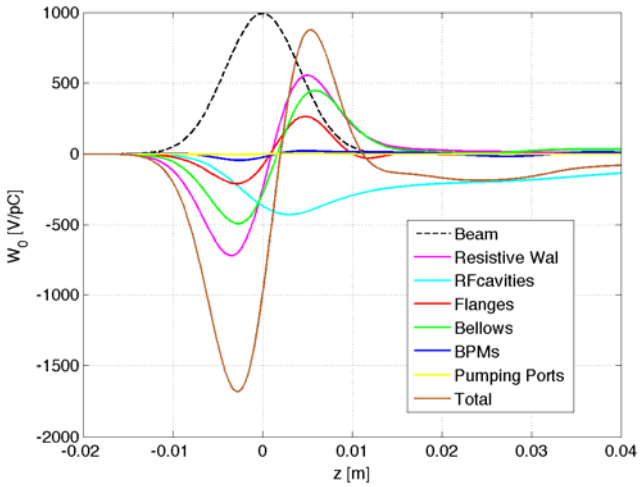

Figure 2.3.1: Longitudinal wake potential at nominal bunch length of 4.1mm.

Table 2.3.1: Summary of the impendence budget.

Components	Number	R, kΩ	L, nH	$Z_{\|\|}/n$, mΩ	k_{loss}, V/pC	HOM power, kW
Resistive wall	-	6.7	487.7	17.0	138.4	106.3
RF cavities	384	14.9	-132.7	-	307.5	236.1
Flanges	~10000	0.7	165.5	5.8	15.1	11.6
BPMs	2300	0.6	21.4	0.7	11.6	8.9
Bellows	~10000	5.9	331.5	11.6	122.3	93.9
Pumping ports	~10000	0.007	3.1	0.1	0.1	0.1
Total		28.8	876.5	35.2	595.0	456.9

The calculation gives total longitudinal effective impedance of 35 mΩ. The total longitudinal loss factor is 0.6 kV/pC/m, and the corresponding total HOM power is around 457kW. The longitudinal impedance is mainly contributed by the resistive wall impedance and the elements with large quantity. We can see that the broadband impedance budget already exceeds the analytical threshold. Detailed studies with simulation are required. Moreover, a better impedance model is needed to include more impedance contributors.

2.3.4 Single-Bunch Effects

Broadband impedance can induce single bunch instabilities, which will lead to emittance blow-up, bunch lengthening or beam losses. Since the bunch intensity is quite high in CEPC, the single bunch instability is more critical compared to the coupled bunch instability.

2.3.4.1 Microwave Instability

The longitudinal microwave instability is estimated according to the Boussard or Keil-Schnell criterion. With a longitudinal impedance of $|Z_{\|}/n|$=35 mΩ, the threshold bunch current is around 0.17 mA, which is lower than the design current of 0.25mA. This instability will rarely induce beam losses, but may reduce the luminosity due to the deformed beam distribution and increase of the energy spread. For short bunches, the impedance seen by the beam is dominated by high frequency resonances; therefore, the analytical criteria used is often believed to be too weak. However, the high frequency part of the impedance may lead to turbulent distributions in longitudinal phase space. More detailed simulation studies are required.

2.3.4.2 Coherent Synchrotron Radiation

Coherent synchrotron radiation (CSR) is generated when beam passes through the bending magnets. It can induce microwave instability at high bunch intensity. According to the studies in Ref. [8], coasting beam theory with shielding impedance is used to estimate the threshold. The beam becomes unstable when

$$I_b > \frac{3\sqrt{2}\alpha_p \gamma \sigma_e^2 I_A \sigma_z}{\pi^{3/2} h}. \qquad (2.3.12)$$

where α_p is the momentum compaction, γ the relativistic energy, σ_e the relative energy spread, and I_A=17045 A. The instability threshold given by analytical theory is about 30 times higher than the design bunch population. Therefore, CSR is not a concern in the present design.

2.3.4.3 Transverse Beam Tilt

In the transverse plane, when a beam passes through an impedance with a transverse offset, the tail particles will receive transverse kicks, which can lead to a transverse displacement of the bunch tail at the interaction point and increase the beam emittance. With the parameters of CEPC, the kick angle along the bunch due to a single RF cavity is shown in Fig. 2.3.2. The maximum kick angle at the bunch tail is 1.2 nrad. As there are 384 cavities located in 8 places in the ring, the displacement at IP is around 23 nm, which is about one fifth of the beam size at the IP.

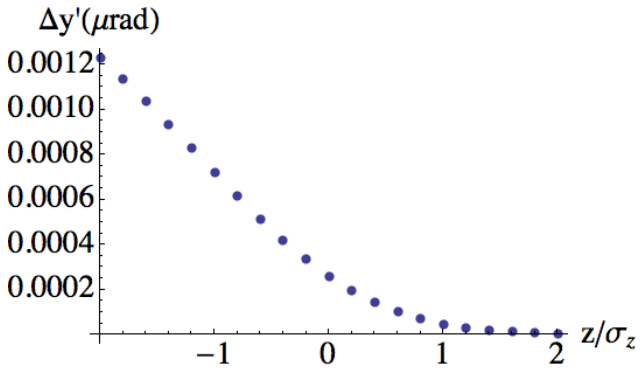

Figure 2.3.2: Transverse kick angle along the bunch due to single RF cavity in CEPC ring.

2.3.4.4 Transverse Mode Coupling Instability

The threshold for the transverse mode coupling instability is estimated using both an analytical formula and Eigen mode analysis. For a Gaussian bunch, the threshold intensity can be expressed with the transverse kick factor [9, 10]

$$I_0^{th} = \frac{2\nu_s \omega_0 E/e}{\sum_j \beta_{y,j}\kappa_{y,j}}\Theta. \qquad (2.3.13)$$

where ν_s the longitudinal tune, ω_0 the angular revolution frequency, E the beam energy, $\beta_{y,j}$ the betatron function at the jth impedance element, $\kappa_{y,j}$ the transverse kick factor, and $\Theta \approx 0.7$. With the impedance model considered, the total kick factor is 18.9 kV/pC/m. The analytical criterion gives a threshold bunch current of 0.9mA.

The Eigen mode analysis gives the dependences of the head-tail mode frequencies on the bunch current as shown in Fig. 2.3.3. The Eigen mode analysis shows the threshold bunch current is around 1.9 mA, which is about two times higher than the analytical formula. Both analyses leave enough safety margin to avoid transverse mode coupling instability.

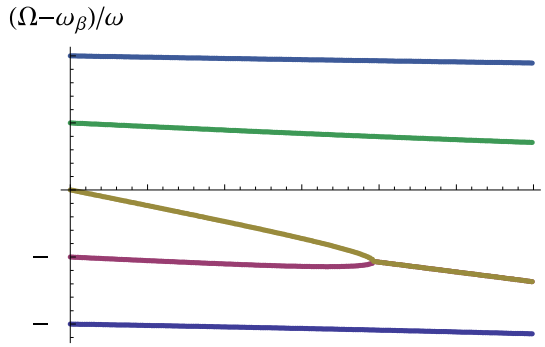

Figure 2.3.3: Dependence of the head-tail mode frequencies on the bunch current**.**

2.3.5 Multi-bunch Effects

In large-scale circular colliders, the revolution frequency is low, and this results in the generation of dense beam spectra and is more easily coupled to narrowband impedances. The interaction of the beam with the narrowband impedances may induce coupled bunch instabilities.

In the present design of CEPC, a partial double ring design is proposed. The electron and positron beam will share the beam pipe except in the collision region. Each beam has a long bunch train of 67 bunches, which will be filled in about 3.2 km in the ring circumference, so that there is a long beam gap between the bunch train. Therefore, multi-bunch effects with uneven fills are investigated.

2.3.5.1 Coupled Bunch Instabilities with Uneven Fills

Coupled bunch instabilities are uaually studied with equal bunch spacing [4]. In the general framework of an uneven filled ring, there are two effects due to the uneven fill: damping from the additional tune spread and modulation coupling of the strong even-fill eigenmodes. Here, only the second effect is investigated.

Consider a long bunch train of M identical bunches with bunch spacing of T_b. The longitudinal and transverse beam oscillation with rigid bunch model can be described as

$$\ddot{z}_n(t)+\omega_s^2 z_n(t)=-\frac{Nr_0\alpha_p c}{\gamma T_0}\sum_{m=0}^{M-1}\sum_{k=0}^{\infty}W_0'(-kC-(m-n)T_b c+z_n(t)-z_m(t-kT_0-(m-n)T_b)), \quad (2.3.14)$$

and

$$\ddot{y}_n(t)+\omega_\beta^2 y_n(t)=-\frac{Nr_0 c}{\gamma\beta T_0}\sum_{m=0}^{M-1}\sum_{k=0}^{\infty}y_m(t-(kT_0+(m-n)T_b))W_1(-(kT_0+(m-n)T_b))\cdot \quad (2.3.15)$$

respectively, where N is the bunch intensity, r_0 the classical radius of electron, T_0 the revolution time, β the relativ-istic velocity, and C the circumference. By solving the above equation, the tune shift can be ex-pressed in the form of impedances as

$$\Delta\Omega=\Omega-\omega_s=\frac{iNMr_0\alpha_p}{2\gamma T_0^2\omega_s}\sum_{p=-\infty}^{\infty}(\omega_0(p+\frac{\mu}{M})M'+\omega_s)Z_0(\omega_0(p+\frac{\mu}{M})M'+\omega_s), \quad (2.3.16)$$

$$\Delta\Omega=\Omega-\omega_\beta=-\frac{iNMr_0 c}{2\gamma\beta T_0^2\omega_\beta}\sum_{p=-\infty}^{\infty}Z_1(\omega_0(p+\frac{\mu}{M})M'+\omega_\beta). \quad (2.3.17)$$

where $M'=T_0/T_b$.

2.3.5.2 Transverse Resistive Wall Instability

One dominant contribution to the coupled bunch instability is the resonance at zero frequency of the transverse resistive wall impedance. Figure 2.3.4 shows the growth rate of the transverse resistive wall instability with different mode numbers. The growth rate for the most dangerous instability mode is 3.1 Hz, which is much lower than the transverse radiation damping. So the beam should be safe from the resistive wall coupled bunch instability.

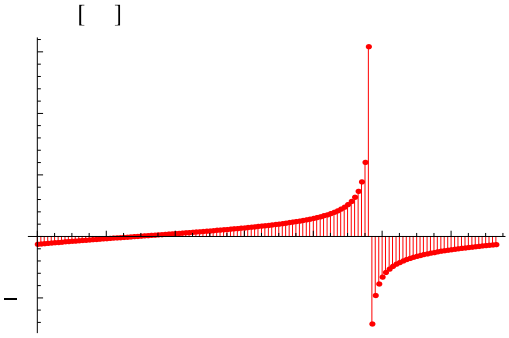

Figure 2.3.4: Growth rate of the transverse resistive wall instability with mode numbers.

2.3.5.3 Coupled Bunch Instability Induced by the RF HOMs

Another important contribution to the coupled bunch instability is from the HOMs of the accelerating cavities. To keep the beam stable, the rise time of any oscillation mode should be larger than the radiation damping time. At resonance, the threshold for the shunt impedances of any HOMs are given by

$$\frac{R_L^{thresh}}{\mathrm{M\Omega}}\frac{f_L}{\mathrm{GHz}} < \frac{2(E/e)\nu_s}{N_c I_0 \alpha_p \tau_z} = 16.9. \qquad (2.3.18)$$

and

$$\frac{R_T^{thresh}}{\mathrm{M\Omega/m}} < \frac{2(E/e)}{N_c f_{rev} I_0 \beta_{x,y} \tau_{x,y}} = 17.6. \qquad (2.3.19)$$

where N_c is the cavity number along the ring, f_L the frequencies of the HOMs, f_{rev} the revolution frequency in the ring, I_0 the beam current, $\tau_{x,y,z}$ the damping time in transverse and longitudinal directions, and $\beta_{x,y}$ the transverse beta functions. With two counter-rotating beam sharing the RF cavities, the threshold impedance could be further reduced by a factor of two.

However, considering the whole RF system, the threshold value greatly depends on the actual tolerances of cavity construction. Assuming the resonant frequencies of the RF cavities have a Gaussian distribution with rms frequency spread of 0.5MHz, the threshold shunt impedance considering the whole RF system can be increased by a factor of 50.

The threshold for the longitudinal impedance is estimated as shown in Fig. 2.3.5. The threshold for the transverse impedance is shown in Fig. 2.3.6.

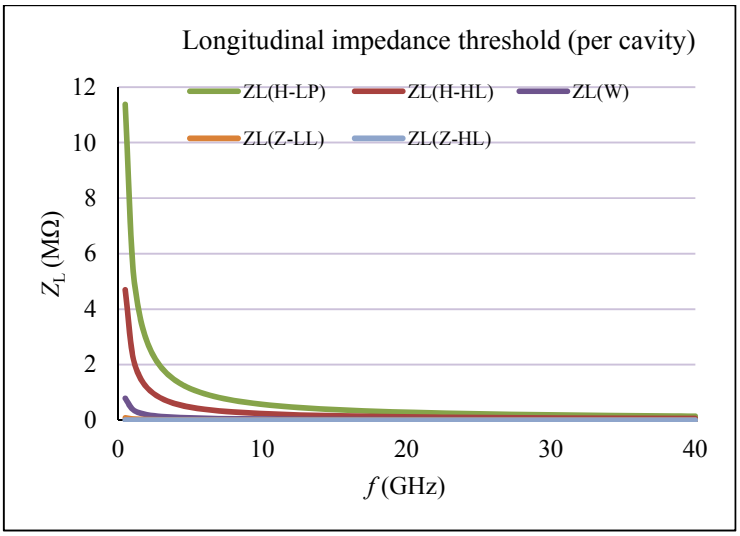

Fig. 2.3.6: Longitudinal impedance threshold of the RF HOM's.

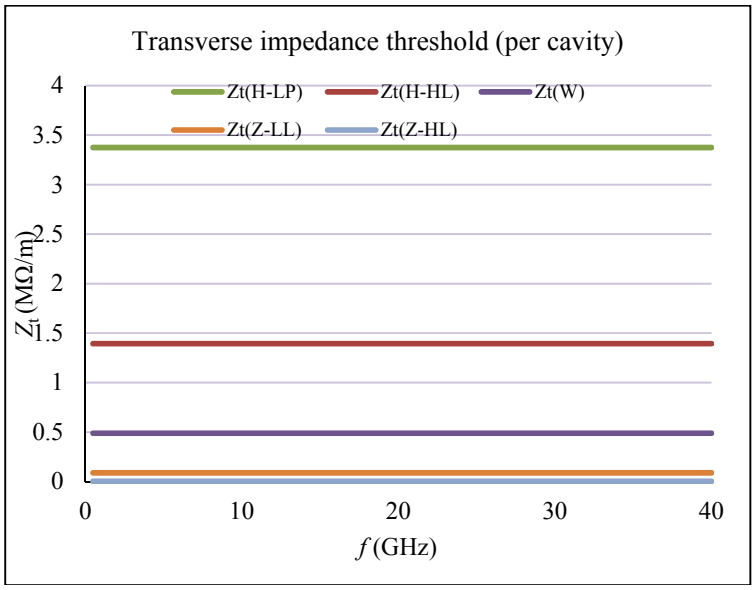

Fig. 2.3.7: Transverse impedance threshold of the RF HOM's.

2.3.6 Bunch Lengthening for Different Designs

An empirical equation for bunch lengthening in an electron storage ring is proposed based on ref. [11]. The equations are as follows:

$$R_z^2 = 1 + \frac{\sqrt{2\ell}R_{av}Rk(\sigma_{z0})I_b}{\gamma^{3.5}(R_z)^{\zeta}} + \frac{\ell(R_{av}Rk(\sigma_{z0})I_b)^2}{\gamma^7(R_z)^{2\zeta}} \qquad (2.3.20)$$

where $R_z = \sigma_z / \sigma_{z0}$,

$$\ell = \frac{576\pi^2 \varepsilon_0}{55\sqrt{3}\hbar c^3} \tag{2.3.21}$$

R_{av} is the average radius of the ring, R is the local bending radius, γ is the normalized particle energy, I_b is the bunch current, $k(\sigma_{z0})$ is the total longitudinal loss factor at natural bunch length, ε_0 is the permittivity in vacuum, $\hbar$ is Planck's constant, c is the velocity of light. If the SPEAR scaling law is used, $\zeta = 1.21$.

The energy spread is:

$$R_\varepsilon^2 = 1 + \frac{\ell (R_{av} R k(\sigma_{z0}) I_b)^2}{\gamma^7 (R_z)^{2\zeta}} \tag{2.3.22}$$

where $R_\varepsilon = \varepsilon_z / \varepsilon_{z0}$.

Then, a bunch lengthening equation and the equation for the increase in the energy spread of the bunch due to wake potential are given. According to ref. [12], we use a function of three parameters, i.e., bunch length σ_z, total loss factor $k(\sigma_z)$, and total inductance $L(\sigma_z)$, to describe the total wake potential of the machine. The expression is:

$$\begin{aligned} W(z) &= -ak(\sigma_z)\exp(-\frac{2z^2}{7\sigma_z^2}) \times \cos((1+\frac{2}{\pi}\mathrm{a\,tan}(\mathrm{a\,tan}(\frac{Z_i}{2Z_r})))\frac{z}{\sqrt{3}\sigma_z} + \mathrm{a\,tan}(\frac{Z_i}{2Z_r})) \\ &= Ak(\sigma_z) + Bk(\sigma_z)\frac{z}{\sigma_z} + Ck(\sigma_z)(\frac{z}{\sigma_z})^2 + O(z^3) \end{aligned} \tag{2.3.23}$$

where a=2.23, $Z_i = 2\pi L / T_0$, $Z_r = k(\sigma_z)\frac{T_b^2}{T_0}$, $T_0 = 2\pi R_{av} / c$, $T_b = 3\sigma_z / c$, R_{av} is the average radius of the ring, c is the velocity of light, z=0 corresponds to the center of the bunch.

$$A = -\frac{a}{\sqrt{1+(\frac{Z_i}{2Z_r})^2}} \tag{2.3.24}$$

$$B = \frac{0.289 a Z_i (1 + 0.637\,\mathrm{atan}(\mathrm{atan}(\frac{Z_i}{2Z_r})))^2}{Z_r \sqrt{1+(\frac{Z_i}{2Z_r})^2}} \tag{2.3.25}$$

$$C = \frac{a}{\sqrt{1+(\frac{Z_i}{2Z_r})^2}} \times (\frac{2}{7} + \frac{(1 + 0.637\,\mathrm{atan}(\mathrm{atan}(\frac{Z_i}{2Z_r})))^2}{6}) \tag{2.3.26}$$

With the wake potential and its Taylor expansion, the bunch lengthening, energy spread and the threshold of particle population inside the bunch are expressed as follows:

$$R_z^2 = 1 + \frac{eBk(\sigma_{z0}) J_\varepsilon I_b R}{m_0 c^3 \alpha C_q \gamma^3 (R_z)^\zeta} + \frac{\ell (R_{av} RBk(\sigma_{z0}) I_b)^2}{\gamma^7 (R_z)^{2\zeta}} \tag{2.3.27}$$

$$R_\varepsilon^2 = 1 + \frac{\ell (R_{av} RBk(\sigma_{z0}) I_b)^2}{\gamma^7 (R_z)^{2\zeta}} \tag{2.3.28}$$

$$C_q = \frac{55\hbar}{32\sqrt{3}m_0 c} \tag{2.3.29}$$

$$J_\varepsilon = 1 + \frac{\alpha R_{av}}{R} \tag{2.3.30}$$

$$N_{e,th} = \sqrt{\frac{2}{3}} \frac{\sigma_{z0} V \cos(\phi_{s0})}{eCk(\sigma_{z0}) T_0 f_{s0} \lambda_{rf}} \tag{2.3.31}$$

where T_0 is the revolution period, f_{S0} is the synchrotron oscillation frequency, λ_{rf} is the wavelength of RF field, φ_{s0} is the synchrotron phase and V is the peak RF field. $N_{e,th}$ is the so-called phase instability threshold above which the particles will execute stochastic motions.

2.3.6.1 Bunch Lengthening for the 61 km Circumference Design

The beam parameters for 61 km design is shown in Table 2.1.1.

The loss factor and inductance for different components are shown in Table 2.3.2. It is important to note that the bunch length for the impedance calculation is 4.1 mm. The coupling impedance is dominated by resistive wall impedance, vacuum elements with large numbers (RF cavities, flanges, BPMs, bellows, etc.) and vacuum elements with large impedances (IP duct, collimators, kickers, etc.).

Table 1.3.2: Loss factor and inductance for different components.

Components	Number	R, kΩ	L, nH	$Z_\parallel/n$, mΩ	k_{loss}, V/pC
Resistive wall	-	6.7	487.7	17.0	138.4
RF cavities	384	14.9	-132.7	-	307.5
Flanges	~10000	0.7	165.5	5.8	15.1
BPMs	2300	0.6	21.4	0.7	11.6
Bellows	~10000	5.9	331.5	11.6	122.3
Pumping ports	~10000	0.007	3.1	0.1	0.1
Total(σ=4.1mm)		28.8	876.5	35.2	595.0

The total loss factor of the different components shown in Table 2.3.2 is 595 V/pC (σ=4.1 mm), the total inductance is 876.5 nH. The SPEAR scaling law shows $k \sim \sigma^{-1.21}$ [13]. So, when σ_z=2.9 mm, the total loss factor is 904.66 V/ pC. The bunch lengthening results for the 61 km design parameters are shown in Table 2.3.3. The bunch lengthening for H-low power design is 32.9% and the energy spread is 8.4%. Fig. 2.3.8 shows the bunch lengthening (black line) and energy spread increasing (red line) vs. the bunch current with the H-low power design. Fig. 2.3.9 shows that the wake potential for the whole ring using equation (2.3.23).

Table 2.3.3: Bunch lengthening results for 61 km design parameters.

	H-HL	H-LP	W	Z
Bunch number	107	70	400	1000
Beam current (mA)	16.9	11.0	36.5	67.6
SR power /beam (MW)	50	32.5	21.3	4.1
V_{RF} (GV)	3.48	3.51	0.74	0.11
f_{RF} (MHz)	650	650	650	650
Total σ_z (mm)	2.95	2.9	3.35	4.0
Cavity no.	384	384	384	384
loss factor (V/pC)	886.14	904.66	759.77	613.05
inductance (nH)	876.5	876.5	876.5	876.5
R_z	1.325	1.329	1.566	2.414
$R\varepsilon$	1.082	1.084	1.215	1.888

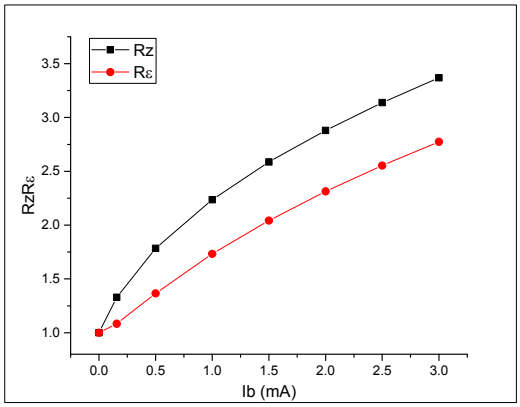

Fig. 2.3.8: The bunch lengthening (black line) and energy spread increase (red line) vs. the bunch current.

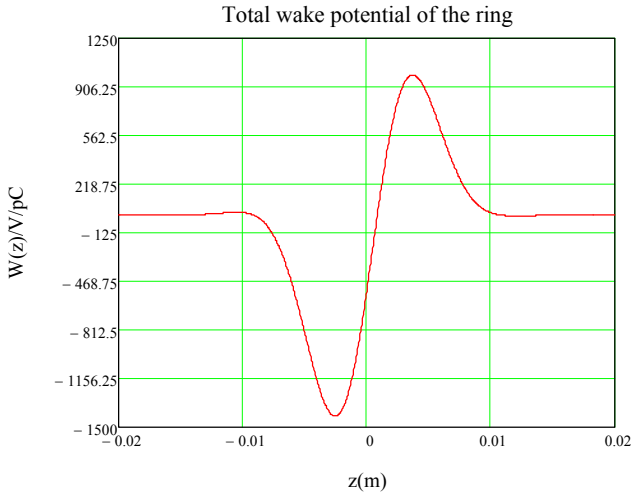

Fig. 2.3.9: The wake potential for the whole ring using equation (2.3.23).

2.3.6.2 Bunch Lengthening for the 100 km Circumference Design

The beam parameters for the 100-km design is shown in Table 2.1.2.

The loss factor and inductance for different components are shown in Table 2.3.3. It is important to note that the bunch length used for the impedance calculation is 2.9 mm.

Table 2.3.3: Loss factor and inductance for different components.

Components	Number	R, kΩ	L, nH	$Z_{\parallel}/n$, mΩ	k_{loss}, V/pC
Resistive wall	-	15.7	863.1	16.3	458
RF cavities	384	12.6	-79.1	-1.5	366.7
Flanges	~18500	5.2	310.4	5.8	151.6
BPMs	4300	1.5	30.4	0.6	42.6
Bellows	~18500	17.7	375.1	7.1	515.6
Pumping ports	~18500	0.02	5.3	0.1	0.7
Total(σ=2.9mm)		52.7	1505.2	28.4	1535.2

The total loss factor of the different components shown in Table 2.3.3 is 1535.2 V/pC (σ=2.9 mm), the total inductance is 1505.2 nH. SPEAR scaling law shows $k \sim \sigma^{-1.21}$ [13]. So, when σz=4 mm, the total loss factor is 1040.4 V/ pC. The bunch lengthening results for 100 km design parameters are shown in Table 2.3.4. The bunch lengthening for H-low power design is 41.3% and the energy spread is 12.6%. Fig. 2.3.10 shows the bunch lengthening (black line) and energy spread increase (red line) vs. the bunch current with the H-low power design. Fig. 2.3.11 shows the wake potential for the whole ring using equation (2.3.23).

Table 2.3.4: Bunch lengthening results for 100 km design parameters.

	H-HL	H-LP	W	Z		
Bunch number	644	425	1000	10520	65716	65716
Beam current (mA)	29.97	19.8	50.6	232.1	1449.7	1449.7
SR power /beam (MW)	50	33	16.7	8.0	50	50
V_{RF} (GV)	2.22	2.22	0.63	0.11	0.11	0.11
f_{RF} (MHz)	650	650	650	650	650	650
Total σ_z (mm)	2.9	2.9	3.9	4.0	4.0	4.0
Cavity no.	384	240	128	16	64	384
loss factor (V/pC)	1535.2	1397.688	901.88	802.194	812.548	1040.4
inductance (nH)	1505.2	1534.862	1557.93	1581.004	1577.708	1505.2
R_z	1.444	1.413	1.894	2.707	2.719	2.986
$R\varepsilon$	1.142	1.126	1.45	2.152	2.164	2.411

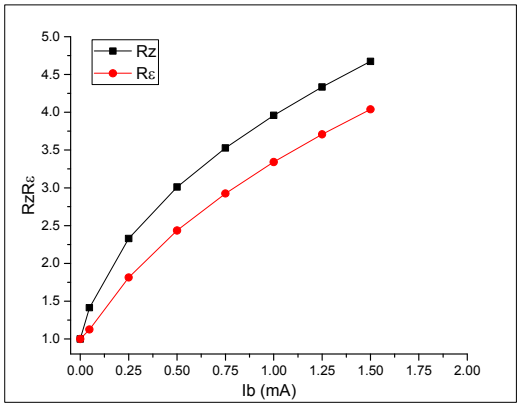

Fig. 2.3.10: The bunch lengthening (black line) and energy spread increase (red line) vs. the bunch current.

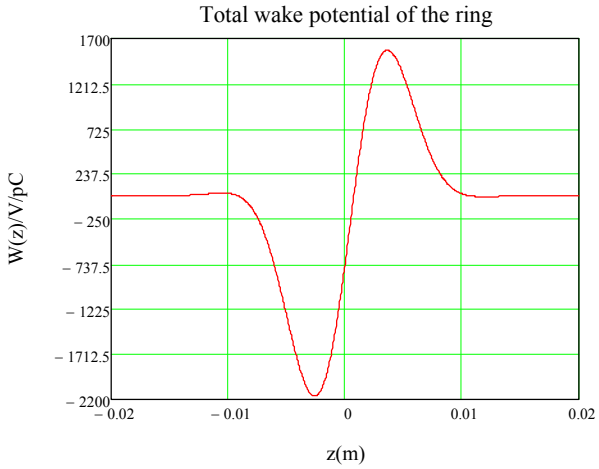

Fig. 2.3.11: The wake potential for the whole ring using equation (2.3.23).

2.3.7 References

1. E. Keil, W. Schnell, CERN/ISR-TH/69-48 (1969).
2. D. Boussard, CERN/PS-BI (1972).
3. S. Krinsky, Proceedings of PAC07, TUPMS074 (2007).
4. A. Chao, Physics of collective beam instabilities in high energy accelerators, John Wiley & Sons, Inc., (1993).
5. ABCI Home Page, http://abci.kek.jp/abci.htm
6. www.cst.com
7. K. Bane, SLAC-PUB-14151 (2010).
8. Y. Cai, "Theory of microwave instability and coherent synchrotron radiation in electron storage rings", Proceedings of IPAC2011, 2011.
9. S. Krinsky et al., "Collective effects in the NSLS-II storage ring", Proceedings of PAC07, 2007.
10. L. Wang and G. Stupakov, "Transverse single bunch instability in PEP-X", SLAC-PUB-13658, 2009.

11. J. Gao, On the single bunch longitudinal collective effects in electron storage rings, Nuclear Instruments and Methods in Physics Research A 491(2002) 1-8.
12. J. Gao, An empirical equation for bunch lengthening in electron storage ring, Nuclear Instruments and Methods in Physics Research A 432 (1999) 539-543.
13. P. Wilson, et al., Bunch lengthening and related effects in SPEARII, IEEE Trans. Nucl. Sci. NS-24 (1977) p.1211

2.4 Beam-Beam Effects

During the preparation of the Pre-CDR a great deal of work was done on beam-beam effects in order to optimize the machine main parameters [1,2]. The focus of that work was to optimize luminosity and lifetime based on beamstrahlung effect. The baseline design was the pretzel scheme in a single ring where there are about 100 parasitic crossing points in the arc. Since the lattice with pretzel scheme is not yet finalized, we evaluate the parasitic beam-beam effect roughly using the weak-strong LIFETRAC code [3].

In the earlier work on the Pre-CDR the Z-factory luminosity was not a high priority. While the option for a Z-factory was kept open, the emphasis of the Pre-CDR was on Higgs factory and its requirements on the machine design, That has now changed. In this report we want CEPC to be designed to have luminosity of a Z-factory at 1×10^{34} $cm^{-2}s^{-1}$ or higher. In Appendix 3 of the Pre-CDR, is a discussion of operating CEPC at lower energy and higher luminosity as a Super Z factory [4]. But the pretzel scheme is complicated. The crab-waist collision scheme [5] with a double ring is easier and more flexible. This is the base line design of FCC-ee [6]. It is easier to achieve high luminosity in a wider energy region with the crab-waist scheme in such a machine, since the emittance is smaller at lower energy, a requirement for implementing crab-waist. The large circumference can accommodate many bunches. Refs. [7] and [8] propose a "bowtie" scheme to implement a crab-waist scheme with a partial double ring. This avoids the complicated pretzel scheme. The new machine parameters are presented in Sec. 2.1. Here we show some beam-beam calculations to check the reasonability of these new parameters.

In previous estimations of the lifetime and how it is limited by momentum acceptance and transverse dynamic aperture, it was supposed that the aperture boundary is rectangular. However, the boundary is more like an ellipse than a rectangle. Here we compare the lifetime between the two cases. We use the weak-strong code LIFETRAC and BBWS to calculate the lifetime. The two codes are both weak-strong codes, but different quasi-strong-strong methods are used [1, 9]. We also use the code IBB [10] to consider the beamstrahlung effect. IBB is a strong strong code and used to simulate the lifetime in the Higgs factory mode.

The main parameters from the Pre-CDR and the new partial double ring scheme are presented in the next section.

2.4.1 Parasitic Beam-Beam Effect

In the pretzel scheme, the beam is separated in horizontal direction with $10\sigma_x$. There is one parasitic collision point every 4π phase advance in the horizontal direction, and 100 parasitic crossing points totally. The parasitic tune shift is calculated using

$$(\xi_x, \xi_y) = \frac{Nr_e}{2\pi\gamma}\frac{(\beta_x,\beta_y)(x^2-y^2)}{(x^2+y^2)^2}$$

ξ_x from one crossing point is about -0.0007, and the total tune shift is about -0.07. We use LIFETRAC to simulate the parasitic beam-beam effect. With all crossing in phase, the lifetime would drop by 3 orders. This I not acceptable due to the short lifetime. One solution is to enlarge the separation. Figure 2.4.1 shows the luminosity and lifetime with 15 σ_x separation. However, a larger pretzel orbit causes more complicated optics distortion and requires larger magnet aperture.

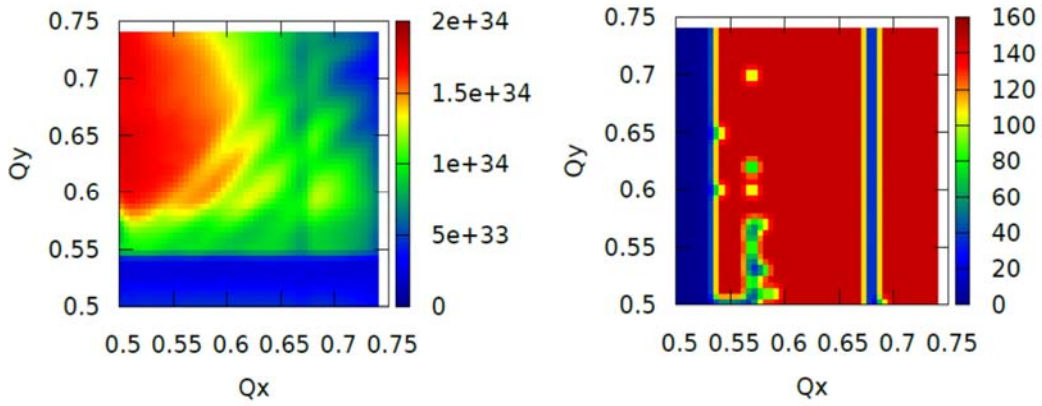

Figure 2.4.1. The luminosity/IP(left) and lifetime (right) limited by beamstrahlung effect with $15\sigma_x$ separation in the pretzel scheme.

We also check a case of different phase advance between PCs and IP: $\Delta\phi_x = 0, \Delta\phi_y = 0$ for one half, and $\Delta\phi_x = \frac{\pi}{4}, \Delta\phi_y = \frac{\pi}{4}$ for the other half. However, this does not help compensate for the poor lifetime.

2.4.2 Benchmark

The IBB code is a strong-strong code developed by Yuan Zhang at IHEP [10]. It is mainly used for BEPCII. Its model is similar to that of BBSS. Now the beamstrahlung effect is taken into account. With momentum acceptance of 0.02, the beamstrahlung lifetime estimated by LIFETRAC/BBWS is 85/250 min respectively. The difference between the two codes comes from the different quasi-strong-strong model. The cause has been discussed in Refs. [1, 9]. The result from IBB is 336 min for momentum acceptance of 0.021. The difference is comparable; a more detailed benchmark will be done in the future.

2.4.3 Elliptical *vs* Rectangular Dynamic Aperture Boundary

For the same rectangular dynamic aperture, the lifetime given by LIFETRAC is about 20 min for $40\sigma_y$, and by BBWS about 200 min. But it is only 3 min from IBB. It is still not clear if this difference comes from the weak-strong and strong-strong models. It should be noticed that for the pure strong-strong simulation, we enlarge the field solution region to enclose halo particles and it is necessary to enlarge the grid number to ensure accuracy for the core particle with the PIC method. The result is that the computation takes much more time which becomes unreasonable. A better method is to calculate the field felt by the halo particle with synchro-beam mapping [11]. In fact it is noticed that the lifetime is sensitive to the grid region if the region area is too small.

Preliminary result shows that the lifetime limited by an elliptical boundary is reduced by a factor of 1.5 compared to a rectangle, as shown in Figure 2.4.2.

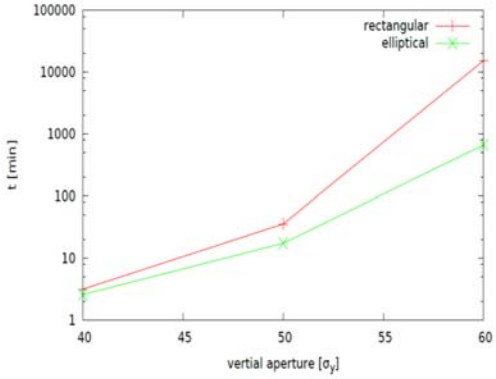

Figure 2.4.2. Lifetime limited by rectangular and elliptical apertures using code IBB.

The beam lifetime limited by Y-Z elliptical aperture has also been calculated by K. Ohmi and D. Zhou with BBWS and is shown in Figure 2.4.3.

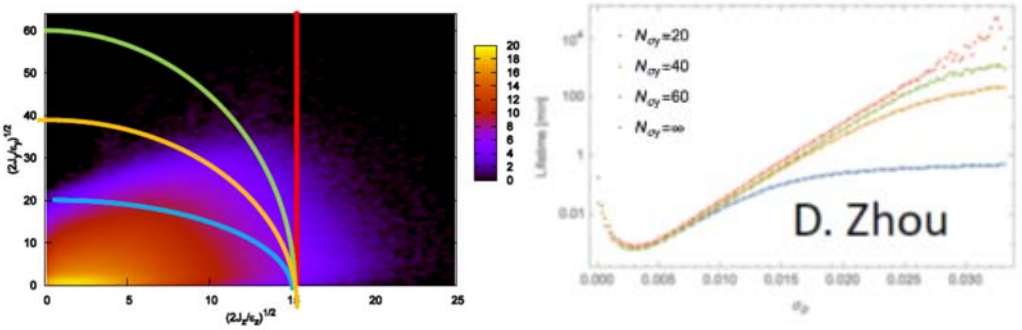

Figure 2.4.3. Y-Z distribution and aperture boundary (left); beam lifetime limited by Y-Z elliptical aperture (right).

2.4.4 Check of the New Machine Parameters

The strong-strong code IBB is used to simulate the beam-beam performance with the new parameters. For the case of a low-power Higgs factory, the luminosity/IP could reach 1.9×10^{34} $cm^{-2}s^{-1}$. The beamstrahlung lifetime is about 200 min with momentum acceptance 2%. The luminosity of W/Z could reach $3.5/2.6 \times 10^{34}$ $cm^{-2}s^{-1}$. The factor of bunch lengthening coming from beamstrahlung is about 1.3 for H/W/Z. Thus parameter choice is reasonable from the point view of the beam-beam interaction.

2.4.5 100 km Double Ring Scheme

At the end of 2016, the double ring scheme of the CEPC was considered carefully. The main parameters are presented for H/W/Z energy, which is shown in Sec.2.1. We also examined the feasibility of these parameters and the beam-beam performance by simulation.

The following figures show the luminosity performance and beam size blow-up for β_y=1mm at Higgs energy. In the first few hundred turns, there exist serious beam size changes in the X direction. The change comes from in-phase <xz> oscillation between colliding bunches, and the maximum tilt angle is about 5 mrad. The tilt angle oscillation could be suppressed by choosing a better working point, for example (0.51, 0.55) instead of (0.54, 0.61). There also exist similar phenomena at the W/Z energy.

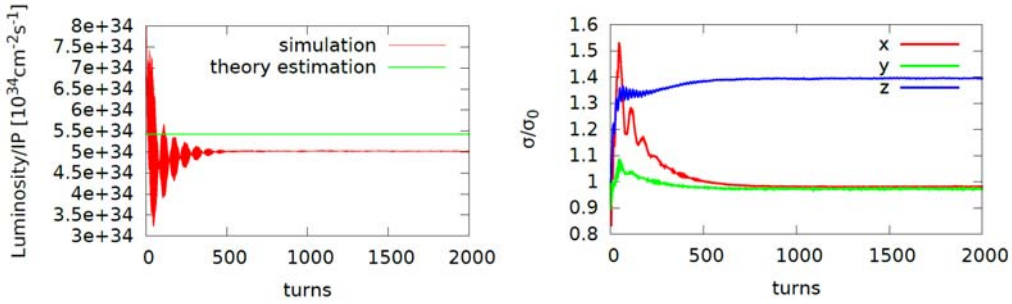

Figure 2.4.4. β_y=1mm, Higgs, 100 km. Qx/Qy=(0.54, 0.61), nus =0.0272 for half ring.

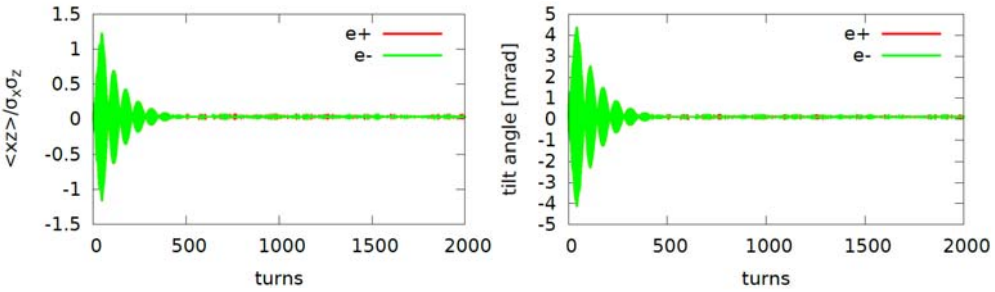

Figure 2.4.5. In-phase <xz> oscillation. β_y=1mm, Higgs, 100km. Qx/Qy=(0.54, 0.61), nus =0.0272 for half ring.

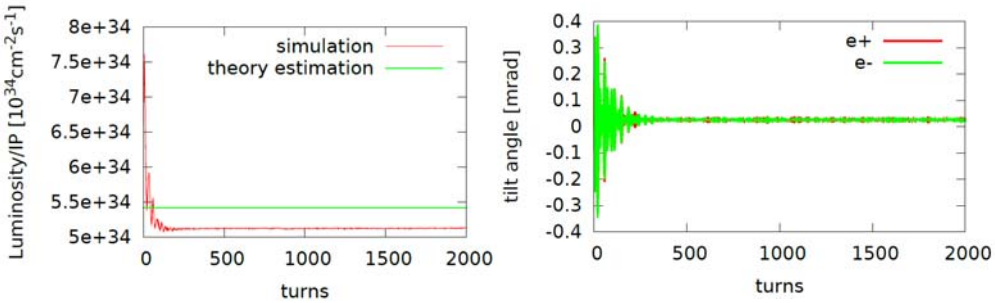

Figure 2.4.6. β_y=1mm, Higgs, 100km. Qx/Qy=(0.51, 0.55), nus =0.0272 for half ring.

The peak luminosity of Higgs could reach about 3 $\times 10^{34}$ $cm^{-2}s^{-1}$ per IP with β_y=2mm.

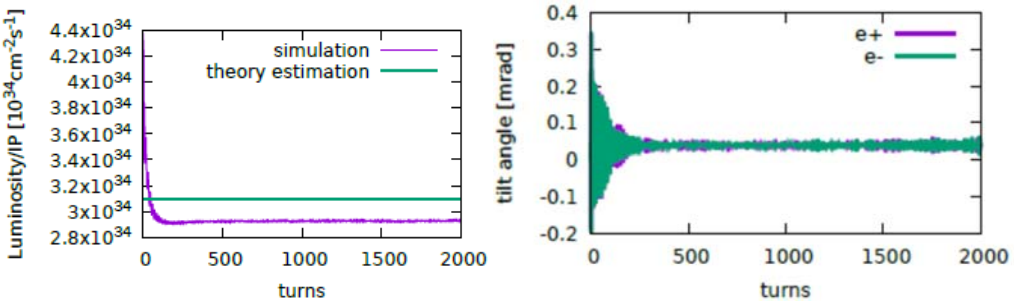

Figure 2.4.7. β_y=2mm, Higgs, 100km. Qx/Qy=(0.53, 0.61), nus =0.037 for half ring.

The peak luminosity of W could reach about 3 $\times 10^{34}$ $cm^{-2}s^{-1}$ per IP with β_y=1mm.

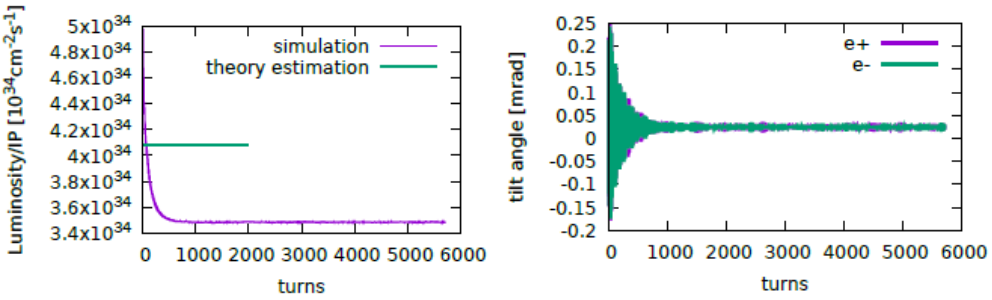

Figure 2.4.8. β_y=1mm, W, 100km. Qx/Qy=(0.535, 0.61), nus =0.0425 for half ring.

The peak luminosity of W could reach about 1 $\times 10^{34}$ $cm^{-2}s^{-1}$ per IP with β_y=1mm.

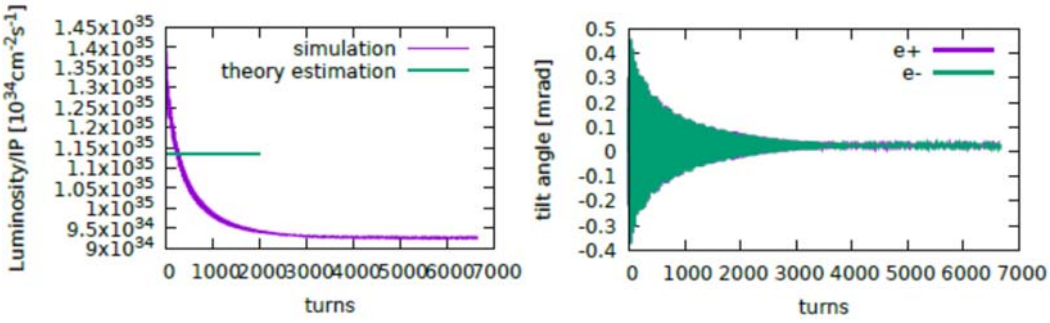

Figure 2.4.9. β_y=1mm, W, 100km. Qx/Qy=(0.54, 0.61), nus =0.0256 for half ring.

2.4.6 Summary

The beam-beam code IBB now includes the beamstrahlung effect. It is used to evaluate the beam-beam performance of CEPC. The new machine parameters with the partial double ring scheme are reasonable from the beam-beam point of view. The parasitic beam-beam effect in the pretzel scheme is simulated using LIFETRAC, indicating that we may need larger separation. The main parameters of 100-km double

ring design is also examined by simulation. It is found that there exist clear <xz> in-phase oscillation if the working point is not properly chosen.

2.4.7 References

1. K. Ohmi, D. Shatilov, D. Zhou and Y. Zhang, Beam-beam simulation study for CEPC, in Proc. 5th Int. Particle Accelerator Conf. (Dresden, Germany, 2014)
2. K. Ohmi and F. Zimmermann, FCC-ee/CEPC Beam-beam simulations with Beamstrahlung, in Proc. 5th Int. Particle Accelerator Conf. (Dresden, Germany, 2014)
3. D. Shatilov, Part. Accel. 52, 65 (1996).
4. CEPC-SPPC Preliminary Conceptual Design Report, March 2015.
5. P. Raimondi, 2nd SuperB Workshop, Frascati, 2006
6. http://cern.ch/fcc
7. M. Koratzinos, Mitigating performance limitations of single beam-pipe circular e+e- colliders, in Proc. 6th Int. Particle Accelerator Conf. (Richmond, VA, USA, 2015)
8. J. Gao, Private communication
9. K. Ohmi and D. Shatilov, Status of Benchmark of LIFETRAC and BBWS, FCC-ee Meeting, 31 Aug, 2015
10. Y. Zhang, K. Ohmi, and L. Chen, "Simulation study of beam-beam effects", Phys. Rev. ST Accel. Beams 8, 074402 (2005)
11. K. Hirata, H. Moshammer and F. Ruggiero, Part. Accel. 40, 205 (1993)

2.5 Dynamic Aperture Optimization by MODE

There is a lot of successful multi-objective optimization in the design of storage ring based light sources, such as the APS [1], where there was direct optimization of dynamic aperture and Touschek lifetime. Experimental tests validated the method, which brought significant improvements to APS operations. In NSLS-II [2], they demonstrated a correlation between dynamic aperture and low-order nonlinear driving terms, and using both numerical tracking results and analytical estimates of the driving terms, resulting in faster convergence. Genetic algorithms are very popular and Huang tried a particle swarm algorithm during the nonlinear dynamics optimization of a low emittance upgrade lattice for SPEAR3 [3]. The performance of the two algorithms are compared. The result shows that the particle swarm algorithm converges significantly faster to similar or better solutions than the genetic algorithm and it does not require the seeding of good solutions in the initial population. In photo injector design, there is also growing interest in using multi-objective beam dynamics optimization to minimize the final transverse emittances and to maximize the final peak current of the beam. Most previous studies in this area were based on genetic algorithms. J. Qiang proposed a new parallel multi-objective optimizer based on the differential evolution algorithm for photo injector beam dynamics optimization [4]. the dynamic aperture with hundreds of sextupole families in the optics design of FCC-ee [5]. There are a total of 18 sextupole families in BEPCII and 56 sextupole families in SuperKEKB. It is probably a useful approach to use hundreds of sextupole families in future e+e- storage ring collider, such as CEPC and FCC.

2.5.1 Differential Evolution Algorithm

In 1995, Price and Storn proposed a new floating point encoded evolutionary algorithm for global optimization and named it DE [6] owing to a special kind of differential operator, which they invoked to create new offspring from parent

chromosomes instead of classical crossover or mutation. Easy methods of implementation and negligible parameter tuning made the algorithm quite popular.

DE is a very simple and powerful population based, stochastic function minimizer. The crucial idea behind DE is a scheme for generating trial parameter vectors. In fact, there are a few strategies, and we choose `rand-to-best` which attempts a balance between robustness and fast convergence. A perturbed vector v_i is generated according to

$$v_{i,j} = \begin{cases} x_{i,j} & , \ if\ rand(j) > CR \\ x_{i,j} + F\times[x_{b,j} - x_{i,j}] + F\times[x_{r1,j} - x_{r2,j}], \end{cases}$$

where rand() is a uniform random number between 0 and 1. As we see in the above equation, there are two setting parameter F and CR. Another parameter is the population size NP, which is usually ten or twenty times the parameter number. In our simulation, CR is chosen between [0.8,1.0], and F is randomly chosen between 0 and 1 for each generation. If the new trial solution produces a better objective function value compared to its parent, it will be put into the next generation population, otherwise the old one is kept unchanged.

Most problems in nature have several objectives to be satisfied. Many of these problems are frequently treated as single-objective optimization problems by transforming all but one objective into constraints. This is the method used in MAD [7], where the single objective function is defined as the sum of all the constraints with different weight. But the weight is hard to determine, especially when the objective are possibly conflicting.

A true multi-objective optimization means finding a solution which would give the values of all the objective functions acceptable to the decision maker. In mathematical language, a solution x1 is said to dominate another solution x2, if both the following conditions are true: (1) the solution x1 is no worse than x2 in all objectives. (2) the solution x1 is strictly better than x2 in at least one objective. Among a set of solutions, the non-dominated set of solutions are those that are not dominated by any member of the set. Kung's algorithm [8] is used to find the non-dominated set. Attention is paid to Pareto optimal solutions, which cannot be improved in any of the objectives without degrading at least one of the other objectives. The set of Pareto optimal outcomes is often called the Pareto front.

The differential evolution algorithm for multi-objective optimization is based on Qiang's work [4]. The code is called MODE. The algorithm in each generation can be summarized in the following steps:

1) Generate the offspring population using the above differential evolution algorithm.
2) Find the non-dominated population set, which is treated as the best solutions in DE to generate offspring in the next generation.
3) Sorting all the population, select the best NP solution as the parents in the next generation.
4) Return to step 1, if the stopping condition is not met.

In the original single objective DE, the comparison is done between the new trial vector solution and its corresponding parent and the better one is kept for next generation. In the multi-objective DE, the comparison is done between all the population sets, the better one is kept.

2.5.2 Application in CEPC

We try to optimize a single ring lattice design of CEPC to test the method. The lattice design work is evolving continuously [9]. The main parameters are listed in the following Table.

Table 2.5.1. CEPC parameters

horizontal emittance	6.12e-9 mrad
emittance coupling	0.003
energy Spread(SR)	0.0013
β_x^*	0.8 m
β_y^*	0.003 m

The beam-beam study shows that the dynamic aperture should be larger than $20\times\sigma_x\times40\sigma_y\times0.02$. The transverse aperture of the original lattice is shown in the following figure.

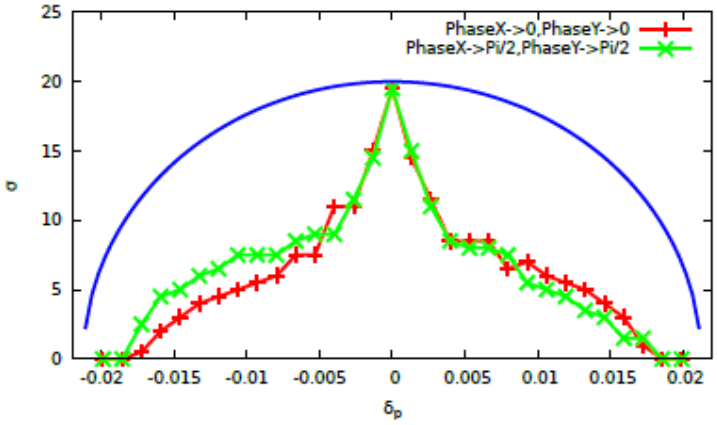

Figure 2.5.1. The dynamic aperture before optimization ($\beta_y^* = 3$mm).

There are only one family for SF/SD in the arc of the original lattice. Since the arc consist of a 60°/60° FODO cell, we set the sextupoles interleaved 180° each pair. There are a total of 240 sextupole pairs used in the optimization. The objectives are listed in the following:

- The tune Qx is in the range [0.05,0.31] and Qy [0.10,0.31] for δ [-0.02,0.02].
- X-Z aperture objective is defined as an ellipse $\frac{x^2}{20^2}+\frac{z^2}{16^2}=1$, where x is the transverse amplitude in unit of RMS size with 0.3% coupling, and z in unit of RMS energy spread.
- X-Y-Z aperture objective is defined as an elliptical ball $\frac{x^2}{20^2}+\frac{y^2}{50^2}+\frac{z^2}{16^2}=1$.

The optimized solution enlarges the dynamic aperture significantly, as shown in the following figure.

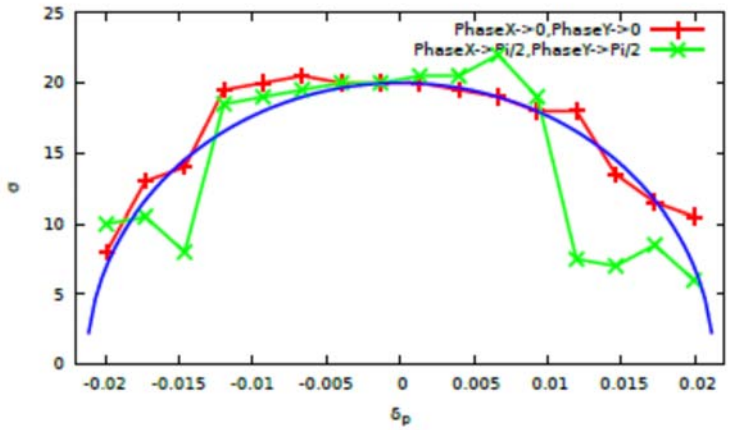

Figure 2.5.2. The optimized dynamic aperture with MODE ($\beta_y^* = 3$mm).

Since there exists strong synchrotron radiation in the Higgs factory, the radiation effect on DA should be also studied. The tracking shows that the damping really helps especially for large momentum offset particles, but quantum fluctuation may reduce the DA for small momentum offset particle.

The brute-force dynamic aperture tracking is very time consuming. To save computing time, we usually first simplify the objective, for example only track 100 turns instead of 1000 turns. In the multi-objective optimization, some objective is very time consuming, while others may be much faster such as linear optics calculation. We first optimize the fast objective, and then do the slow calculation when some constraints are satisfied, a method used Ehrlichman's [10].

2.5.3 Summary

One of the most urgent tasks is to speed up the convergence of the optimization. We need to find better chosen objective functions from physics to save the computing time. The success of DE in solving a specific problem crucially depends on appropriately choosing the trial vector generation strategy and their associated control parameter values. There is a lot of work on the self-adaptive DE algorithm [11], which promises more effective, more stable optimization. Das et al. proposed a new scheme of adjusting the velocities of the particles in PSO with a vector differential operator borrowed from the DE family. The mutual synergy of PSO with DE leads to a more powerful global search algorithm(PSO-DV) [12], which should also be tried.

2.5.4 References

1. M.Borland, “Parallel tracking-based optimization of dynamic aperture and lifetime with application to the APS", in 48th ICFA Beam Dynamics Workshop on Future Light Sources, Menlo Park, California, 2010
2. L. Yang et al., “Multiobjective optimzation of dynamic aperture”, Phys. Rev. ST Accel. Beams, vol. 14, 054001, 2011.
3. X. Huang et al., “Nonlinear dynamics optimization with particle swarm and genetic algorithms for SPEAR3 emittance upgrade”, Nucl. Instr. Meth. in Phys. Research A, 757, 48--53, 2014.

4. J. Qiang et al., “A parallel multi-objective differential evolution algorithm for photoinjector beam dynamics optimization”, in Proc. IPAC'13.
5. K. Oide, “A design of beam optics for FCC-ee”, presented at CEPC AP Meeting, Beijing, China, Sep. 2016, unpublished.
6. Differential Evolution, http://www1.icsi.berkeley.edu/~storn/code.html
7. MAD - Methoical Accelerator Design, http://mad.web.cern.ch/mad
8. H. Kung et al., “On finding the maxima of a set of vectors”, J. ACM, 22, 469-476, 1975.
9. Y. Wang et al., “Dynamic aperture study of the CEPC main ring with interaction Region”, in Proc. IPAC’16.
10. M. Ehrlichman, “A Genetic algorithm for chromaticity correction in diffraction limited storage rings”, arXiv:1603.02459.
11. A. Qin et al., “Differential evolution algorithm with strategy adaptation for global numerical optimization”, IEEE Trans. on Evo. Comp., 13, 398-416, 2009
12. S. Das et al., “Particle swarm optimization and differential evolution algorithms: technical analysis, applications and hybridization perspectives”, in Studies in Computational Intelligence, 116, 1-38, 2008

2.6 Machine-Detector Interface Design

2.6.1 Beam Induced Backgrounds at CEPC

After the Higgs boson was discovered by the ATLAS and CMS experiments [1, 2] at the CERN Large Hadron Collider (LHC), it becomes necessary to measure the Higgs boson properties with high precision beyond the ultimate reach of the LHC and HL-LHC [3]. This will be done at future lepton colliders (so-called “Higgs Factories”). The Circular Electron Positron Collider (CEPC) [4] is a proposed Higgs factory to measure the properties of the Higgs boson and test the standard model with high precision. It will be operated at a center of mass energy of 240 GeV. The luminosity will be about 2×10^{34} $cm^{-2}s^{-1}$.

A large amount of synchrotron radiation photons will be generated as the beam particles circulate through the magnetic fields at CEPC. These photons are the beam induced background. The power of the synchrotron radiation in the whole ring will be about 50 MW. The flux of photons in the detector could be too high to reconstruct the events if these photons are not well shielded. Also very serious is that some critical devices of the machine and the detector might be damaged. To suppress the radiation level on the machine and the detector, the radiation level of the synchrotron radiation must be carefully evaluated and the shielding must be well designed.

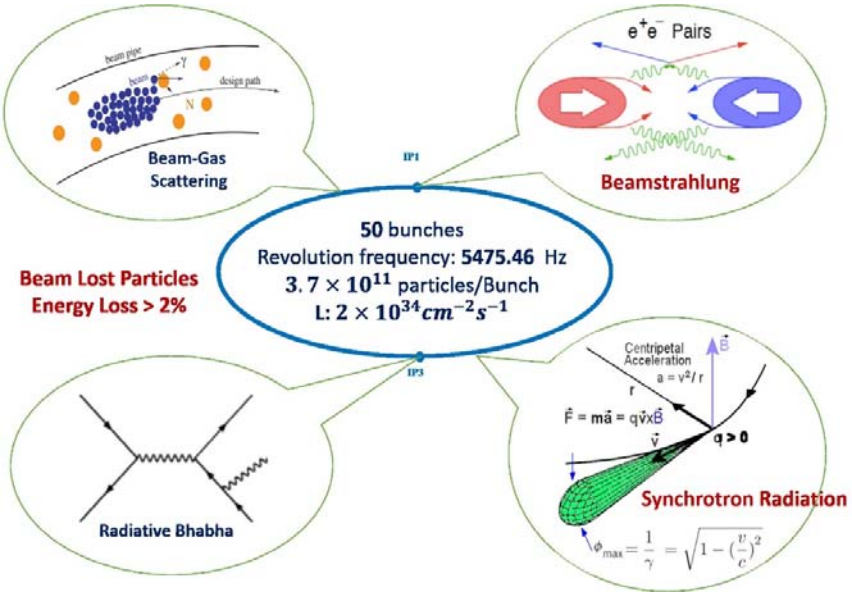

Figure 2.6.1: The most important beam induced backgrounds at CEPC

Besides the synchrotron radiation, the beam loss particles and beamstrahlung [5] effects are the other important components to the beam induced backgrounds at CEPC. The beam loss particles are beam particles lost from the beam after they are scattered by other particles or materials and their energy loss are greater than 2% of the beam energy. The scattering processes that cause the energy loss include radiative Bhabha scattering and beam-gas scattering. Beamstrahlung is one kind of synchrotron radiation that is emitted when two bunches with opposite charges cross each other. During the bunch crossing, the trajectories of beam particles in one bunch will be bent by the induced electromagnetic field of the other bunch and a large number of synchrotron photons with high energy will be emitted. These high energy photons might further interact with each other and induce other processes, including the electron-positron pair production and hadronic background [6].

The most important beam induced backgrounds at CEPC including synchrotron radiation, beam loss particles and beamstrahlung are shown in Figure 2.6.1. In this section, the radiation level of these most important beam induced backgrounds is evaluated and preliminary results are summarized.

2.6.2 General Method to Evaluate Beam Induced Backgrounds

The beam induced backgrounds are simulated with the Monte-Carlo method to evaluate the radiation level on the detector. The hit density and the radiation dose on the detectors will be extracted to evaluate the radiation level of beam induced backgrounds. General procedures for the simulation of beam induced backgrounds are shown in Figure 2.6.2.

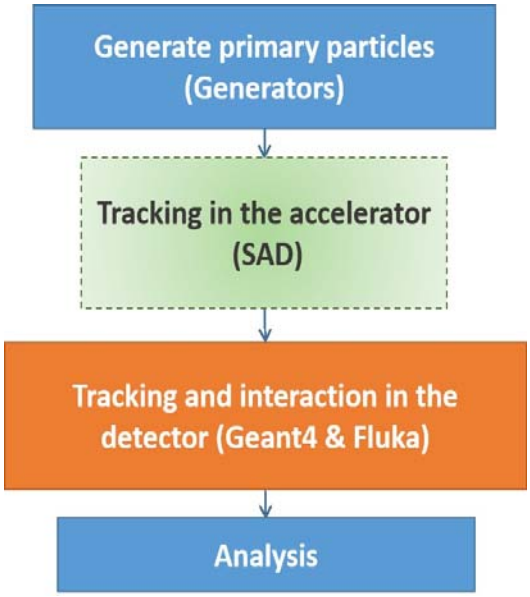

Figure 2.6.2: General procedures for the simulation of beam induced backgrounds

First, samples with all information of primary particles will be generated by proper generators for each kind of beam induced backgrounds. Because the production mechanism of all backgrounds can't be well simulated by one generator, the most common generators are used for each kind of beam induced backgrounds. For instance, the synchrotron radiation samples are generated by the model embedded in Geant4 [7], the radiative Bhabha samples are generated with the BBBrem [8] and the beamstrahlung samples are generated by Guinea-Pig++ [9].

Second, the propagation of the primary particles will be simulated in the accelerator or in the detector according to their propagation history. For beam lost particles whose primary particles are generated in the accelerator, they will first be tracked by SAD [10] inside the accelerator until they encounter the beam pipe or a collimator. Then these particles will be tracked by Geant4 or Fluka [11] to simulate the interaction between the particles and the materials. Other kinds of backgrounds whose primary particles will not be affected by the lattice of the accelerator, will be tracked by Geant4 or Fluka directly.

Finally, the hit information in the detector will be extracted to calculate the hit density and radiation dose in the detector.

When the primary background particles hit the materials, lots of secondary particles will be formed from the interactions of the primary background particles with detector materials. The radiation level of the secondary background particles strongly depends on the detector layout and material distribution and can be extracted from the detector simulation. Fig. 2.6.3 shows the current design of the interaction region layout. Because the single ring and double ring schemes are both considered by CEPC, there are also two possible scheme for the IR design. For the single ring scheme, the two beams will collide in head on mode, there will be no crossing angle between the two beams. For the double ring scheme, a crossing angle of 30 mrad will be used. Hit density and radiation damage, which are crucial parameters for detector design, are extracted based on these two different IR layouts. The tracking system is composed of the vertex detector (VTX), the silicon tracker and the time projection chamber (TPC). The VTX consists of 6 layers of

pixel detectors, which are assembled on both sides of 3 layers of mechanical support structures. An electromagnetic calorimeter (LumiCal) is designed to precisely measure the luminosity by counting the radiative Bhabha events. The final focusing magnets QD0 are placed at a short focal length of L^* = 1.5 m, *i.e.* the distance between the final quadrupole QD0 and the IP, to achieve high luminosity.

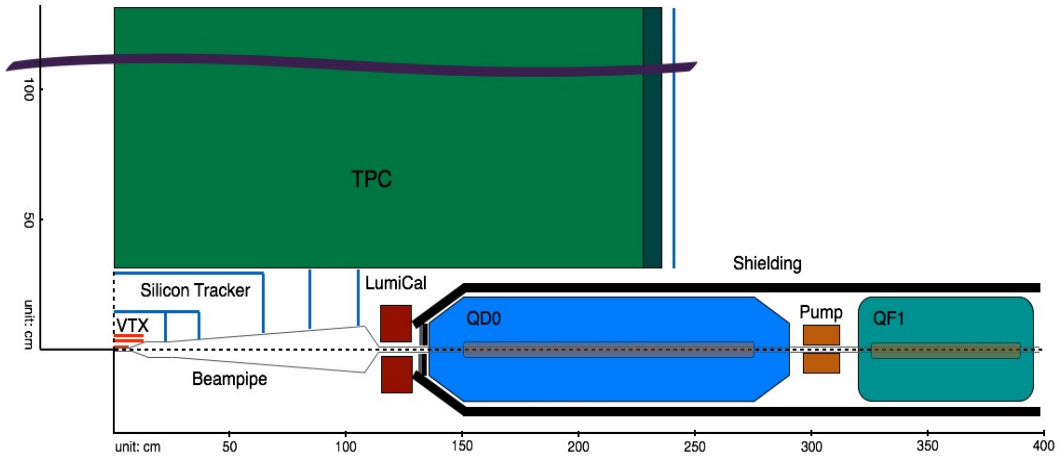

(a) Single Ring Scheme

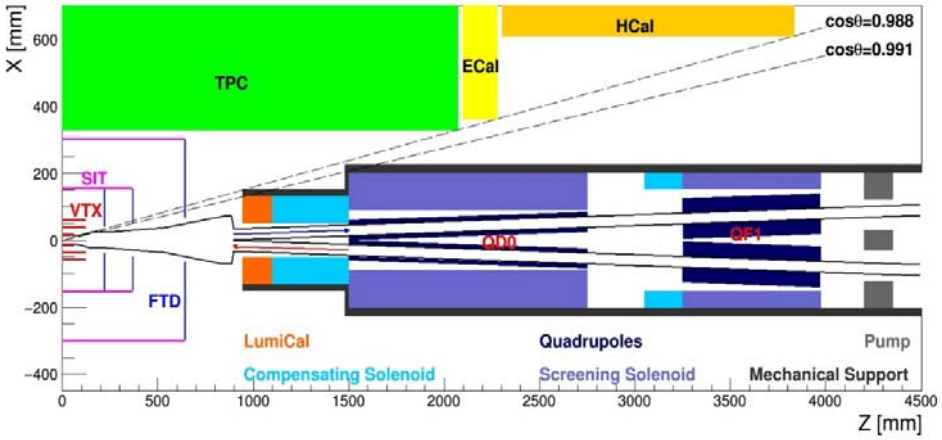

(b) Double Ring Scheme

Figure 2.6.3: The proposed layout of the CEPC interaction region.

The details of the simulation of each kind of beam induced backgrounds will be shown in the sections below. Because the design of the lattice hasn't been completed, a preliminary version of the single ring scheme is used to develop and test the simulation software for the beam induced background.

2.6.3 Synchrotron Radiation

Because the beam energy of CEPC is high and the number of beam particles in one bunch is large, the synchrotron radiation (SR) emitted from the beam in the dipole and quadrupole magnets will be the most serious beam induced background at CEPC. The number and the energy spectrum of the photons that might enter the detector must be well evaluated to check whether the background level is acceptable to the experiments. The synchrotron radiation in the dipole magnets can be easily estimated with the analytical formulas of classical electrodynamics. However, in the quadrupole magnets which are used to focus the beam, because the fields are non-uniform, the radiation power will be related to the transverse size and trajectories of beam particles inside the quadrupoles. To study the synchrotron radiation from the dipole and quadrupole magnets uniformly, a Monte Carlo simulation program is developed based on Geant4 and BDSIM [12] to generate and track photons.

2.6.3.1 Generator of the Synchrotron Radiation

The simulation of synchrotron radiation at the interaction region of a collider can be usually subdivided into 3 steps.

First, the magnetic field along the beam pipe will be modeled according to the lattice design with BDSIM which is a C++ program that utilizes the Geant4 toolkit to simulate both the transport of particles in an accelerator and their interaction with the accelerator components.

Second, the beam particles will be tracked along the beam line with BDSIM and the synchrotron radiation photons will be generated, by the synchrotron radiation process. This is implemented in Geant4 using H. Burkhardt's algorithm, along the beam particle trajectories. When tracking the beam particles, the energy loss due to synchrotron radiation is included.

Finally, the interaction between photons and materials will be simulated. In this step, two strategies with different speeds can be employed. One is called fast simulation, in which only the beam pipes are constructed in Geant4 so that the number of photons and power deposited along the beam pipe can be used as the indicator of synchrotron radiation level. The other method is called full simulation, in which both the detector and the accelerator are constructed in Geant4 so that the hit density and energy deposition in each sub-detector can be exactly simulated.

When a bunch passes through an accelerator element, the radiation power of beam particles is related to their radial position in the bunch and the magnetic field of the element. In dipoles, because the trajectories of all beam particles are bent by the magnetic field, all beam particles will emit a similar number of photons. However, in quadruples which are used to focus the beam, the halo particles which are far from the beam orbit in the radial direction will emit more photons than core particles which are near the orbit because the fields of quadruples far away from the beam orbit are much stronger than the field near the orbit. Obviously, the position and momentum distribution of beam particles at a certain element will be highly dependent on the initial states of the beam particles at the initial point of the tracking. In our simulation, the initial distribution of beam particles are determined from the accelerator parameters at the starting point. For synchrotron radiation in the quadrupole magnets, the beam particles far away from the central orbit are more important because the tail particles produce more photons.

2.6.3.2 Normalization

To evaluate the radiation level of beam induced backgrounds correctly, it's very important to normalize the number of generated beam induced particles. Because the production mechanism of each kind of beam induced background is very different, the methods for their normalization are also different. The synchrotron radiation can be normalized according to classical electrodynamic. Assume that a single electron is in a uniform magnetic field and its momentum is perpendicular to the field, the orbit will be a circular. The average number of photons generated by the electron in one turn is [13]

$$N_c = \frac{5\pi\alpha\gamma}{\sqrt{3}} \tag{2.6.1}$$

where N is the average number of photons generated by the electron in one turn, α is the fine structure constant and γ is the Lorentz factor.

For non-uniform magnetic field, the path of the charged particle in the magnetic field can be subdivided into small pieces and the magnetic field in each small piece can be considered as uniform. In this case, for the motion of charged particles, only the components perpendicular to the magnetic field will contribute to the production of synchrotron radiation. The average number of photons generated in the small piece will be

$$n_i = \frac{l_i}{2\pi\rho_i} N_c = \frac{5\alpha\gamma l_i}{2\sqrt{3}\rho_i} \tag{2.6.2}$$

where n_i is the average number of photons generated in the *i-th* small piece by one electron, ρ_i is the radius of curvature in the *i-th* small piece and l_i is the path length in the *i-th* small piece. The total average number of photons generated by one charged particle is the sum of the average number of photons generated in each small piece

$$N = \sum n_i$$

This is the method used in Geant4 to generate the synchrotron radiation photons. The small pieces are replaced by the steps of one trajectory in Geant4. Thus, the average number of synchrotron photons generated by a single charged particle in the magnetic field has been normalized in Geant4. Assuming the number of particles in one bunch is n_p and the number of bunch crossing in unit time is n_{BX}, the total average number of photons generated in unit time by one beam will be

$$N_T = N \cdot n_p \cdot n_{BX}$$

2.6.3.3 Preliminary Results

2.6.3.3.1 Synchrotron Radiation from Dipoles

Because the single ring lattice is not optimized for synchrotron radiation, preliminary results show that the SR rate is much higher than can be tolerated by the detector. The number of photons from one bunch at the interaction region from the last dipole is shown in Figure 2.6.4. The photon flux at the first layer of the vertex detector will be about $10^{10} cm^{-2} BX^{-1}$. The detector can't work in such a harsh radiation environment, so it's

necessary to design a collimator system to shield the detector from the synchrotron photons.

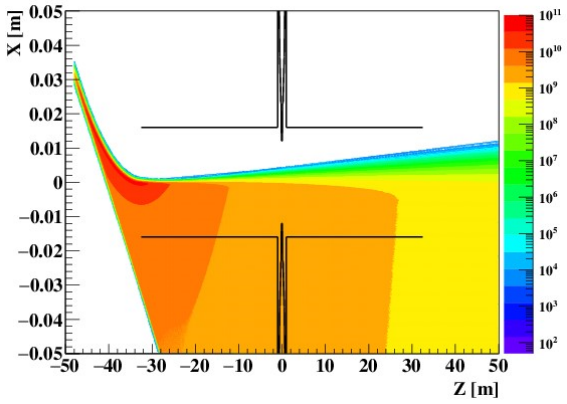

Figure 2.6.4: The number of photons per bunch from the last dipole. The black line represents the inner radius of the beam pipe. The radius of beam pipe at IP (z=0) is smaller because it is necessary to place the vertex detector very close to the interaction point.

To cope with the synchrotron radiation, two methods are used. One is to optimize the lattice design to reduce the radiation power of the synchrotron radiation in the IR. The other is to insert collimator in the IR to absorb the SR radiation before it enters the detector region. To design a good collimator system, there are several important parameters to consider: position, aperture, thickness, shape and materials. The collimator aperture should be as small as possible to block the photon paths but without blocking the beam particles. The criteria for the collimator design of CEPC will be discussed in Section 2.6.4.

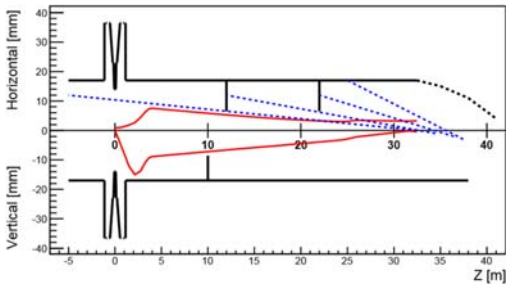

Figure 2.6.5: Preliminary collimator design for the IR. The path of photons to the detector is blocked by the collimator. The collimator is kept out of the beam-stay-clear region which is denoted with red lines.

Figure 2.6.5 shows the preliminary design of a collimator system to block synchrotron radiation. Two collimators are placed in the horizontal direction at 12 m and 22 m from the IP and one collimator is placed in the vertical direction at 10 m from the IP. The collimators are represented by the vertical black lines inside the beam pipe, and the beam-stay-clear region is denoted by the red line in Figure 2.6.6.

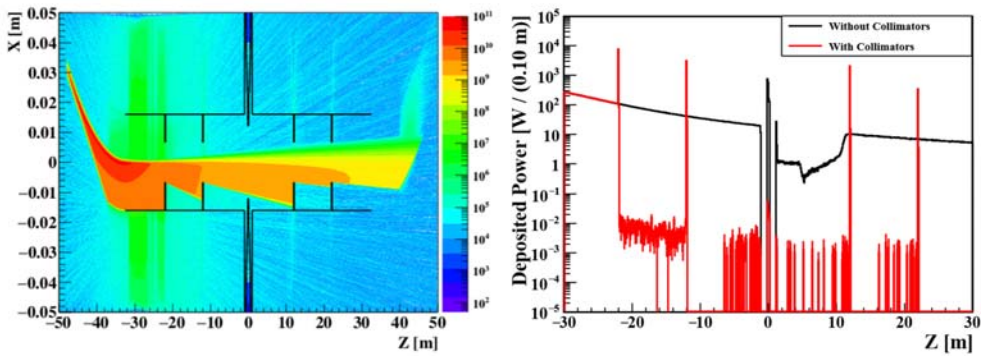

(a) Interaction between photons and collimators (b) Power Deposition

Figure 2.6.6: (a) The horizontal bold lines represent the beam pipe. The vertical line at Z = 0 m is the interaction point. Other vertical lines away from IP are the collimators. The color represents the spatial distribution of number of photons from the last dipole magnet. The collimator can suppress the number of photons significantly by absorbing and scattering. (b) The power deposited at beam pipe from the last dipole. The black line is the power without collimator and the red line is with collimator. The collimator suppresses the radiation level by a factor of 10^4 .

The interaction between synchrotron photons and collimator are shown in Figure 2.6.6 (a). The number of photons that can hit the vertex detector are much smaller than that in Figure 2.6.4. The power deposited at the beam pipe and collimator are shown in Figure 2.6.6 (b). The radiation level can be suppressed by a factor of about 10^4 with the collimator. It should be noted that the critical energy at the last dipole is about 1.08 MeV in this preliminary lattice. It will be decreased to about 100 keV in future design, so the absorbing power of the collimator will be increased.

2.6.3.3.2 Synchrotron Radiation from the Quadrupole

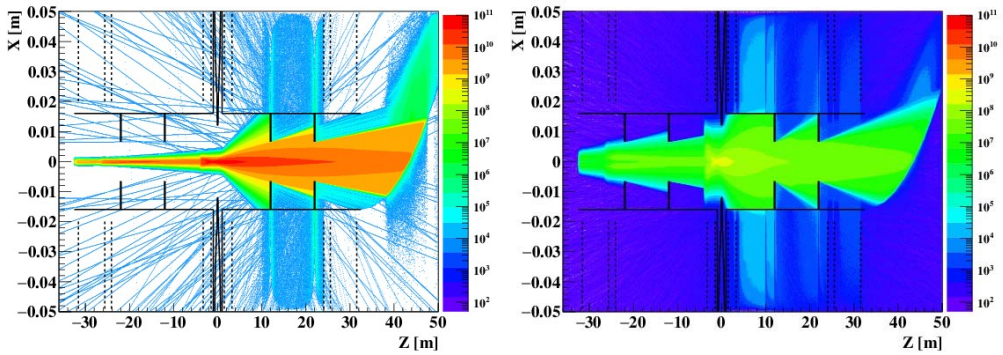

(a) Beam Core (b) Beam Halo

Figure 2.6.7: Synchrotron radiation from quadruples. The vertical dashed line are positions of quadruples.

Besides the dipole magnets, the quadruples are also an important source of synchrotron radiation. In this study, the transverse distribution of beam particles in the quadruples are

simulated with a double Gaussian function. The core particles are described by a narrow Gaussian and the halo particles are described by a wider Gaussian. The size of the beam halo is assumed to be $\sigma_x^{halo} = 3.4\sigma_x^{core}$, $\sigma_y^{halo} = 10\sigma_y^{core}$ and the number of particles in the halo is 0.5% of that in the core. The results are shown in Figure 2.6.7. If there is no beam halo (Figure 2.6.7(a)), all the photons from the beam core will pass through the interaction point and a small fraction of the photons will be backscattered by the downstream collimator. In reality, photons from beam halo will hit the vertex detector directly (Figure 2.6.7(b)). To suppress the synchrotron radiation level from quadruples, the beam halo should be well suppressed before entering the interaction region.

2.6.4 Beam Loss Particles

The energy acceptance of CEPC is designed to be 2%. If the energy loss of the beam particles is larger than 2% of the beam energy, these particles will be lost from the beam.

2.6.4.1 Generators for Beam Loss Particles

Beam particles might abruptly lose a large fraction of energy through some scattering process such as radiative Bhabha, beam-gas scattering or other processes. To evaluate the level of beam loss particles, these scattering processes will first be simulated by specific generators. For instance, the radiative Bhabha scattering is simulated by BBBrem. Because the position of these particles are unclear when the scattering occurred, these scattered particles must be tracked by accelerator tracking tools such as SAD to determine the loss position. Figure 2.6.8(a) shows the tracking of beam lost particles in SAD. The particles will be flagged as lost if the transverse position of the particles touch the inner wall of the beam pipe. Particles might be lost at any position along the accelerator, however, only the particles lost near the IP are important. Figure 2.6.8(b) shows the orbit of some particles lost in the IR after being tracked by SAD. The information at the loss position of the lost particles will be used as input to the Geant4 simulation to evaluate the radiation level at the detector. To save calculation time, only the particles lost near by the IR are simulated by Geant4.

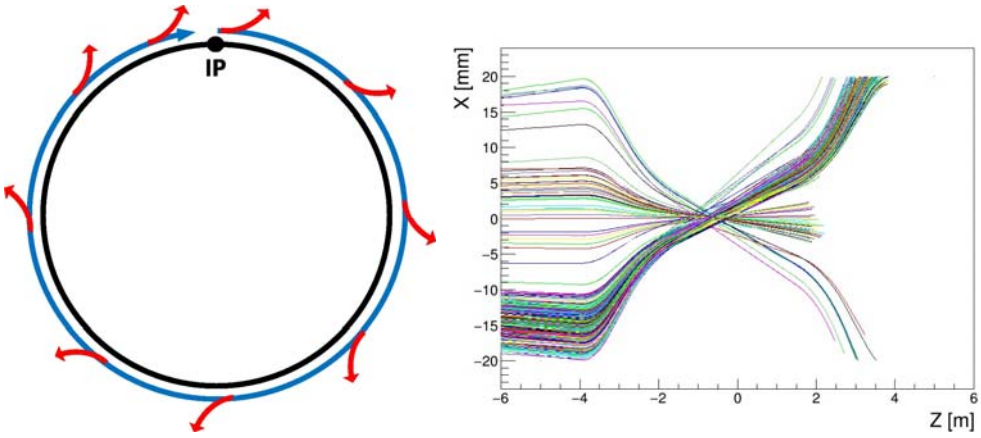

(a) Tracking in the accelerator. (b) Orbits of some particles lost in IR.

Figure 2.6.8: (a) Tracking of beam loss particles in the accelerator with SAD. The blue arrow is the beam orbit and the red arrows represent the lost particles. (b) Orbits of particles lost in the IR. The inner radius of the beam pipe is 20 mm. Particles touching the beam pipe are flagged as lost.

2.6.4.2 Normalization

For the beam loss particles, the cross section of scattering processes can be calculated from theory or by using generator code. In our study, the cross section of the radiative Bhabha scattering with very small angle and relative energy loss larger than 2% is calculated with BBBrem. Considering the beam size effect, the cross section σ is about 154 mb when the center of mass energy is 240 GeV. The number of radiative Bhabha events produced in unit time will be

$$N = L \cdot \sigma$$

and the number of events that will enter the detector will be

$$N_r = N \cdot \epsilon$$

The efficiency ϵ of entering the detector after the particles are lost is related to the detector acceptance and the lattice design of the accelerator. The efficiency is determine by tracking the lost particles with SAD. Assuming the number of radiative Bhabha events generated by BBBrem is N_g and the number of events that can enter the detector after tracked by SAD is N_e, the efficiency will be

$$\epsilon = \frac{N_e}{N_g}$$

2.6.4.3 Preliminary Results of Beam Loss Particles

Figure 2.6.9(a) shows the loss position of radiative Bhabha events in the interaction region. The relative hit density on the vertex detector is shown in Figure 2.6.9(b). If there

aren't any collimators, a large number of particles will be lost in the IR and the hit density on the vertex detectors will be very high. To suppress the number of particles lost in the IR and the hit density on the detector, a set of collimators are inserted into the ring before the IR to stop the lost particles. Different collimator apertures are used to study the collimator stop efficiency. The results show that the number of particles lost in the IR will be significantly suppressed as the aperture of the collimators are reduced.

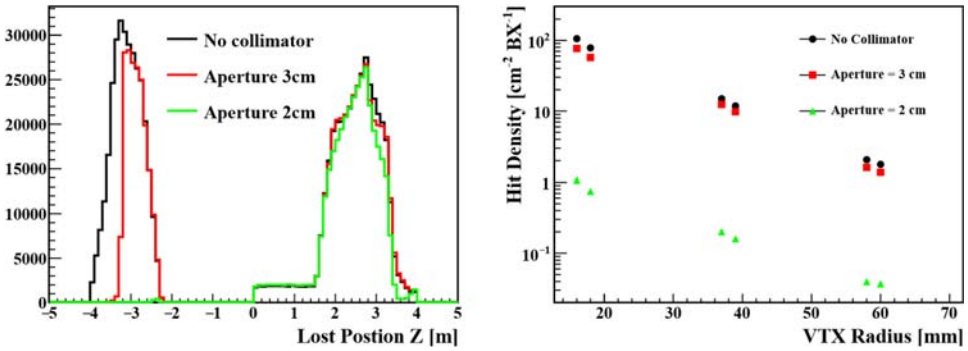

(a) Lost Position in IR. (b) Hit Density in the vertex detector

Figure 2.6.9: (a) The loss position of radiative Bhabha events in the IR. Z = 0 m is the IP. QD0 occupies the space from Z = 1.5 m to 2.75 m, QF1 from Z = 3.25m to 3.97m, and the quadruples of the two beams are symmetric around the IP. Thus, most particles are lost inside the two final focusing quadruples. (b) The hit density in the vertex detector. The horizontal axis represents the radius position of each layer of the vertex detector. The radius of the first layer is 16 mm.

2.6.4.4 Criteria for the Collimator Design

A collimator inserted into the beam line will reduce the number of particles lost in the IR. The aperture of the collimator should be as small as possible to absorb lost particles; however, the beam core shouldn't be affected by the collimator. Thus there are limitations and optimizations on the collimator design.

2.6.4.4.1 The Geometry and Material of the Collimator

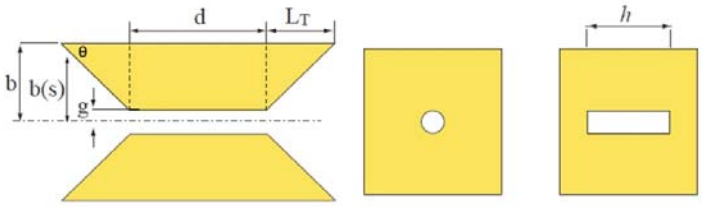

Figure 2.6.10: Geometric design of the collimator

Collimators are usually designed to be isosceles trapezoid to absorb lost particles as much as possible and retain beam stability at the same time. The important design parameters are shown in Figure 2.6.10: *b* is the radius of the beam pipe, g the aperture of the collimator and *d* the thickness of the collimator. The taper angle θ should be as small

as possible to make sure the beam pipe aperture is changed smoothly; otherwise the HOM and transverse mode coupling instability [14] will become serious. The aperture shape could be round or rectangular. At CEPC, a rectangular shape is used. The atomic number of collimator materials should be as high as possible to increase the stopping ability. We have chosen tungsten for the collimator material.

2.6.4.4.2 Constraints for the Aperture and Position of the Collimator

The aperture of the collimator should be proportional to the transverse size of the beam to keep the beam stable; thus the aperture is dependent on the betatron function of the accelerator. If the limitations on the betatron function are determined, the position along the beam line of where to insert the collimator will also be determined.

First, the collimator should stop most lost beam particles before they enter the IR. To achieve this goal, we require the ratio between the aperture and the transverse beam size where we locate the collimator be smaller than that in the IR as shown in the following equation:

$$\frac{d_c}{\sqrt{\varepsilon\beta_c}} \leq \frac{r_{IR}}{\sqrt{\varepsilon\beta_{IR,max}}} \tag{2.6.1}$$

where ε is the transverse emittance, d_c and β_c are the aperture and β function at the collimator, r_{IR} is the minimum radius of the beam pipe in the IR and the $\beta_{IR,max}$ the maximum β function in the IR. It should be noted that the horizontal and vertical direction should be considered separately.

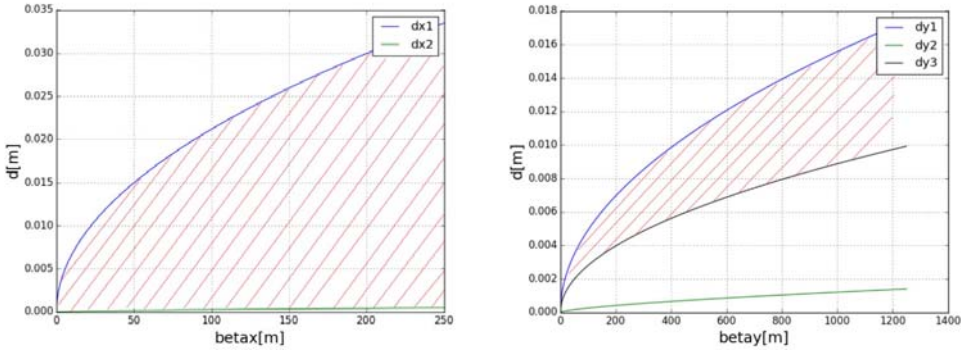

(a) Feasible region for the collimator in the horizontal direction, (b) Feasible region for the collimator in the vertical direction

Figure 2.6.11: Feasible regions for placement of the collimator. The blue curve is calculated from Equation (2.6.1), the green curve is Equation (2.6.2) and the black curve is Equation (2.6.3). The shaded area between these constraints are the feasible regions.

Second, the collimator shouldn't increase the transverse mode coupling instability (which is also called fast head-tail instability or strong head-tail instability). The transverse mode coupling instability will give an upper limit to the beam current. If the aperture of the collimator is too small, the beam current can't attain the desired goal. Thus, the aperture will be limited by the following equation:

$$d_c \geq \left(\frac{0.215AIZ_0qc\beta_c}{Bf_sE}\right)^{\frac{2}{3}} \left(\frac{\theta}{\sigma_z}\right)^{\frac{1}{3}} \tag{2.6.2}$$

In this equation, A is a constant (about 1), I is the current of a bunch, Z_0 is the impedance of the vacuum (about 377 Ω), q is the charge of an electron, c is the speed of light, B is another constant (about 8), f_s is the synchrotron frequency, E is the beam energy, θ is the taper angle of the collimator and σ_z is the length of the bunch. Notice that this equation is derived with the assumption that only one collimator is installed. For the multi-collimator case, this equation needs to be modified.

Third, the collimator shouldn't affect the injection of beam [15]. The beam will be injected to the main ring from the booster in the vertical direction, thus the vertical acceptance of the injected beam and the vertical aperture of the collimator should satisfy the following relationship:

$$d_{c,y} \geq \sqrt{a_y\beta_{c,y}} \tag{2.6.3}$$

Considering the constraints from the above three equations, we can obtain the feasible region for placement of the collimator. Figure 2.6.11 shows the feasible region in both horizontal and vertical direction.

2.6.5 Beamstrahlung

Beamstrahlung can be characterised by the parameter Υ:

$$\Upsilon = \frac{2}{3}\frac{\hbar\omega_c}{E} \tag{2.6.4}$$

where $\hbar\omega_c = \frac{3}{2}\hbar\gamma^3 c/\rho$ denotes the critical energy of synchrotron radiation, ρ the bending radius of the charged particle trajectory, γ the Lorentz factor of the beam particles, and E the beam particle energy before radiation. The higher the Υ, the more beamstrahlung photons with higher energies will be emitted. Assuming Gaussian charge distributions inside the two colliding beams, the average Υ can be estimated with the following formula:

$$\Upsilon_{av} \approx \frac{5}{6}\frac{Nr_e^2\gamma}{\alpha(\sigma_x + \sigma_y)\sigma_z} \tag{2.6.5}$$

where r_e is the classical electron radius, α the fine structure constant, σ_x/σ_y the transverse size of the bunch and σ_z the bunch length [16].

Table 2.6.1: Machine parameters of LEP2, CEPC, FCC-ee and ILC and their average beamstrahlung parameters Υ_{av} calculated with Eq. (2.6.5).

Parameters	Symbol	LEP2	CEPC	FCC-ee	ILC250
Center of mass energy	E_{cm} [GeV]	209	240	240	250
Bunch population	N [$\times 10^{10}$] σ_x	58	37.1	37	2
Horizontal beam size at IP	[nm]	270000	73700	61000	729
Vertical beam size at IP	σ_y [nm]	3500	160	120	7.7
Bunch length	σ_z [μm]	16000	2260	2110	300
Horizontal beta function at IP	β_x [mm]	1500	800	500	13
Vertical beta function at IP	β_y [mm]	50	1.2	1	0.41
Normalized horizontal emittance at IP	$\gamma\epsilon_x$ [mm ·mrad]	9.81	1594.5	1761.3	10
Normalized vertical emittance at IP	$\gamma\epsilon_y$ [mm ·mrad]	0.051	4.79	3.52	0.035
Luminosity	L [10^{34} cm^{-2}s^{-1}]	0.013	1.8	5.08	0.75
Beamstrahlung parameter	Υ_{av} [$\times 10^{-4}$]	0.25	4.7	6.1	200
Relative average energy loss per BX due to Beamstrahlung	σ_{av} [%]	0.0001	0.005	0.0075	1.0

From the machine parameters of LEP2 [17], CEPC [4], FCC-ee [18] and ILC [19], as listed in Table 2.6.1, the average beamstrahlung parameters Υ_{av} of these colliders are calculated with Eq. (2.6.5). The bunch sizes ($\sigma_{x,y,z}$) of CEPC, FCC-ee and ILC are expected to be significantly smaller than those of LEP2, leading to non-negligible beamstrahlung effects. Nevertheless, the bunch sizes of CEPC and FCC-ee are much larger than those of ILC and the beamstrahlung effects will be smaller accordingly.

2.6.5.1 Generators of Beamstrahlung

Beam-beam interactions at CEPC have been simulated with Guinea-Pig++ (Generator of Unwanted Interactions for Numerical Experiment Analysis Program Interfaced to GEANT), which allows detailed studies of the emission of beamstrahlung photons, incoherent pair production and hadronic events. In the Guinea-Pig++ simulation, the bunches are cut into slices in the longitudinal direction. Because the beam particles are ultra-relativistic, the electromagnetic field of both slices is flattened into a plane perpendicular to the beam direction. Thus, each slice interacts consecutively with each slice in the other bunch and interactions between two slices can be simplified as a two-dimensional problem. Each slice is further cut into cells forming a grid in the transverse direction and the potentials on the grid points can be calculated according to the charge distribution. The forces on beam particles can be derived from the potentials. In addition, the charge distributions in both colliding bunches are assumed to be Gaussian. The relevant configuration parameters are listed in Table 2.6.1. To reduce the simulation time, electron-positron pairs with energies less than 5 MeV are not tracked as they can be safely confined in the beam pipe with a solenoidal magnetic field.

2.6.5.2 Normalization

The beamstrahlung effect is one kind of multi-body effect. It's the consequence of interactions between the beam particles of two bunches with opposite charges. Actually, the normalization has been implemented in the generator for the two crossing bunches. In our simulation, we need to normalize the number of events produced in one bunch crossing per unit time by multiplying the number of bunch crossing in unit time.

2.6.5.3 Preliminary Results

2.6.5.3.1 Beamstrahlung Photons

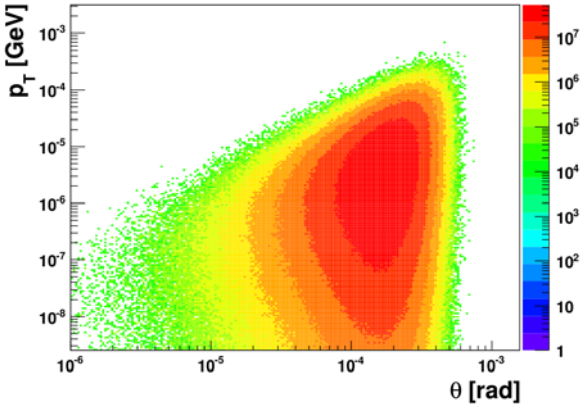

Figure 2.6.12: p_T versus θ distribution of the beamstrahlung photons at the CEPC.

Figure 2.6.12 shows the transverse momentum distribution versus the polar angle of the beamstrahlung photons originating from the beam-beam interactions. The photons are confined within a small angle of $|\theta| < 1$ mrad, so most of them will leave the interaction region without interacting with the beam pipe and will have a negligible effect on the detector backgrounds.

2.6.5.3.2 Incoherent Electron-Positron Pairs

Electron and positron pairs might be produced through incoherent pair production processes when two photons collide. These pairs are usually produced with large polar angle and high transverse momentum. They can contribute to the detector backgrounds in both direct and indirect ways:

- If the primary particles are produced with large polar angles, they will hit the detector directly;
- If the primary particles are produced with small polar angles, they might hit the beampipe or the detector components in the very forward region and produce secondary particles. Those particles can be back-scattered into the central region of the detector.

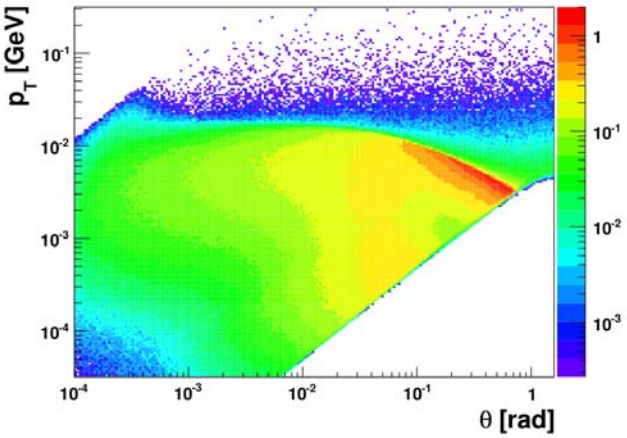

Figure 2.6.13: p_T versus θ distribution of electrons and positrons from incoherent pair production.

Figure 2.6.13 shows the p_T versus θ distribution of the electrons and positrons from incoherent pair production. The empty region in the bottom-right corner is formed because electrons/positrons with energy below 5 MeV are not tracked in the Guinea-Pig++ simulation. In Fig. 2.6.13, most of the electrons and positrons are concentrated in the area under an envelope (the so-called "kinematic edge"), which can be fit to the following empirical formula:

$$pT = 0.0202\, p0Z.297 \tag{2.6.6}$$

Assuming perfect helical trajectories in a solenoidal magnetic field of 3.5 T, the charged particles along the envelope can develop a trajectory profile as shown in Fig. 2.6.14. The beam pipe (shown by the polyline) and any detector components must be kept sufficiently far away from the kinematic edge to avoid drastic particle showering.

2.6.5.3.3 Hadronic Background

The collision of two beamstrahlung photons might also produce quark pairs. The quark pairs will become mini-jet events through fragmentation. Because the Guinea-Pig++ can only give the energy of the two photons, Pythia 6.4 [20] is used to simulate the fragmentation process of the quark pairs. The final particles of the mini-jet can be used as input to Geant4 simulation to evaluate the radiation of hadronic backgrounds

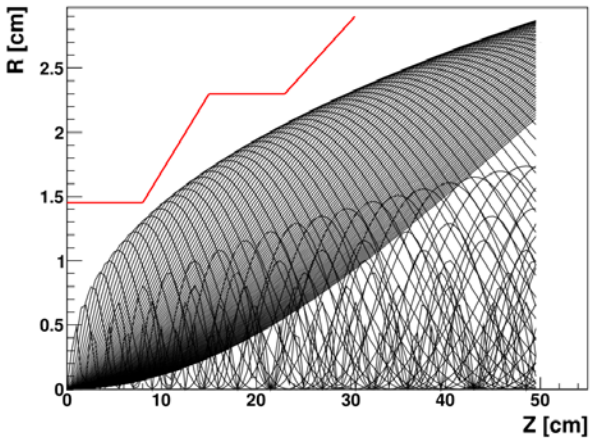

Figure 2.6.14: The helical trajectories of electrons/positrons from pair production in a solenoidal magnetic field of 3.5 T. The polyline indicates the position of the beam pipe in the current design.

2.6.5.3.4 Hit Density

Although most of the particles originating from beamstrahlung and subsequent pair production will leave the interaction region without hitting the beam pipe, a small fraction of them will enter the detector directly, or hit the beam pipe and/or detector components in the forward region, which can introduce back-scattered particles. The resulting detector background will increase detector occupancy and cause radiation damage to silicon devices close to the interaction point.

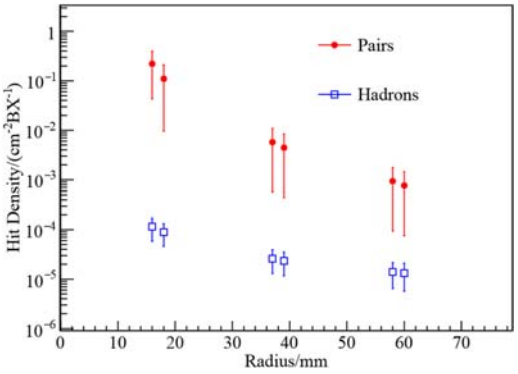

Figure 2.6.15: Hit density of pairs and hadronic backgrounds at 6 layers of the VTX detector with radii 16 mm, 18 mm, 37 mm, 39 mm, 58 mm and 60 mm.

The estimated hit densities at the 6 layers of the vertex detector (VTX) are shown in Fig. 2.6.15. At the innermost VTX layer positioned at r = 1.6 cm, the hit density is □0.2 hits/cm^2/BX. With a bunch spacing of about 3.6 μs for the current CEPC single-ring design, the resulting detector occupancy will be well below 0.5% for the first VTX layer, assuming a pixel pitch size of 20 μm and readout time of 20 μs.

2.6.5.3.5 Radiation Damage

Although the estimated hit density per bunch crossing is rather low, the potential detector radiation damage can be considerable given the high repetition rate of CEPC, *i.e.* □ 2.8×10^5 bunch crossings per second in the current design. The radiation damage to the CEPC sub-detectors, in particular the vertex detector close to the interaction point, should be carefully evaluated. The effects of radiation damage on the silicon detector can be roughly characterized as non-ionizing energy loss (NIEL) and total ionizing dose (TID).

NIEL can lead to crystal defects by displacing the silicon atoms from their lattice sites (so-called "bulk damage") [21]. The effects induced by any particle with a given energy can be normalized to the equivalent damage caused by one MeV neutrons and denoted as n_{eq}. In this study, the electron flux at a given point is obtained by tracking all the particles with the assumption of perfect helices. The total NIEL per year is calculated with the same method used in Ref. [22], assuming machine operation for 10^7 seconds (referred to as a "Snowmass Year"). In addition, a safety factor of 10 is used in the calculation to account for imperfect knowledge and uncertain issues of the machine design at this early stage. Fig. 2.6.16 shows the NIEL distribution in the CEPC vertex detector. At the first vertex detector layer, the annual value for NIEL is about 10^{11} one MeV n_{eq}/cm^2.

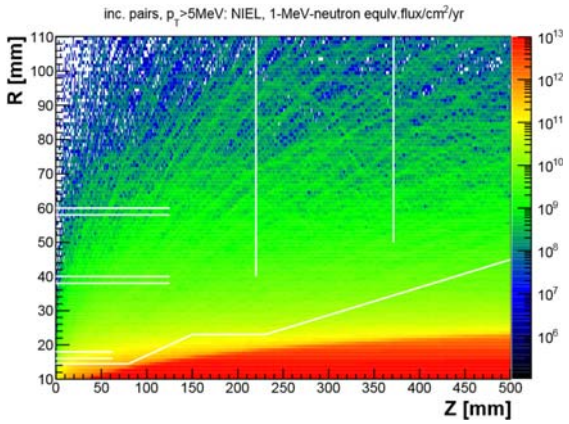

Figure 2.6.16: NIEL distribution in the CEPC vertex detector. The white polyline and horizontal line segments indicate the positions of the beam pipe and the 6 VTX detector layers, respectively.

TID can introduce ionization at the Si-SiO_2 interface, leading to performance degradation of silicon devices [23]. TID can be determined by:

$$D = \frac{E_{dep}}{m} = \frac{E_{dep}}{\rho \cdot V} \tag{2.6.7}$$

where E_{dep} is the energy deposited in the material, and m, ρ and V are the mass, density and volume of the matter, respectively. These input parameters are extracted from the full detector simulation. In the TID calculation, a safety factor of 10 is also taken into account. The annual TID values at the 6 VTX detector layers are shown in Fig. 2.6.17 and the highest annual TID is found to be about 300 kRad at the first vertex detector layer.

The potential radiation damage due to beamstrahlung and consequent pair production is found to be tolerable for most silicon detectors used in high energy physics experiments, but there are other backgrounds at circular electron-positron colliders, e.g. radiative

Bhabha scattering and synchrotron radiation. Further investigations into these background sources are necessary to thoroughly understand the radiation tolerance requirements.

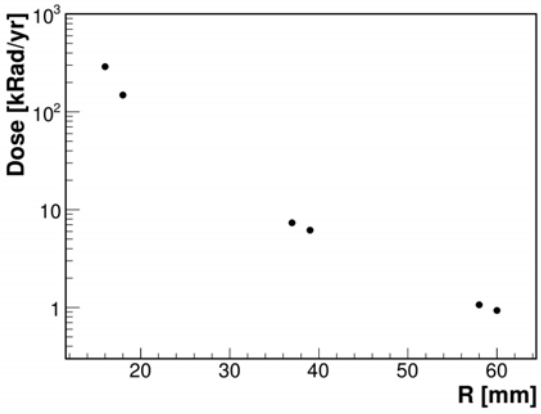

Figure 2.6.17: TID at the vertex detector layers.

2.6.6 Comparison of Geant4 and Fluka

Geant4 and Fluka are used to simulate the transport of particles in the detector and the interaction between the particles and materials. Geant4 is usually used to obtain the hit density on the detector and Fluka is usually used to extract the radiation dose in the detector. To validate our simulation, some results of Geant4 are compared with those of Fluka. Figure 2.6.18 shows the energy deposited in the detector calculated by Geant4 and Fluka. The results of the two codes are consistent with each other.

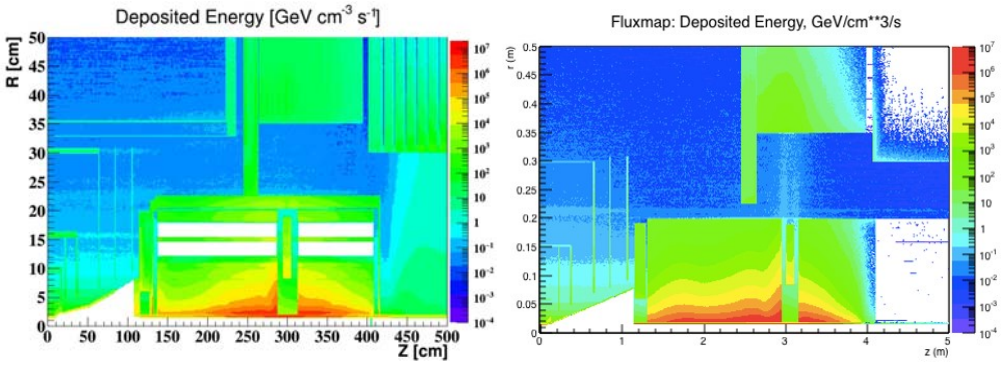

(a) Deposited Energy from Geant4 (b) Deposited Energy from Fluka

Figure 2.6.18: Energy deposited in the detector

2.6.7 Summary

The most important beam induced backgrounds have been evaluated for CEPC. Because the lattice design hasn't been completed, a preliminary version of the single ring lattice is used to develop the software and tools. By now, the software and tools for the background simulation have all been developed and validated. As there are modification of the accelerator or detector, the radiation level can be evaluated much more rapidly than before. The software used for the simulation and the preliminary results without any shielding are shown in Table 2.6.2.

Table 2.6.2: The software for the simulation and the preliminary results of each beam induced background without any shielding.

Background type	Generators	Sub-type of background	Particle flux at IP [$cm^{-2}BX^{-1}$]	Particle energy [GeV]
Synchrotron Radiation	Geant4; BDSIM	Dipole	~ 10^{10}	~ 0.001
		Quadruple	~ 10^{6}	~ 0.007
Beam lost particles	BBBrem; SAD	Radiative Bhabha	~ 10	~ 120
		Beam-Gas Scattering	↑	↑
Beamstrahlung	Guinea-Pig++; Pythia6	Pairs	~ 10^{-2}	~ 0.05
		Hadrons	~ 10^{-5}	2

The radiation level at the detector is highly dependent on the lattice design and the shielding design. The preliminary results show that the radiation level from synchrotron radiation is very high. The reason is that the lattice wasn't optimized for the beam induced backgrounds. To suppress the background level to be acceptable for the detector, both the lattice design and the shielding design need be further studied. For the lattice design, the strength of the last several dipole magnets should be decreased to suppress the critical energy and radiation power of synchrotron. For the shielding design, the position, aperture, thickness and material of collimator should be further optimized and more shielding materials should be inserted into the IR.

2.6.8 References

1. The ATLAS Collaboration. Observation of a new particle in the search for the Standard Model Higgs boson with the ATLAS detector at the LHC. *Phys. Lett. B*, 716:1–29, 2012.
2. The CMS Collaboration. Observation of a new boson at a mass of 125 GeV with the CMS experiment at the LHC. *Phys. Lett.*, B716:30–61, 2012.
3. The ATLAS Collaboration. Projections for measurements of Higgs boson signal strengths and coupling parameters with the ATLAS detector at a HL-LHC. *ATL-PHYS-PUB-2014-016*, Oct 2014.
4. The CEPC-SPPC Study Group. CEPC-SPPC Preliminary Conceptual Design Report, Volume II Accelerator. *IHEP-CEPC-DR-2015-01, IHEP-AC-2015-01*, 2015.

5. J.E. Augustin, N. Dikansky, Ya. Derbenev, J. Rees, Burton Richter, et al. Limitations on Performance of e+ e- Storage Rings and Linear Colliding Beam Systems at High Energy. *eConf*, C781015:009, 1978.
6. Daniel Schulte. *Study of Electromagnetic and Hadronic Background in the Interaction Region of the TESLA Collider*. PhD thesis, DESY, 1997.
7. S. Agostinelli et al. GEANT4: A Simulation toolkit. *Nucl.Instrum.Meth.*, A506:250–303, 2003.
8. R. Kleiss and H. Burkhardt. BBBREM: Monte Carlo simulation of radiative Bhabha scattering in the very forward direction. *Comput. Phys. Commun.*, 81:372–380, 1994.
9. D. Schulte, M. Alabau, Philip Bambade, O. Dadoun, G. Le Meur, et al. GUINEA PIG++ : An Upgraded Version of the Linear Collider Beam Beam Interaction Simulation Code GUINEA PIG. *Conf.Proc.*, C070625:2728, 2007.
10. K. Hirata. An Introduction to SAD. In *2nd ICFA Advanced Beam Dynamics Workshop Lugano, Switzerland, April 11-16, 1988*, pages 62–65, 1988.
11. Giuseppe Battistoni et al. Overview of the FLUKA code. *Annals Nucl. Energy*, 82:10–18, 2015.
12. I. Agapov, G. A. Blair, S. Malton, and L. Deacon. BDSIM: A particle tracking code for accelerator beam-line simulations including particle-matter interactions. *Nucl. Instrum. Meth.*, A606:708–712, 2009.
13. John David Jackson. *Classical Electrodynamics*. Wiley, 1998.
14. Alexander Wu Chao, Karl Hubert Mess, Maury Tigner, and Frank Zimmermann, editors. *Handbook of accelerator physics and engineering*. World Scientific, Hackensack, USA, 2013.
15. Yiwei Wang. Study on the design of the cepc final doublet. *Unpublished note*.
16. Kaoru Yokoya and Pisin Chen. Beam-beam phenomena in linear colliders. *Lect.Notes Phys.*, 400:415–445, 1992.
17. V.I. Telnov. Restriction on the energy and luminosity of e^+e- storage rings due to beamstrahlung. *Phys.Rev.Lett.*, 110:114801, 2013.
18. M. Bicer et al. First Look at the Physics Case of TLEP. *JHEP*, 01:164, 2014.
19. Chris Adolphsen, Maura Barone, Barry Barish, Karsten Buesser, Philip Burrows, John Carwardine, Jeffrey Clark, Hlne Mainaud Durand, Gerry Dugan, Eckhard Elsen, et al. The International Linear Collider Technical Design Report - Volume 3.II: Accelerator Baseline Design. 2013.
20. Torbjorn Sjostrand, Stephen Mrenna, and Peter Z. Skands. PYTHIA 6.4 Physics and Manual. *JHEP*, 05:026, 2006.
21. R. C. Newman. Defects in silicon. *Rep. Prog. Phys*, Vol. 45, 1982.
22. G. Lindstrom. Radiation damage in silicon detectors. *Nucl. Instrum. Meth.*, A512:30–43, 2003.
23. T. R. Oldham and F. B. McLean. Total Ionizing Dose Effects in MOS Oxides and Devices. *TRANSACTIONS ON NUCLEAR SCIENCE*, Vol. 50, No. 3:483 – 499, 2003.

2.7 Sawtooth Effect in PDR and APDR

Synchrotron radiation is emitted when the electron/positron trajectories are changed by the arc bending magnets. The energy loss caused orbit distortion, which can be compensated by the next RF cavity. This is called the sawtooth effect.

In CEPC, this strong sawtooth effect causes a mismatch between the magnet strength and beam energy. Bending magnets cause orbit distortion, quadrupoles make optics distorted, and sextupoles degrade the chromaticity correction and reduce the dynamic aperture.

2.7.1 Sawtooth Effect in PDR

The sawtooth effect on optics, orbit and dynamic aperture are studied in PDR by scaling the strength of all magnets. Lattice version: CEPC-ARC4-PDR3-IR1 was used in this study.

Table 2.7.2: Twiss parameters with and without sawtooth effect in PDR

	NO Sawtooth	Sawtooth
μ_x	0.0800001	0.0895183
μ_y	0.2200000	0.2272822
β_x^*	0.219915	0.218720
β_y^*	0.001000	0.001000
ε_x	2.15121nm	5.49688 nm
ε_z	3.38423E-6 m	3.57412E-6 m
Bunch length	2.53716622 mm	2.79435492 mm

With the sawtooth effect, there is little tune change or change in the β function; horizontal emittance increased nearly three times; and the bunch length enlarged. Since luminosity is inversely proportional to the emittance, a large emittance growth cause the luminosity reduction.

Since horizontal emittance ε_x is proportional to I5/I2, we analysed the emittance growth by calculating the I5/I2 of the whole ring, and also part of the ring which has the largest emittance growth.

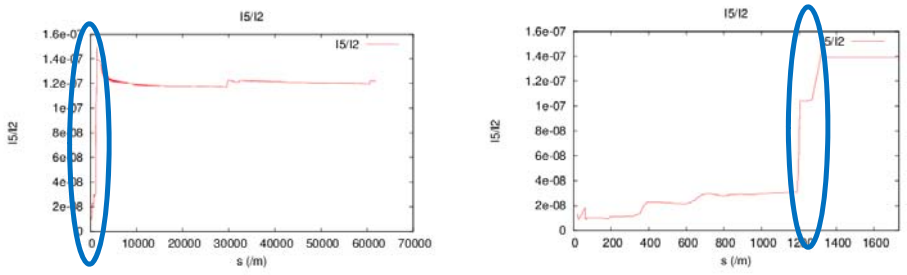

Figure 2.7.1. I5/I2 of whole ring (left) and I5/I2 from IP to the arc entrance (right)

From Figure 2.7.1 we can see that the significant increase in ε_x caused by the separators in transition area between the PDR and the arc. The dynamic aperture for both on-momentum and off-momentum particles is reduced greatly from the sawtooth effect. The off-momentum DA for particles with momentum deviation greater than 1% is reduced to zero. This is far below the required dynamic aperture of CEPC: on-momentum ($20\sigma_x$, $20\sigma_y$), off-momentum ($5\sigma_x$, $5\sigma_y$).

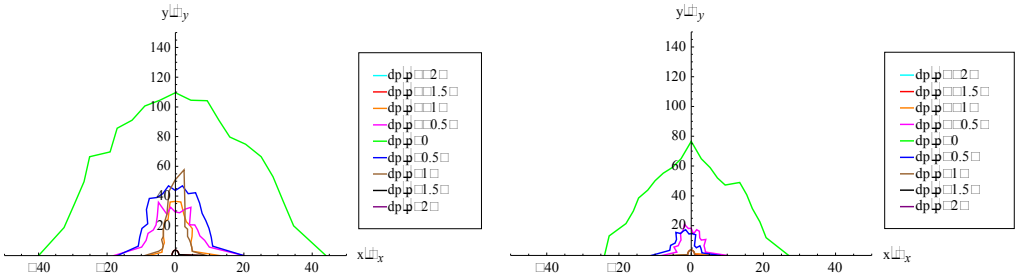

Figure 2.7.2. PDR DA without sawtooth (left) and with sawtooth (right)

The dynamic aperture is reduced due to a significant increase of resonance coefficients with sawtooth compared to the one without sawtooth.

Table 2.7.2: Harmonic function with and without sawtooth effect in CEPC PDR

		No sawtooth	With sawtooth
Resonance coefficients	3000	7.505871E-11	3.246853E-02
	2100	-3.365819E-10	-2.792628E-03
	1020	3.166457E-09	5.405187E-02
	1002	5.325543E-09	-2.019829E-02
	1011	2.672939E-08	3.082794E-02
1st order chromaticity	Q1′	-43.39516853	-43.42476251
	Q2′	17.82255966	17.84104701
2nd order chromaticity	Q1″	1979.50975070	1985.65039387
	Q2″	1098.55865448	1246.28222447

There are several methods to mitigate the sawtooth effect:

- Increase the number of RF stations (which is equivalent to reducing the synchrotron radiation between stations)
- Optimize the IR and separator design to reduce the emittance growth
- Change the RF voltage and phase to be different between different stations
- Optimize the dynamic aperture, to mitigate the degradation by sawtooth effect, but it is difficult to find sextupole settings to satisfy both electrons and positrons.

We studied the first option to reduce the synchrotron radiation to 1/2, 1/5, 1/10, 1/15, 1/20. The sawtooth effect on the orbit became weaker and weaker.

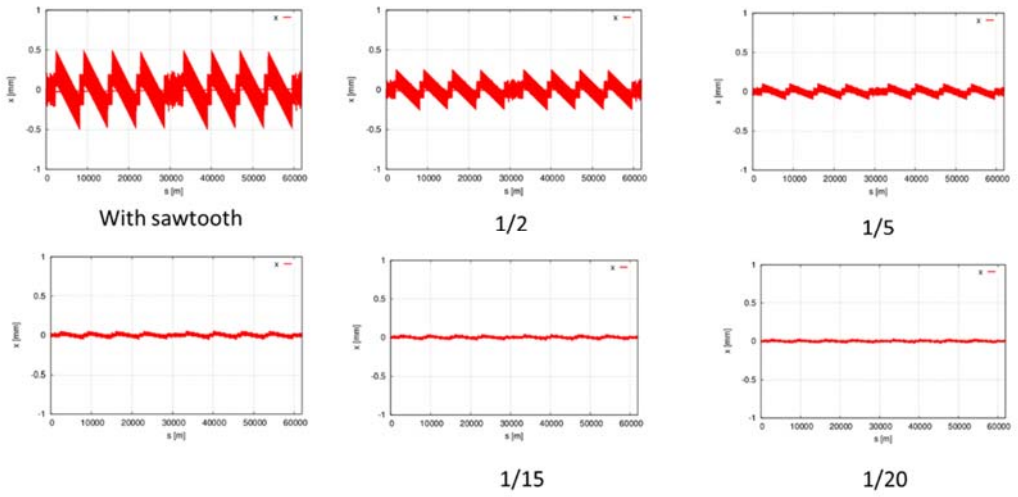

Figure 2.7.3. The horizontal orbit change with reduction of synchrotron radiation in PDR

Table 2.7.3: Twiss parameters change with reduction of synchrotron radiation

	NO Sawtooth	Sawtooth	1/2	1/5	1/10	1/20
μ_x	0.0800001	0.0895183	0.0845194	0.0817528	0.0808675	0.0804316
μ_y	0.2200000	0.2272822	0.2240538	0.2217279	0.2208823	0.2204458
β_x^*	0.219915	0.218720	0.219434	0.219747	0.219834	0.219875
β_y^*	0.001000	0.001000	0.0009994	0.0009996	0.0009997	0.000999
ε_x	2.15121 nm	5.49688 nm	3.53031nm	2.48252nm	2.25480nm	2.18389nm
ε_z	3.38423E-6 m	3.57412E-6 m	3.76753e-6m	3.87392e-6m	3.89533e-6m	3.90137e-6m
Bunch length	2.53716622 mm	2.79435492 mm	2.87238027 mm	2.91461168 mm	2.92307962 mm	2.92547315 mm

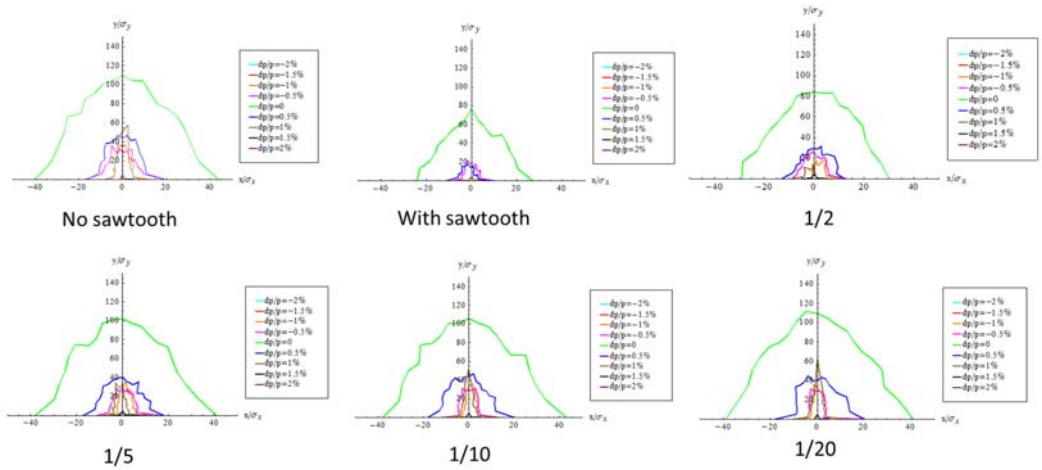

Figure 2.7.4. The DA change with reduction of synchrotron radiation

By reducing synchrotron radiation, the orbit sawtooth effect is mitigated. Synchrotron radiation is reduced to 1/2 (equivalent to the 100-km lattice), and the RF station number is doubled. In this case, the emittance is reduced by about 1/3; however, both on-momentum and off-momentum DA still can't be recovered. If one reduces synchrotron radiation to 1/20, horizontal emittance can almost be recovered. But that requires a very large number of RF stations. And the DA still can't be recovered with a SR reduction to 1/20, and is far from meeting the requirements. To compensate the DA reduction due to the sawtooth effect, sextupole strength at the same location is different for electrons and positrons, which makes the DA compensation quite difficult.

2.7.2 Sawtooth Effect in APDR

The sawtooth effect on optics, orbit and dynamic aperture are calculated in APDR by scaling the strength of all magnets. We use lattice version: CEPC-APDR-v0.0.1 for this study.

The horizontal tune is reduced to zero and the horizontal orbit is unstable. The dynamic aperture is reduced to zero.

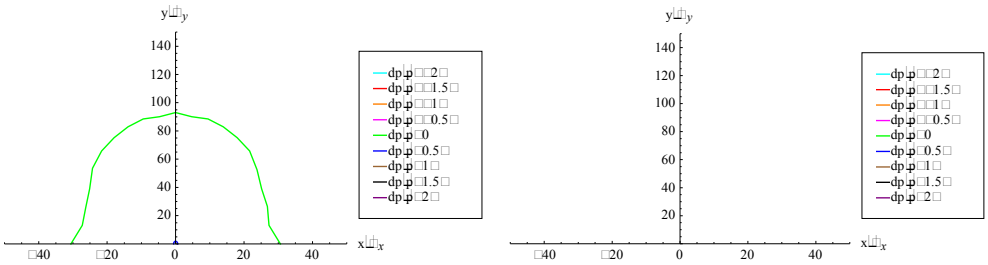

Figure 2.7.5. Dynamic aperture without sawtooth (left) and with sawtooth (right)

To mitigate the strong sawtooth effect, synchrotron radiation is reduced to 1/2, 1/5, 1/10, 1/20. Twiss parameters are compared below in Table 2.7.4; horizontal orbit and dynamic aperture changes are shown in Figures 2.7.6 and 2.7.7.

Table 2.7.4: Twiss parameters change with reduction of synchrotron radiation

	NO Sawtooth	Sawtooth	1/2	1/5	1/10	1/20
μ_x	0.0800094	0.0000000	0.0392321	0.0650136	0.0726207	0.0763370
μ_y	0.2201892	0.1378555	0.1758617	0.2016766	0.2108015	0.2154624
β_x^*	0.250022	0.999999	0.150019	0.219629	0.235873	0.243181
β_y^*	0.001361	0.001459	0.001391	0.001369	0.001365	0.001363
ε_x	2.95372nm	3.00332nm	3.40487nm	2.98311nm	2.96047nm	2.99618nm
ε_z	4.1139E-6 m	4.13995E-6 m	4.1242e-6m	4.1174e-6m	4.1156e-6m	4.1148e-6m
Bunch length	2.9359 mm	2.9506 mm	2.9422mm	2.9382mm	2.9370mm	2.9365mm

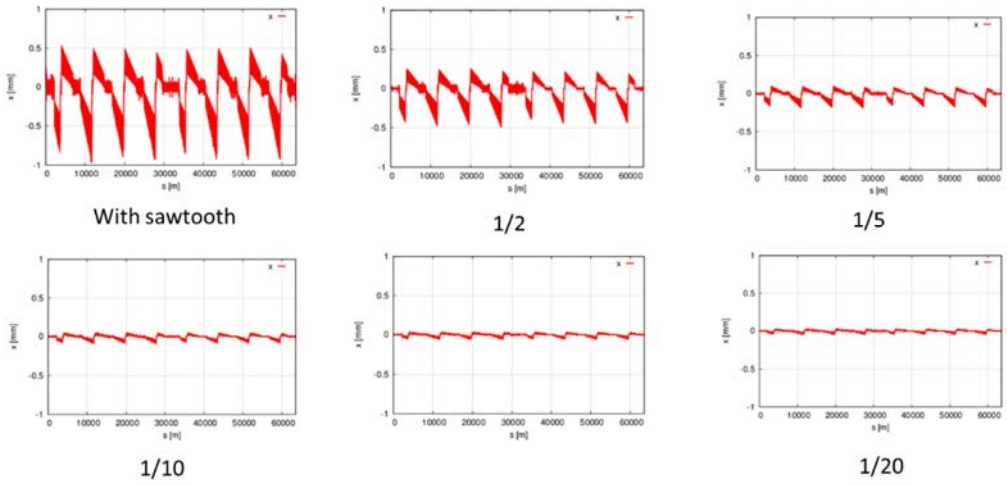

Figure 2.7.6. The horizontal orbit change with reduction of synchrotron radiation in APDR

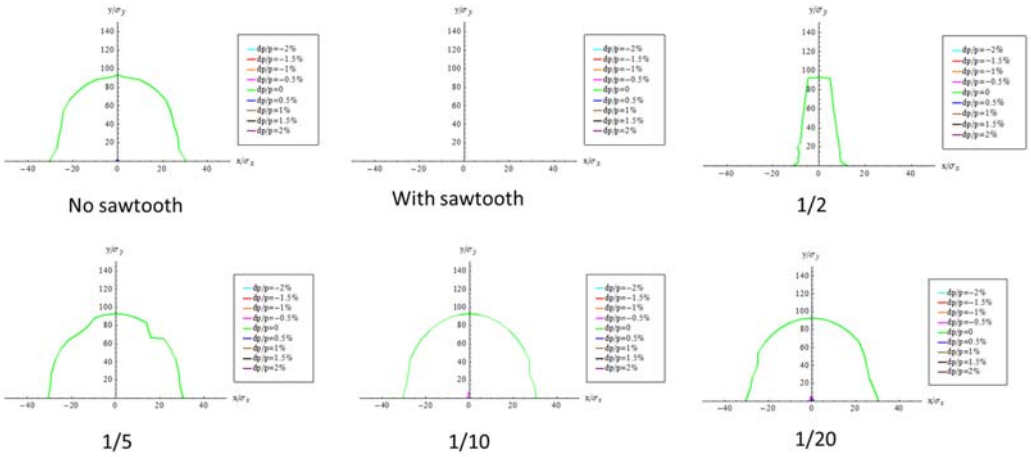

Figure 2.7.7. Dynamic aperture change with synchrotron radiation reduction in APDR

By reducing synchrotron radiation, which is equivalent to increasing the number of RF stations, the orbit sawtooth effect is mitigated. Synchrotron radiation is reduced to 1/2 equivalent to the 100-km lattice, and the RF station number is doubled. In this case, the emittance seems not to be improved, and both on-momentum and off-momentum DA still can't be recovered. If the synchrotron radiation is reduced to 1/20, both horizontal emittance and DA can almost be recovered; however, the beta function still can't be recovered. To compensate the DA reduction due to the sawtooth effect, the sextupole strength at the same location is different for electrons and positrons.

Since horizontal emittance ε_x is proportional to I5/I2, we analysed the emittance growth by calculating the I5/I2 for the whole ring and also for the part which has the largest emittance growth.

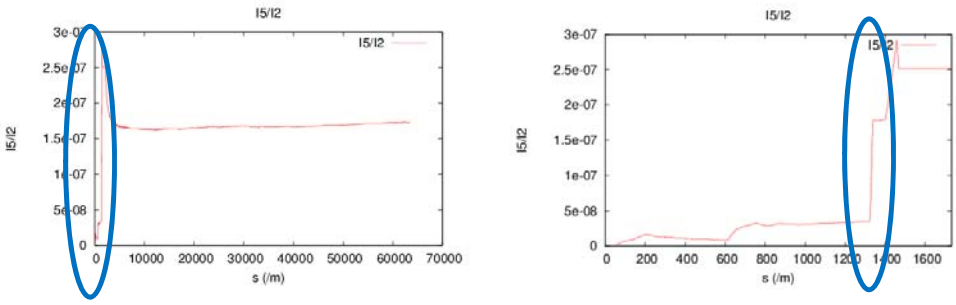

Figure 2.7.8. I5/I2 of whole ring (left) and I5/I2 from IP to entrance of arc (right)

The significant increase of ε_x is caused by the separators.

2.8 Baseline and Alternative Options

Based on the systematic study of the four options – single ring with pretzel, partial double ring, advanced partial double ring and fully partial double ring (i.e., double ring), as shown in Figs. 2.8.1 and 2.8.2, it was decided that:

1) The CEPC baseline accelerator is a fully partial double ring (i.e. double ring) configuration with a circumference of 100 km and shared SCRF in each beam line of electron and positron as shown in Fig, 2.8.3(a).
2) The booster has the same circumference as the collider and is in the same tunnel. The linac injection energy is 10 GeV for both electrons and positrons.
3) There are two IPs.
4) The full crossing angle is 33 mrad with L* = 2.2 m.
5) The SCRF system for Higgs and Z-pole operation are independent from each other.
6) The baseline design is to reach a luminosity higher than 2×10^{34} $cm^{-2}s^{-1}$ at the Higgs energy with ~30 MW synchrotron radiation power per beam, and a luminosity higher than 1×10^{34} $cm^{-2}s^{-1}$ for Z-pole operation.
7) The advanced partial double ring scheme with 8 partial double ring regions is defined as an alternative scheme, as shown in Fig. 2.8.3(b) with the aim to reduce the construction cost and to study possible solutions for the sawtooth and beam loading effect.
8) The SppC will be in the same tunnel together with the CEPC and have two IPs. In principle, the CEPC and SppC can operate at the same time.

For the SCRF system, the followings were decided:

1) Layout: a double ring with two RF sections; each section has equal number of RF cavities in each ring, which are to be shared by both e+ and e- beams.
2) Operation energies: The Higgs, W and Z operation will use the same cavities and cryomodules but with different RF power.
3) Operation at high luminosity: The total number of cavities (input power limited), cell number per cavity (gradient and HOM power limited) and number of klystrons are designed with a margin to run in high luminosity or high voltage mode for the Higgs, W and Z.

The SppC baseline design as shown in Fig. 2.8.4 has the following features:

- Tunnel circumference: 100 km
- Dipole magnet field: 12 T, using iron-based HTS technology
- Center of mass energy: >70 TeV
- Injector chain: 2.1 TeV
- Relatively lower luminosity in the first stage, followed by a luminosity upgrade in the second stage
- Development plan for high-field SC magnet: Starting to develop required HTS magnet technology; before applicable iron-based HTS wires are available, models by YBCO and LTS wires can be used for specific studies (magnet structure, coil winding, stress, quench protection method, etc.)

Subject to the progress in the SC magnet technology development, it is envisioned that the SppC will have an energy upgrade phase:

- Dipole magnet field: 20-24 T, iron-based HTS technology
- Center of mass energy: >125 TeV
- Injector chain: 4.2 TeV (adding a high-energy booster ring in the main tunnel replacing the CEPC)

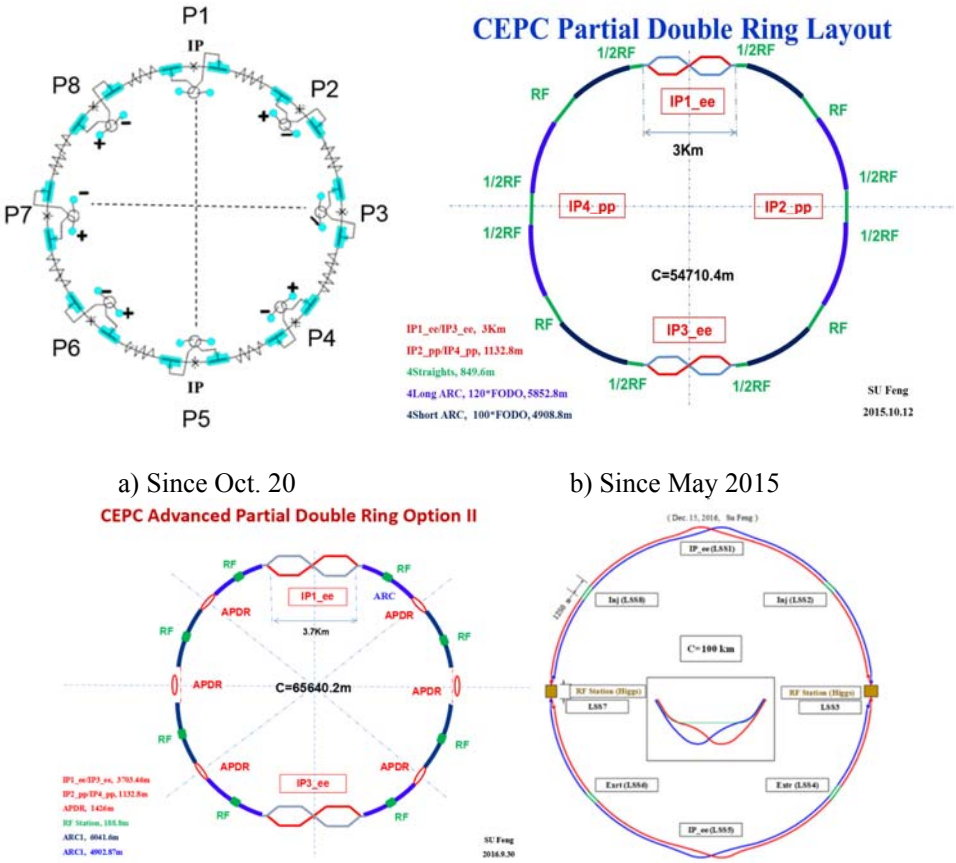

a) Since Oct. 20 b) Since May 2015

c) Since May 2016 d) Since Nov. 2016

Fig. 2.8.1: The four options for comparison

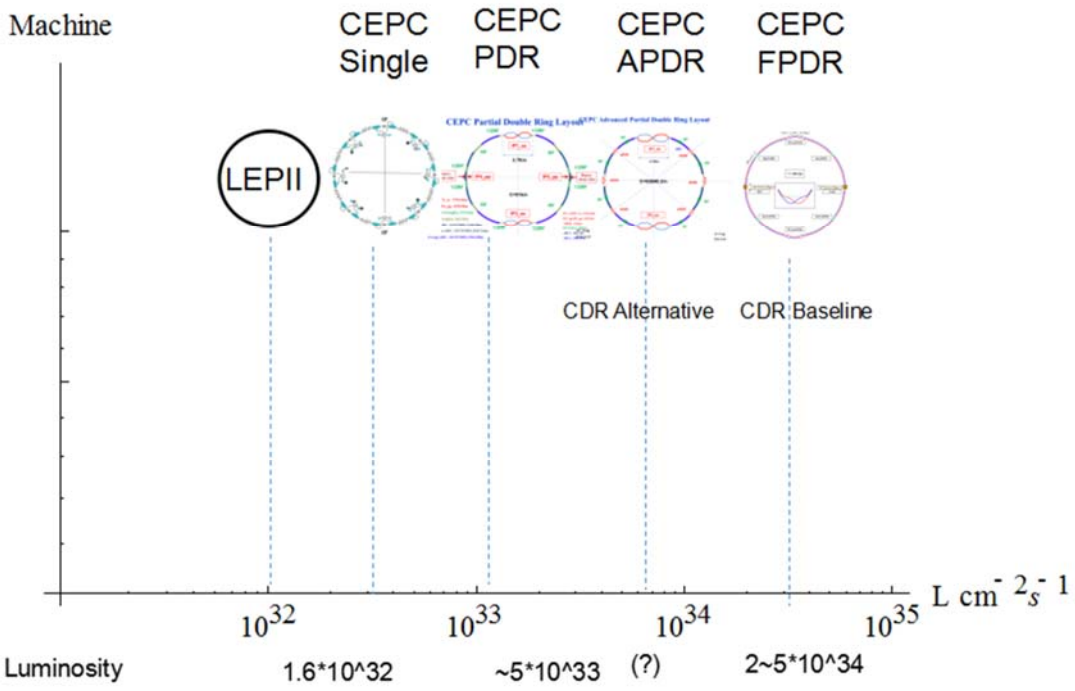

Fig. 2.8.2: Luminosity potentials corresponding to the four options

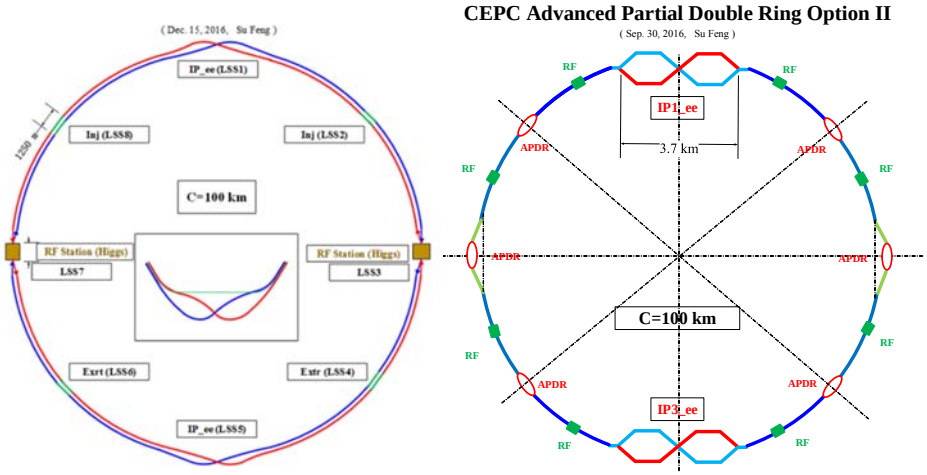

CEPC baseline design (a) CEPC alternative design (b)

Fig. 2.8.3: CEPC baseline and alternative schematic layout

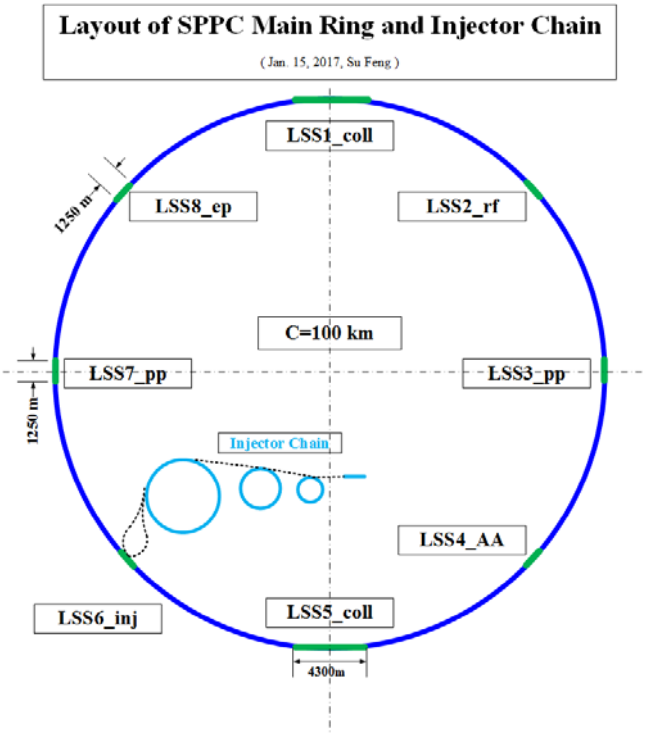

Fig. 2.8.4: SppC baseline schematic layout

3 CEPC – Technical Systems

3.1 Superconducting RF System

3.1.1 Introduction

The RF system accelerates the electron and positron beams, compensates for synchrotron radiation loss and provides sufficient RF voltage for energy acceptance and the required bunch length in the CEPC Booster and collider rings. Superconducting radio frequency (SRF) cavities are used because they have much higher continuous wave (CW) gradient and energy efficiency as well as larger beam aperture compared to normal conducting cavities. These substantial advantages result in fewer cavities, lower impedance and thereby less disruption to the beam; also the AC power consumption is less. The CEPC SRF system will be one of the largest and most powerful SRF accelerator installations in the world. The SRF system is one of the most important technical systems of CEPC and is a key for achieving its design energy and luminosity. Together with the associated RF power source and cryogenic system, it will dominate the overall machine cost, efficiency and performance. To deliver the target integrated luminosity, high-availability SRF components as well as rapid commissioning and efficient operation with minimal downtime are required.

CEPC will use 650 MHz cavities for the collider (Main Ring) and 1.3 GHz cavities for the Booster. The baseline of the collider is a double-ring with 650 MHz cavities shared between the two collider rings. The two RF sections are located at IP2 and IP4. A RF section contains two RF stations. One of the RF stations is in the outer ring, and the other is in the inner ring. The collider electron or positron beams will go through the two RF stations in each RF section. Half of the ring buckets will be filled to avoid collisions in the RF section. When operating at the W and Z-pole, part of the "Higgs" cavities will be used in each RF station, and the electron or positron beams will go through only one of the two RF stations of a RF section. The unused cavities will be powered off and detuned. The W and Z-pole bunches will be uniformly distributed in the two rings. If the W and Z-pole beam current is limited by the coupled-bunch instability (CBI), the remaining cavities should be off-line. If the higher luminosity Z-pole is further limited by HOM power and CBI, high current (e.g. KEKB/BEPCII type) cavities and cryomodules will be used with separate or shared cavities for the two rings. An advanced partial double ring with four electron bunch trains and four positron trains is chosen as an alternative design. Transient beam loading is the most serious concern for bunch train operation.

The feasibility of 1.3 GHz cavities for the Booster operating in high luminosity W and Z-pole injection should also be investigated. Enough RF straight section length should be retained for future upgrades.

The collider cavities operate in CW. The Booster cavities operate in quasi-CW mode with the following time sequence: first, stay at 1 MV/m for one second of electron injection from the Linac, followed then by a ramp up to 20 MV/m in four seconds, followed by one-second extraction to the collider and then the RF is turned off. After a four-second magnet ramp down, the same ten-second cycle begins for positrons. The RF and cryogenic duty factor of the Booster, with respect to a purely CW operating mode, is about 20 % for continuous alternative injection and extraction of electrons and positrons.

An RF section consists of several collider cryomodules and Booster cryomodules. The collider module will be mounted on the tunnel floor and the Booster module hung from the ceiling in series with the collider module string at a different beamline height. Each of the 10 m-long collider cryomodule contains six 650 MHz cavities, and each of the 12 m-long Booster cryomodule contains eight 1.3 GHz cavities. A Euro-XFEL/ILC-type cryomodule structure slightly modified for CW or quasi-CW operation will be used. Modifications envisioned are enlargement of the two-phase pipe and helium vessel chimney diameters, removal of a portion of the 5 K shield while keeping the intercepts, and without superconducting quadrupoles inside. The collider cryomodule will have one beamline HOM ferrite damper at each end at room temperature.

During the conceptual design phase, significant effort is needed to identify high-risk technical challenges that require R&D. The highest priority items are efficient and economical damping of the HOM power with minimum dynamic cryogenic heat load, achieving the cavity gradient with high quality factor in the vertical test and real accelerator environment, robust high power input couplers that are design compatible with cavity clean assembly and low heat load. The hardware specifications for the CEPC SRF systems are summarized in Table 3.1.1.

Table 3.1.1: CEPC SRF Hardware Specifications

Hardware	Qualification	Normal Operation	Max. Operation
650 MHz 2-cell Cavity	VT 4E10 @ 22 MV/m HT 2E10 @ 20 MV/m	2E10 @ 16.5 MV/m	2E10 @ 20 MV/m
1.3 GHz 9-cell Cavity	VT 3E10 @ 25 MV/m	2E10 @ 20 MV/m	2E10 @ 23 MV/m
650 MHz Input Coupler	HPT 300 kW sw	< 254 kW	280 kW
1.3 GHz Input Coupler	HPT 20 kW peak, 4 kW avr.	< 15 kW peak	18 kW peak
650 MHz HOM Coupler	HPT 1 kW	< 0.2 kW	1 kW
650 MHz HOM Absorber	HPT 5 kW	< 2 kW	5 kW
650 MHz Cryomodule (six 2-cell cavities)	static loss 5 W @ 2 K	static loss 8 W @ 2 K	static loss 10 W @ 2 K
Tuner (MR & Booster)	tuning range and resolution 400kHz/1Hz	200 kHz / 1 Hz	400 kHz / 1 Hz

In parallel with design and key R&D, extensive development of SRF personnel, infrastructure and industrialization is essential for the successful realization of CEPC. A large SRF infrastructure and talent pool needs to be built. Chinese industry should participate in the R&D and pre-production work as early as possible. A more detailed SRF R&D, infrastructure and pre-production plan is described in Chapter 6.

3.1.2 Collider 650 MHz SRF System

The superconducting RF system is crucial to reach the target performance and explore the full potential of CEPC. Due to the wide range of SRF parameters in terms of RF voltage and beam current, it is impossible to have a single common system for the

highest possible luminosity in each mode (Higgs, W, and Z-pole) with 50 MW synchrotron radiation power per beam. A staged SRF complex with upgrade possibility is inevitable. In the same time, the baseline SRF parameters should be chosen to have operating margin and flexibility.

For Z-pole operation, cavity impedance at high current and small damping is of the most concern. The smallest number of cavities is preferred to provide up to the required 100 MW power to the beams. This results in very high input coupler power. Because of the high HOM power SuperKEKB / BEPCII type cryomodules (one 1-cell cavity per module) are preferred. For Higgs and W operation, handling the large HOM power in the multi-cavity cryomodule is the most challenging problem. The LEP2 and LHC HOM coupler experience is an important reference. For a possible energy upgrade, the high RF voltage (both Main Ring and Booster) requires both high gradient and high Q, which can be realized by pushing SRF technology to control the capital and operations cost.

Different designs for the collider ring have been proposed and studied in detail for several years. A double ring with shared cavities is chosen as the baseline design. The advanced partial double ring with four electron bunch trains and four positron trains is an alternative. The comparison of these schemes from the point of view of the SRF system is shown in Table 3.1.2.

Table 3.1.2: Comparison of SRF system for different collider ring designs

	Single Ring (SR)	Partial Double Ring (PDR)	Advanced Partial Double Ring (APDR)	Double Ring with Common Cavity (DRcc)	Double Ring (DR)
Luminosity	HL-H too many bunches for pretzel; Z too low; Showstopper	bunch number limited by PDR; Z low Problematic	bunch number limited by APDR; Z low Problematic	tt, H, W same with DR; highest Z lower than DR	Best
SRF Operation	H high impedance, instability	beam current severely limited by transient beam loading Showstopper	beam loading better than PDR, very serious for HL-W & Z Problematic	no beam loading problem	Best
SRF Technology	HOM power Problematic	pulsed HOM power; LLRF control; beat cavity?	pulsed HOM power; LLRF control; beat cavity?	higher input and HOM power for shared cavities Not good	Best
SRF Cost	H cost higher than DRcc	similar to DRcc; beat cavity will add cost	similar to DRcc; beat cavity will add cost	BEST especially for H and possible ttbar upgrade	twice SRF and cryogenic cost of DRcc Problematic

3.1.2.1 Layout and Parameters

The baseline SRF system layout and parameters (Table 3.1.3) are chosen to meet the minimum luminosity requirement for each operating energy, and with possible higher luminosity. The total cavity number (input power limited), cell number per cavity (gradient and HOM power limited) and klystron number are determined with a margin to run in high luminosity or high voltage mode for Higgs, W and Z. The SRF system is optimized for the Higgs mode of 30 MW SR power per beam, with an allowance for 50 MW per beam. The cavity gradient in the Higgs mode has an allowance for higher voltage and RF trips.

It is assumed to use part of the Higgs cavities for W and Z operation, which has the same RF power source and distribution as the Higgs operation, and detune the unused cavities and keep them at 2 K to extract HOM power. If this configuration is limited by beam instabilities, beam feedback capability, HOM damping or power handling capability, we will push the unused cavities out of the beam-line or use separate cavities especially for high luminosity Z running. For high luminosity Z operation, direct loop and comb filter loop feedback will be used to cure the fundamental mode instability (as done in PEP-II and LHC). The bunch by bunch method may not work.

Due to RF mismatch at different beam energy and current, the input coupler should have variable coupling to avoid extra power.

Table 3.1.3: Collider superconducting RF system parameters (100 km DR)

Machine parameters: Wangdou20170224	H Baseline	W Baseline	Z Baseline	H High-L	W High-L	Z High-L
Luminosity / IP [10^{34} cm^{-2} s^{-1}]	2	1	1	3.1	5.1	12
SR power / beam [MW]	32	6.3	1.3	50	32	16.1
RF frequency [MHz]	650	650	650	650	650	650
RF voltage [GV]	2.1	0.41	0.14	2.1	0.41	0.14
Beam current / beam [mA]	19.2	19.0	38.8	30	97.1	466
Bunch charge [nC]	15.5	5.8	7.3	15.5	5.8	7.3
Bunch length [mm]	2.9	3.4	4	2.9	3.4	4
Cell number / cavity	2	2	2	2	2	2
Cavity number in use / beam	336	72	24	336	120	48
Gradient [MV/m]	14	12	13	14	7.4	6.3
Input power / cavity [kW]	190	87	56	298	267	335
Cavity number / klystron	2	2	2	2	2	2
Klystron power [kW]	800	800	800	800	800	800
Klystron number in use	168	72	24	168	120	48
HOM power / cavity [kW]	0.4	0.1	0.2	0.6	0.3	1.8
Cavity number / cryomodule	6	6	6	6	6	6
Cryomodule number in use	56	24	8	56	40	16
Q_0 @ 2 K at operating gradient	1E10	1E10	1E10	1E10	1E10	1E10
Total wall loss @ 4.5 K eq. [kW]	23	8	3	23	5	1
Optimal QL	1.0E6	1.8E6	3.0E6	6.4E5	2.1E5	1.2E5
Relative opt. QL (to H-baseline)	1.0	1.8	3.0	0.6	0.2	0.12
Extra power (to H-baseline)	/	9 %	33 %	5.1 %	72 %	155 %
Extra power (to H-HL)	5.1 %	30 %	71 %	/	33 %	84 %
Cavity bandwidth [kHz]	0.7	0.4	0.22	1.0	3.1	5.3
Optimal detuning [kHz]	0.25	0.13	0.44	0.39	1.13	10.54
Cavity time constant [μs]	488	885	1447	312	104	60
Cavity stored energy [J]	46	39	40	46	14	10
Max relative voltage drop for 4+4 APDR [MV]	10 %	11 %	22 %	16 %	96 %	538 %
Max bunch train phase shift for 4+4 APDR [deg]	9.8	10.9	13.2	15.3	92.3	/

3.1.2.2 Transient Beam Loading Compensation for Bunch Train Operation

In the CEPC APDR scheme, the transient beam loading effects due to bunch train structure is the most import issue to be studied. A bunch extracts cavity stored energy when passing through, and the power source will recover the cavity voltage when the next bunch comes. When the bunch spacing is much smaller as is the case with bunch train operation, the cavity stored energy and voltage will drop continuously due to lack of power. The later bunch will move towards the voltage peak by auto-phasing, resulting in a bunch phase shift, less longitudinal focusing, smaller energy acceptance, and possible lifetime reduction (especially when Beamstrahlung dominated) and luminosity degradation or other dynamical problems. The synchrotron tune spread between bunches enhances Landau Damping, which is good for instability suppression. The small phase shift can be estimated, as shown in Table 3.1.3 for the APDR scheme. From symmetry, the phase shift will be the same for an electron and positron colliding bunch pair, thus the interaction point will not move.

There are several methods for transient beam loading compensation. The reduction methods include: 1) increase cavity stored energy. 2) change fill pattern and RF distribution (spread as uniformly as possible). 3) increase synchrotron phase (change beam parameters). The correction methods include: 1) global correction: provide via the RF generator an additional current to fully cancel out beam current variations in each cavity. But this method needs a special RF source with high peak power and high repetition rate. Special techniques are needed to reduce the filling power and average power due to low RF-to-beam power efficiency. 2) local correction: travelling wave cavity or beat cavity.

The concept of beat cavity compensation is to tune the frequency of some RF sources and cavities slightly different from the normal RF sources (650 MHz) and cavities (optimal detuning), and then use the linear part of the beat wave to compensate for the voltage and phase variation due to transient beam loading. The non-linearity will increase with bunch train length. Higher order beats are more effective but are more non-linear.

3.1.2.3 Cavity

The choice of RF frequency is determined by several factors. Lower frequency is preferred for energy acceptance, beam stability and low parasitic loss. Higher frequency is better for bunch length, and especially the size, cost and quality control of the cavity. Since the Booster has 2.6 % of the beam current of the collider and 20 % duty cycle, we chose the frequency of 1.3 GHz, a frequency which has been developed worldwide since the early 1990s. The CEPC collider will use 650 MHz, the second sub-harmonic of the Booster frequency. These frequencies minimize the construction and operating cost, fulfill the beam dynamics and luminosity requirements and allow CEPC to use mature technology developed by TESLA and adopted for XFEL and LCLS-II. These frequencies have the most synergy with other ongoing SRF projects in China and abroad.

Given the total synchrotron radiation power, parasitic loss and RF voltage, the collider cavity numbers and voltages are mainly determined by the input coupler power handling capability. The collider input coupler operating power has been chosen to be less than 300 kW, nearly double the BEPCII power level. This is a balance between SRF system capital cost, coupler operational risk, and cavity gradient and impedance, etc.

The cavity gradient is determined by the cell numbers when the cavity RF voltage and frequency are fixed. More cells is better for low gradient, but will increase the cavity

HOM power and impedance and lower the coupling of the HOMs. We have chosen 2-cell and 20 MV/m for the 650 MHz cavity. Each cryomodule consists of 6 cavities, as shown in Figure 3.1.1. Because of the low current and duty cycle of the Booster, for the 1.3 GHz cavity we chose 9-cell at 20 MV/m.

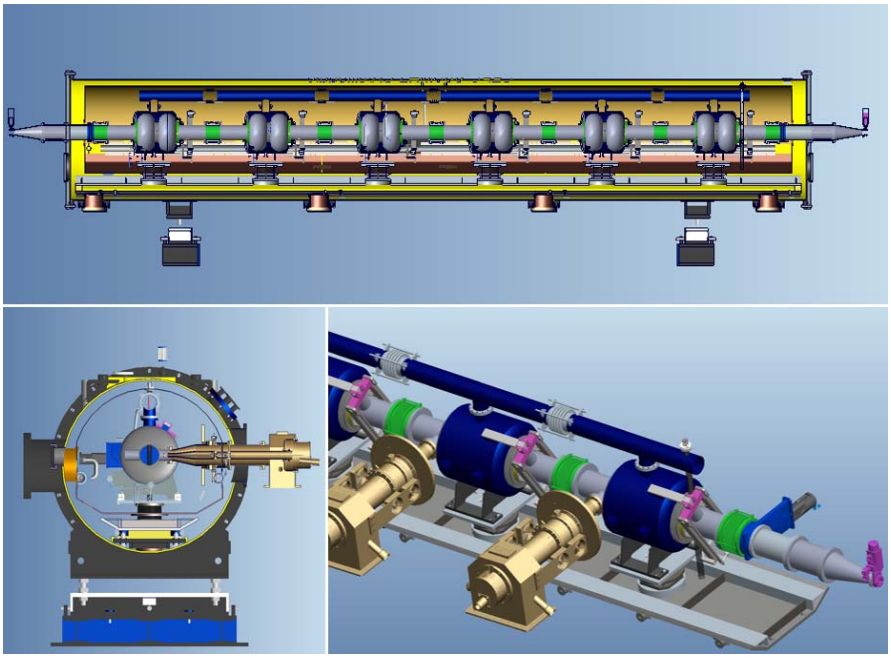

Figure 3.1.1: Layout of the CEPC 650 MHz cavity

The 650 MHz 2-cell cavity (Figure 3.1.2) baseline is bulk niobium operating at 2 K. The main RF parameters of this 650 MHz 2-cell cavity are listed in Table 3.1.4. The 1.3 GHz 9-cell cavity baseline is bulk niobium operating at 2 K with Q0 = 2E10 at 20 MV/m, and Q0 = 3E10 at 25 MV/m for the vertical acceptance test. New nitrogen-doping and flux expulsion technologies for the high Q SRF cavity could be used to reach these targets, which have shown good performance at LCLS-II [3]. Thin film technology (such as Nb3Sn) will be also studied as an alternative.

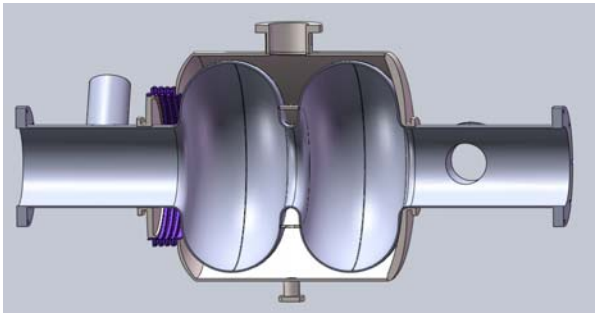

Figure 3.1.2: Schematic of the 650 MHz 2-cell cavity with helium vessel

Table 3.1.4: Parameter of 650 MHz 2-cell Cavity

Parameter	Value
R / Q	212.7 Ω
G	284.1 Ω
E_p / E_{acc}	2.38
B_p / E_{acc}	4.17 mT / (MV/m)
Length	1060 mm
Equator diameter	410 mm

Ultra clean cavity surface processing and string assembly is required to avoid field emission. Electro-polishing and the vertical test are also important to verify the performance of the cavities before their assembly into the cryomodule.

3.1.2.4 HOM Damping

3.1.2.4.1 Impedance Budget and HOM Damping Requirement

In a storage ring, the beam instabilities in both the longitudinal and transverse directions caused by the RF system are mainly from the cavities themselves. To keep the beam stable, the radiation damping time should be less than the rise time of the multi-bunch instability. The beam instability calculation gives the upper limit to the external quality factor of the HOMs with high R/Q. This is shown in Table 3.1.5 for the 650 MHz cavity. During operation at the W and Z-poles, beam will go through half of the 650 MHz cavities. The large HOM frequency spread from cavity to cavity will relax the Q_e requirement. It is possible to reach the Q_e values for Higgs and W operation with the LEP/LHC type HOM coupler for the modes below the cut-off frequency and with the beam pipes for the modes above cut-off. But for the Z-pole mode, the required damping is too strong to be realized with a coaxial HOM coupler. A beam feedback system is needed to alleviate this requirement. Assuming a five-turn feedback time with margin, the growth time limit is about 3 ms, while the longitudinal radiation damping time for Z-pole running is about 400 ms. Thus the Q_e requirement will be 100 times higher with the feedback system. For higher current at the Z-pole, faster feedback (within one turn) is needed. Another concern related to the HOMs is that some modes far above the cut-off frequency may become trapped among cavities in the cryomodule due to the large frequency spread.

Table 3.1.5: Damping requirements of prominent HOMs of the 650 MHz 2-cell cavity with baseline SRF parameters and with all "Higgs cavities" on line for W and Z-pole running.

Monopole mode	f (MHz)	R/Q^* (Ω)	Q_e (H)	σ_{fR}=1MHz	Q_e (W)	σ_{fR}=1MHz	Q_e (Z)	σ_{fR}=1MHz
TM011	1165.536	63.38	1.10×10^5	7.11×10^6	1.57×10^4	2.92×10^5	6.01×10^2	9.29×10^2
TM020	1384.302	1.128	5.21×10^6	9.45×10^8	7.45×10^5	7.49×10^7	2.84×10^4	7.50×10^5
TM021	1705.479	6.9	6.91×10^5	8.02×10^7	9.88×10^4	4.66×10^6	3.77×10^3	1.55×10^4
TM012	1832.731	16.17	2.74×10^5	1.92×10^7	3.92×10^4	9.25×10^5	1.50×10^3	3.70×10^3
Dipole mode	f (MHz)	R/Q^{**} (Ω/m)	Q_e (H)	σ_{fR}=1MHz	Q_e (W)	σ_{fR}=1MHz	Q_e (Z)	σ_{fR}=1MHz
TE111	844.666	276.62	1.25×10^4	2.58×10^5	3.75×10^3	2.86×10^4	2.44×10^2	3.00×10^2
TM110	907.469	414.84	8.34×10^3	1.03×10^5	2.50×10^3	1.32×10^4	1.62×10^2	1.81×10^2
TM&TE (hybrid)	1232.745	243.84	1.42×10^4	2.17×10^5	4.25×10^3	2.34×10^4	2.76×10^2	3.20×10^2
TE121	1468.139	12.61	2.74×10^5	2.08×10^7	8.22×10^4	3.90×10^6	5.35×10^3	2.85×10^4
TM120	1662.309	15.21	2.27×10^5	1.70×10^7	6.81×10^4	2.93×10^6	4.43×10^3	2.08×10^4

* Longitudinal R/Q with the accelerator definition and $k_{/\!/\,\mathrm{mode}} = 2\pi f \cdot (R/Q) / 4$ [V/pC]

** Transverse R/Q: $k_{\perp\,\mathrm{mode}} = 2\pi f \cdot (R/Q) / 4$ [V/(pC·m)]

3.1.2.4.2 HOM Power and Damping Scheme

Higher-order-modes excited by the intense beam bunches must be damped to avoid additional cryogenic loss and multi-bunch instabilities. This is accomplished by extracting the stored energy via HOM couplers mounted on both sides of the cavity beam pipe and the HOM absorbers inside the cryomodule (for the Booster) or outside the cryomodule (for the collider).

The average power losses can be calculated as single pass excitation. As shown in Fig. 3.1.3, HOM power damping of 0.8 kW for each 650 MHz 2-cell cavity is required for the CEPC collider. Resonant excitation should be considered especially for the low frequency modes below cut-off. The cut-off frequency of the waveguide modes for the beam pipe are 1.471 GHz (TM01) and 1.126 GHz (TE11). All the HOM power below the cut-off frequency should be coupled by the HOM coupler which mounted on the beam pipe and the propagating modes will be absorbed by the two HOM absorbers at room temperature outside the cryomodule.

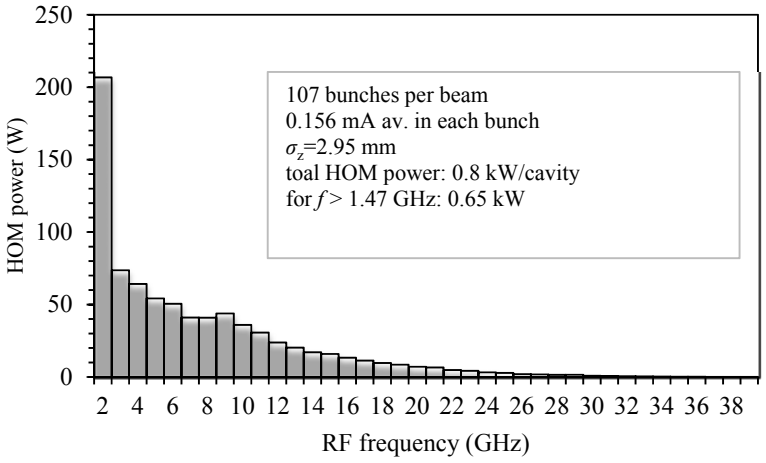

Figure 3.1.3: Frequency distribution of HOM power (Higgs operation at high luminosity).

About 80 % of the HOM power is above the cut-off frequency of the cavity beam pipe and will propagate through the cavities and finally be absorbed by two HOM absorbers at room temperature outside the cryomodule. Each absorber has to damp several kWs of HOM power, thus the absorber can't be placed in the cryogenic region.

3.1.2.4.3 HOM Coupler

The HOMs of the cavities must be damped sufficiently to prevent coupled bunch instabilities and to limit parasitic mode losses. To damp different polarization HOMs, at least two HOM couplers per cavity are needed. The couplers need to damp the HOMs at frequencies from 780 MHz to1471 MHz as shown in Figure 3.1.4.

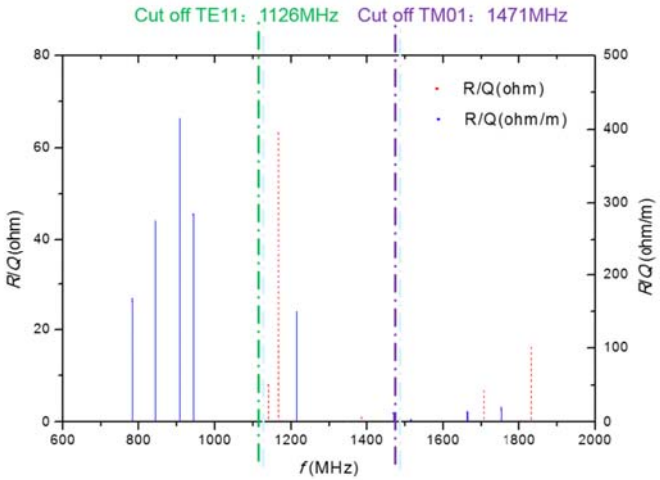

Figure 3.1.4: 650 MHz 2-cell cavity mode spectrum and the beam pipe cut-off frequency.

The primary focus in finding an appropriate design lies in the RF transmission behavior, which must be optimized for the operating frequency (high damping) and the

HOM spectrum (low damping) of the cavities. The multipacting sensitivity as well as the resulting heat loss also play a crucial role because they can seriously affect accelerator operation. The complexity of the mechanical design and the tolerances are limited to keep the costs reasonable.

A probe type HOM coupler is given by transmission line models (see Figure 3.1.5). Three low-Q coupler resonances have a large frequency range from 780 MHz to 1471 MHz. M23 is the inductance of the wedge-shaped mechanical support of the inner conductor of the coupler. It also provides a convenient path for helium into the coupler to cool the inner part of the coupler. The 3D model is then optimized by simulations with CST MWS, as shown in Figure 3.1.6. For analyzing the pure transmission characteristic, only the HOM tube with the coupler was considered for the simulation. The bottom side of the tube terminated with a waveguide port, excites monopole as well as dipole modes, whereas the coaxial output port excites the TEM mode. The results for the preliminary optimization of the coupler are shown in Figure 3.1.7.

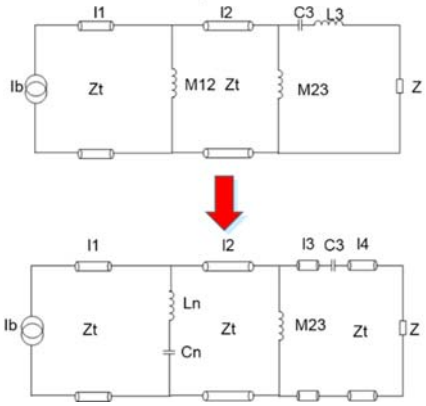

Figure 3.1.5: Equivalent circuits of the probe coupler.

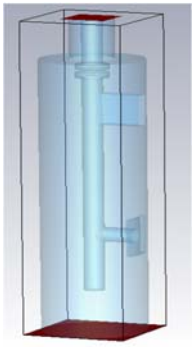

Figure 3.1.6: Geometry of the probe coupler.

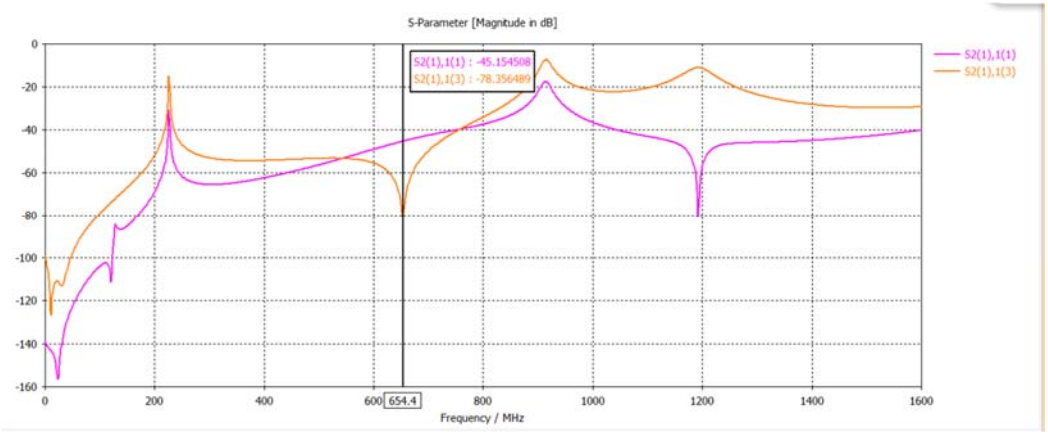

Figure 3.1.7: S21 of the couplers (S2(1),1(1) represents TE11-TEM transmission, S2(1),1(3) represents TM01-TEM transmission).

The Q values are calculated with a 2-cell cavity equipped with two probe HOM couplers. The angle between two couplers is 120 degree, as shown in Figure 3.1.8. The damping results compared with the impedance thresholds are shown in Figures 3.1.9 and 3.1.10. As can be seen, the damping for all the monopole modes of the design are below the longitudinal impedance threshold. The Q_e for the TE111 mode can not meet the requirement both for Higgs and Z operation. This mainly is caused by the small frequency difference between this mode and the fundamental mode. For Z, the damping results for both monopole modes and dipole modes need to be improved. It is noteworthy that we didn't take into account the spread in the resonance frequencies of different cavities. If the frequency spread is 0.5 MHz, the impedance threshold can increase by 1~2 orders of magnitude. More work is needed to optimize the broadband damping results as well as rejection of the fundamental mode.

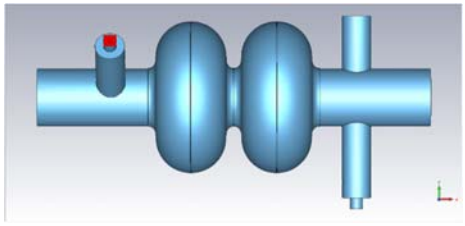

Figure 3.1.8: 2-cell cavity with two probe HOM couplers.

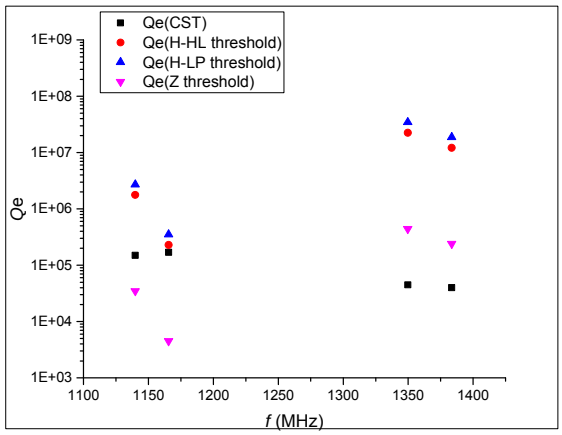

Figure 3.1.9: Monopole modes damping results compared to the impedance threshold.

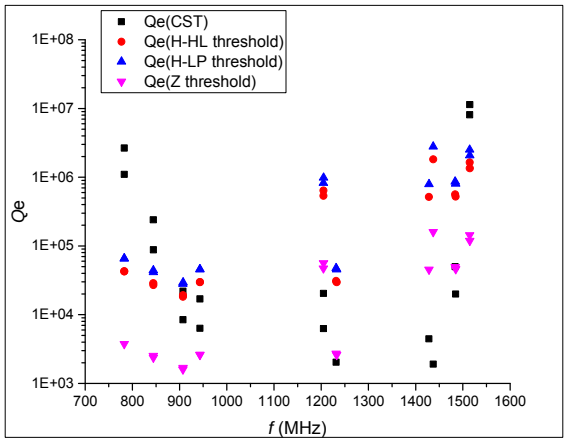

Figure 3.1.10: Dipole modes damping results compared to the impedance threshold.

To improve the damping for TE111 modes, another design scheme was proposed. A loop type HOM coupler is given by transmission line models (see Figure 3.1.11). Two coupled series resonant circuits are used. M is the inductance of the wedge-shaped mechanical support of the inner conductor of the coupler. It also provides a convenient path for helium into the coupler to cool the inner part of the coupler. The 3D model is then optimized by simulations with CST MWS, as shown in Figure 3.1.12 The beam tube with HOM coupler model was used for analyzing the transmission characteristics. Both sides of the tube terminated with a waveguide port, excites monopole as well as dipole modes, whereas the coaxial output port excites the TEM mode. The results for the preliminary optimization of the coupler are shown in Figure 3.1.13.

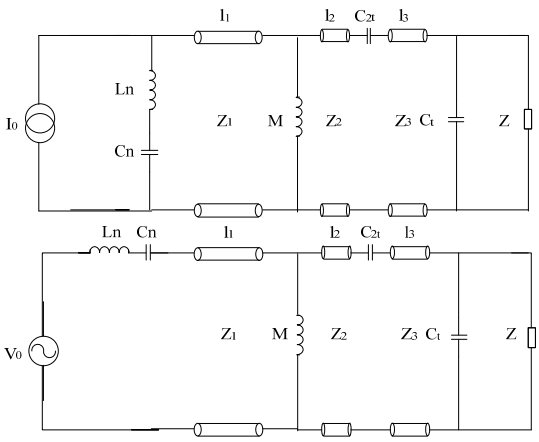

Figure 3.1.11: Transmission line circuits of the loop coupler (up: electric coupling, down: magnetic coupling).

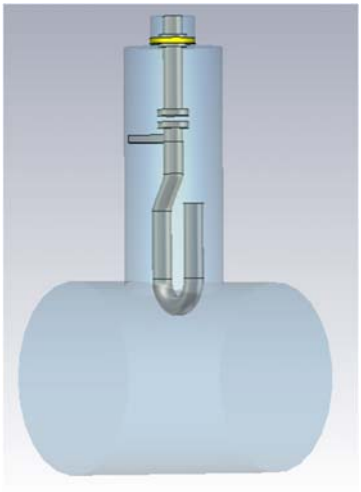

Figure 3.1.12: Geometry of the loop coupler.

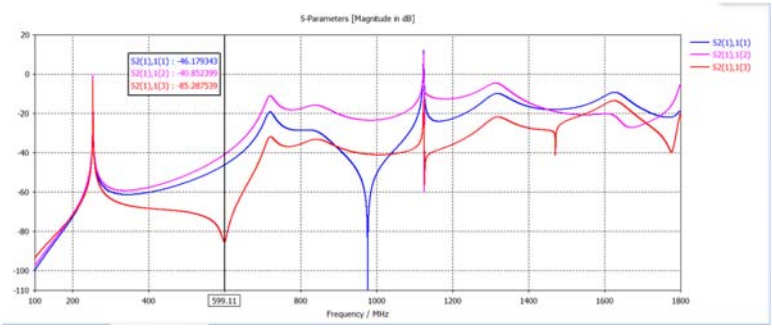

Figure 3.1.13: S21 of the couplers (S2(1),1(1) & S2(1),1(2) represents TE11-TEM transmission, S2(1),1(3) represents TM01-TEM transmission).

The damped Q values are calculated for a 2-cell cavity equipped with loop HOM

couplers. The angle between two couplers is 120 degree, as shown in Figure 3.1.14. The damping results compared with the impedance thresholds are shown in Figures 3.1.15 and 3.1.16. As can be seen from the results, the damping for almost all the monopole modes and dipole modes of the design are below the longitudinal impedance threshold. The Q_e for the TM011 mode and almost all the dipole modes cannot meet the requirement for operating at the Z-pole. For the Z-pole, different damping methods should be used. It should be noted that we didn't take into account the spread in the resonance frequencies of different cavities. If the frequency spread is 0.5 MHz, the impedance threshold can increase 1~2 orders of magnitude.

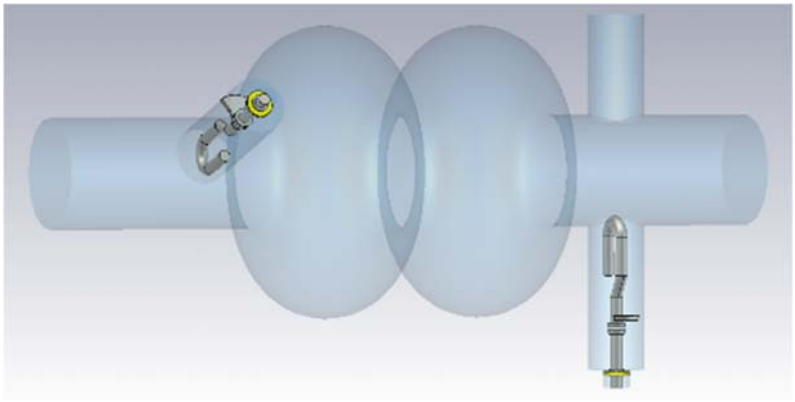

Figure 3.1.14: 2-cell cavity with two-loop HOM couplers.

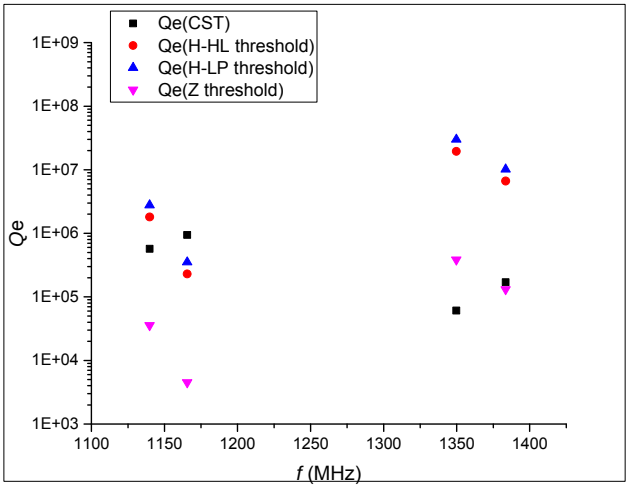

Figure 3.1.15: Monopole modes damping results compared with the impedance threshold.

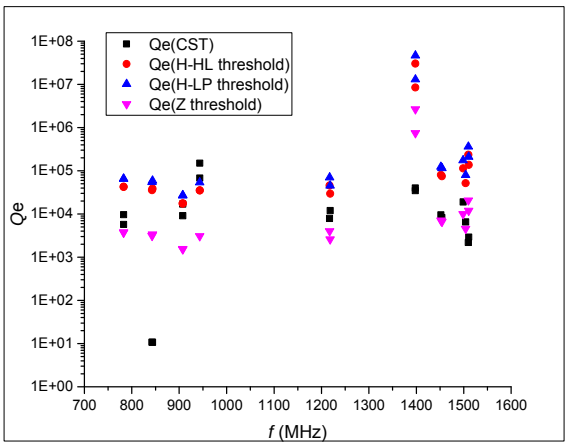

Figure 3.1.16: Dipole modes damping results compared with the impedance threshold.

3.1.2.4.4 HOM Absorber

The HOM absorber is mainly used to damp the HOM power above 1.4 GHz. The structure of the HOM absorber is similar to a circular waveguide. Then the microwave absorbing material will be brazed onto the inner surface of the waveguide. Due to the high Q_e threshold of HOM above 1.4 GHz, which is 10^6 or larger, one or two types of absorbing material will be adequate for the wide frequency range.

The size of the waveguide of the absorber is the same as the beam pipe of the 650 MHz cavity. According to experience at BEPC-II, in the initial design the ferrite is used to absorb the HOM power. The RF model of the HOM absorber is shown in the Figure 3.1.17. The ferrite shape is cut into a rectangular brick. This will reduce the fabrication cost dramatically and will also lessen the difficulty in ferrite machining and brazing. For further higher damping requirement, this structure makes it feasible to mount different kinds of absorbing material to fulfill broad band operation.

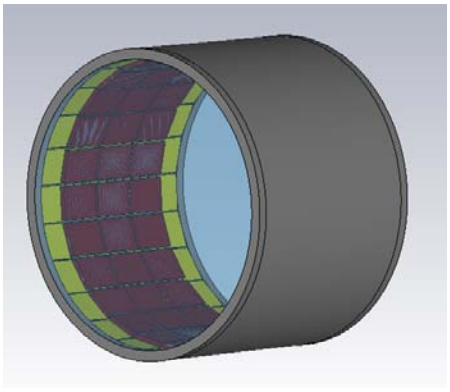

Figure 3.1.17: RF model of HOM absorber.

The absorber will damp about 3 kW HOM power, so the absorber cannot be placed in the cryomodule. The absorber temperature will rise, so the ferrite must be water cooled. Effective cooling for each ferrite brick is accomplished with the cooling structure shown in Figure 3.1.18. At this stage in the mechanical design, there is a balance between

structure complexity and cooling efficiency. Further simulation and optimization of the mechanical design will be performance in the future.

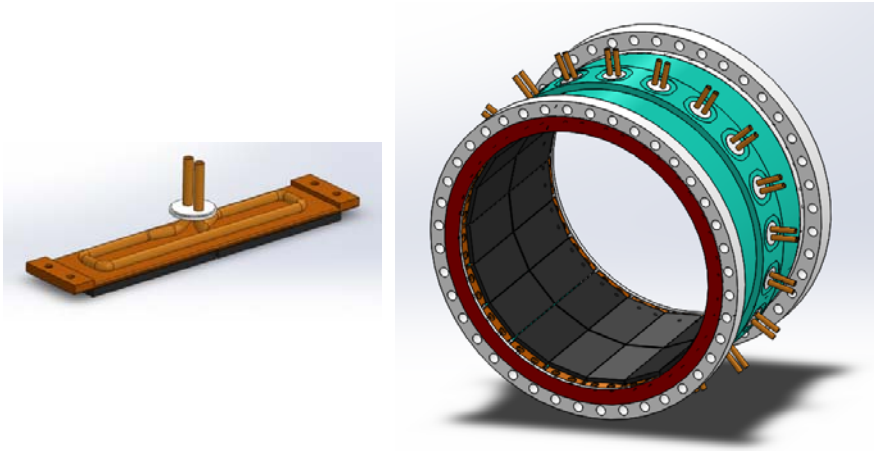

Figure 5.1.18: Cooling structure of ferrite (left) and initial mechanical design of absorber (right).

3.1.2.5 Power Coupler

For CEPC, one of the key technology challenges is the very high power handling capability of the input power coupler for the main ring SRF cavity. Both the Q_0 and the accelerating gradient for SRF cavities are high, which requires that the coupler be assembled with the cavity in a Class 10 cleanroom. In addition, considering the large number of couplers, heat load (both dynamic and static) is another important issue to be solved. The main challenges of the input power couplers are as follows: very high power handling capability (CW 300 kW), two windows for vacuum safety and cavity clean assembly, very small heat load, simple structure for cost saving, and high yield and high reliability.

Considering the excellent performance, close frequency and experiences obtained at IHEP, the BEPC-II 500 MHz SCC coupler design is taken as the baseline. Several modifications are considered for the CEPC collider SRF cavity: reduce the distance between the window and the coupling port, putting the window into the cryostat profile and thus have the window and cavity assembled in a Class 10 cleanroom, add one waveguide or cylindrical type warm window for vacuum safety, and redesign the mechanical structure for higher power capacity and lower heat load.

For the Booster 1.3 GHz cavity, since the average input power is less than 4.4 kW, the KEK STF1-type coupler developed by IHEP (high power conditioning test to 800 kW with 0.75% duty factor, i.e. average power 6 kW) can be used. If higher input power and/or variable coupling is needed, a KEK cERL main linac coupler [11] can be the reference for our design. Table 3.1.6 lists the main parameters of the input power couplers for the main ring and the Booster SRF cavities.

Table 3.1-6: Parameters of the input power couplers for CEPC SRF cavities.

Parameters	Collider	Booster
Frequency	650 MHz	1.3 GHz
Maximum power	CW, 300 kW	Average < 4.4 kW (20 kW peak)
Q_{ext}	2E6	1E7
Coupling type	Antenna	Antenna
Coupler type	Coaxial	Coaxial
Number of windows	2	2
Window type	One waveguide or cylindrical warm window; One coaxial Tristan type warm window	Two same size coaxial Tristan type windows: one warm, one cold

For CEPC, one of the key components is the input coupler. A large number of couplers is needed in both the collider and Booster. Considering the very high input power and low heat load, the coupler design is a challenge. To keep the high Q0 and high accelerating gradient of the SC cavity, the coupler assembly must be in Class 10 cleanroom. This means that the coupler assembly will be done before the cryomodule assembly.

For the Booster 1.3GHz cavity, the coupler is operated in pulsed mode. The peak power is 20kW, and the average input power is less than 5kW. The KEK STF-I type or DESY TTF-III type coupler can be used. A high power test of the STF-I type coupler developed by IHEP was completed. The coupler can support the 6 kW average power (800 kW, 0.75% duty cycle). TTF-III couplers have been operated at 4.5 kW average power (peak power 1100 kW) for 15 years. If higher input power is needed, the KEK cERL main linac coupler (based on the KEK STF-I) or Cornell ERL injector coupler can be our reference. Two Cornell ERL injector couplers (made by CPI) was tested at PKU.

For the collider 650 MHz cavity, the coupler was operated in CW mode. The input power for each coupler is 215~254 kW beam power, (Higgs high luminosity mode:215 kW, Z mode 254 kW). Because of the difficulty of cooling, the cold window was never used above 100 kW. Considering the technology and cost, the choice is for a single window coupler. Based on the experience at BEPC-II 500 MHz SCC coupler, a single coaxial Tristan type warm window will be used for CEPC. 650 MHz ADS coupler was made at IHEP. But in this design, different Qe in different operating modes was noticed. That means if three Qe numbers can't be close, then probably in the CEPC we will need at least 160 variable couplers for W and Z mode operation. We have only LHC and APT couplers for reference.

3.1.2.5.1 RF Design

The 650 MHz ADS coupler window is used for CEPC. The S11 of window is -22dB. Figure 3.1.19 shows the RF model and the S11 curve of window. The RF transfer performance of the whole coupler will be adjusted with new waveguide-coax transfer. The RF design will be changed and re-calculated after the mechanical design is completed.

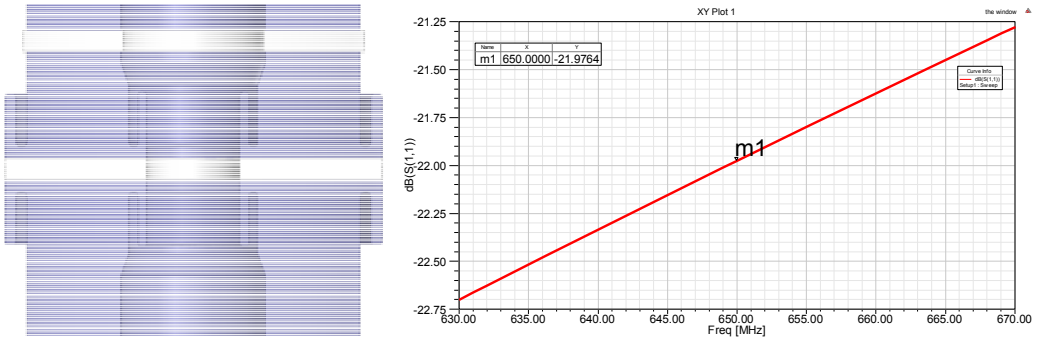

Figure 3.1.19: The 650MHz window RF model and the S11(-22dB @650 MHz)

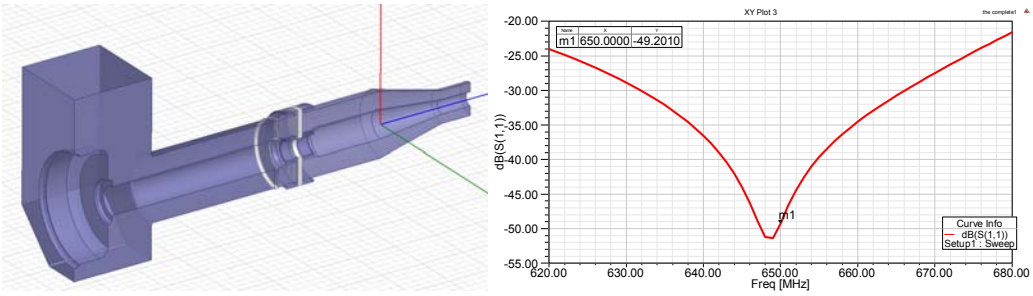

Figure 3.1.20: The 650MHz coupler RF model and the S11(-49dB @650MHz)

3.1.2.5.2 Mechanical and Thermal Design

A coax plate window is used. It has a water cooled inner conductor and a He gas cooled outer conductor.

For mechanical design of the coupler we have a rough model. This was done by adjusting the connector of ADS 650 MHz coupler to suit the CEPC cavity.

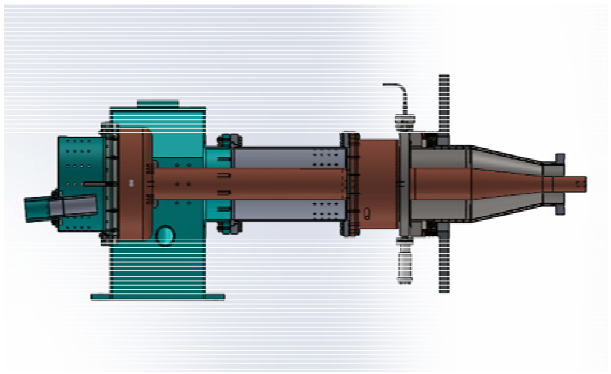

Figure 3.1.21: The coupler rough model

For the variable coupler, we have two rough designs: one is to add the bellows to the inner conductor, another is to add the bellows to the outer conductor. Figure 3.1.22 shows the bellows position.

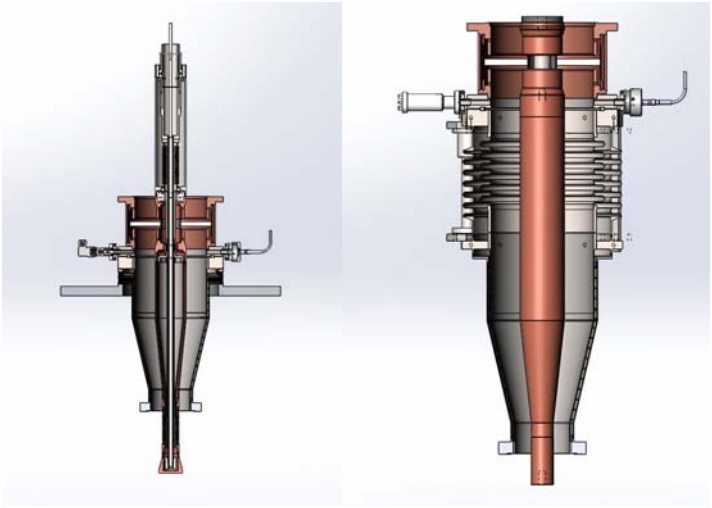

Figure 3.1.22: The variable coupler rough model

3.1.2.5.3 Fabrication

The window was fabricated by brazing; the inner conductor was connected by EBW. The copper plating was made by electroplating. Its thickness will depend on RF calculation.

3.1.2.5.4 Conditioning

A vacuum wave guide will connect two couplers as at the KEK-B or TTF-III test station. The assembly will be done in class 10 cleanroom. A new auto conditioning system will be prepared for a high power test.

3.1.2.6 Tuner

3.1.2.6.1 Specification

Tuners for superconducting cavities are an important part of the superconducting system. Tuners compensate or damp the cavity frequency change due to Lorenz forces, beam loading effects, and microphonics. The development of the frequency tuning system is very difficult because of material shrinkage, large tuning range, high resolution and the difficult working conditions at low temperature, and the ultra high vacuum and radiation.

Table 3.1.7: Main parameters of tuner

Parameters	Unit	Booster tuners	Main ring tuners
Operation frequency	MHz	1300	650
Cooling-down uncertainties	kHz	50	50
Beam loading	kHz	＜0.7	~ 0.32/0.78
LFD	kHz	~ 0.4	~ 0.3
Detuning protection	kHz	200	200
Tuner parameters			
Coarse (slow) tuner frequency range	kHz	400	400
Coarse tuner frequency resolution	Hz	＜ 20	＜ 20
Fine (fast) tuner frequency range	kHz	＞ 2	＞ 1.5
Fine tuner frequency resolution	Hz	2	2
Motor and Piezo working temperature	K	5~10	5~10
Motor number	——	1	1
Piezo number	——	2	2

The total number of tuners for CEPC is 736 (480 for the collider cavities, 256 for the Booster cavities). Highly reliable and maintainable tuners are required. The parameters of the tuning system are listed in Table 3.1.7 and are based on beam and operation requirements.

3.1.2.6.2 Mechanical Design and Analysis

An improved version of the ADS type lever tuner is chosen as the baseline design for the collider 650 MHz 2-cell cavity, and the Saclay type tuner for the Booster 1.3 GHz 9-cell cavity.

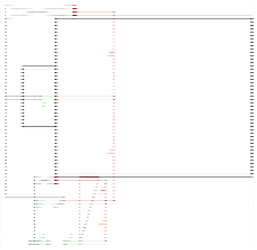

Figure 3.1.23: Working principle of 650MHz cavity tuner

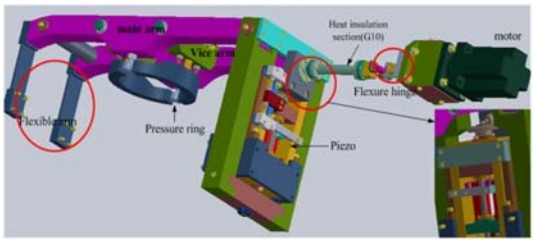

Figure 3.1.24: ADS type tuner

Figure 3.1.23 is a schematic of the double lever mechanism that allows coarse and fine tuning of the cavity. This is improved from the ADS type tuner as shown in Figure 3.1.24. A main arm hinged at one end and connected to the actuation system at the other end has a probe that tunes the cavity physically by pushing on the beam pipe. The actuation system consists of a stepper motor held by a bracket and connected to a second arm. This arm is hinged at the other end and keeps the piezo electric elements in series with the motor.

3.1.2.7 Cryomodule

3.1.2.7.1 Cryomodule Design

The 650 MHz cavity cryomodule concept is not yet a reliable and mature technology worldwide. High Q_0 requirements drive some of the new design features. Cavities will be capable of operating at 20 MV/m CW with a Q_0 = 2e10 at 2 K. The cryomodule is operating at 2 K in superfluid helium. It houses six 2-cell 650 MHz superconducting cavities, six high power couplers, six mechanical tuner and two HOM absorbers. The cryomodule can be separated into three parts, the outer vacuum vessel, the cold mass and the cavities string assembly which comprises the six 650MHz cavities and their associated auxiliary components. The technology of fast cool-down is introduced. "Fast" means 2–3 K/minute below the niobium 9.2 K critical temperature. The static heat load of the whole cryomodule is 5 watts at 2 K.

The 650 MHz cavity cryomodule can be separated into three parts, the outer vacuum vessel, the cavities string assembly which comprises the six 650MHz cavities and their associated auxiliary components (high-power input coupler, helium tank, mechanical tuner etc.), the so-called cold-mass of the cryostat, which includes the cryogenic pips, support fixtures (for the cavity string), thermal shields, etc.

The design of the accelerator module is described as follows: a carbon steel vacuum vessel with a standard diameter about 1300 mm, strongback at the room temperature acting as a support structure, together with 6 posts on top of the strongback, a 2 K two-phase pipe connected to the cavity Helium vessels, a 5-8 K forward and return line, an 80 K forward and return line, a warm-up/cool-down line with capillaries to the bottom of each cavity vessel, and aluminum thermal shields with stiff upper parts for 4 K and 80 K with 10 layers of super-insulation (MLI) for 4 K and 30 layers for 80 K, attached to the support structure. Six completed cavities are attached to the strongback. The cavities can be aligned individually. In addition, the cavity Helium vessels and 2 K two-phase pipe are wrapped with 10 layers of MLI to reduce the heat transfer. Manually operated valves terminate the beam tube at both ends. Four C-shaped stainless steel elements clamp a Titanium pad welded to the Helium tank. Lateral and vertical position are defined by reference screws. The longitudinal position error should be very small.

Pressure drops must be analysed for each helium flow path to ensure that steady-state operation matches system design and that non-steady conditions (cool-down, emergency venting, warm-up) are properly controlled.

3.1.2.7.2 Cryomodule Heat Load

The static heat load of the whole cryomodule will be 5 watts at 2 K. The static and dynamic heat loads are used to evaluate the thermal performances of the cryomodule. The static heat loads arise from the overall cryomodule design and are present during cold operation of the accelerator there are two main contributors: thermal radiation between

the “hotter” environment to the 2K bath and the direct thermal conduction through the cold mass support system. The latter is the conduction of the outer pipe of RF power couplers that bring signals and RF power from the room temperature environment to 2K. The dynamic heat loads originate during RF and beam operations from specific components: thecavities the RF power couplers and the High Order Mode (HOM) coupler/ absorbers.

The posts are the low thermal conduction structural supports for the CM cold mass. The cold mass and cavity string is suspended via tension-loaded posts to the vacuum vessel. Each post is an assembly of a low thermal conduction composite material pipe (fiberglass pipe, G10) and four stages of shrink-fit aluminum and steel discs and rings. The two stainless steel disc/ring sets are connected respectively to the room temperature and to the 2K cold mass environments at the two pipe extremities. The heat transfer mechanisms considered for the support posts are the conduction through the G-10 tube and the radiation between surfaces at different temperatures.

Each cryomodule contains 6 cavities while each cavity has a single coaxial type input coupler with fixed coupling. The input coupler must deliver RF power in CW mode up to 6 kW. Heat loads of the coupler on the cryogenic environment are calculated by ANSYS. The outer conductor is made of stainless steel with 10 μm thick copper electro-plated on the surface carrying the RF currents, so as to reduce RF loss and improve RF performance. The location of the two copper thermal anchors and the total length of the coaxial line are carefully optimized to reduce the static loss to 2 K and 5 K.

Multi-Layer Insulation(MLI) is the most thermally efficient insulation system used in cryogenic applications to reduce the heat load due to radiation between components at different temperatures. The MLI system is generally composed of a series of radiation shields (such as aluminized Mylar) alternating with low conductivity spacers (such as silk or Dacron netting). Theheat flux through the MLI system depends on acombination of solid conduction between layers of different material, thermal radiation between two radiating layers and conduction in residual gas. Conduction in residual gas can be neglected at low residual gas pressure ($< 10^{-3}$ Pa).

The 2K cryogenic helium is needed to remove the heat deposited on the cavity surface when a specified power RF field is present inside the cavity. We call this heat: cavity dynamic heat loads.

3.1.2.7.3 Fabrication and Integration

The design of the accelerator module is described as follows: a carbon steel vacuum vessel with a standard diameter about 1300 mm, the cavity string assembly of the six 650 MHz cavities and their associated auxiliary components (high-power input coupler, helium tank, mechanical tuner etc.); and the cold-mass of the cryostat, which includes the cryogenic pipes, support fixtures (for the cavity string), thermal shields, etc.

The vacuum vessel provides the insulating vacuum for the cold mass and the superconducting RF cavities. It provides mechanical support to the main cryomodule components during normal operation and transportation. The material used in the fabrication of the vacuum vessel and cold mass components conforms to these specifications. Final precision machining is required after all welding has been completed. All ports/openings that have welded piping/tubing connections to the vacuum vessel shall be leak-checked with a calibrated Helium Mass Spectrometer Leak Detector (HMSLD). All welding processes, inspection and testing must be in accordance with relevant standard pressure vessel codes.

The cryomodule assembly will be done with the tools and technology of a moderate to high vacuum service. The interior of the vacuum vessel shall be bead or sand blasted to remove all rust and foreign material. The Manufacturer shall prepare a project specific Quality Assurance Plan. The manufacturer shall conduct quality control procedures and tests to guarantee that the cryostats is in full conformance with these specifications.

3.1.2.7.4 Fast Cool-Down Technique

The technology of fast cool-down is introduced, where "fast" means 2-3 K/minute below the niobium 9.2 K critical temperature. During fast cool-down, we cool one cryomodule at a time. A close-ended warm-up/cool-down manifold will be created for each cryomodule by providing a cool-down/warm-up valve on each cryomodule. Cooling must be slow from 300 K until most thermal contraction is complete (around 80 K). Cool-down rates (dT/dy and dT/dt) are based on the measurements and analysis at other laboratories. The requirement is to limit stresses on the support posts as well as in the Gas Return Pipe (GRP). The GRP vertical gradient is < 15 K, the longitudinal gradient < 50 K. The GRP cool-down rate is 10 K/hr. "Fast" means 2–3 K/minute ("slow" < 0.5 K/minute). Since thermal shield is ~35 K–55 K, in the analysis we use 40 K delta-T at 3 K/minute. This gives us 13 minutes for transition from thermal shield temperature to below the niobium 9.2 K critical temperature. The required cool-down rate can be provided with our design. "Fast" cool-down comparable to single cavity tests can be provided in a cryomodule.

3.2 RF Power Source

3.2.1 Introduction

Accelerators used for experiments in high-energy physics require high power radio frequency sources to provide the energy needed to accelerate the particles. The RF power needs to be stable and predictable such that any variation in the supplied RF power has a limited and acceptable impact on the beam quality.

The RF power source delivers energy to the electrons to compensate for the energy loss from synchrotron radiation and from interactions with the beam chamber impedance. The RF power source also delivers energy to the beam when ramping to higher energy and captures and focuses the electrons into bunches. The beam and the RF stations are two dynamic systems which strongly interact; and this complicates stability considerations for the combined system.

The CEPC collider beam power is 100 MW. So, if amplifier efficiency is low, the AC input power will exceed the CEPC primary power limit of 300 MW. Therefore, high power klystrons are the more attractive option because of their potential for higher efficiency than the solid state amplifier.

The CEPC SRF system consists of 384 RF stations. Each RF station includes a 5-cell 650MHz accelerating superconducting cavity. In addition to the energy losses due to radiation in dipoles, quadrupoles, damping wigglers and undulators, the RF power transmitter must provide for the HOM losses excited by the beam. A minimum transmitter power of 280 kW is required to meet the sum of the radiated, HOM and reflected power demands [2]. Table 3.2.1 shows the RF power demands for the CEPC collider SRF system. The collider RF power source configuration is shown in Figure 3.2.1.

Table 3.2.1: CEPC collider SRF system parameters

Parameters	Unit	Value
Operation frequency	MHz	650+/-0.5
Cavity Type		5-cell
Cavity number		384
RF input power	kV	280

The CEPC Booster RF system consists of 1300 MHz superconducting RF cavities. There are 32 cryo-modules, each containing eight 9-cell superconducting cavities. These cavities need 256 sets of 1300 MHz power sources and will have reasonable efficiency (~50%) with high reliability and also require no solenoid, high voltage power supply (HVPS), filament power supply or vacuum pump. For the Booster, 256 solid state amplifiers comprise the required 1300 MHz CW power source. CEPC booster SRF system parameters are shown in Table 3.2.2.

Table 3.2.2: CEPC booster SRF system parameters

Parameters	**Unit**	**Value**
Operation frequency	MHz	1300+/-0.5
Cavity Type		9-cell
Cavity number		256
RF input power	kW	20 peak/cavity
RF source number		256 (25 kW SSA)

The injector for CEPC is a 500 m long S-band Linac with maximum electron and positron beam energy of 6 GeV. To keep a reasonable length at high center-of-mass energy, the main Linac of an electron-positron linear collider must be operated at a high accelerating gradient. For copper (non-superconducting) accelerator structures, this implies a high peak power per unit length and a high peak power per RF source with the assumption that a limited number of discrete sources are used. To enhance the peak power produced by an RF source, the SLED RF pulse compression scheme is use on existing linacs. New compression methods that produce a flatter output pulse are being considered for CEPC.

The main high power RF components of the CEPC Linac are composed of 35 units of 80 MW S-band klystrons and 50 MW C-band klystrons and conventional pulse modulators. Figure 3.2.1 is a simplified schematic of the RF power source.

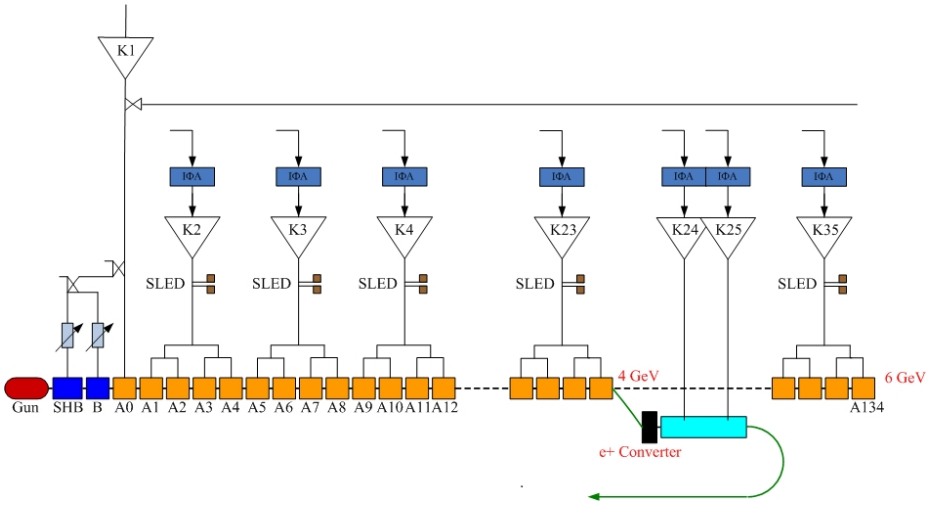

Figure 3.2.1: Simplified schematic of the RF power source

3.2.2 High Efficiency Klystron

3.2.2.1 650MHz Klystron

Considering the klystron operation lifetime and power redundancy, each cavity will be individually powered with a CW klystron amplifier capable of delivering more than 400 kW. With one klystron powering two cavities, the specified saturation power of the klystron should be in the range 700 to 800 kW taking into account linear operation of the klystron and circulator and waveguide losses. The klystron characteristics and performance are summarized in Table3.2.3.

Table 3.2.3: Klystron key design parameters

Parameters	Unit	Value
Center frequency	MHz	650
Bandwidth (-1dB)	MHz	0.5
Output power	kW	800
Beam Voltage	kV	81.5
Beam Current	A	16
Efficiency	%	65(80)

3.2.2.1.1 Gun

An initial design of the CEPC klystron is a single beam klystron for technical reasons. A preliminary design study of electron gun for the CEPC klystron has been carried out at IHEP [3, 4]. The calculated parameters of the CEPC klystron gun are summarized in Table 3.2.4.

Table 3.2.4: Calculated parameters of the CEPC klystron gun

Parameters	Unit	Value
Applied Voltage on Cathode	kV	−81.5
Applied Voltage on MA	kV	−48.0
Beam Waste Diameter	mm	35.6
Beam/Gun Perveance	$\mu A/V^{3/2}$	0.64/1.45
Max. Field on BFE/MA	kV /mm	3.94/2.51
Av. Cathode Density (given)	A/cm2	0.45
Cathode Uniformity	---	1.24

The electron gun was chosen to be a triode type with a modulating anode (MA). Therefore, it is possible to operate it in both pulsed mode and CW mode and vary the beam current or the perveance without varying the beam voltage. Applied voltage, current and beam diameter were determined from the interaction region design. The parameters of the electron gun with a spherical cathode are summarized in Table 3.2.4. The MA gun with the Pierce gun design [5] is achieved by using various simulation codes such as DGUN [6], EGUN [7], and CST [8]. Most of the work was done by DGUN and then the reliability of the results was checked with the other codes. Considering the need for long life time, we chose a cathode diameter of 70 mm in order to have a current density less than 0.6 A/cm^2. With beam voltage of 81.5 kV and the modulating anode voltage of 48 kV, beam current of 15.1A and an average current density of 0.45 A/cm^2 were achieved. A Ba-dispenser cathode having a ϕ 10 mm hole at the center is used to avoid possible damage from ion bombardment which is harmful for CW operation. The M-type dispenser cathode was chosen as it is used in existing high power CW klystrons (1.2 MW manufactured by Toshiba and SLAC BFK) having lifetimes of more than 50,000 hours [9, 10].

Damage from ion bombardment is known, but recently such an emission slump by ion bombardment was also clearly simulated [11]. Since we employ a demountable structure and proceed by possibly reusing gun and collector, residual gases tend to increase. This may be more harmful to cathode operation in CW mode than in pulsed mode. This makes the choice of cathode with a hole is adequate. The focusing magnetic field and electric field are simulated by the POISSON code [12].

Fig.3.2.2 illustrates the simulation results of the MA gun using DGUN code along with the maximum field on the electrode and the current density on the cathode. The ratio of beam radius to drift tube radius is 0.64 and is the same as required from the RF simulation. From this design, a cathode uniformity of 1.24 is obtained. Since the gun is subjected to high electric fields where the breakdown and arcing phenomena tends to occur, the electric field on the electrode and HV ceramic seal are set to be less than the allowed values given in Ref. [13]. A simulation and a design of the HV gun envelop of CEPC klystron has been checked by POISSON code. The obtained maximum electric field on the beam focusing electrode, modulating anode electrode and anode electrode are 3.90kV/mm, 2.51 kV/mm and 1.77 kV/mm respectively which are all less than the maximum acceptable experimental values of electric fields for starting breakdown in CW.

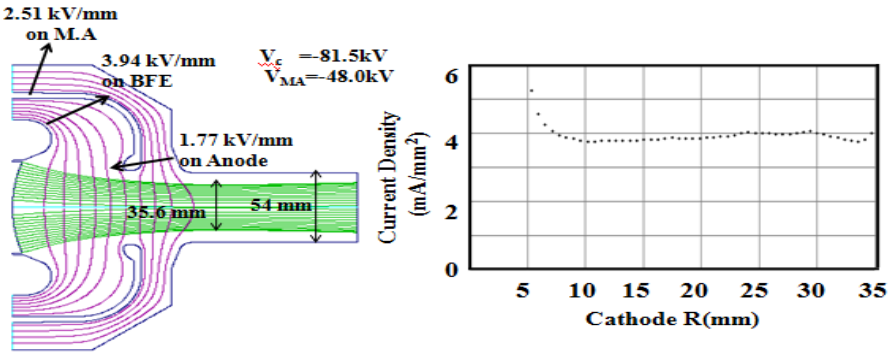

Figure 3.2.2: DGUN simulation results.

An axial magnetic field was used to keep the electron beam focused during its propagation through the drift tube region. The solenoid magnet was designed by the POISSON code and the output results of this code were used as the input data to D-GUN and E-GUN codes. We assume the semi-confined flow of magnetic field to be 26 Gauss on the cathode and 180 Gauss for the drift tube region (with Brillouin field of 111 Gauss).

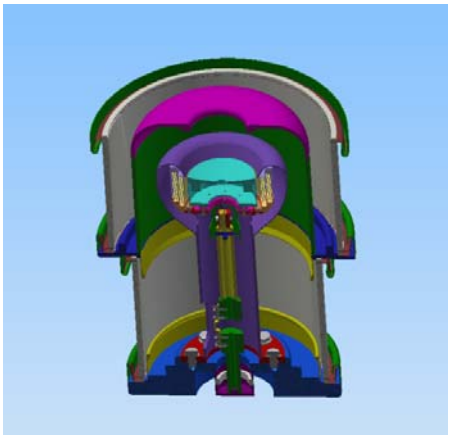

Figure 3.2.3: 3D socket design of CEPC gun

The HV ceramic seal was designed using the POISSON code. Average (max) fields on the ceramic were 0.32(0.52) kV/mm (C-MA) and 0.25(0.47) kV/mm (MA-A) along the length (about 150 mm) of ceramic. Layout of electron gun ceramics relates to an outside layout of a socket tank and a magnet design (usually with existence of an extra coil in the gun region) for which a consistent design is required. But, we carefully chose the design with no extra coil near the gun region in the oil tank. A cross sectional view of the 3D socket design is shown in Figure 3.2.3.

3.2.2.1.2 RF Interaction and Cavities

The RF section plays an important role in klystron performance: gain, bandwidth and overall efficiency. For the CEPC collider that requires more than 100 MW RF power, the efficiency is the most important figure of merit for klystrons to reduce the operations cost. The klystron efficiency depends largely on the quality of electron bunching. High fundamental beam current and low velocity spread are prerequisites for obtaining high efficiency. During decades of development, the theory and technology of high efficiency

klystrons have made great progress. Some techniques are mature such as perveance reduction, high order harmonic cavity application and multi-beam klystrons, and some methods are speculative at this time such as adiabatically bunching, COM, BAC and depressed collector [14, 15, 16, 17, 18, 19, 20].

The CEPC klystron consists of five fundamental frequency cavities and a second harmonic cavity. To obtain maximum efficiency, all fundamental cavities have been tuned to frequencies which are higher than the nominal operating frequency. The third cavity is a second harmonic cavity, tuned to slightly less than the second harmonic frequency. This can reduce the bunch-core charge density to bunch more electrons so as to produce the high fundamental RF current. The fourth and fifth cavities have great influence on klystron efficiency, which are tuned to be outside the band pass at the high frequency side.

With the aid of AJDISK [21], the lengths of the drift sections between the six cavities and the cavity characteristic parameters such as frequency, R/Q and coupling coefficients are optimized to obtain maximum efficiency.

To gain experience, the tried and true method will be used to get a moderate efficiency of 65% at first. Then the newer, less well established method will be applied to get efficiency higher than 80% [22]. These two different designs are optimized using AJDISK as shown in Figure 3.2.4 and the parameters are summarized in Table 3.2.4.

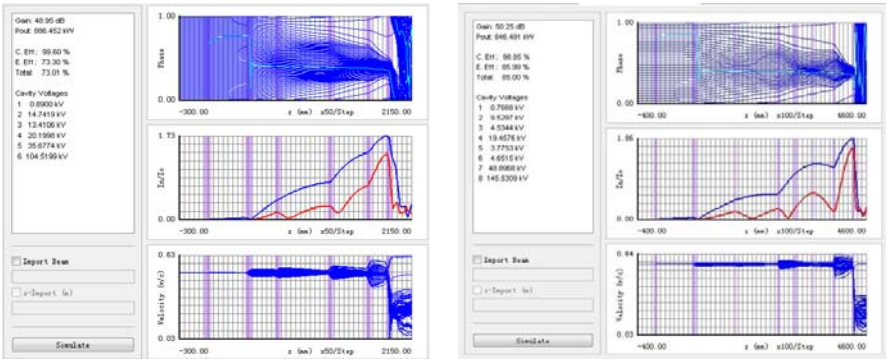

(a) (b)

Figure 3.2.4: Results of AJDISK (a) Traditional klystron (b) Klystron with BAC

The bandwidth response and the transfer curve are shown in Figures 3.2.5 and 3.2.6 respectively.

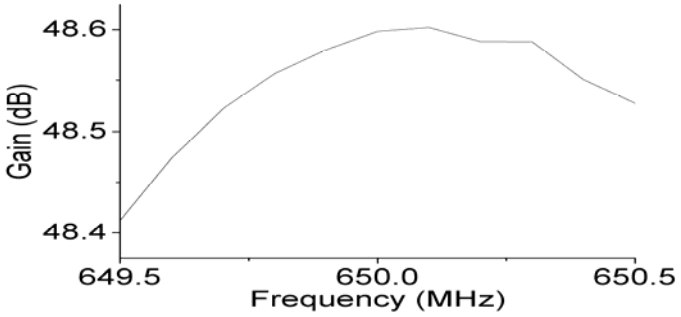

Figure 3.2.5: Bandwidth response

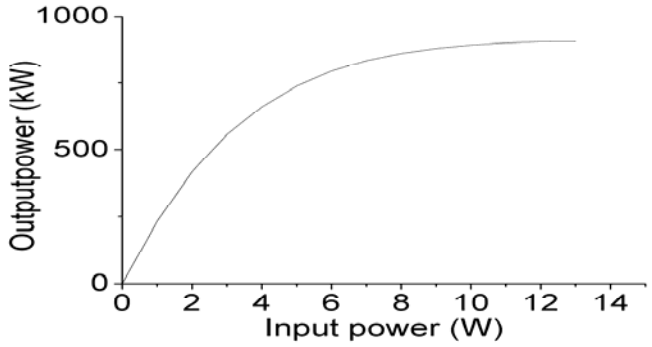

Figure 3.2.6: Transfer curve

Cylindrical re-entrant cavities with a knife edge nose cone are used in the RF section of the CEPC klystron. They are designed to operate in the TM010 mode. Oxygen free high conductivity (OFHC) copper will be used for fabrication of the cavities. Electric breakdown, high order modes oscillation and multipacting effects are taken into account during cavity design.

With the aid of electromagnetic simulation tools such as SUPERFISH [23], CST Microwave Studio and High Frequency Structure Simulator (HFSS) [24], all cavities have been optimized to meet the RF section requirement. The electromagnetic field distribution of the TM010 mode from CST is shown in Figure 3.2.7. The relationship between the radius and the height to keep the frequency of TM010 constant is shown in Figure 3.2.8.

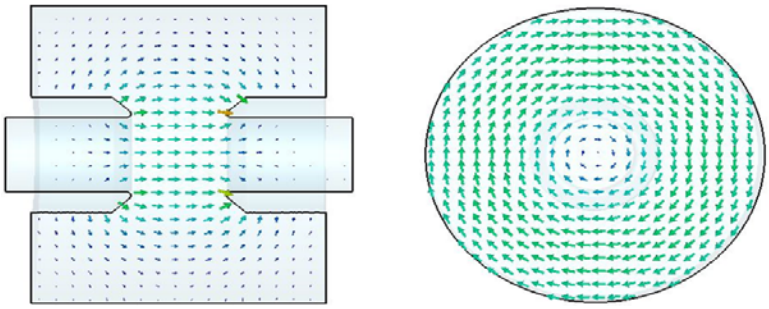

Figure 3.2.7: Electromagnetic field pattern of TM010

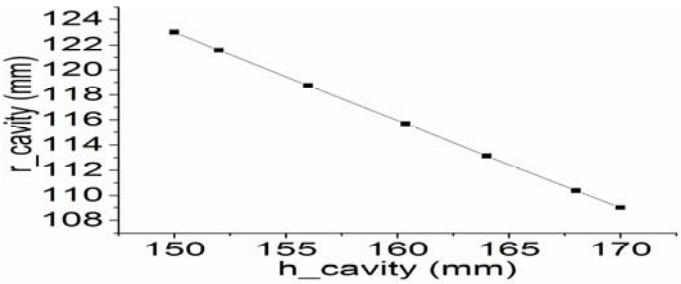

Figure 3.2.8: The relation between the radius and the height to keep the frequency of TM010constant

The preliminary design of the RF section for 800 kW CW klystrons operating at 650 MHz has been completed using AJDISK code. The validation and optimization of design parameters of the complete RF section using 2D and 3D codes are in process. The results of different CAD tools for cavity design give good agreement.

3.2.2.1.3 Output Window

The coaxial output window is designed as one of the key issues for developing the high-power klystrons. In the windows design, an average power capability and multipacting analysis for fundamental and harmonic frequencies are challenging issues. The electromagnetic simulation of an output window was carried out using the CST Microwave Studio Code. We have optimized the return loss, a loss that is not only at the desired frequency but also in the entire range of desired bandwidths. Figure 3.2.9 shows the parameter optimization of the reflection coefficient in the desired frequency range.

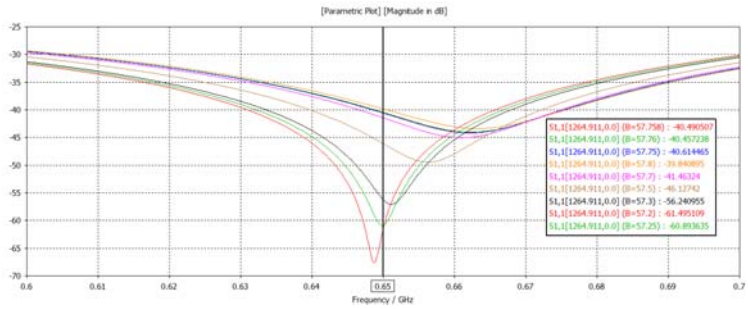

Figure 3.2.9: Parameter optimization of the reflection coefficient

The magnitude of the S-parameter for operation at 800 kW power and 650 MHz can reach -60 dB; however, all magnitudes of the S-parameter lie below -30dB in the frequency range 600MHz – 700 MHz.

Multipacting is a phenomenon of resonant electron multiplication in which a large number of electrons build up an electron avalanche. This avalanche absorbs RF energy and leads to large power loss and wall heating. Multipacting is one of the serious problems for high power RF components and may cause ceramic window breakdown in high power klystrons' operation. So, to understand and prevent the loss of a ceramic window, multipacting simulation and experimentation is necessary. Codes such as CST Particle Studio and Multipac [25] were used to perform multipacting simulation. The results from the two codes are compared in Figures 3.2.10 and 3.2.11.

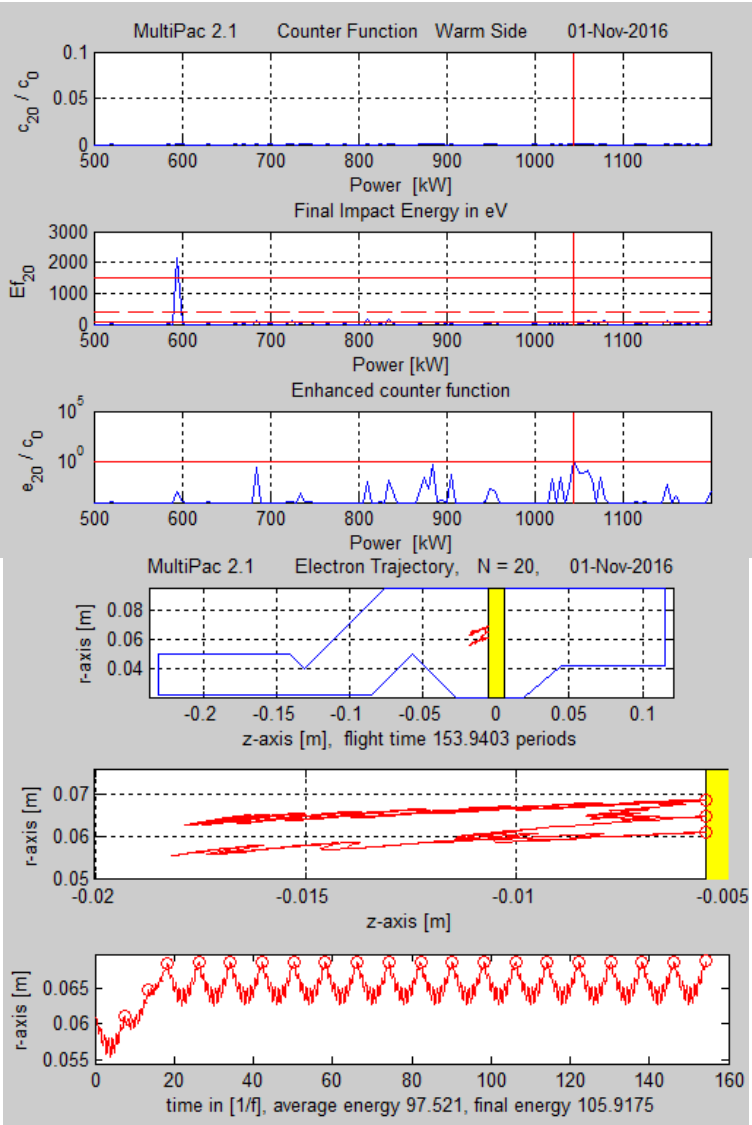

Figure 3.2.10: Multipacting simulation results from the Multipact code.

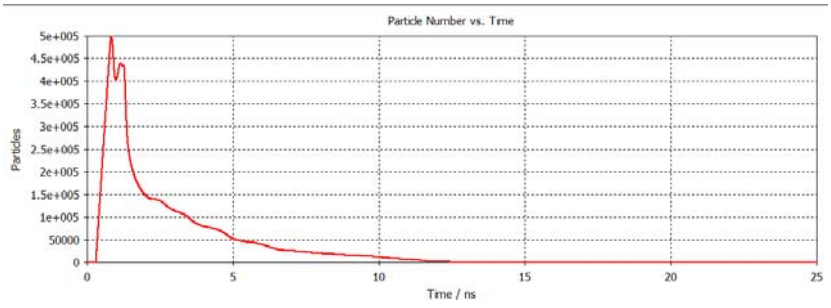

Figure 3.2.11: Multipacting simulation results from the CST code.

In Figure 3.2.10, we see the electron counter function, the average impact energy of the last impact in eV and the enhanced electron counter. The horizontal axis gives the average incident power in kW. The enhanced counter function e20/C0 is the ratio of the total number of secondary electrons after 20 impacts to the initial number of electrons; so, if the relative enhanced counter function exceeds unity or the final impact energy of the electron after 20 impacts is in the range for which the secondary emission coefficient is larger than 1, multipacting is probable. The left-hand side figure shows that multipacting may occur, but the right-hand side figure shows that the e20/C0 ratio is lower than one and the average energy is not in the range of secondary emission coefficient that is larger than 1. So, we may conclude that multipacting does not exist from the Multipact code result. Figure 3.2.11 strengthens this result that multipacting does not exist form the CST simulation result. The particles number rapidly decreases with time.

3.2.2.1.4 Collector

The capability of collector beam dissipation is an issue. If the entire beam power is dissipated without RF drive, it could reach 1.2 MW. The collector dissipated power is limited while klystron input power is switched on and is less than 400 kW [26]. A deionized water cooling system is chosen. To examine the collector design and its feasibility, a gun-collector test module is planned to be manufactured and tested before fabrication of a klystron prototype. Due to a possible furnace size problem in China, we need to reduce the collector size to have the full length of the gun-collector test module less than 2 m. The beam test module employing a modulated anode (MA) gun will be manufactured and tested. The pulsed operation of he MA gun gives different pulsed power to the structure which is important to evaluate the collector performance. Figure 3.2.12 shows the profile of the collector. The beam trajectory in the collector was cross-checked by the EGUN and MAGIC 2D codes. Figure 3.2.13 shows the beam trajectorysimulation for the gun-collector test module.

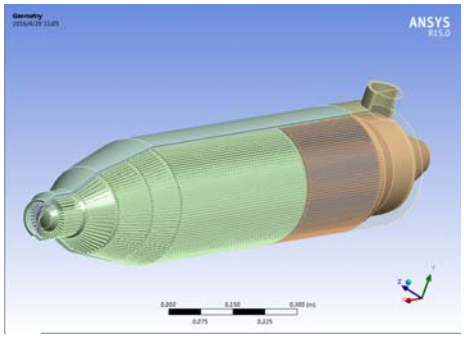

Figure 3.2.12: Collector profile.

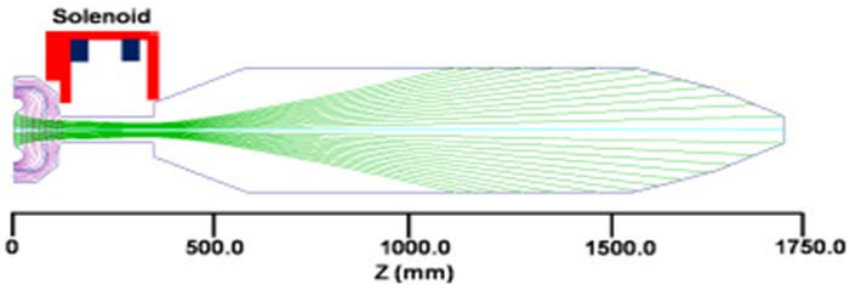

Figure 3.2.13: trajectory simulation for the gun-collector test module.

For the collector design, we assumed the capability of full beam energy dissipation and chose the design criterion for the surface dissipation power density to be the conservative value of 200 W/cm^2. Initially, the analysis was performed using a universal spread beam trajectory and an analytical formula for collector power dissipation. Maximum dissipation appears in the location where the beam rim hits the wall and where the collector radius changes. The choice of surface dissipation power density less than 200 W/cm^2, results in a large collector having large bore diameter and length. Then we changed the collector dissipation to 500 W/cm^2, which is also an acceptable value [27].

The collector outer surface is grooved to enhance cooling efficiency. The number of grooves, water flow rate and other parameters are optimized by a fluid flow and coupled heat transfer simulation. The maximum peak power dissipation density for the full beam power exceeds 500 W/cm^2 for this reduced-size collector. Through this simulation, we have been assuming that the tentative limit of the thermal interface temperature is 100° C but when the pulsed duty factor reaches 0.6, the thermal interface temperature exceeds 100° C. The collector's thermal analysis is show in Figure 3.2.14.

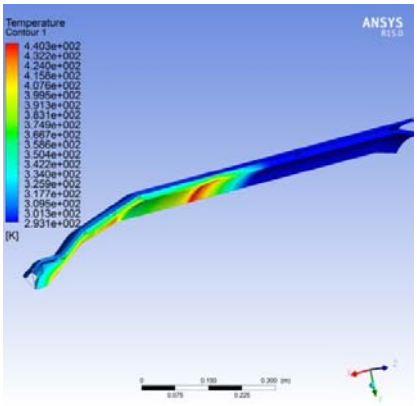

Figure 3.2.14: Collector thermal analysis

3.2.2.2 5712 MHz Klystron

Development of C-band high power klystrons would be scaled from exiting S-band klystrons, a successful experience at KEK. The parameters are listed in Table 3.2.5. Based on thees parameters and reference to safely operated electron guns on S-band klystrons, the gun and beam optics parameters are listed in Table 3.2.6.

Table 3.2.5: klystron concept parameters

Parameters	Unit	Value
Output power	MW	50
Perveance	up	1.5
Efficiency	%	45
Cathode current density	A/cm^2	8
Frequency	MHz	5712
Gain	dB	>50

Table 3.2.6: electron gun and beam optics parameters of the C-band klystron

Parameters	Unit	Value
High voltage	kV	350
Current	A	310
Cathode radius	mm	35
Beam radius	mm	5
Tunnel radius	mm	8
Beam Area Convergence		50
Brillouin Flux	Gauss	1134

The electron gun voltage will be set to 350kV, which is verified by well operated S-band (2856MHz/50MW) high power klystrons. By using the beam optics simulation code EGUN, a preliminary result of the beam trajectory is shown in Figure 3.2.15. The simulated gun perveance is 1.48 μP with beam voltage of 350 kV.

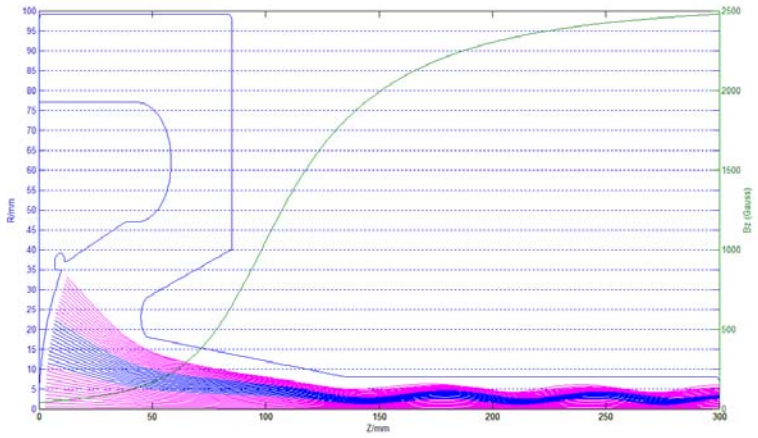

Figure 3.2.15: Beam trajectory of C band klystron

As a preliminary step, the interaction region might be a compact five cavities layout: the input cavity, two gain cavities, the penultimate cavity and the output cavity. Figure 3.2.16 shows the simulation result of AJDISK, which is a 1-D code for cavity layout optimization. The 2-D PIC codes like MAGIC and FIC will be used to do further optimization for beam-cavity interaction in the future.

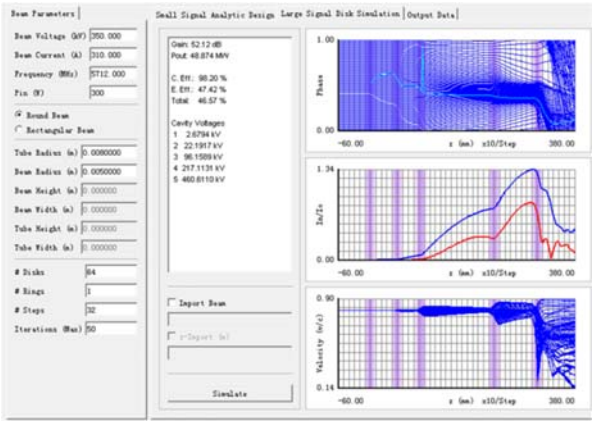

Figure 3.2.16: 1-D simulation of C band klystron by AJDISK

3.2.2.3 2856 MHz Klystron

The CEPC Linac injector low energy section includes 20 sets of S-band normal conducting traveling wave structures which will be driven by 10 sets of 80 MW pulsed klystrons operating at a frequency of 2856 MHz. Up to now IHEP and the 4404 factory have successfully developed S-band 65 MW klystrons used in the BEPC-II Linac injector [28]. Based on extensive klystron operation and development experience in IHEP and existing equipment and manufacturing experience in the 4404 factory, the BAC method will be adopted for the S-band 65 MW klystron to increase the efficiency from 45% to 60% [29-31]. Then the CEPC power requirement can be met. The new design will insert four cavities between the 4th cavity and 5th cavity but keep the same layout and total length as in the original design. The other parts such as gun, coil and collector will be re-used to save R&D and reduce fabrication cost. The 1D simulation results using AJDISK and klystron specification are shown in Figure 3.2.17 and Table 3.2.7 respectively.

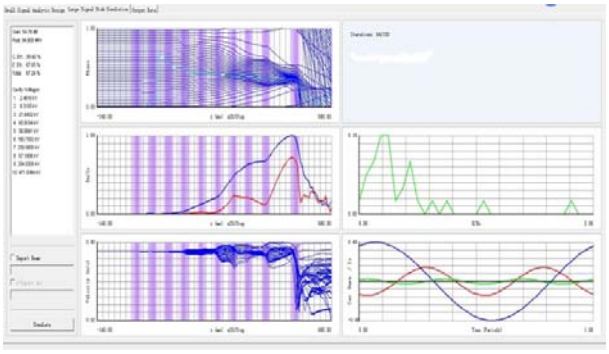

Fig.3.2.17: 1D simulation of S band klystron by AJDISK

Table 3.2.7 2856 MHz/80 MW klystron specification

Parameters	value
Frequency	2856 MHz
Output power	87 MW
Pulse width	4 μ s
Voltage	350 kV
Current	415 A
Perveance	μP
Gain	>50 dB
Efficiency	60%

3.2.3 RF Distribution System

3.2.3.1 Introduction

The purpose of the RF power distribution system (PDS) is to deliver the power from the RF power sources in the gallery to the RF cavities in the tunnel. Given the power levels the PDS design must have high transmission efficiency, low reflections, and be flexible, reliable and cost-effective. The PDS design for the Booster and collider will be described in detail below.

3.2.3.2 Booster PDS

The Booster includes 256 superconducting 9-cell cavities. Each individual cavity will be feed by one 30 kW solid state amplifier (SSA) operating at 1.3 GHz. The RF power produced by the SSAs will be delivered by standard WR650 waveguides. Either WR650 or WR770 can be used at 1.3 GHz. The allowed frequency band for WR650 is 1.12-1.7 GHz and for WR770 is 0.96-1.5 GHz. Because WR770 is bulky, WR650 is selected for the Booster PDS. The waveguide material can either be copper or aluminium. Copper is more costly and heavier than aluminium, thus aluminium is preferred for waveguides in spite of increased loss. Half-height waveguide will not be considered because of its thermal loss. The Booster PDS schematic is shown in Figure.3.2.18.

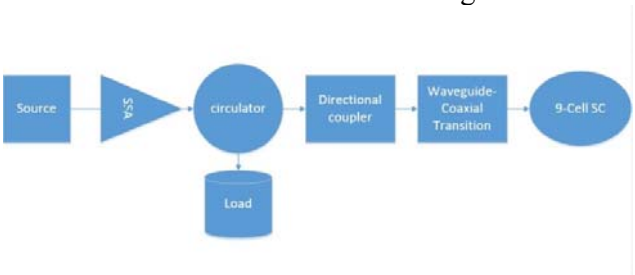

Figure 3.2.18: Schematic of the Booster PDS

One source per cavity simplifies RF power delivery. No splitters or phase shifters are needed. Length differences and thermal phase drifts are easily compensated and tracked by the individual LLRF controls. In addition to bend and straight sections, each feed line will include a circulator with load, a directional coupler, a waveguide-coaxial transition and a flexible waveguide [32]. The circulator is used to protect the SSA from

excessive reflected power. The circulators insertion loss should be less than 0.05 dB at the center frequency. The isolation for the three ports of circulator is greater than 30 dB. The high power circulator is a key and expensive component, which is not commercially available from domestic manufacturers. Due to circulator with load in each individual power module of the SSA, the high power circulator maybe eliminated after reliability test and evaluation. The circulator and dummy load can be integrated as an isolator with water-cooling. The directional coupler is used to monitor forward and reflected signals which provide the low-level RF control system with information on the forward and reflected cavity power levels. The directivity of the directional coupler should be more than 30 dB. Also the RF pickups can be integrated in the input and load ports of the circulator. The waveguide-coaxial transition is used to connect the waveguide system with the coaxial coupler for the 9-cell superconducting cavity. A short flexible waveguide is used for fine tuning in case of mechanical errors.

3.2.3.3 Collider PDS

3.2.3.3.1 Two Cavities per Source

The CEPC collider SRF system consists of 480 2-cell superconducting cavities. Each cavity requires 280 kW to meet the totality of the radiated, HOM, and reflected power demands. With one klystron for two cavities, the specified saturation power of the klystron needs to be 800 kW. This takes into account linear operation of the klystron, as well as the transmission losses. The RF power produced by the klystron will be delivered by standard WR1500 aluminum waveguide. The schematic of the collider PDS is shown in Figure 3.2.19

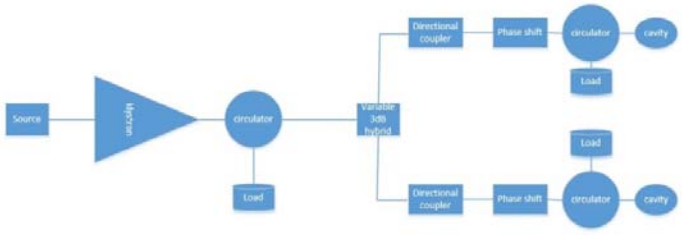

Figure 3.2.19: Schematic of the collider PDS

A variable 3 dB hybrid is needed to split the power to the two cavities. The power to each cavity differs due to the spread of the cavity gradient. So the coupling of the hybrid should be adjustable, as well as remotely controlled. Each cavity feed line is comprised of a remotely-controllable phase shifter, a circulator with load and a directional coupler. In order to protect the klystron from large reflected rf power, in each feed line a CW 400 kW circulator is installed to block the power that is either reflected or discharged from the cavity. The circulators insertion loss should be less than 0.05 dB at the center frequency. The isolation for the three ports of the circulator is greater than 30 dB. Also the circulators in the feed line can eliminate the mutual interference of the cavities. Even if one of the cavities is not functional, the adjacent cavities can still be operating normally. The directional coupler will provide both forward and reflected pick up signals with better than 30 dB directivity. Also the RF pickups can be integrated in the input and load ports of the circulator. Remotely-controllable phase shifters are used to correct any phase differences introduced to the waveguide system.

3.2.3.3.2 Four or More Cavities per Source

There are two typical types of PDS, the tree type and the TESLA type. Either can be used with four or more cavities per source system, as shown in Figures 3.2.20 and 3.2.21. Both systems have been evaluated and tested in the S1-Global test for the ILC. The latter was selected for the ILC PDS in their Technical Design Report [33]. The TESLA type PDS can be used with any number of cavities in the system [34]. The components are almost the same as two cavities per source system described above. Half-height WR1500 will be considered for the feed line to reduce the waveguide size and cost. Also it will save space and handling will be easier.

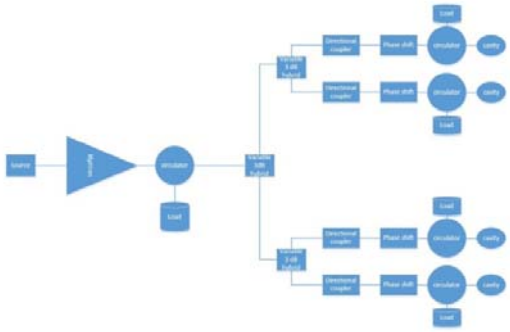

Figure 3.2.20 Tree type PDS

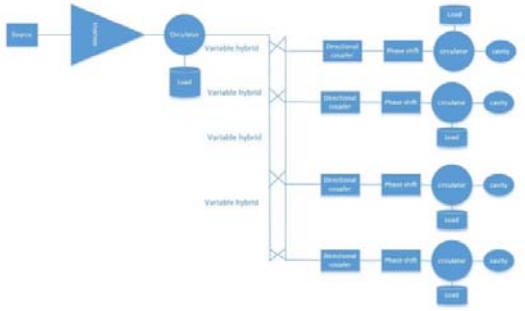

Figure 3.2.21 TESLA type PDS

3.2.4 High Voltage Power Supply

3.2.4.1 PSM Power Supply

The power supply of the RF amplifier-klystron is of the PSM type HVDC (PSM: pulse step modulation, HVDC: high voltage direct current). The performance of the PSM power supply will determine the RF microwave and beam quality of CEPC. Other auxiliary powers supplies are integrated into the PSM power supply. These include anode DC power, filament power, focus power and ion pump power. The power supplies and the control system are housed in three different cabinets which together belong to a single mechanical unit.

The DC power supply for the cathode is a PSM supply currently used in broadcast transmitters. PSM switching power supplies have the benefit of low energy storage and fast turn-off capability of the IGBT (Insulated Gate Bipolar Transistor). This eliminates

the need for a crowbar circuit to protect the klystron. The power supply will have redundant built-in switching module and will operate at full capacity even with several modules failing at the same time. Designed for 100kV/20A, this PSM essentially consists of 140 power modules which are connected in series and supplied through their own secondary windings from four transformers. The four transformers are shifted in phase, resulting in 24-pulse loading of the mains with a 6-pulse rectification in the module chain. Every HV transformer distributes power to 35 DC modules. Each module can provide 800-volt power, which can be switched (ON/OFF) individually by fast IGBT switches operating at 1 kHz. The switching sequence and pulse duration is generated and monitored by the PSM control system such that the thermal loading of all modules is distributed equally. The switching frequency feedthrough can be suppressed at the output of the module chain, by means of a low pass filter. The schematic diagram of the PSM power supply is shown Figure 3.2.22.

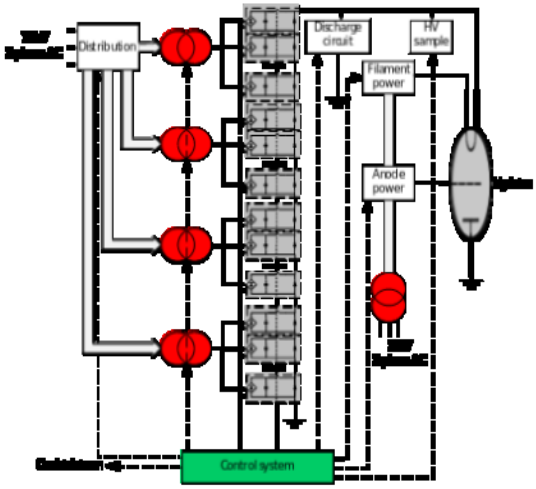

Figure 3.2.22: PSM power supply schematic diagram

The main PSM features are efficiency, regulation speed, accuracy and compatibility with large variations in the load impedance. These fit well with the performance specifications listed in Table 3.2.8. Moreover, the modular concept with high redundancy (this can be up to four defective modules without performance degradation) makes it very reliable, easy to maintain and there is no need for HV crowbars. For better RF source quality, the PSM can operate in PWM (pulse width modulation) mode [35] with switch frequency 1 kHz. Output voltage is smoother and ripple stability can easily be controlled to better than 0.2% [36]. The working duty cycle of IGBT is from 10% to 95%. Therefore, the output voltage of the PSM power supply is from 11.2 kV to 106.4 kV.

Table 3.2.8: PSM performance specification

Parameters	Unit	Value
High voltage	kV	100
Current	A	20
Module quantity		140
Module voltage	V	800
Module switch frequency	Hz	1k
Module number of redundancy		8
Voltage stability	%	< 0.2
Efficiency	%	>95
Turn-off time	us	<5
Stored energy	J	<15

For protecting the klystrons and reducing beam radiation, necessary signals will be processed directly in very fast processor FPGA (Field-Programmable Gate Array). Other signals will be interlocked in a PLC (Programmable Logic Controller).

3.2.4.2 Solid State Modulator

The klystrons are powered by pulsed modulators – a solid state modulator type pulser with well-established technology and reliability.

To accelerate an electron beam with a pulse width of 1 μsec, the flat-top of the klystron beam voltage must be more than 2 μsec. Long-term regulation and pulse flatness of the klystron beam voltage must be less than ±0.15% to prevent RF phase modulation and microwave power fluctuations. Main specifications of modulator are shown in Table 3.2.9.

Table 3.2.9: Main specifications of modulator

Parameters	Value
Peak output power(MW)	200/150
Average output power(kW)	80
Pulse width(us)	＞4us(flat top)
Pulse rate(pps)	100
Pulse Flatness	＜0.5% peak-to-peak
Pulse-Pulse Regulation	＜0.3%

The modulator can be divided into four major sections: a charging section, a discharging section, a pulse transformer tank and a klystron load. In the charging section, there is a series resonant type high voltage charging power supply (HVDC) detector. Figure 3.2.23 is a simplified modulator circuit diagram.

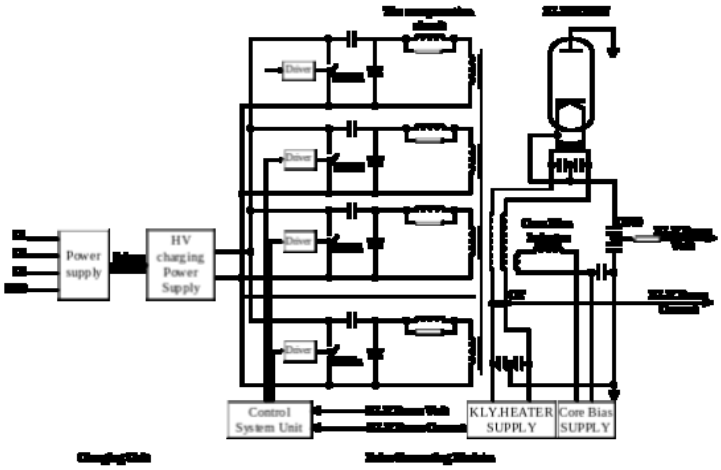

Figure 3.2.23 Simplified modulator circuit diagram

For system and personnel safety, the interlock has static and the dynamic modes. The static mode includes door interlocks, ground hooks, heater PS trips, cooling water flow and temperature status, and over voltage and current trips. The dynamic mode uses an analog signal from the vacuum system.

3.2.5 Solid State Amplifier

The CEPC Booster includes 256 sets of 9-cell superconducting cavities operating at 1300 MHz. Each cavity requires 20 kW of power to accelerate 0.87 mA of beam current at a gradient of 19.7 MV/m. Taking into account LLRF control margin, transmission losses, reflection and power redundancy, the total power requirement is 30 kW per cavity. The one power source to one cavity scheme is chosen to simplify the LLRF controls and waveguide distribution.

Different possible power sources that can provide 30 kW CW power at 1.3 GHz are vacuum tubes (klystron, IOT, tetrode, diacrodes) and solid state amplifier. With the progress in transistor technology, especially the emergence of the sixth generation LDMOSFET, the output power and efficiency of a single transistor has been greatly improved. The high power required can be obtained by operating numerous transistors in parallel. So solid-state based RF power stations have generated increased interest for accelerator applications. Current power capability of SSAs can extend from a few kW to several hundred kW, and the operating frequency from less than 100 MHz to above 1 GHz. Compared with vacuum tubes, there are many advantages to an SSA such as high reliability and flexibility in the module design, high stability, low maintenance requirements, absence of warm-up time and low voltage operation. The efficiency of SSAs is also reasonable. So the SSA is our priority selection for the CEPC Booster high RF power system.

The RF from the SSAs under open loop conditions needs only moderate regulation compared to the closed loop regulation of the cavity fields, which require high stable amplitude and phase of the SSAs. Although the cavity bandwidth (BW) is only 33 Hz, the effective BW of the RF station operating in closed loop will be around 70 kHz. The SSAs are specified to have a delay-line-like transfer function over this BW. Specifically, the SSAs 1 dB requirement needs a bandwidth of more than 1 MHz. The nominal maximum

power is to be achieved with less than 1 dB compression, and the harmonic power output is to be less than -30 dBc. The AC to RF efficiency goal for the SSAs at the rated power is to be at least 40%. The SSAs must include self-protection from internal reflections in the RF combiner circuits due to a failed transistor, and continue in such a situation to operate at reduced power. The SSAs must also be protected from overheating. Each SSA will interface with the global control system via an Ethernet cable, through which various digitized information will be available, including status data, drive power, power supply voltage and temperatures. Also, interlocks are necessary for external faults such as water leaks. The mean time between failures (MTBF) should be larger than 30,000 hours. With this requirement, less than 5% of the power modules will fail per year. With the failure of one module CEPC Booster can still run.

The output port is standard WR650 waveguide. The Booster SSA specifications are listed in Table 3.2.10.

Table 3.2.10: Booster SSA specifications

Parameters	Value
Frequency	1.3 GHz
Power (< 1 dB Compression)	30 kW
Gain	≥65 dB
Bandwidth (1 dB)	≥ 1 MHz
Amplitude stability	≤0.1% RMS
Phase stability	≤0.1°RMS
Phase Variation(1kw-30kW)	≤10°
Harmonic	< 30 dBc
Spurious	< 60 dBc
Efficiency at 30kW	≥45%
MTBF	≥30000 h
Redundancy	1 power module failure can still run

There are many companies and institutes in China that can provide SSA products. Even at 1.3 GHz BBEF successfully developed a 20 kW SSA for Peking University DC-SRF photo-injector in 2013, as shown in Figure 3.2.24 [37]. They also provided 7 sets of 3.8 kW SSA for LCLS-II in SLAC [38]. The efficiency of 400 W power modules is more than 52% and the combined efficiency is more than 40%.

Figure 3.2.24: BBEF 20kW/1.3GHz SSA for Peking University DC-SRF photo-injector

3.2.6 Low Level RF System

3.2.6.1 Introduction

The low level RF (LLRF) system stabilizes the fields of the accelerating structures in both amplitude and phase. The standardized hardware architecture such as mTCA.4 for physics will be adopted for the injector, Booster and collider which include both room temperature RF and superconducting RF cavities [39]. The same platform is chosen to fit different types of accelerating structures and integrate them into the full control system using EPICS.

3.2.6.2 Linac

The 10GeV RF linac accelerates electron and positron beams for injection into the Booster. This is comprised of room temperature bunching systems and hundreds of S-band accelerating structures with the high level RF S-band signals modulated by 50Hz short pulses. There are dozens of MW power levels and pulse lengths on the order of a few μs. The pulse-to-pulse amplitude fluctuation and phase drift should be compensated by LLRF system. Intra-pulse control methods are also considered to be investigated to ensure beam quality and stability.

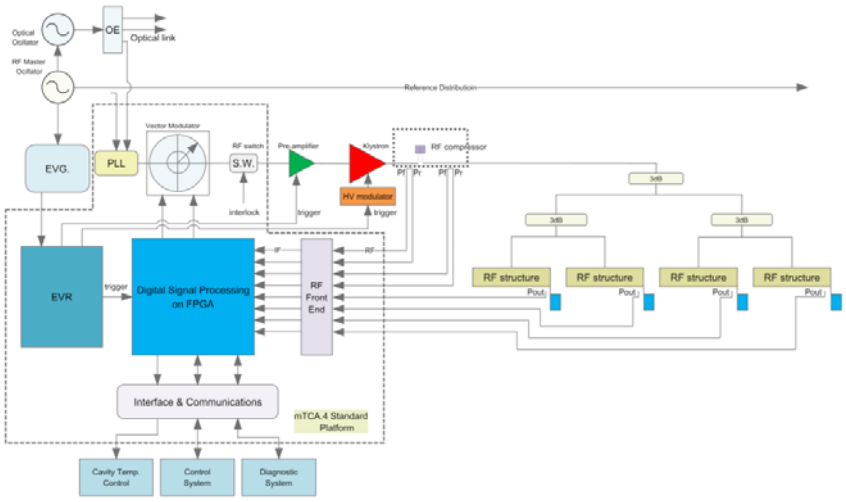

Figure 3.2.25: The LLRF system layout for the injector accelerating structures

The LLRF systems are synchronized to a phase reference system. They control the RF fields in the accelerating structures to meet the beam dynamics tolerance requirements of energy stability, luminosity loss and emittance growth. In the CEPC injector, the 2 sub-harmonic bunchers and the first accelerating tube with S-band buncher structure are fed from one separate RF power source. A single klystron and a RF pulse compressor delivers RF power to two S-band structures at the low energy end of the electron and positron sections. This is in contrast with those sections, where a single klystron delivers RF power to two S-band structures without pulse compressor. A layout of one RF station in the main linac is shown in Figure 3.2.25. The controller will regulate amplitude and phase of the vector sum of a string of those accelerating structures.

Since the RF pulse duration is short， we adopt pulse-to-pulse feedback and adaptive feed-forward techniques to correct slow drifts and repetitive distortions. We also provide an interface for the implementation of beam-based feedback. The phase reference distribution, the phase-locked loops, the vector modulator, the pre-amplifier and the high-voltage modulator together with the klystron determine the pulse-to-pulse stability. Each of these components must meet the required short-term stability.

In addition to control the local RF stations, the LLRF system interface to other systems need to be carefully considered. These include the phase reference system, the global timing system, the local protection system and the Machine Protection System.

3.2.6.3 Booster

The Booster has 8 RF stations consisting of many 1.3GHz 9-cell super-conducting cavities as the accelerating structure. One Booster cycle takes 10 seconds, which is divided into four periods: beam injection 1 second, energy ramp 4 seconds, a 1 second flat top for beam extraction and 4 seconds for the magnets to ramp down. All the cavities are driven by 1.3 GHz-25 kW solid state amplifiers. RF voltages in the cavities are modulated and controlled by the LLRF. It is difficult to accomplish the required bunch structure with a stable and controllable energy gain with this operation mode. Detailed design and optimization will be discussed or determined in the future. The LLRF system layout for the Booster is shown in Figure 3.2.26.

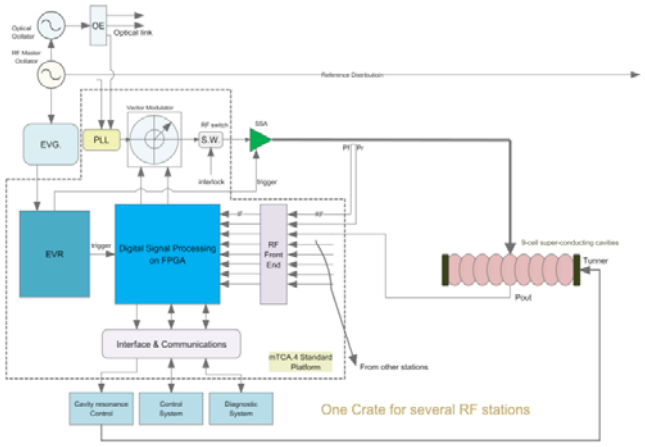

Figure 3.2.26: The LLRF system layout for the Booster

The LLRF system for the superconducting cavities includes the cavity resonance controller, which is placed in the same crate as the motion control for the fast and slow tuners. Those fast motion controller drives the piezo actuators. It may become necessary to adopt iterative learning algorithms corresponding to timing triggers for operation mode.

3.2.6.4 Collider

The 100 km collider ring will use one 800 kW CW klystron to drive two 5-cell superconducting cavities. The successful experience of allocating phase reference and maintaining coherence in large facilities like PEPII and LHC helps greatly [40-43]. We will take the combined advantage of vector sum and signal cavity control methods to meet our user and system requirements. The LLRF system controls that the klystrons work effectively and compensate for the beam loading, Lorentz Force detuning and slow drifts or other interference caused by environment dependency of components.

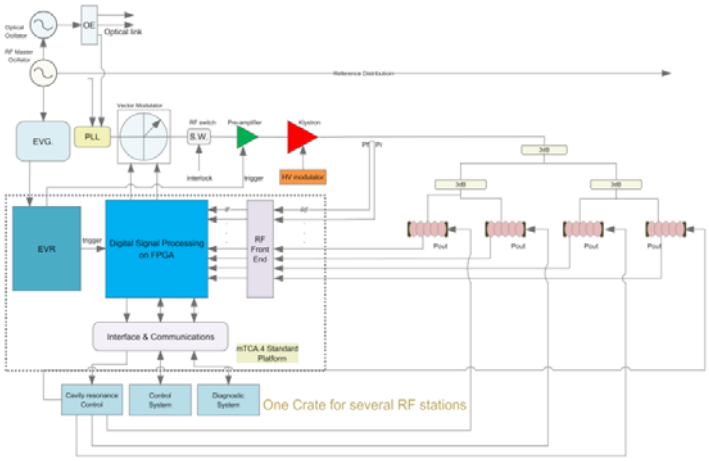

Figure 3.2.27: The LLRF system layout for the collider accelerating structures

The beam interaction of RF stations in the collider strongly influences the longitudinal beam dynamics for both single bunch and collective effects. The non-linearity and noise generated within the RF accelerating voltage strongly affects the

longitudinal beam distribution. Carefully configured feedback loops such as the digital RF feedback, the klystron polar loop and the comb feedback loop improve stability. We have estimated collective effects stability margins and evaluated longitudinal sensitivity to various LLRF parameters and configurations. The LLRF system layout for the collider is shown in Figure 3.2.27.

3.2.6.5 Hardware

The signals from the forward, reflected RF power and pickup signal are down-converted to an intermediate frequency (IF) and subsequently sampled by fast ADCs. Amplitude and phase information is represented by in-phase and quadrature terms for processing by the FPGA based digital signal processing platform. The feedback system requires individual field measurements from which the amplitude, phase and vector are calculated. The sensor signals include cavity field probe signals for control algorithms, forward and reflected power signal of each cavity and RF power source from which cavity detuning and beam loading are derived and which are used for system diagnostics. The field detection is accomplished in the rear transition modules (RTM) boards by down converting the cavity signal from the probe to an IF signal which is sampled by the ADC from which the field amplitude, phase of vector is calculated. To ensure ADC accuracy, each channel should have a programmable attenuator to adapt to different input power levels. The same boards are also used for converting the baseband signal to an RF signal to drive the power source which is implemented using a vector modulator driven by DACs.

To support a low latency and high accuracy in the feedback loop, 125 MHz with 16-bit resolution or higher grade ADCs and DACs as well as a low latency processing unit based on large FPGAs are required. In the mTCA.4 systems, FPGAs and DSPs for the main RF control algorithms are implemented inside the advanced mezzanine cards (AMC) located at the front of the crate. Communication from the RTM to the AMC takes place through the Zone-3 connector, while communication between AMC modules is covered by the PCIe link in the backplane.

Several other modules also need be installed in the MTCA crate for different functions. For redundancy, each crate requires two power supply modules. One or two micro-TCA carrier hubs (MCH) take care of the shelf and boards management. A processor board can be used to implement an EPICS based control system front end server for remote operation. A timing receiver provides event trigger and clock distribution which is necessary for operation of the LLRF system. Piezo drivers allow fast control of the cavity resonance frequency using piezo actuators for control to compensate Lorentz force detuning.

The local oscillator (LO) generation module is also required by the system. The reference signal from the timing system is internally divided, multiplied and mixed to produce an LO signal used by the down converters, and external clock (CLK) signals used by the digitizes.

3.2.6.6 Software

LLRF software provides functional, flexible and user-friendly interfaces to the high level system for RF system control. Hundreds of software applications must be installed, maintained and upgraded as needed and as experience is gained. The diagram of LLRF software is shown in Figure 5.2.28 and should satisfy the following:

- All the codes should be version controlled.

- All the software should be easily maintained and updated.
- Special tools will be developed for remote access and automatic processing.

The software of the LLRF system includes:

- Device driver for the MicroTCA system;
- EPICS IOC (Input Output Controller) of the hardware;
- Application software (e.g. automatic control scripts);
- Graphic user interface (GUI) for operator/physicist.

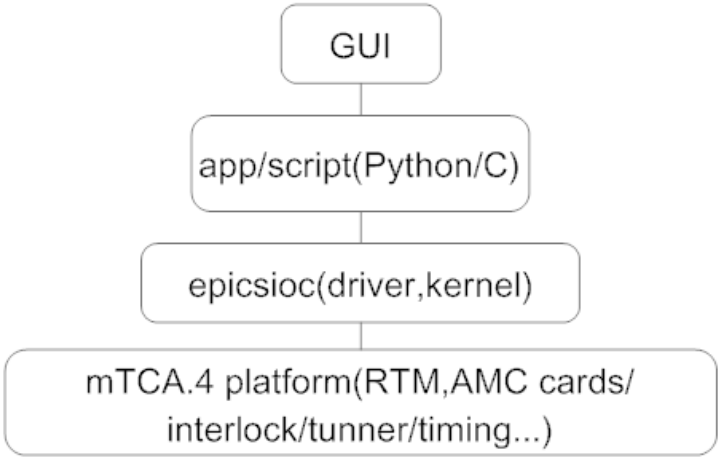

Figure 3.2.28: Software of LLRF system

Device driver of the MicroTCA system

The device driver supports standard interfaces to handle the hardware according to higher level call functions.

EPICS IOC (Input Output Controller) of the hardware

The IOC connects EPICS data recording with the physical hardware data (e.g. sampling data or registers) through record support and device support functions. It provides PVs to higher level.

Application software

Specific applications (e.g. automatic control scripts) can fulfill complex needs based on all the PVs and non-PV data. This level is optional for the operators. Many tools or languages are available: languages like Python, C etc. and tools like Matlab, Labview etc. Software for automatic ramping of cavity voltage and automatic conditioning of cavities are two useful cases which will be developed.

Graphic user interface (GUI) for operator/physicist

Many GUI software is available in the accelerator community. Control System Studio (CSS) will be the main option for LLRF GUI development.

3.2.7 Phase Reference System

The Phase Reference System provides short-term low-noise, long-term stabilized and coherent phase reference for the entire accelerator complex. In principle, both the phase and amplitude of the accelerating field are stabilized by the Low-Level Radio Frequency (LLRF) system to meet beam physics requirements. The stabilization of the amplitude of multiple cavities does not need a reference as the amplitude is a local and absolute factor for different cavities. However, the phase of all the cavities is correlated and relative to guarantee the beam quality. Thus, the phase reference for each cavity should be derived from synchronized with one single source [44].

3.2.7.1 Introduction

The phase reference system of CEPC must:

1) Provide a frequency standard to the Main Ring(650MHz), the Booster(1.3GHz) and the Injector(5712MHz, 2856MHz, 571.2MHz and 142.8MHz). These drive and reference all the accelerating tubes, superconducting RF cavities, LLRF system and beam diagnosis system;
2) Provide reference to the timing system which may be synchronized with the electric power grid;
3) Maintain the phase and frequency stability at multiple reference points (or keep the reference signals coherent) around the accelerator complex during over long time operation periods;
4) Support high reliability, easy extensibility and a human friendly maintenance environment; and
5) Support real-time self-status-monitoring (e.g. slow phase drift of multiple reference paths).

3.2.7.2 Design Consideration

A 2-layer phase reference system is proposed; long-distance distribution and short-distance local routing. Each long-distance distribution path transports only one reference signal which is then distributed locally to the desired LLRF/RF stations [45].

The phase reference system of CEPC will include three parts:

1) The phase/frequency standard source
2) The distribution of RF reference signals with several frequencies
3) The receiver of RF reference signals and short-distance routing

3.2.7.3 The Phase/Frequency Standard Source

The phase drift of the standard source called Master Oscillator (MO) is a common-mode factor for all the down-stream reference phases. The MO phase noise will impart additional timing jitter to the reference signal in the time domain. The frequency stability of the MO will influence the phase error over long running periods. Therefore, the standard source should have low phase noise and high frequency stability. An atomic clock or crystal oscillator with phase noise of -150dBc/Hz@10kHz and frequency stability of 10^{-11} will satisfy this requirement.

3.2.7.4 RF Reference Signals

Transporting RF signals through long coaxial cables will suffer greatly from attenuation, temperature drift, mechanical vibration and electromagnetic radiation. So, phase-stabilized optical fiber is chosen for the RF transport medium. But the length variation of optical fiber caused by temperature/humidity change also brings in-phase drift in signal transmission. So, the length of optical fibers must be stabilized by measure-and-feedback technique. The phase variation can be monitored and recorded at the same time. An rms 50 fs (0.05º for 2856MHz) long-time stability after 1km can be achieved according to some XFEL facility results [46].

The collider and the Booster contain 10 RF stations (including 4 1/2 stations at detector points). Each RF station is less than 120 m in length; so within one RF station the phase drift is small and the reference signal can be distributed through coaxial cables with careful environmental control. There is only one operating frequency in the collider (650 MHz) and the Booster (1.3GHz).

The injector linac is more than 500m long and the phase stability requirement is higher than in the two rings. It will also adopt optical fiber to transfer the phase reference signal. The linac contains over 30 S-band (2856MHz)/C-band (5712MHz) LLRF/RF stations, one 142.8MHz and one 571.2MHz Sub-Harmonic Buncher (SHB). The phase reference systems are shown in Figure 3.2.29.

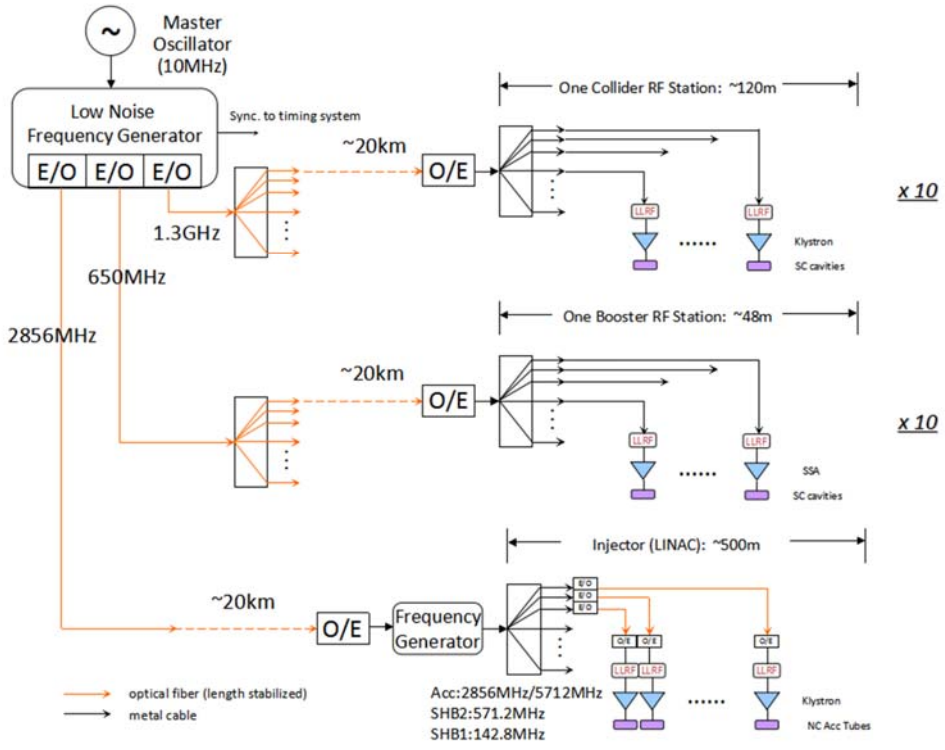

Figure 3.2.29: Phase Reference System of CEPC

3.2.8 References

1. Preliminary Conceptual Design Report IHEP-AC-2015-01(2015).
2. Zhou Z S, Fukuda S, Wang S C, Xiao O Z, Dong D, Nisa Z U, Lu Z J and Pei G X 2016 7th International Particle Accelerator Conference (Busan, Korea 8-13 May 2016) p 3891
3. Symons R S, 1986 International Electron Devices Meeting (Los Angeles, CA 7-10 December) p 156
4. Nisa Z U, Fukuda S, Zhou Z S, Wang S C, Xiao O Z, Dong D, Lu Z J and Pei G X 2016 7th International Particle Accelerator Conference (Busan, Korea 8-13 May 2016) p 546
5. Gilmour A S 1994 Principle of Travelling Wave Tube (Artech House, Boston) chap 6 p103
6. Larionov A and Ouglekov K 2000 6th International Computational Accelerator Physics Conference (Darmstadt, Germany 11 September) p 17
7. Herrmannsfeld W B 1988 SLAC-PUB-331 (1988)
8. http://www.cst.com
9. Isagawa S, Takeuchi Yo, Baba H, Tanaka J, Ohya K, Kawakami Y and Hosoi S 1987 IEEE Particle Accelerator Conference (Washington, DC 16-19 March 1987) p 1934
10. Demmel E, Lutgert S, Offermann B and Schwarz H 1996 5th European Particle Accelerator Conference (Sitges, Spain 10-14 June 1996)
11. Higuchi T, Sasaki M, Matsumoto S and Fukuda S 2012 9th International Vacuum Electronics and Electron Sources Conference (Monterey, California 24-26 April 2012) p 469
12. "Poisson code, Los Alamos National Laboratory Report," LA- UR-87-126 (1987).
13. Staprans A 1985 High Voltage Workshop (Monterey, California 26 February 1985)
14. E. L. Lien, “High efficiency klystron amplifier”, Proc. 8th Int. Conf. on Microwave and Optical Generation and Amplification (MOGA’70), Amsterdam, Netherlands, September 1970, pp. 1121-1127
15. A. Yano, S. Miyake, “The Toshiba E3736 Multi-Beam Klystron”, in Proc. LINAC’04, Lubeck, Germany, August 2004, paper. THP445, pp.706-708
16. F. Peauger, “High efficiency-high perveance Klystron”, presented in EnEfficiency RF sources Workshop, 2014.
17. I. A. Guzilov, “BAC Method of Increasing the Efficiency in Klystrons”, in Pro. IVEC’14, pp.1-2
18. V. A. Kochetova, et al., “Klystron amplifier with high RF efficiency. Some aspects of the theory and experiments” (in Russian), Radio-Tech. Electron., vol. 26, No. 1, Jan. 1981.
19. M. A. Kemp, et al., “A Self Biasing, Pulsed Depressed Collector”, IEEE Trans. Electron Devices, vol. 61, no. 60, pp. 1824-1829, June, 2014
20. A. Y. Baikov, et al., “Toward High-Power Klystrons with RF Power Conversion Efficiency on the Order of 90%”, IEEE ED, Vol. 62, No. 10, p. 3406, 2015.
21. AJDISK Manual, 2008
22. Xiao O Z, Fukuda S, Zhou Z S, Wang S C, Dong D, Nisa Z U, Lu Z J and Pei G X 2016 7th International Particle Accelerator Conference (Busan, Korea 8-13 May 2016) p 543
23. "Poisson code, Los Alamos National Laboratory Report," LA- UR-87-126 (1987).
24. HFSS Manual, 2011
25. MultiPac 2.1 manual, 2001
26. Wang S C, Fukuda S, Zhou Z S, Xiao O Z, Dong D, Nisa Z U, Lu Z J and Pei G X 2016 7th International Particle Accelerator Conference (Busan, Korea 8-13 May 2016) p 540
27. Smith M J and Phillips G 1995 Power klystrons Today (Somerset, England) chap 7 p170
28. BEPCII annual report, 2016
29. I.A. Guzilov, BAC Method of Increasing the Efficiency in Klystrons , International Vacuum Electron Sources Conference, 2014:1-2
30. Aaron.Jensen, Michael.Fazio, Andy.Haase et al, Retrofitting the 5045 Klystron for Higher Efficiency, IEEE International Vacuum Electronics Conference, 2015:1-2

31. Aaron Jensen, Andy Haase, Erik Jongewaard, Increasing Klystron Efficiency Using COM and BAC Tuning and Application to the 5045 Klystron, SLAC-PUB-16466，2016
32. LCLS-II Final Design Report DRAFT,2014
33. ILC Technical design report, 2013
34. MATSUMOTO Toshihiro, RF Power Distribution Development for STF,2016
35. Engineering Report of PSM High Voltage power, ADS, 2011, 19-20.
36. Development of 8 MW Power Supply Based on Pulse Step Modulation Technique for Auxiliary Heating System on HL-2A, Plasma Science and Technology, Vol.14, No.3, Mar. 2012, 263-265.
37. F. Wang et al, Using A 1.3 GHz 20 kW Solid State Amplifier As RF Power Supply For DC-SRF Photo-Injector, Proceedings of ERL2015, Stony Brook, NY, USA
38. R,G.Carter, Review of RF power sources for particle accelerator
39. http://mtca.desy.de/
40. THE INTERNATIONAL LINEAR COLLIDER Technical Design Report | Volume 3II: Accelerator Baseline Design;
41. SwissFEL Conceptual Design Report
42. LHC Design Report Volume I, chapter 6 ,THE RF SYSTEMS AND BEAM FEEDBACK
43. Architecture and Performance of the PEP-II Low-Level RF System.
44. Holger Schlarb. Femtosecond synchronization for free electron lasers.Workshop on Advanced Photon Sources, 2008.
45. L. de Jorge and J. Sladen. RF reference distribution for the LEP energy upgrade. Proceeding of EPAC1994, England, 1994.
46. H. Maesaka et al. Design and Performance of the Optical Fiber Length Stabilization System for SACLA. IPAC2014, Germany, 2014

3.3 Cryogenic System

3.3.1 Overview

The CEPC has two rings, the Booster ring and the collider ring. There are 736 superconducting cavities in total. In the Booster, there are 256 ILC type 1.3 GHz 9-cell superconducting cavities with cavity quality factor Q0=2E10 at 20 MV/m; eight of them will be packaged in one 12-m-long module. There are 32 such modules. In the main collider ring, there are 480 650 MHz 2-cell cavities with cavity quality factor Q0=2E10 at 16MV/m; six of them will be packaged in one 10-m long module. There are 80 of them. All the cavities will be cooled in a liquid-helium bath at a temperature of 2 K to achieve a good cavity quality factor. The cooling benefits from helium II thermo-physical properties of large effective thermal conductivity and heat capacity as well as low viscosity and is a technically safe and economically reasonable choice. The 2 K cryostat will be protected against heat radiation by means of two thermal shields cooling with 5-8K helium as well as 40-80K helium from a refrigerator.

The CEPC ring is separated into 8 sections by 8 straight sections. The superconducting RF and cryogenic systems are thus installed at these straight sections. There are 8 cryo-units along the 61 km circular collider with the physical design of an advanced partial double ring, as shown in Fig 3.3.1. Generally, each cryo-unit is supplied from a common cryogenic plant, with one refrigerator and one distribution box.

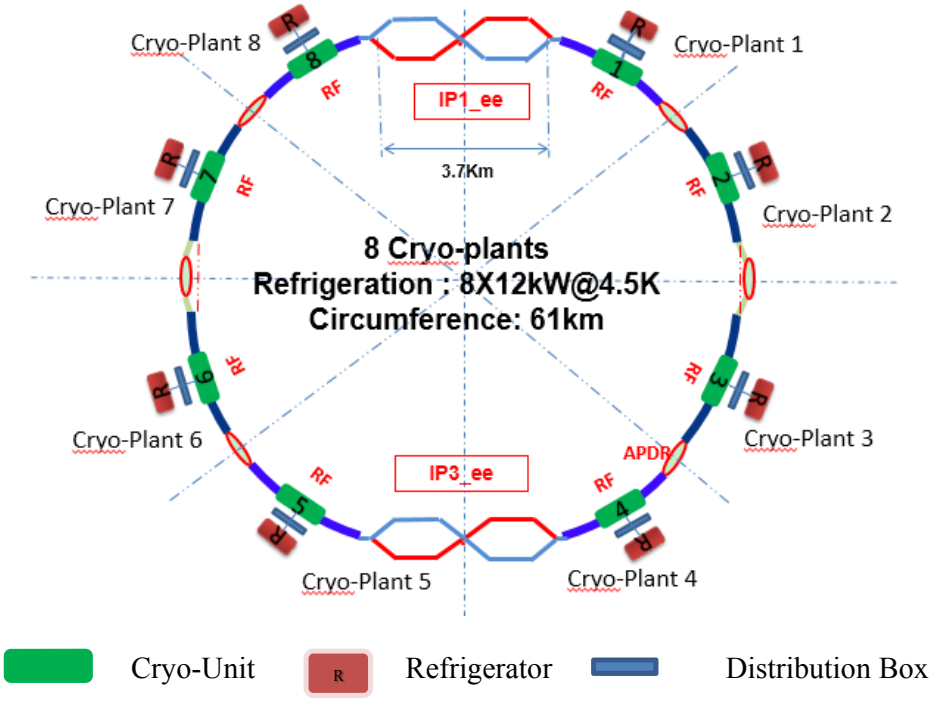

Figure 3.3.1: Layout of the CEPC Cryogenic system

The cryogenic system is designed for fully automatic operation during extended periods. Reliability and stability are what concerns us most.

3.3.2 Layout of Cryo-Units and Cryo-Strings

Each cryo-unit (Fig 3.3.2) includes two strings, one string is grouped with 4 modules from the Booster and the other is grouped with 10 modules from the collider.

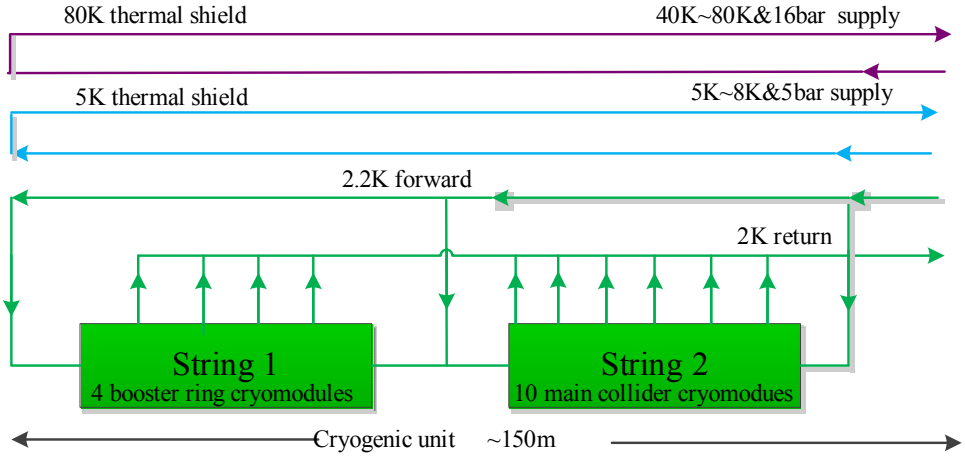

Fig 3.3.2 Cryogenic unit

Saturated HeII cools the RF cavities at 2 K. In view of the high thermodynamic cost of refrigeration at 2 K, the thermal design of the CEPC cryogenic components aims at intercepting heat loads at higher temperature as large as possible. Hence helium-gas-cooled shields intercept thermal radiation and thermal conduction at 40 ~80 K and at 5~ 8 K. The 40~80 K thermal shield is the first major heat intercept, sheltering the cold mass from the bulk of heat in-leaks from ambient. 5~8 K for lower temperature heat interception.

During the operation, one-phase helium of 2.2K and 1.2bar is provided by the refrigerator to all cryomodules. Every two cryomodules share one valve box with three valves. The JT-valve is used to expand helium to a liquid helium separator. A two-phase line (liquid-helium supply and concurrent vapor return) connects each helium vessel and connects to the major gas return header once per-module. A small diameter warm-up/cool-down line connects the bottoms of the helium vessels with two ends. The cavities are immersed in baths of saturated superfluid helium, gravity filled from a 2K two-phase header. Saturated superfluid helium flows along the two-phase header which is connected to the pumping return line and then to the refrigerator.

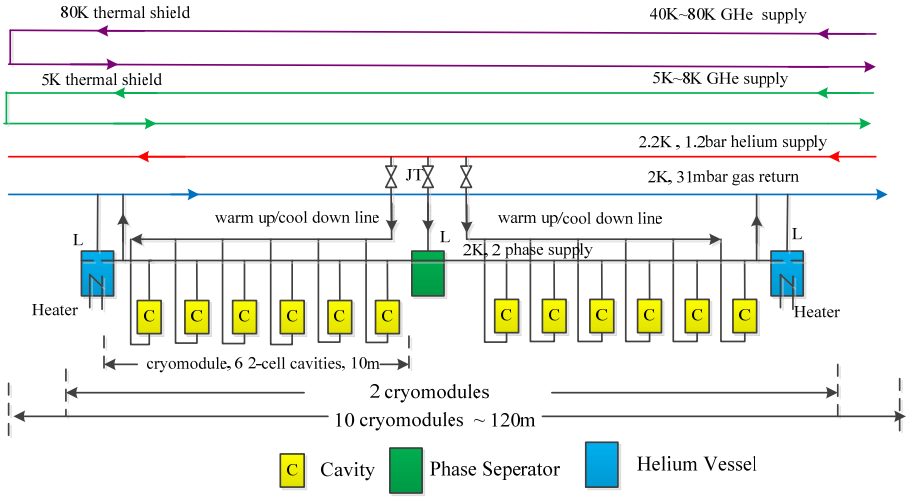

Fig 3.3.3 main ring cryomodules for string 2

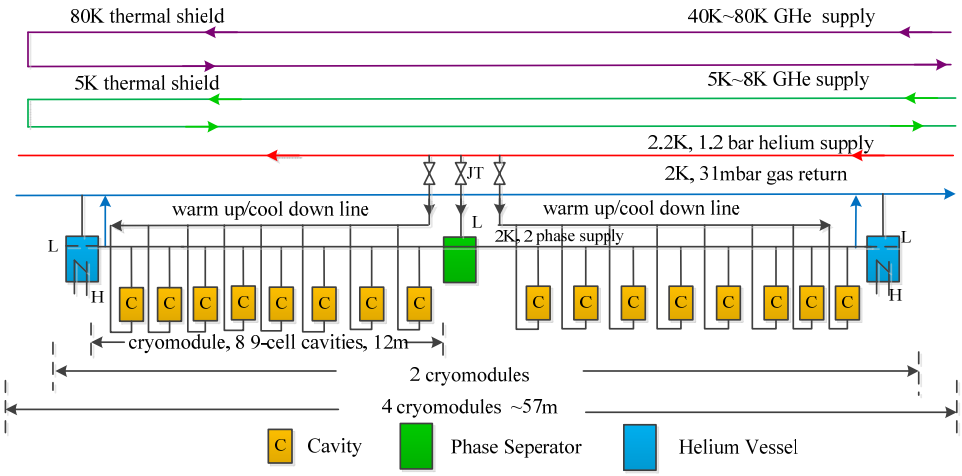

Fig 3.4.4 booster ring cryomodules for string 1

3.3.3 Heat Load

The heat load is mainly from the superconducting cavities. As mentioned, two types of superconducting cavities provide the energy for the booster and the main collider. The 1.3GHz TESLA like 9-cell cavities with quality factor of 2E10 @ 20MV/m is for the Booster and the 650MHz 2-cell cavities with the quality factor of 2E10 @ 16MV/m for the collider. There are two different designs for the main collider, they are single ring and partial double ring with different parameters. Table 3.3.1 shows the detailed parameters of the booster ring and the main collider, as well as the total dynamic heat load from the cavity wall.

Table 3.3.1 Parameters of the Booster and collider ring cavities

	Booster	Collider				
		Higgs Single ring	Advanced partial double ring (APDR)			
			H-LP	H-HL	W	Z
Frequency(MHz)	1300	650	650	650	650	650
Cavity operating voltage (MV)	20	17.89	7.37	7.31	3.91	3.75
Duty factor	15%	CW	CW	CW	CW	CW
HOM power/cavity (KW)	1.96	3.7	0.5	0.7	0.8	0.9
Number of cells per cavity	9	5	2	2	2	2
Total number of cavities	256	384	480	480	192	32
Total number of modules	32	96	80	80	32	16
Eacc (MV/m)	20	16.2	16	15.8	8.5	8
R/Q	1038	514	206	206	206	206
Q0	2.00E+10	4.00E+10	2.00E+10	2.00E+10	2.00E+10	2.00E+10
Operation temperature (K)	2	2	2	2	2	2
Cavity dynamic heat load (W)	3.11	16.97	13.21	12.88	3.73	3.30
Total dynamic heat load (kW)	0.8	6.52	6.34	6.18	0.71	0.1

From the table, we can see that the dynamic heat load in the main collider comprises the largest cryogenic cooling load and therefore dominate the design of the cryogenic system. Compared with the type of single ring of the collider, the advanced partial double ring (APDR) has a less dynamic heat load and can work with different physical parameters. The APDR collider is preferred.

Table 3.3.2 summarizes the static and dynamic heat loads of CEPC Booster and APDR collider with low power mode in the nominal operating conditions at different temperature levels. This amounts to a total equivalent entropic capacity of 74.93 kW at 4.5 K.

Table 3.3.2 CEPC heat load

	Unit	BOOSTER			COLLIDER		
		40-80K	5-8K	2K	40-80K	5-8K	2K
Module static heat load	W	140	20	3	300	60	12
Module dynamic heat load	W	140	10	24.91	300	60	79.23
HOM loss per module	W	180	11	15.7	90	9	3
Connection boxes	W	50	10	10	50	10	10
Total heat load	kW	15.51	1.47	1.56	59.2	11.12	8.34
Total predicted mass flow	g/s	74.37	45.93	73.41	283.69	346.96	393.53
Overall net cryogenic capacity multiplier		1.54	1.54	1.54	1.54	1.54	1.54
4.5K equiv. heat load with multiplier	kW	1.8	2.05	7.66	6.85	15.49	41.08
Total 4.5K equiv. heat load with multiplier	kW	11.51			63.42		
Total 4.5K equiv. heat load of booster and collider	kW	74.93					

The figures in Table 3.3.2 include an "overall net cryogenic capacity multiplier," a multiplier of the estimated heat loads, and is in general use in the cryogenic community. This factor includes a margin for plant regulation, a buffer for transient operating conditions, a buffer for performance decreases during operation and a buffer for general design risks. This multiplier parameter is from the ILC Design report [1].

In the ILC design [4], the real COP at 40~80K, 5~8K and 2K are 16.4, 197.9 and 700.2 respectively. With our installed power estimate shown Table 3.3.3, the total installed power for both booster and collider ring is about16.39MW.

Table 3.3.3 CEPC cryogenic system installed power requirement

	40-80 K	5-8 K	2 K
Booster heat load（kW）	23.90	2.27	2.40
Collider heat load（kW）	91.17	17.12	12.84
CEPC TOTAL（kW）	115.07	19.39	15.24
COP（W/W)	16.4	197.9	700.2
Install power（MW）	1.89	3.84	10.67
Total install power（MW）	16.39		

3.3.4 Refrigerator

The CEPC heat loads shown in Table 3.3.2 result in the requirement of the helium refrigerator plants to have a total capacity over 74.93kW at 4.5K. Eight individual refrigerators will be employed for the CEPC cryogenic system. The cryogenic plant capacities are equivalent to 12kW at 4.5K for each cryogenic station. The total cryogenic capacities are equivalent to 96kW at 4.5K.

Many aspects must be taken into account during refrigerator design, including cost, reliability, efficiency, maintenance, appearance, flexibility, and convenience of use. The initial capital cost of the cryogenic system as well as the high energy costs of its operation over the life of the facility represent a significant fraction of the total project budget, so

reducing these costs has been the primary focus of our design. Reliability is also a major concern, as the experimental schedule is intolerant of unscheduled down time.

The refrigerator main components include compressor station with oil removal system, vacuum pumps and the cold box which is vacuum insulated and houses the aluminum plate-fin heat exchangers and several stages of turbo-expanders.

The fundamental cooling process expanding compressed helium gas to do work against low-temperature expansion engines, then recycling the lower pressure exhaust gas through a series of heat exchangers and subsequent compression is a variant of the Carnot process that has been in use for many decades.

There are five pressure levels in the cryo-plant, which are 20bara, 4bara, 1.05bara, 0.4bara, 3kPa and obtained with the high pressure screw compressor group, middle pressure screw compressor group, warm compressors and cold compressors. There are 6 temperature levels in the system with 5-class turbine expansions and 11 heat exchangers. LN2 precooling is used to increase the cooling power during the cool-down, which will be replaced by the 1st stage turbine string during normal operation. At the 40K and 5K temperature levels helium flows are directed to the thermal shields of the cryomodules. The corresponding return flows are fed back to the refrigerator at suitable temperature levels. Inside the refrigerator cold-box the helium is purified from residual air and neon and hydrogen by switchable absorbers at the 80K and 20K temperature levels, respectively.

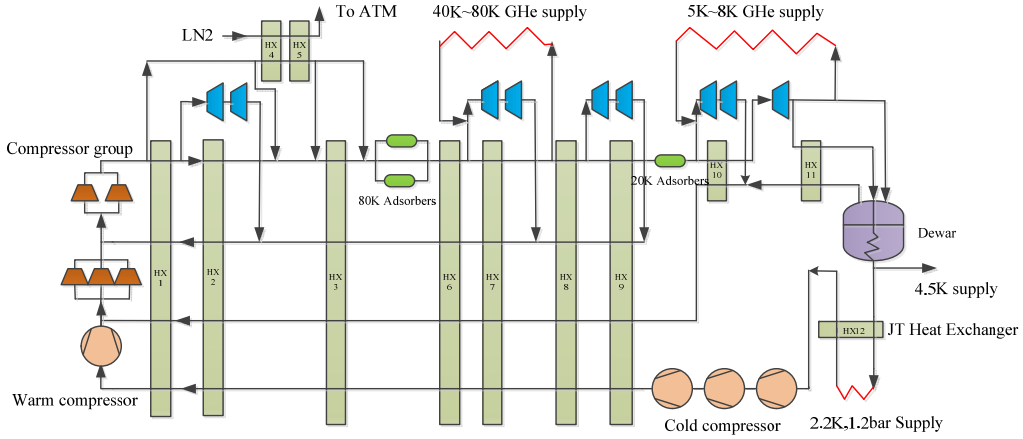

Figure 3.3.6: 2 K refrigerator flow diagram

The cryo-plant will supply 4.5K and 2.2K helium to the cryomodules. At each cryomodule the helium goes through a phase separator and a counter flow heat exchanger to recover the cooling power, then expanded to 31 mbar via a JT-valve, resulting in helium II liquid at 2K. The low pressure helium vapor from the 2K saturated baths surrounding the cavities returns to the refrigerator through the gas return pipe. The vapor is pumped away and returned to the cryo-plant.

There are two options for such a pumping system. One relies solely on cold compressors; the other employs a set of cold compressors followed by a final stage of warm compression. After superheating in the counter flow heat exchanger, the gas is compressed in the multiple-stage cold compressors to a pressure in the 0.5 to 0.9 bar range. This stream is separately warmed up to ambient in exchangers and goes back to the warm compressors. The choice of a warm vacuum compressor makes it easier to adjust for the

heat load variations. This approach, which CERN uses in the LHC plants [2], also allows for an easier restart of the 2K system after a system stoppage.

3.3.5 Infrastructure

The 2K cryogenic system consists of oil lubricated screw compressors, a liquefied-helium storage vessel, a 2K refrigerator cold box, cryomodules, a helium-gas pumping system and high-performance transfer lines. The cryogenic station is alongside the RF station. The cooling power required at each RF station will be produced in a 12kW at 4.5K refrigerator, which are installed at eight cryogenic stations, and distributed to the adjacent superconducting cavities [5,6].

For reasons of simplicity, reliability and maintenance, the number of active cryogenic components distributed around the ring is minimized and the equipment locations chosen following these principles:

1) Equipment is installed as much as possible above ground to avoid the need for excavation of further large underground caverns. Normal temperature equipment should be installed at ground level.
2) For safety reason, nitrogen is not allowed in the tunnel.
3) To decrease heat loss, the equipment working at temperatures below liquid nitrogen temperatures shall be installed near the cryomodules [3].

Equipment at ground level includes the electrical substation, the warm compressor station, storage tanks (helium and liquid nitrogen), cooling towers, the upper cold-boxes with liquid nitrogen precooling and helium purification. Underground are the lower cold-boxes, 2K cryomodules, multiple transfer lines, and distribution valve boxes. Fig. 3.3.7 shows the general architecture of the cryogenic system. The cryogenic system schematic is shown in the Fig. 3.3.8.

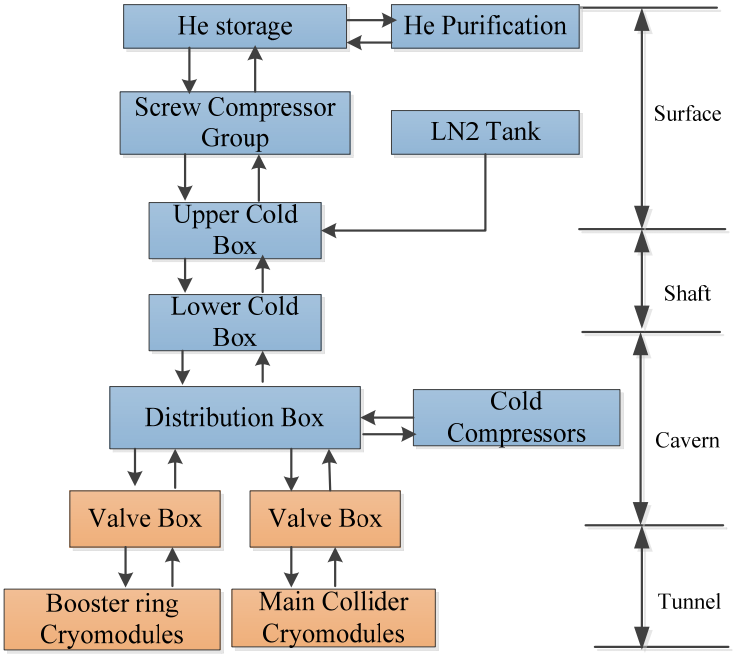

Figure 3.3.7: General architecture of the CEPC cryogenic system

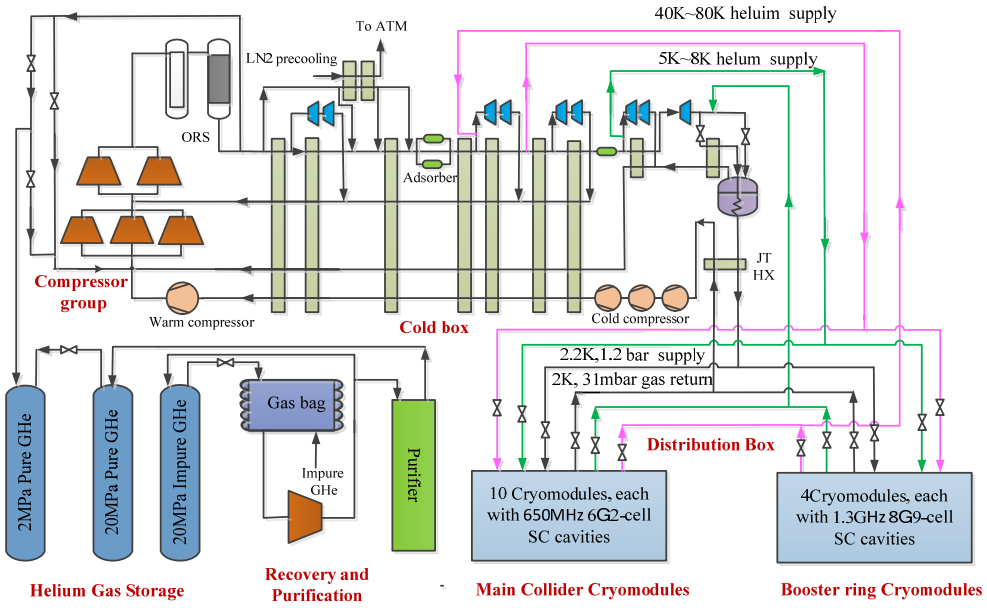

Figure 3.3.8: General schematic of the CEPC cryogenic system

3.3.6 References

1. ILC Technical Design Report: Volume 3, Part II, p.54
2. P. Lebrun. "Large cryogenic helium refrigeration system for the LHC." In Proceedings of the 3rdInternational Conference on Cryogenics & Refrigeration, ICCR2003, pages 11-13. 2003.
3. LHC design report, volume 1, chapter 11, cryogenic system
4. ILC Technical Design Report, VOLUMN III, PART II, P54
5. XFEL TDR, p514
6. Lebrun, P. Cryogenic refrigeration for the LHC (2009). http://www-fusion-magnetique.cea.fr/matefu/school_2/Tuesday/lebrun-LHCcryogenicrefrigeration.pdf.

3.4 Magnet

There is no major change in the design of main dipoles and quadrupoles from the Pre-CDR. In this report, we present the design of sextupole and Interaction Region (IR) superconducting magnets.

3.4.1 Sextupole Magnet

There are two types of sextupole magnets in the CEPC Main Ring, with the same aperture and cross section but different magnetic lengths. Like the conventional magnets for other accelerators, the cores of the sextupole magnets are made from 1.5 mm thick low carbon steel laminations. To reduce the cost of the magnet, the coils will be wound with hollow aluminum. A 2D model of the sextupole is shown in Figure 3.4.1. By optimizing the pole face shape, all the high harmonic errors can be reduced to less than 5.0×10^{-4}.

The magnets are composed of six parts; three of them are welded together to form the upper and lower halves, which are then bolted together. This makes vacuum chamber

installation convenient. The main parameters of the two type of sextupole magnets are listed in Table 3.4.1.

Table 3.4.1: The main parameters of the sextupole magnets for the CEPC collider

	SD	SF
Quantity	992	992
Magnetic Length (mm)	700	400
Strength of sextupole field (T/m^2)	180	180
Aperture diameter(mm)	120	120
Good field region, GFR radius (mm)	100	100
Harmonic field errors across GFR	0.10%	0.10%
Excitation amp-turns（At）	5156.620	5156.620
Size of conductor（mm）	20*10D5	20*10D5
Area of conductor（mm^2)	130.00	130
Coils turns on each pole	16	16
Current（A）	322.29	322.29
Current density（A/mm^2)	2.48	2.48
Ampere factor	1.02	1.02
Average turn length (mm)	1792.2	1174.2
Total conductor length in each coil (m)	28.68	18.79
Weight of conductor (kg)	60.43	39.60
Resistance (Ohm）	0.03745	0.02454
Voltage drop on resistance (V)	12.07	7.91
Power loss (kW)	3.890	2.549
Inductance (H)	0.01480	0.00854
Width/Height of iron core (mm)	520	520
Length of iron core (mm)	670	370
Weight of iron core (kg)	586.85	300
Total weight of each magnet (ton)	0.680	0.357
Number of parallel circuits	6	6
Water pressure drop (kg/cm^2)	6	6
Inner diameter of cooling water pipe (mm)	5	5
Length of each parallel circuit (m)	31.54	20.67
Velocity of water flow (m/s)	2.53	3.22
Water flow（l/s）	0.2982	0.3797
Temperature rise (deg)	3.11	1.60

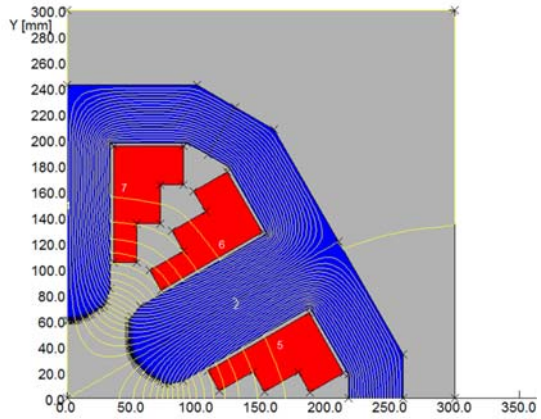

Fig. 3.4.1: 3D model of the sextupole magnet

3.4.2 Superconducting Magnet in the Interaction Region

3.4.2.1 Superconducting Quadrupole Magnet

3.4.2.1.1 Overall Design Consideration

Compact high gradient quadrupole magnets are needed in interaction region of the CEPC partial double ring/ double ring. The requirements of the QD0 superconducting quadrupole magnet are listed in Table 3.4.2.

Table 3.4.2: requirements of CEPC Interaction Region QD0 quadrupole magnet

Field gradient (T/m)	Magnetic length (m)	Field harmonics	Coil inner radius (mm)
200	1.46	$B_n/B_2<5.0\times10^{-4}$ @r=8mm (each aperture)	12.5

The final focus QD0 is a double aperture superconducting magnet. Its field gradient is 200T/m, which is the highest attained in existing electron machines. The L* in beam optics is 1.5m, and the crossing angle between the two beam lines of QD0 is 30mrad. The minimum distance between two aperture center lines is only 45mm, and the coil inner radius is 12.5mm. So a very tight radial space is available for QD0. Serpentine winding coil using direct winding technology is selected for its high efficiency and high compactness.

Serpentine coil is a novel coil pattern developed at BNL for direct winding of superconducting magnets. It allows winding a coil layer of an arbitrary multipolarity on a support tube in one continuous winding process and greatly simplifies the magnet design and production. All the pole coils in one layer is wound once. Figure 3.4.2 shows an example planar view of a serpentine quadrupole coil.

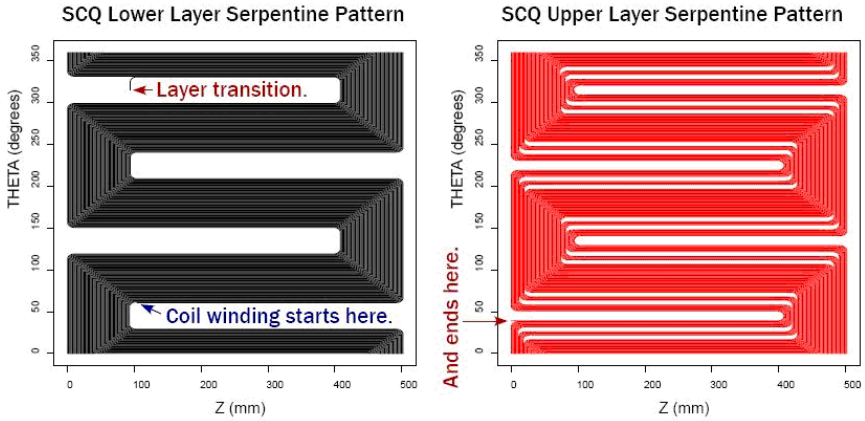

Figure 3.4.2: Planar view of serpentine quadrupole coil

The QD0 magnet is fully inside the field of the detector magnet with a central field of 3.5T. To minimize the effect of the longitudinal detector solenoid field on the accelerator beam, a compensating solenoid before QD0 and a screening solenoid outside QD0 are needed. Their magnetic field directions are opposite to the detector solenoid. Total integral longitudinal field generated by the detector solenoid and anti-solenoid coils is zero.

3.4.2.1.2 2D Field Calculation

The QD0 magnet is an iron-free small-aperture long magnet. Its coils will be made of 0.5mm round NbTi-Cu conductor using direct winding technology. Eight serpentine coil layers are used for the QD0 coil. 2D magnetic field calculation is performed using OPERA from Cobham Technical Services.

First, one aperture of the QD0 magnet is included, and only one quarter is modelled. The magnetic flux lines and magnetic flux density distribution are shown in Figs. 3.4.3 and 3.4.4, respectively. After optimization, the field quality in each aperture is very good. The whole coil cross section of single aperture is shown in Fig. 3.4.5.

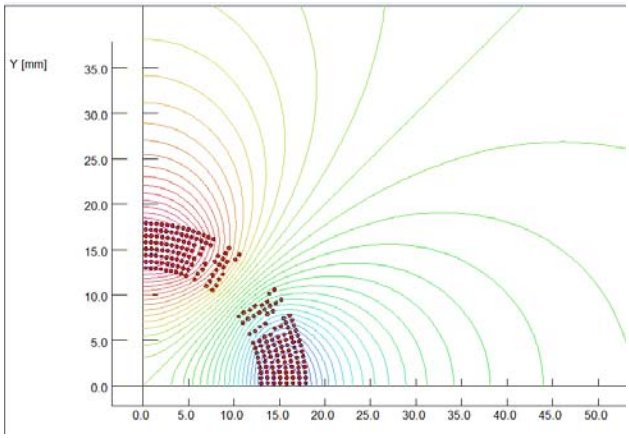

Figure 3.4.3: 2D flux lines (One quarter cross section)

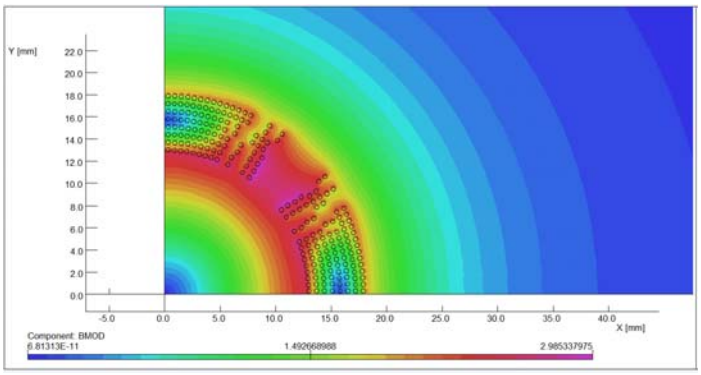

Figure 3.4.4: Magnetic flux density distribution

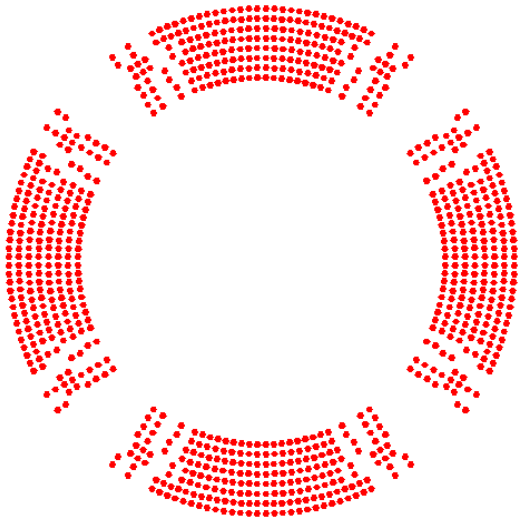

Figure 3.4.5: Coil layout (single aperture)

The calculated relative multipole field components are listed in Table 3.4.3.

Table 3.4.3: 2D field harmonics （unit, 1×10^{-4}）

n	B_n/B_2@R=8mm
2	10000
6	-1.5
10	-0.7
14	-0.96

The field in one aperture is affected due to the field generated by the coil in another aperture. Field cross talk of the two apertures is modelled and studied in OPERA-2D. Figure 3.4.6 shows an example of flux lines in the two aperture coils.

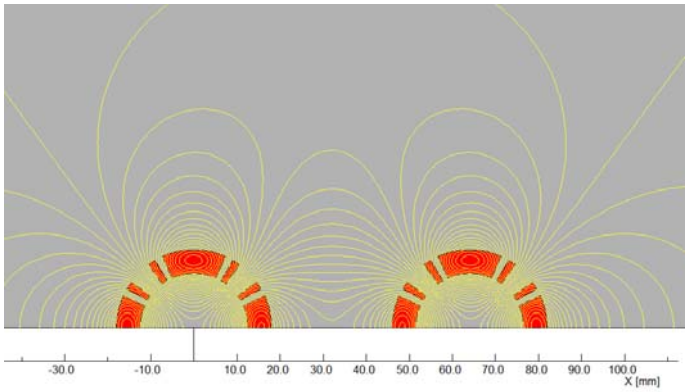

Figure 3.4.6: Flux lines of two aperture coils

Multipole field in one aperture as a function of aperture central distance is presented in Fig. 3.4.7 (unit, 1×10^{-4})

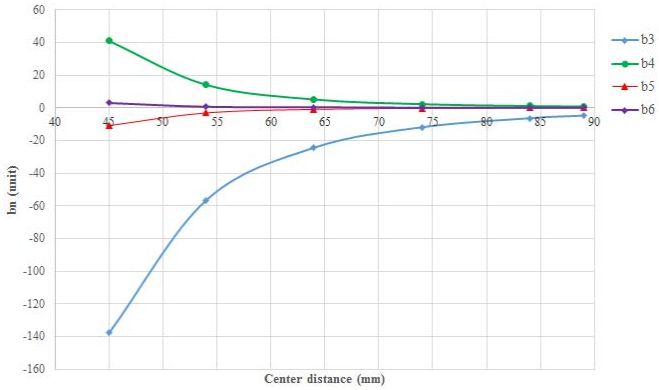

Figure 3.4.7: Multipole field in each aperture as a result of field cross-talk

Since the small distance between the two QD0 apertures, the field cross talk is serious. The most serious multipole field is the sextupole field. One layer of shield coil needs to be introduced outside the quadrupole coil to improve the field quality.

3.4.2.1.3 3D Field Calculation

QD0 coils are modelled in OPERA-3D, and the multipole fields induced by the field cross talk of the two apertures are obtained. Since the coil is very long with a small bore diameter, only the straight coil parts are included in the calculation.

Figure 3.4.8: OPERA-3D model of the QD0 coil

The calculated multipole field contents in one aperture are listed in Table 3.4.4.

Table 3.4.4: 3D field harmonics （unit, 1×10^{-4}）

n	B_n/B_2@R=8mm
2	10000.0
3	35.89715
4	8.803811
5	1.988995
6	-1.09837
7	0.089753
8	0.017058
9	4.31E-03
10	-0.66945
11	-2.4E-04
12	5.36E-04

It is shown that the sextupole and octupole field components in the aperture are very large.

3.4.2.1.4 Shield Coil Design

One layer of the shield coil is placed just outside the quadrupole coil to improve the field quality. The shield coil is not symmetric within each aperture, but the shield coils for two apertures are symmetric. After optimization, the shield coil in the left aperture is shown in Fig. 3.4.9, and the multipole field components in the left aperture with a shield coil is listed in Table 3.4.5.

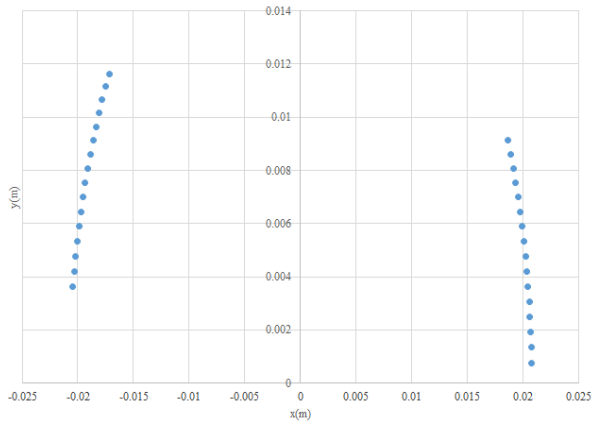

Figure 3.4.9: Shield coil in one aperture (half)

Table 3.4.5: 3D field harmonics in one aperture with shield coil （unit, 1×10^{-4}）

N	B_n/B_2@R=8mm
2	10000.0
3	0.134246
4	2.654574
5	1.896048
6	-2.12393
7	0.542855
8	-0.0706
9	0.073393
10	-0.67047
11	7.41E-03
12	9.57E-04

It can be seen that the calculated field quality in the aperture with a shield coil is very good.

3.4.2.1.5 Anti-Solenoid Design

The screening solenoid produces a field equal and opposite to the detector solenoid and screens the QD0 from the detector solenoid field. The compensating solenoid locates in front of the screening solenoid, and has a field higher than that of the detector solenoid, so the field integral seen by the beam from the IP point to the end of compensating solenoid is zero. The schematic layout of the Interaction Region is shown in Fig. 3.4.10.

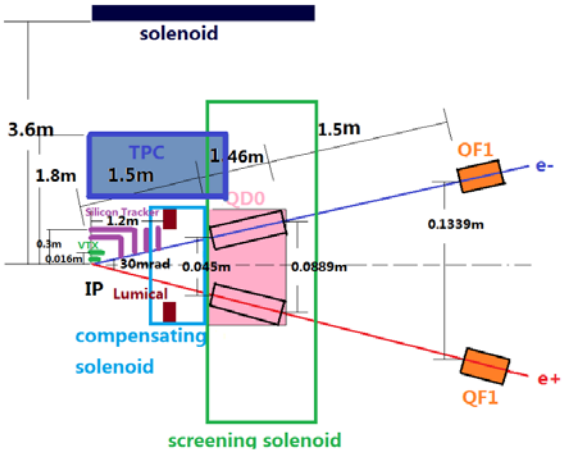

Figure 3.4.10: Layout of the CEPC Interaction Region

The central field of the screening solenoid (at the same location of QD0) is 3.3T, which is equal to the field of the Detector magnet. Its magnetic length is also the same as QD0. The longitudinal field inside the quadrupole bore is nearly zero.

For the compensating solenoid, there are different options which differ in the magnetic length and the field strength. Because of the limited space available in the beam direction in the interaction region, Nb_3Sn is chosen for the compensating solenoid with a central field of 13T and magnetic length of 0.4m.

Magnetic field calculations are performed using an axial-symmetric model in OPERA-2D. Figures 3.4.11 and 3.4.12 show the flux lines and field distribution of compensating solenoid, respectively.

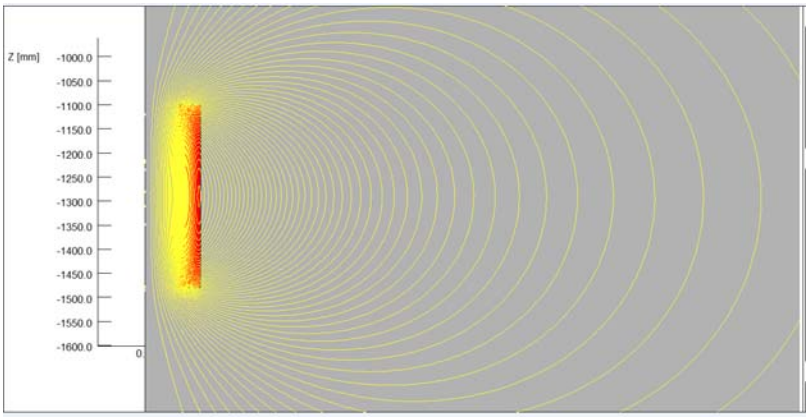

Figure 3.4.11: Flux lines of compensating solenoid

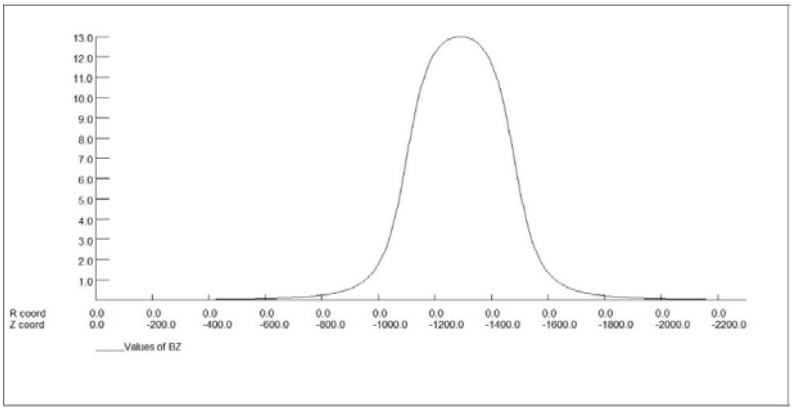

Figure 3.4.12: Field distribution of compensating solenoid

To reduce the magnet size, energy and cost, the screening solenoid is divided into 3 sections, with different inner coil diameters. Figs. 3.4.13 and 3.4.14 show the model and Bmod distribution of the screening solenoid, respectively.

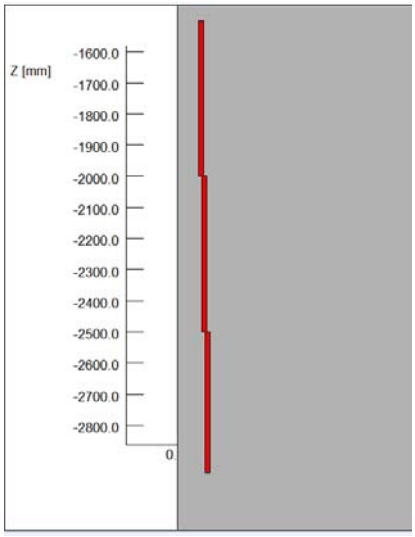

Figure 3.4.13: Model of the screening solenoid

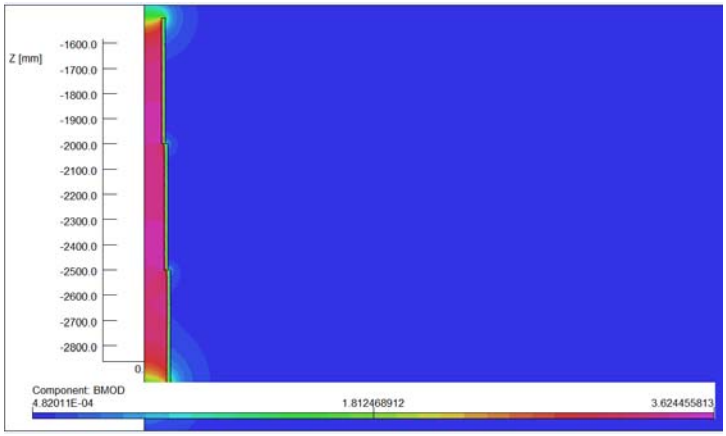

Figure 3.4.14: Bmod distribution of the screening solenoid

3.4.2.1.6 Design Parameters, Force and Magnet Layout

Design parameters, force of QD0 and the anti-solenoid are listed in Tables 3.4.6 and 3.4.7.

Table 3.4.6: Main design parameters of CEPC interaction region quadrupole magnet

Magnet name	QD0
Field gradient (T/m)	200
Magnetic length (m)	1.46
Coil turns per pole	110
Excitation current (A)	340
Shield coil turns per pole	32
Shield coil current (A)	130
Coil layers	8
Conductor size (mm)	NbTi-Cu Conductor, ∅ 0.5mm
Stored energy (KJ)	6.7
Inductance (H)	0.12
Peak field in coil (T)	3
Coil inner diameter (mm)	25
Coil out diameter (mm)	44
X direction Lorentz force/octant (N)	29770
Y direction Lorentz force/octant (N)	-58301

Table 3.4.7: Main design parameters of CEPC interaction region anti-solenoids

Magnet name	Compensating solenoid	Screening solenoid
Central field (T)	13	3.3
Magnetic length (m)	0.4	1.46
Conductor Type	Nb_3Sn, 4×2mm	NbTi-Cu, 4×2mm
Coil layers	23	8
Coil turns	2300	2600
Excitation current (kA)	1.9	1.5
Stored energy (KJ)	582	143
Inductance (H)	0.32	0.13
Peak field in coil (T)	13.2	3.6
Coil inner diameter (mm)	140	140
Coil outer diameter (mm)	230	210
Total radial Lorentz force (N)	12324795	3243373
Cryostat diameter (mm)	400	

The magnet layout of QD0 including the quadrupole coil (inner red), screening solenoid and compensating solenoid (left) is shown in Fig. 3.4.15.

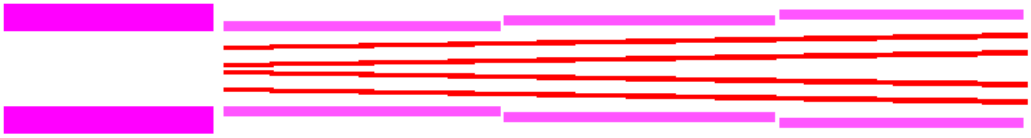

Figure 3.4.15: Layout of QD0

3.4.2.2 Superconducting Sextupole Magnet

3.4.2.2.1 Overall Design Consideration

In addition to the final focus magnet QD0, a high strength superconducting sextupole magnet is also needed. Its requirements are listed in Table 3.4.8.

Table 3.4.8: Requirements of CEPC Interaction Region quadrupole magnet

Strength (T/m^2)	Magnetic length (m)	Field harmonics	Coil inner radius (mm)
12800	0.3	$B_n/B_3<5.0\times10^{-3}$ @r=12mm	18

The superconducting sextupole magnet is also iron-free. Since the field in the sextupole magnet is not very high, serpentine coil using direct winding technology is also used. The conductor of sextupole coil is the same as in QD0.

3.4.2.2.2 2D Calculation

The coils of the superconducting sextupole magnet will be made of 0.5mm round NbTi-Cu conductor using direct winding technology. There are a total of eight serpentine coil layers. 2D magnetic field calculations are performed using OPERA. After optimization, the conductor arrangement of the sextupole coil is obtained.

Only half of the sextupole magnet is modelled, and magnetic flux lines and magnetic flux density distribution are show in Figs. 3.4.16 and 3.4.17, respectively.

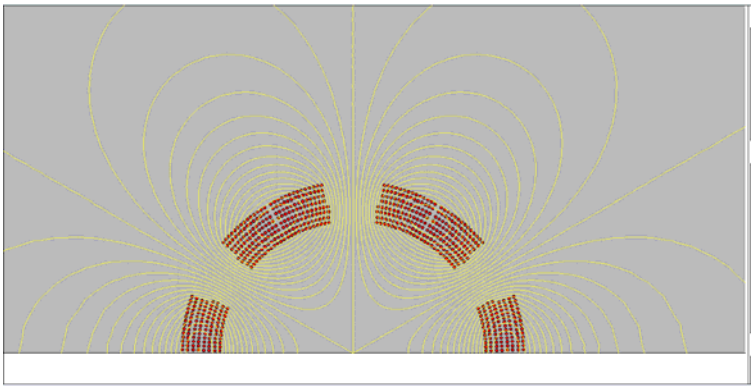

Figure 3.4.16: 2D flux lines (half cross section)

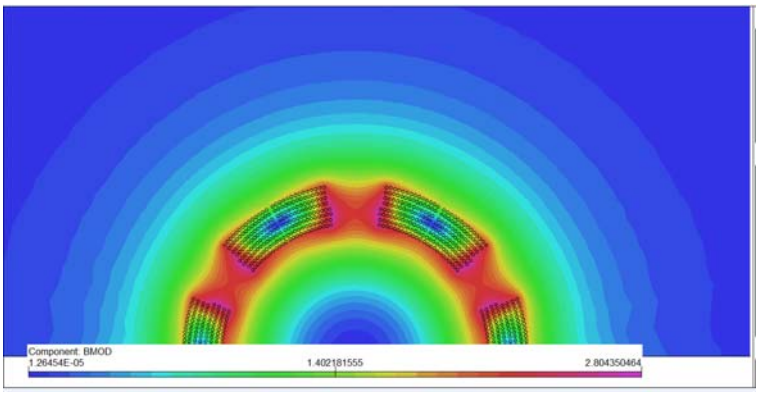

Figure 3.4.17: Magnetic flux density distribution

The calculated relative multipole field contents are listed in Table 3.4.9.

Table 3.4.9: 2D field harmonics （unit, 1×10^{-4}）

n	B_n/B_3@R=12mm
3	10000
9	-21.3
15	-4.2
21	-0.2

3.4.2.2.3 3D Calculation

The sextupole coil is modelled in OPERA-3D. Since the coil is long with respect to the small bore, only the straight parts are included in the calculation. The 3D Opera model and magnetic field distribution along the z axis are show in Figs. 3.4.18 and 3.4.19, respectively.

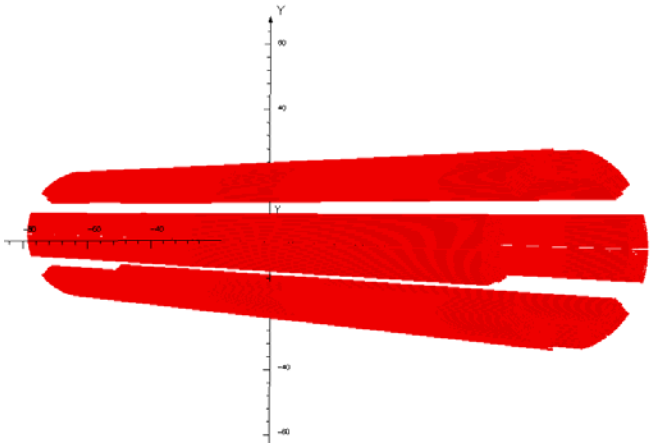

Figure 3.4.18: 3D OPERA model

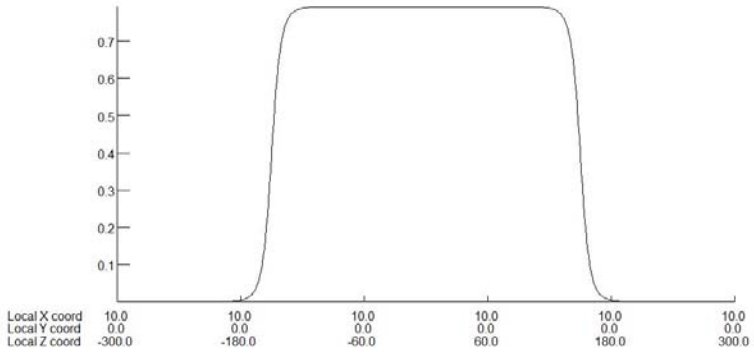

Figure 3.4.19: By distribution along z

In the 3D calculation, a field strength of 12800T/m^2 is achieved, and the harmonic field content is the same as in the 2D calculation.

3.4.2.2.4 Design Parameters, Force and Magnet Layout

Design parameters and force of the superconducting sextupole magnet are listed in Table 3.4.10.

Table 3.4.10: Main design parameters of CEPC interaction region sextupole magnet

Magnet name	Sextupole magnet
Field strength (T/m^2)	12800
Magnetic length (m)	0.3
Coil turns per pole	104
Excitation current (A)	300
Coil layers	8
Conductor size (mm)	NbTi-Cu Conductor, ∅ 0.5mm
Stored energy (J)	750
Inductance (H)	0.017
Peak field in coil (T)	2.9
Coil inner diameter (mm)	36
Coil out diameter (mm)	50
X direction Lorentz force (1/12) (N)	2954
Y direction Lorentz force (1/12) (N)	-8698
Cryostat diameter (mm)	200

The sextupole coil layout is shown in Fig. 3.4.20.

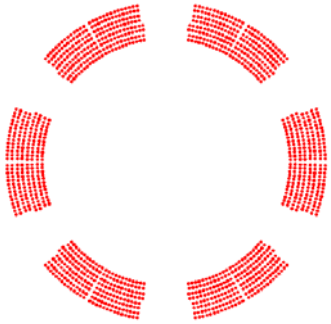

Figure 3.4.20: Coil layout of the sextupole magnet

3.4.3 References

1. LEP design report, CERN-LEP-84-01, CERN, Geneva, 1984
2. K. Tsuchiya, et al., "Superconducting Magnets for the Interaction Region of KEKB," *IEEE TRANSACTIONS ON APPLIED SUPERCONDUCIIVITY*, 9 (2), pp: 1045-1048, June 1999.
3. OPERA, Vector Fields Software, Cobham Technical Services, http://www.vectorfields.com
4. M. Koratzinos, et al., THE FCC-ee INTERACTION REGION MAGNET DESIGN, *Proceedings of IPAC2016*, Busan, Korea, pp: 3824-3827
5. H. Yamaoka, et al., SOLENOID FIELD CALCULATION OF THE SUPERKEKB INTERACTION REGION, *Proceedings of IPAC2012*, New Orleans, Louisiana, USA, pp: 3548-3550
6. Xudong Wang, et al., Design and Performance Test of a Superconducting Compensation Solenoid for SuperKEKB, *IEEE TRANSACTIONS ON APPLIED SUPERCONDUCTIVITY*, 26 (4), pp: 4102205 (1-5), June 2016
7. Brett Parker, et al., BNL Direct Wind Superconducting Magnets, *IEEE TRANSACTIONS ON APPLIED SUPERCONDUCTIVITY*, 22 (3), pp: 4101604 (1-4), June 2012

4 CEPC – Injectors

4.1 Booster

4.1.1 Design Goals

The layout of CEPC Booster is show in Figure 4.1.1. There are 8 arcs and 8 straight sections, and the total length is 63.8 km. The RF cavities are distributed in each straight section. The lattice chosen uses standard FODO cells with 90 degrees phase advance in both transverse planes. This gives us smaller emittance and a clear phase relationship between sextupoles. The design goals are:

1. Emittance of CEPCB at 120 GeV about 3.5×10^{-9} m-rad.
2. Energy acceptance of 1% to provide an adequate quantum life time.
3. Dynamic aperture better than 6 sigma (normalized emittance, which is determined by the beam from the linac) for both on-momentum and off-momentum (1%) particles.

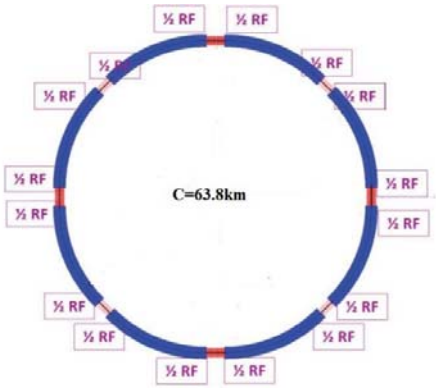

Figure 4.1.1: Layout of the CEPC Booster.

4.1.2 Wiggler Bend Scheme

To make the main dipole stronger to alleviate some of the problems of low magnet field, we split the 30.4 m long bend into 8 pieces. Adjacent dipole pieces have different magnet polarities but the integral field strength of the dipole is the same as the normal dipole. We call this "wiggler scheme" as is shown in Figure 4.1.2. The orbit off-set (the red curve in the figure) becames smaller as the beam energy is ramped up until the negative dipole changes it's field direction and all the dipoles become normal bending magnet at 120 GeV.

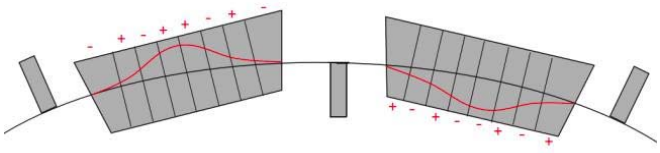

Figure 4.1.2: Wiggler orbit in a FODO cell.

Table 4.1.3: Booster parameters at 6 GeV for the wiggler scheme.

6GeV	unit	value
offset in bend	cm	1.20
Momentum compaction		2.02E-5
Strength of dipole	Gs	-129/180
NB/beam		50
Beam current/beam	mA	7.5E-1
Bunch population		2.00E10
RF voltage	GV	2.10E-1
RF frequency	GHz	1.3
Synchrotron oscillation		2.10E-1
Energy acceptance RF	%	5.93
SR loss/turn	GeV	5.42E-4
energy spread	%	1.47E-2
Horizontal emittance	m*rad	6.38E-11

Table 4.1.2: Booster parameters at 120 GeV for the wiggler scheme.

120GeV	unit	value
offset in bend	cm	0
Momentum compaction		2.38E-5
Strength of dipole	Gs	516.71
NB/beam		50
Beam current/beam	mA	7.5E-1
Bunch population		2.00E10
RF voltage	GV	3.50
RF frequency	GHz	1.3
Synchrotron oscillation		1.40E-1
Energy acceptance RF	%	2.46
SR loss/turn	GeV	2.35
energy spread	%	1.20E-1
Horizontal emittance	m-rad	3.62E-9

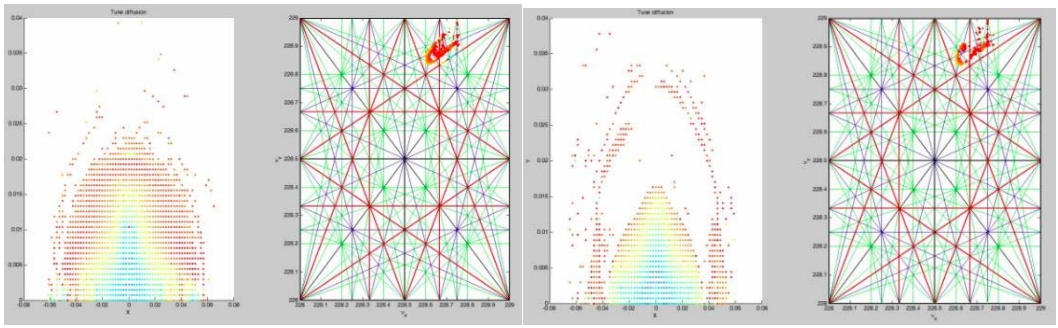

Figure 4.1.3: Dynamic aperture for on-momentum(left) and 1% off-momentum(right) particles.

4.1.3 Normal Bend Scheme

In the normal bend scheme, the bend strength is very low, about 30 Gs, at the beginning of the ramp from 6 GeV to 120 GeV. The earth magnetic field is about 0.5 Gs. This is like a 2% error added to the dipole field. So the earth magnetic field must be shielded or corrected.

Because of the earth field errors there is no stable closed orbit and first turn orbit correction is needed. To correct the first turn, we follow the first turn particles piece by piece and correct them as we go around the ring. As Figure 4.1.4 shows, we divide the whole ring into 8 pieces and correct the orbit piece by piece. The fourth plot in Figure 4.1.4 shows the first turn orbit after the whole ring correction. After the first turn orbit correction, the closed orbit can be obtained as Figure 4.1.5 shows, and then we can implement closed orbit correction. After all the corrections, the orbit distortions can be limited to 10 microns. The right-hand plot in Figure 4.1.5 shows the corrected orbit.

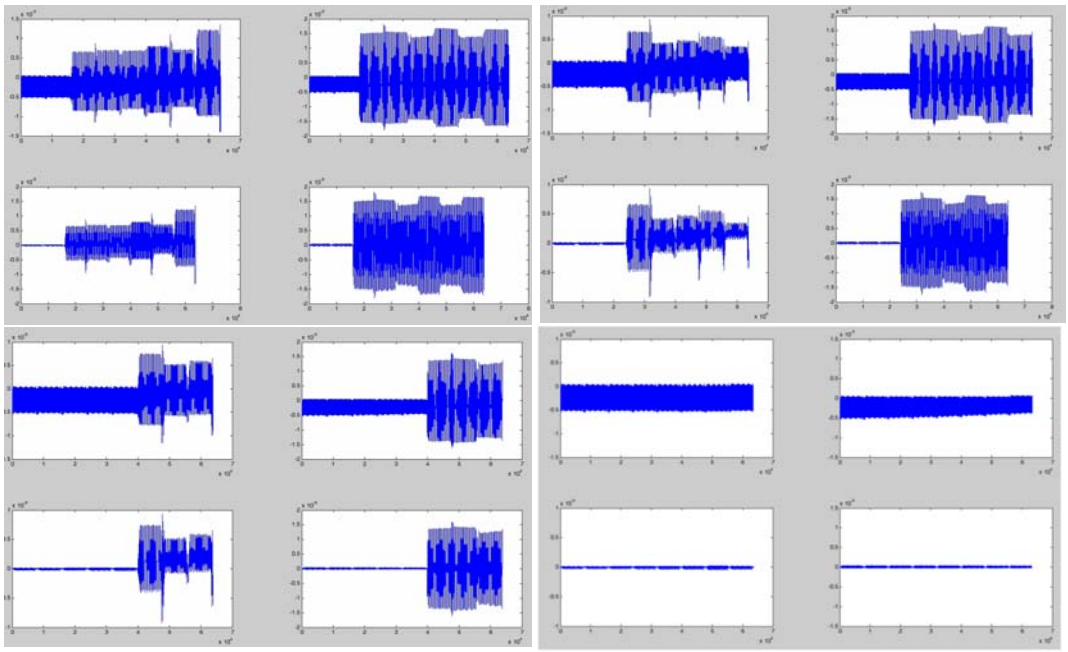

Figure 4.1.4: First turn orbit correction in the Booster.

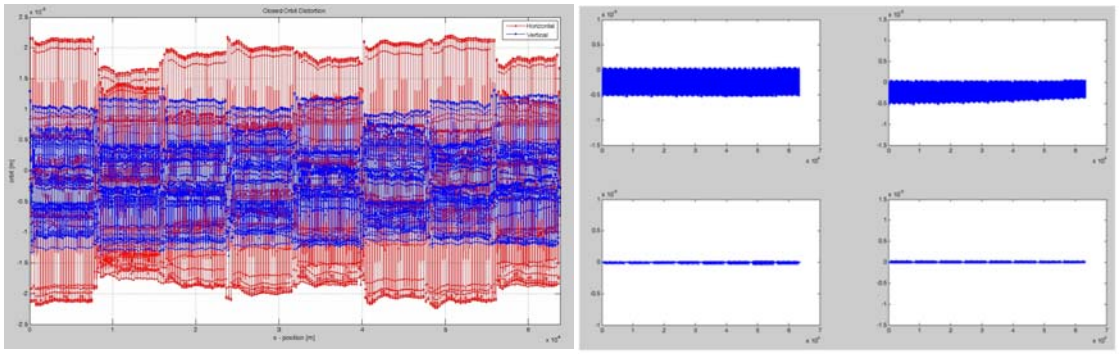

Figure 4.1.5: Closed orbit after first turn orbit corrections (left) and subsequently after closed orbit correction (right)

Table 4.1.3: Booster parameters at 6 GeV for he normal bend scheme.

6GeV	unit	value
offset in bend	cm	0
Momentum compaction		1.91E-5
Strength of dipole	Gs	25.80
NB/beam		50
Beam current/beam	mA	7.5E-1
Bunch population		2.00E10
RF voltage	GV	2.10E-1
RF frequency	GHz	1.3
Synchrotron oscillation		2.10E-1
Energy acceptance RF	%	4.99
SR loss/turn	GeV	1.47E-4
energy spread	%	7.47E-2
Horizontal emittance	m-rad	9.10E-12

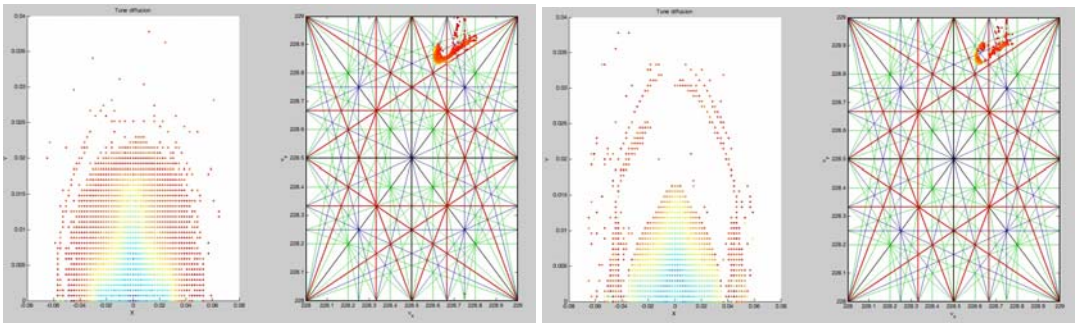

Figure 4.1.6: Dynamic aperture for on-momentum(left) and 1% off-momentum(right) particles

4.1.4 Summary

In this section, two possible implementations for the Booster have been proposed. The low field problem is solved by the wiggler bend scheme and the method for correcting the earth magnetic field is shown in the normal bend scheme.

Normal scheme:

With the earth field error, orbit correction, cavities on and tune 0.61/0.88, the x direction dynamic aperture is 8.6 sigma, and in the y direction the dynamic aperture is 10.1 sigma at dp/p=0% for the injected beam.

With the earth field error, orbit correction, cavities on and tune 0.61/0.88, the x direction dynamic aperture is 6.7 sigma, and in the y direction the dynamic aperture is 6.5 sigma at dp/p=1% for the injected beam.

Wiggler scheme:

With the earth field error, cavities on and tune 0.61/0.88, the x direction dynamic aperture is 9.2 sigma, and in the y direction the dynamic aperture is 9.6 sigma at dp/p=0% for the injected beam.

With the earth field error, cavities on and tune 0.61/0.88, the x direction dynamic aperture is 6.6 sigma, and in the y direction the dynamic aperture is 6.4 sigma at dp/p=1% for the injected beam.

Both designs are reasonable and meet the design goals.

4.2 Source and Linac Introduction

The first element in the injector chain is a normal conducting S-band Linac with frequency 2856.75 MHz. It provides electrons and positrons at an energy up to 10 GeV. The main parameters are shown in Table 4.2.1. The repetition rate is 50 Hz and one bunch per pulse. The linac is comprised of both an electron linac and a positron linac. To achive a 3.2 nC per bunch positron beam, a 4 GeV primary electron beam with bunch charge 10 nC strikes a tungsten target. The large transverse emittance of the positron beam emerging from the target is transformed to match a pre-accelerating section with AMD flux concentrator. The captured positron beam will be pre-accelerated to 200 MeV and then

transported back to the beginning of mian linac. Considering the cycle time and to make the positron beam emittance small, a damping ring is necessary. The positron beam are accelerated up to 1.1 GeV with 20 S-band accelerating tubes without SLED and extacted to a damping ring. Then they are extacted and accelerated up to 10 GeV at the next pulse. The section form 200 MeV to 1.1 GeV is used by both electron beam and positron beams. The entire positron yield and return back time is longer than SLED, so this section can not use SLED. Thus the average gradient is 18 MV/m. For the high energy section from 1.1 GeV to 4 GeV and then up to 10 GeV the accelerating gradient is about 27 MV/m, perhaps can reach of as high as 30 MV/m. Since the linac accelerates both electrons and positrons, it has two operation modes: one is the high bunch charge mode with 10 nC per bunch and 4 GeV energy, and the other is the baseline mode with 3.2 nC per bunch and 10 GeV energy. The linac layout is shown in Figure 4.2..

Table 4.2.1: Main parameters of the CEPC linac.

Parameter	Symbol	Unit	Value
e^- /e^+ beam energy	E_{e^-}/E_{e^+}	GeV	10
Repetition rate	f	Hz	50
e^- /e^+ bunch population	N_{e^-}/N_{e^+}		2×10^{10}
	N_{e^-}/N_{e^+}	nC	3.2
Energy spread (e^- /e^+)	σ_E		$<1\times10^{-3}$
Emittance (e^- /e^+)		mm· mrad	<0.3
e^- beam energy on Target		GeV	4
e^- bunch charge on Target		nC	10

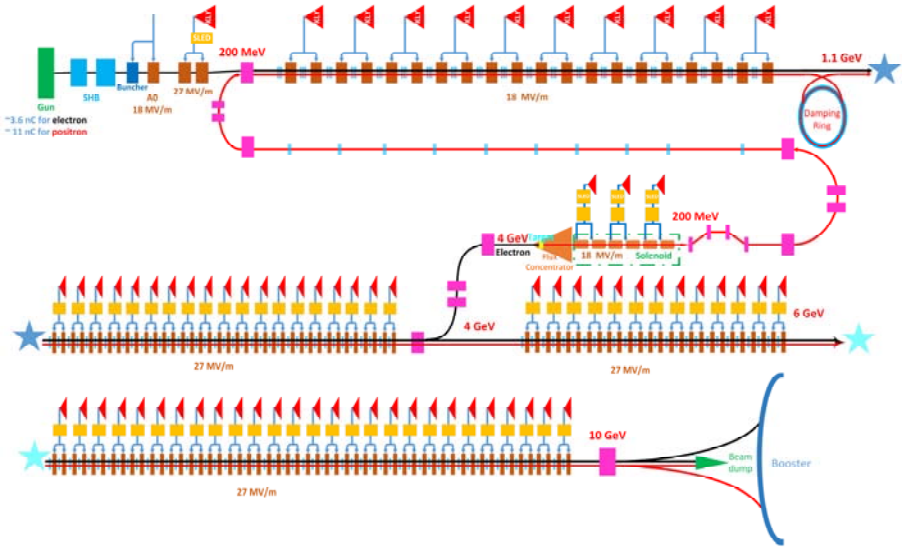

Figure 4.2.1: CEPC linac layout.

4.3 e^+ and e^- Sources

4.3.1 Electron Source

4.3.1.1 Source Design

To meet the design goal, a conventional thermionic electron gun is used. As is done in both BEPC-Ⅱ and KEKB, the electron gun would consist of a flat surface cathode-grid assembly, a focusing electrode and an anode. The widely used EIMAC-Y796 cathode-grid assembly, which has a cathode area of $2cm^2$, will be employed as its dispenser cathode can provide current as high as 12A with long lifetime. The EGUN code is used for the beam optics simulation. Based on the BEPC-Ⅱ electron gun design, the geometric optimization of the electron gun is determined by obtaining minimum emittance at the end port for voltage under 160kV and current of 10A. The electron trajectories are shown in Figure 4.3.1. Figure 4.3.2 shows the phase space of X & Y and Figure 4.3.3 shows the current density on cathode surface.

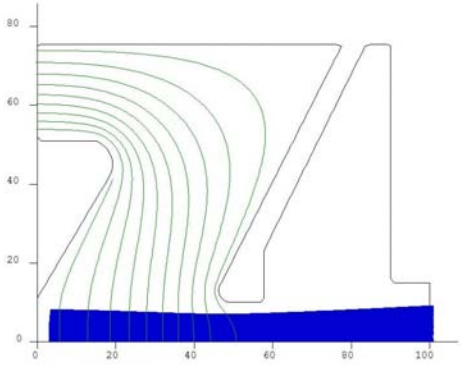

Figure 4.3.1: Beam trajectory in the injector electron gun.

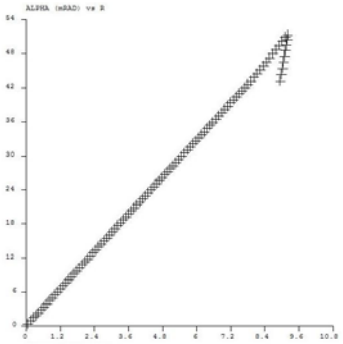

Figure 4.3.2: Phase plane at the exit port

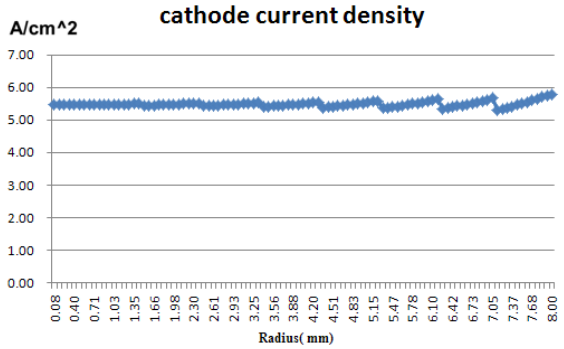

Figure 4.3.3: Current density on the cathode.

The beam trajectory is almost parallel in order to obtain low emittance. At the end port, which is 100mm from the cathode surface, the x and y emittance is 17.84π (mm·mrad). Meanwhile, EGUN predicts a beam perveance of 0.169 μP. Uniform current density on the cathode allows for a long lifetime. Further optimization is under way.

4.3.1.2 Pulser System

The electron gun of the injector linac is a triode gun. The pulser system includes a DC power supply, a control box and the pulser. The scheme is shown in Figure 4.3.4. The electron gun pulser system used in BEPC-II is a proven technique. The DC power supply varies from zero volts to 1 kV. The pulser stores and discharges energy with a switch. The control box controls the amplitude of the trigger pulse. It samples the trigger pulse and monitors the temperature of the connected structure, processes the trigger signal, and provides the interface between the optical and electrical signals. Table 4.3.1 shows the specifications of the electron gun pulser.

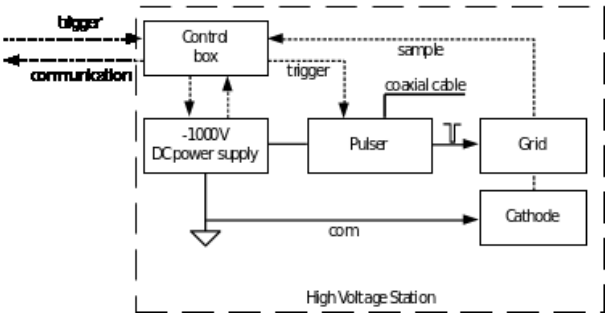

Figure 4.3.4: Pulser system schematic.

The pulser is critical device. The discharge switch is a series-stacked avalanche transistor. Coaxial cable is pulse forming line and energy storage device which is connected to the end of the switch. The pulse width is determined by the length of the coaxial cable which is matched to the pulse width of 1ns to 10ns. The polarity of the pulse is negative. Table 4.3.1 shows the specifications for the pulser system.

Table 4.3.1: Specifications for the pulser system.

Parameter	Unit	Valve
Pulse voltage	V	1000
Pulse width	ns	1-10
Rise time	ns	0.8
Polarity		Negative
Jitter	ps (RMS)	20
AC power supply	V	220 (-10%~+10%)

4.3.1.3 High Voltage System

The electron gun is a triode-type gun, which consists of an anode, cathode and a grid. The electron gun system consists of an electron gun body, a high voltage power supply, a high voltage deck, a pulser and a control unit. The gun should be able to operate in a 1 ns single beam pulse mode to generate the electron beam. The main parameters of the electron gun are shown in Table 4.3.2. The schematic diagram of the electron gun system is shown in Figure 4.3.5. The high voltage system is shown in Figure 4.3.6 .

Table 4.3.2: Main specifications of the electron gun.

Parameters	Value
Type	Triode
Maximum Beam Current(A)	10
Anode High Voltage(kV)	120~200
Filament voltage(V)	6~8
Filament current(A)	5~7.5
Grid bias voltage(V)	0~200
Pulse width	1ns
Pulse rate(pps)	100

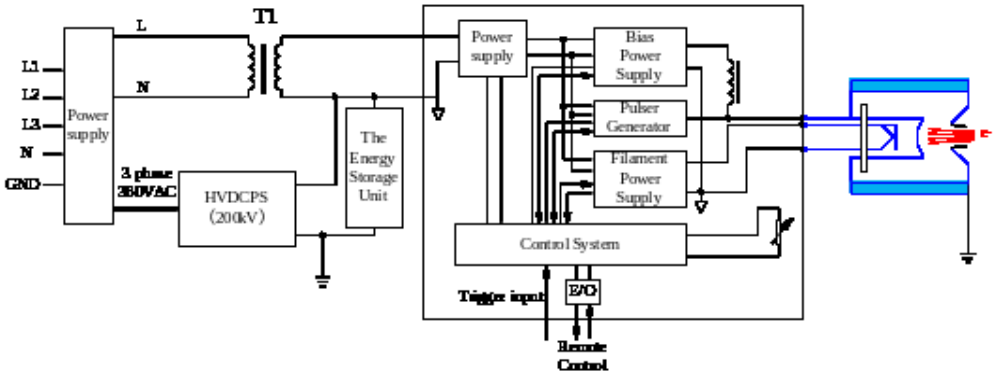

Figure 4.3.5: Schematic diagram of the electron gun system.

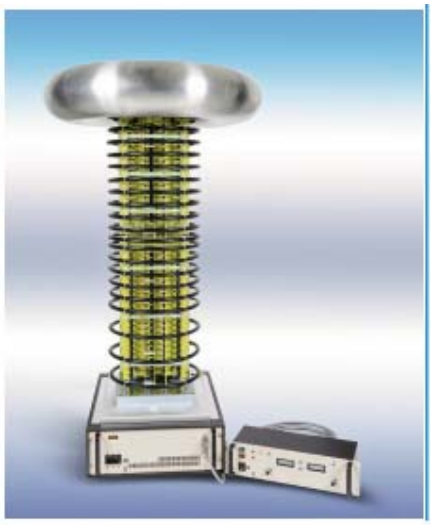

Figure 4.3.6: 200kV high voltage DC power supply.

4.3.2 Positron Source

Positrons are generated using a multi-GeV electron beam impinging on a high-Z, high density target. The positron yield per incident electron is approximately proportional to the electron energy so that the positron current is proportional to the incident power of electron beam. To achieve a 3.2 nC bunch charge positron beam, a 4 GeV primary electron with an intensity of 10 nC/bunch is required. The average beam power is 2 kW at a repetition rate of 50 Hz.

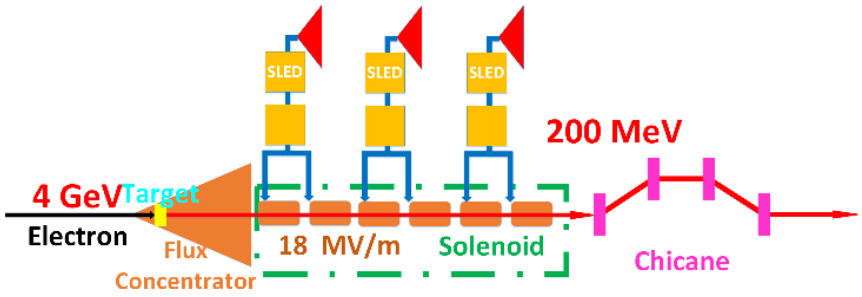

Figure: 4.3.7: Layout of the positron source and pre-accelerating section.

Figure: 4.3.7 is a schematic of the positron source and pre-accelerating section. A 4 GeV electron beam is extracted from the main Linac, and passes through an extraction transport line, and strikes a tungsten target. Emerging from the target is a wide spectrum of low energy electrons, positrons, and photons. The large transverse emittance of the positron beam emerging from the target is transformed to match the pre-accelerating section aperture with a pseudo-adiabatically changing solenoid field consisting of a 6-T pulsed field from a flux concentrator superimposed on a 0.5-T DC solenoid field.

Immediately following the target there are six 2-m length high-gradient constant-impedance S-band (2856.75 MHz) accelerating tubes with large aperture. In this section called the pre-accelerating section one klystron source supplies power for two accelerating tubes with gradient in 18 MV/m and the positrons are accelerated to 200 MeV. The pre-accelerating section uses a uniform solenoid for focusing. After the capture

section, a momentum selection chicane consists of four identical rectangular bending magnets and a collimator will be used to select positrons in the desired energy range. Table 4.3.3 shows the main parameters of the positron source.

Table 4.3.3: Main parameters of the positron source.

Positron source	
e^- beam energy on the target	4 GeV
e^- bunch charge on the target	10 nC
Target material	W
Target thickness	16 mm
Focus device (Flux Concentrator)	6 T
e^+ bunch charge after capture	3.2 nC
e^+ Energy after capture section	200 MeV

A simulation study on positron yield and target thickness has been done by using a G4beamline code. The initial electron beam energy is 4GeV and has a small beam size (rms:1 mm). The positron yield was optimized by scanning the target thickness. As shown in Figure 4.3.8, a thickness of 16 mm for the W material gives the highest positron yield.

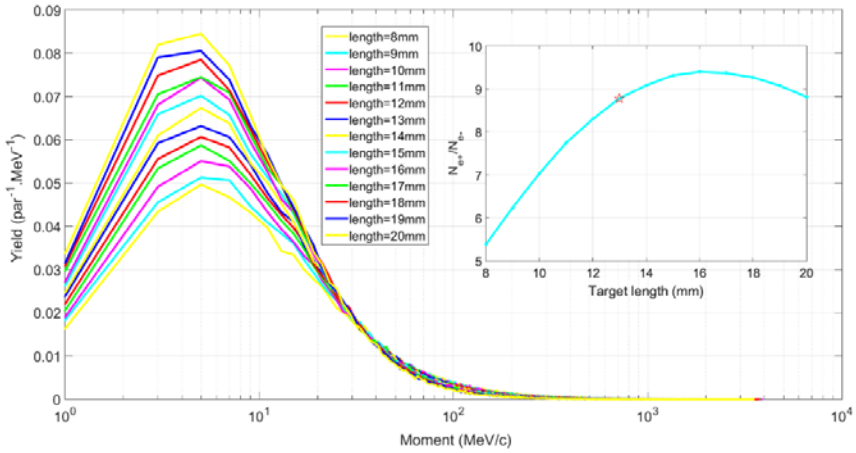

Figure 4.3.8: Target thickness optimization.

FLUKA code was used to calculate the energy deposition in the target. As shown in Figure 4.3.9, the energy deposition is 0.573 GeV/e^- in the case of 4 GeV electron beam energy with 1 mm beam size incident on a 16 mm W target. This means that the power deposition is about 1.14 kW. Considering target cooling we choose an aperture of 10 mm or 20 mm.

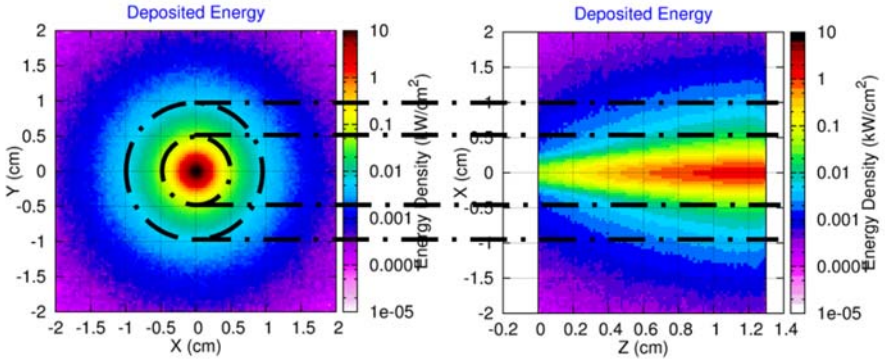

Figure 4.3.9: Energy deposition in the target.

The large transverse emittance of the positron beam emerging from the target is transformed to match the pre-accelerating section with an AMD flux concentrator in the capture section. Using the AMD we transform the beam from large divergence and small beam size to small divergence and large beam size as shown in Figure 4.3.10. Following this the positrons are easily accelerated to 200 MeV in the pre-accelerating section. The beam envelopes are shown in Figure 4.3.11. The normalized rms emittance is 3000 mm-mrad and the energy is 200 MeV at the exit of pre-accelerating seciton. The beam distributions are show in Figure 4.3.12.

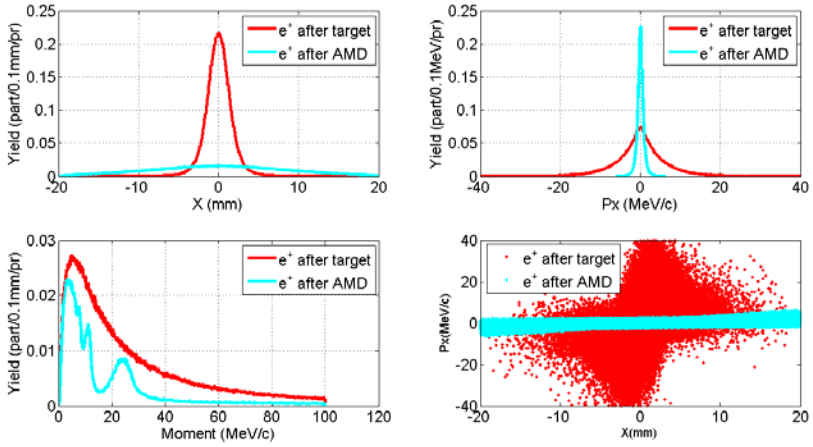

Figure 4.3.10: Beam transformation by the AMD section.

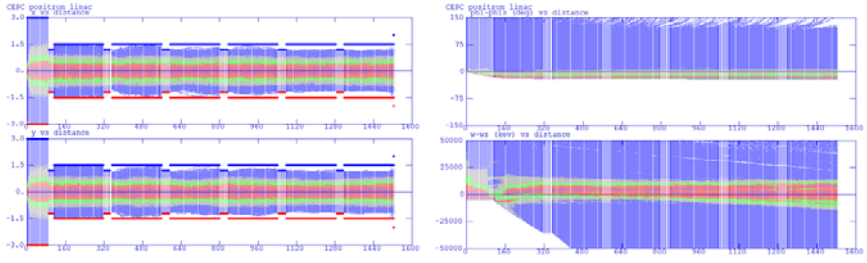

Figure 4.3.11: Beam envelope in the pre-accelerating section.

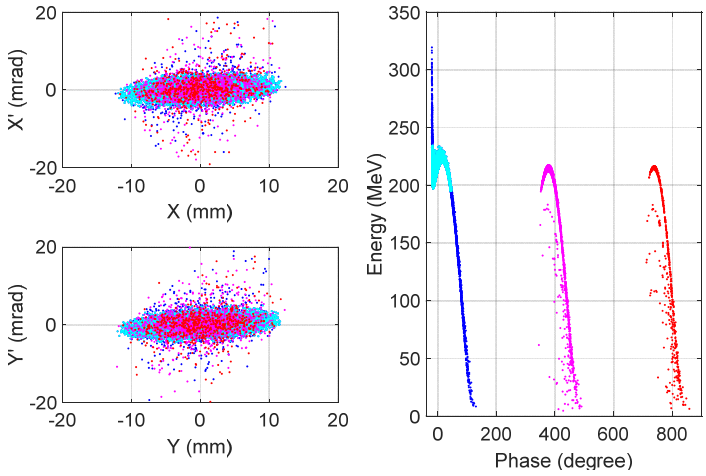

Figure 4.3.12: Beam distributions at the exit of the pre-accelerating section.

4.3.3 Positron Damping Ring and Bunch Compressor

The primary purpose of the damping ring (DR) is to reduce the transverse phase space of the positron beam to a suitably small value at the beginning of the linac and also to adjust the time structure of the positron beam for reinjection into the Linac. The principle of the damping ring is shown in Figure 4.3.14. The DR energy is 1.1 GeV and its circumference is 58.5 m. The DR has a racetrack shape and the arcs are 60 degree FODO cells.

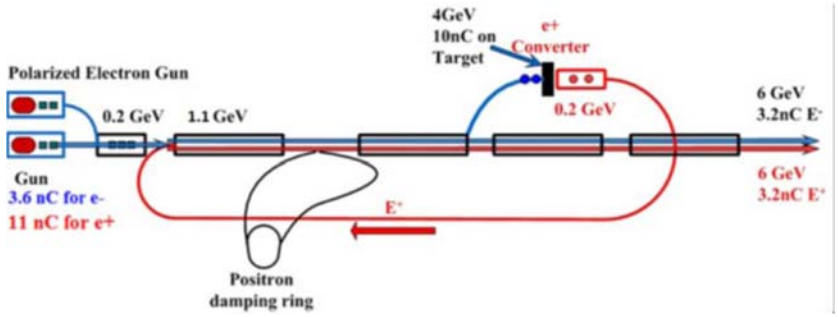

Figure 4.3.13: Sketch of the CEPC Linac

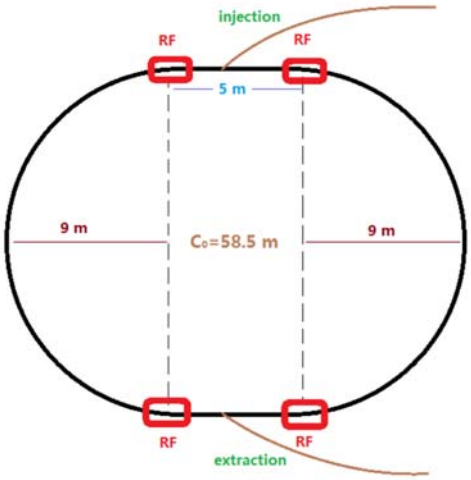

Figure 4.3.14: Sketch of the Damping Ring

Longitudinal bunch length control must be provided to minimize wake field effects in the Linac. Reducing the bunch length in the ring to the required value will need very high (~40 MV) RF voltage, so we add a bunch compressor system after the damping ring. The bunch length will be reduced about 4 times through the bunch compressor.

4.4 Linac

4.4.1 Beam Dynamics Design

4.4.1.1 Bunching System and Pre-Accelerating Section

The bunch charge of electrons and positrons is 3.2 nC, and two operation modes of the electron source are required. One is to provide a 3.6 nC bunch charge for electron injection, and the other is to provide an 11 nC bunch charge as the primary electron beam for positron production, where one assumes the transmission efficiency of the bunching system is 90%. The bunching system consists of two sub-harmonic bunching cavities operating at 142.8375 MHz and 571.35 MHz, an S-band buncher at 2856.75 MHz and a normal S-band accelerating tube at 2856.75 MHz, as shown in Fig. 4.4.1.

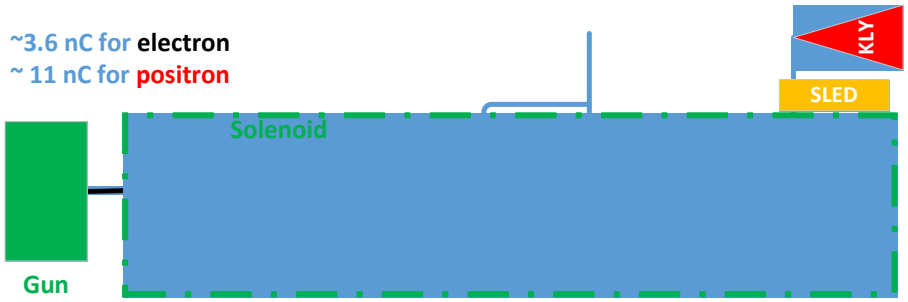

Figure 4.4.1: Layout of the bunching system and pre-accelerating section.

The two sub-harmonic pre-bunchers and the one S-band buncher act to velocity modulate the non-relativistic electron beam emerging from the gun, and compress the pulse before it passes into the linac. A beam pulse of 1.0 ns FWHM length from the gun is compressed into a single bunch of 10 ps (FWHM) by an RF bunching section. The main parameters of the sub-harmonic pre-bunchers and S-band buncher are shown in Table 4.4.1.

Table 4.4.1: The main parameters of the sub-harmonic pre-buncher and the S-band buncher.

First sub-harmonic pre-buncher		
Type		Re-entrant
Frequency	MHz	142.8375
Unloaded Q		8175
Shunt impedance	MΩ	1.4
Esurface, max/Egap, max		2.53
Second sub-harmonic pre-buncher		
Frequency	MHz	571.35
Unloaded Q		13000
Shunt impedance	MΩ	3.7
Esurface, max/Egap, max		2.44
S-Band Buncher		
Type		Constant impedance ,TW, 2π/3-mode
Frequency	MHz	2856.75
Operating temperature	^{o}C	40±0.1
Input and output VSWR		≤1.2
Bandwidth (VSWR ≤ 1.2)	MHz	≥4.0
Peak RF input power	MW	3
Phase velocity (Vp/c)/group velocity (Vg/c)		0.75 / 0.0119
Shunt impedance	MΩ/m	36
Unloaded Q		11000
RF attenuation parameter	Neper/m	0.228
Number of cavities		4＋2×0.5

After bunching the electron beams are accelerated to 200 MeV with two S-band accelerating tubes with gradient 27 MV/m. The focussing in the bunching system and the pre-accelerating section are solenoids as shown in Fig.4.4.2. The envelope in transverse and longitudinal planes are shown in Fig.4.4.3. The transmission efficiency is about 90%.

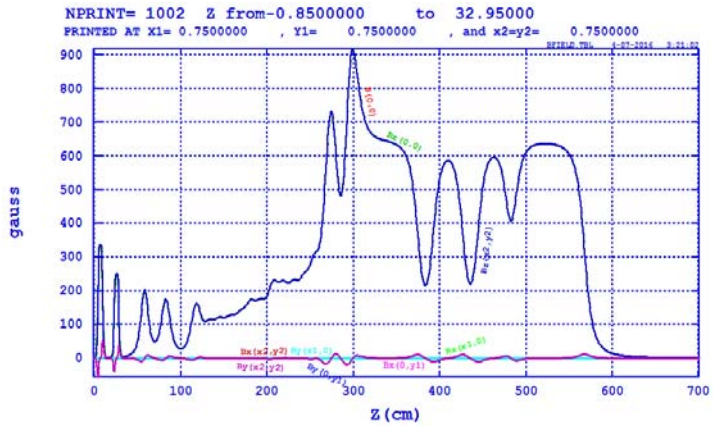

Figur4.4.2: Magnetic field in the bunching system and the pre-accelerating section.

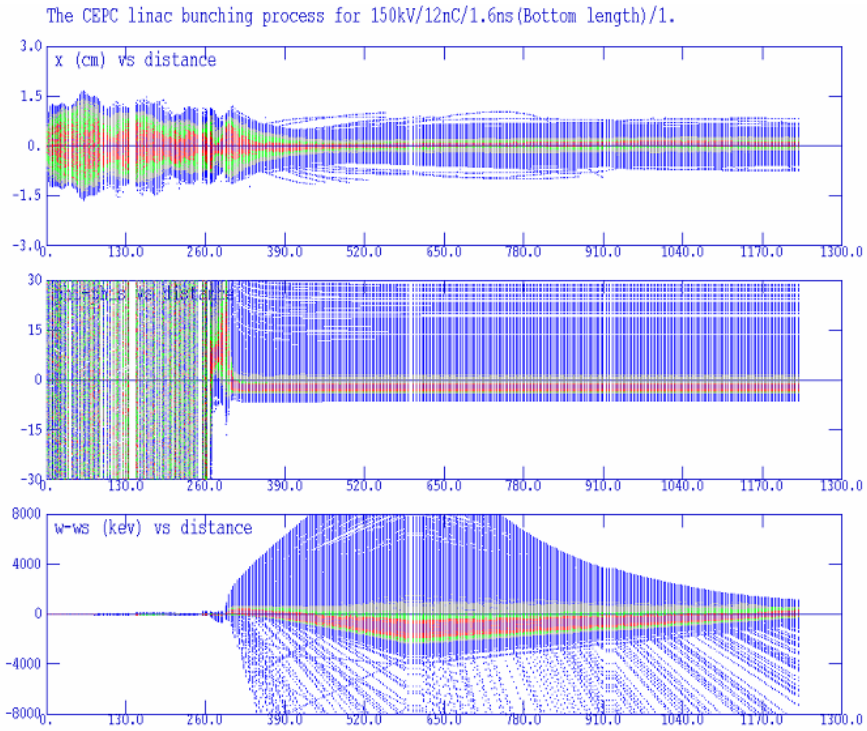

Figur4.4.3: The envelope in the bunching system and the pre-accelerating section.

4.4.1.2 First Accelerating Section of the Main Linac

Considering that the electron and positron beams share the first accelerating section of the main linac, the SLED cannot be used in this section and the acelerating tube gradient is 18 MV/m. In this section the electron beam and positron beam will be accelerated to 1.1 GeV. After that the positron beam will be delivered to the damping ring to await the next period and accelerated to 10 GeV. Because the positron beam emittance is very large, about 3,000 mm-mrad, the lattice should be designed carefully to reduce beam loss. For the front part the FODO structure is adopted and the larger aperture magnets are outside the accelerating tube. Each accelerating tube has two FODO fousing periods. In the latter

part a triplet structure is used and the magnets are between accelerating tubes. Between the two parts there is an additional quadrupole magnet for matching. The schematic diagram of the foucsing structure is shown in Fig.4.4.4 and the simulation results are shwon in Fig.4.4.5.

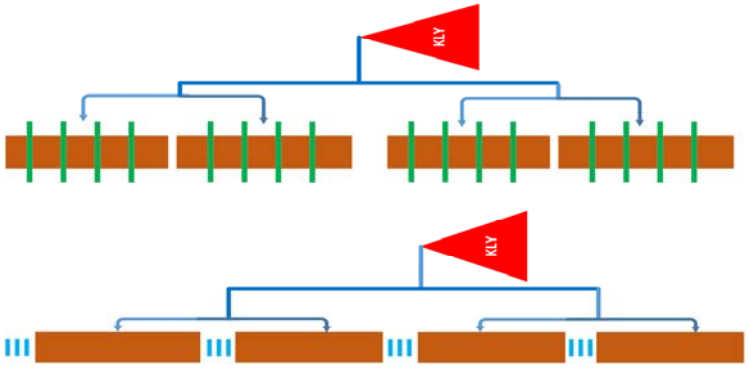

Figur4.4.4: Schematic diagram of the focusing structure.

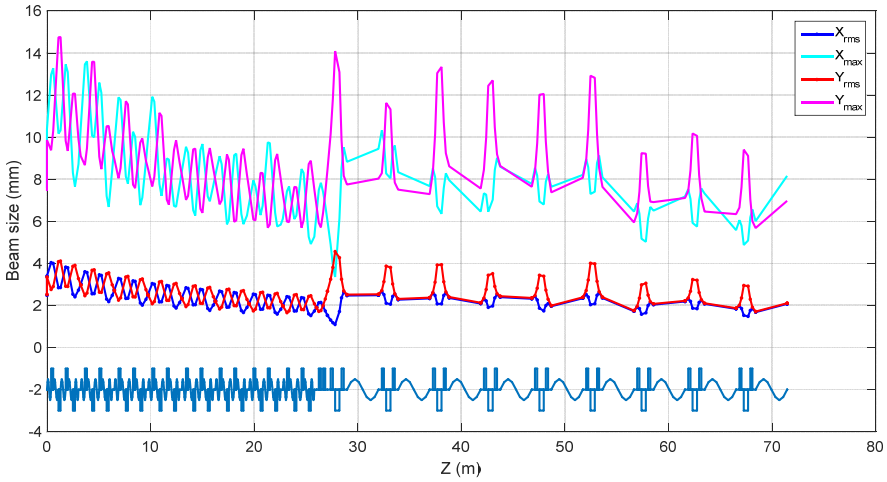

Figur4.4.5: The beam envelope in the first accelerating section of the main linac.

4.4.1.3 Main Linac Design

The main linac is 10 GeV energy and 3.2 nC bunch charge. For positron production the 10 nC bunch charge electron beam is accelerated to 4 GeV. The bunch charge is high, so we need to consider longitudinal and transverse wakefields. We use Yokoya's wakefield model for a periodic linac structure [1]. The wakefield of the S-band accelerating tube is shown in Fig.4.4.6. The accelerating tube gradient is 27 MV/m and one klystron supplies two tubes. Figure 4.4.7 shows the beam distribution at 4 GeV with a 10 nC electron beam for positron production. Figure 4.4.8 shows the beam distribution at 10 GeV with a 3.2 nC positron beam. Figure 4.4.9 shows the emittance of the positron beam along the linac. The emittance is 0.15 mm-mrad without errors. This meets the requirement. Figure 4.4.10 shows the energy spread of the positron beam. The energy spread at the linac exit is 1.2×10^{-3}, which almost meets our requirement.

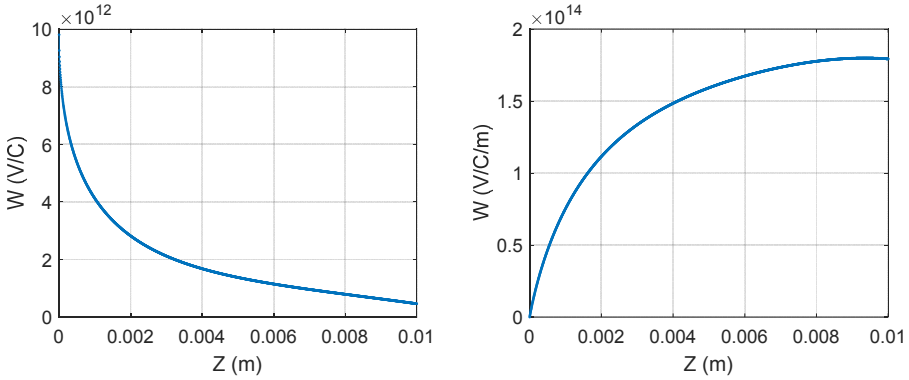

Figure 4.4.6: The short-range wakefield in the S-band accelerating tube. Left is the longitudinal wakefield and right the transverse wakefield.

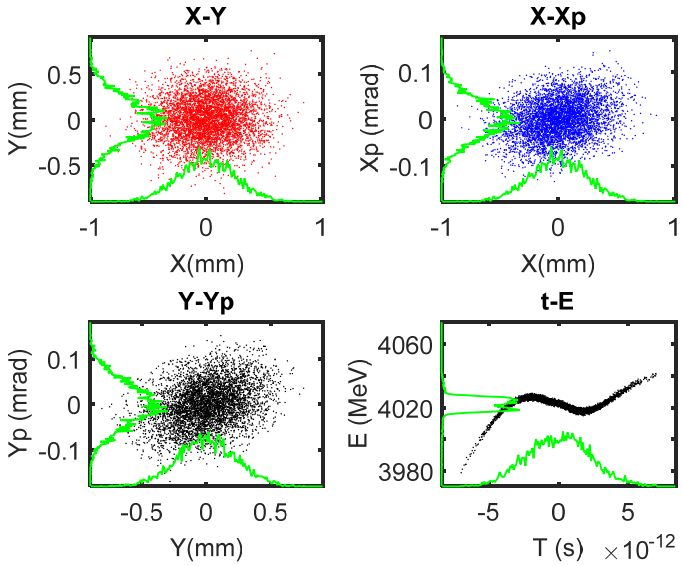

Figure 4.4.7: Beam distribution at 4 GeV with a 10 nC electron beam.

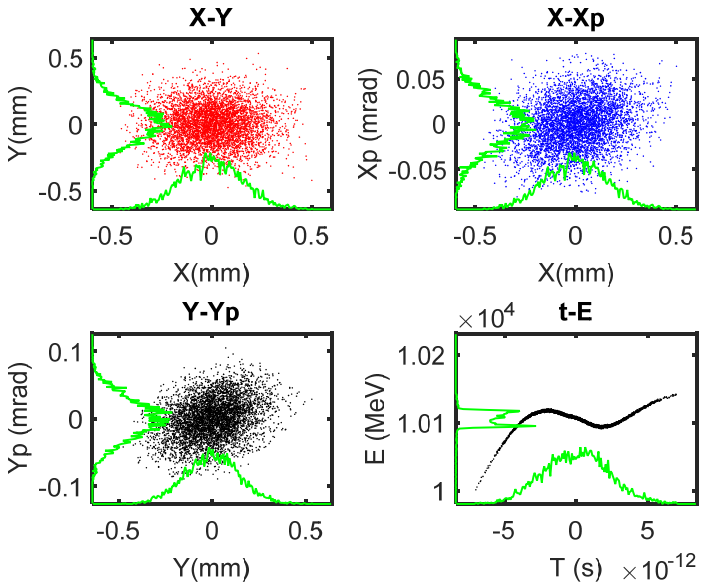

Figure 4.4.8: Beam distribution at 10 GeV with a 3.2 nC positron beam.

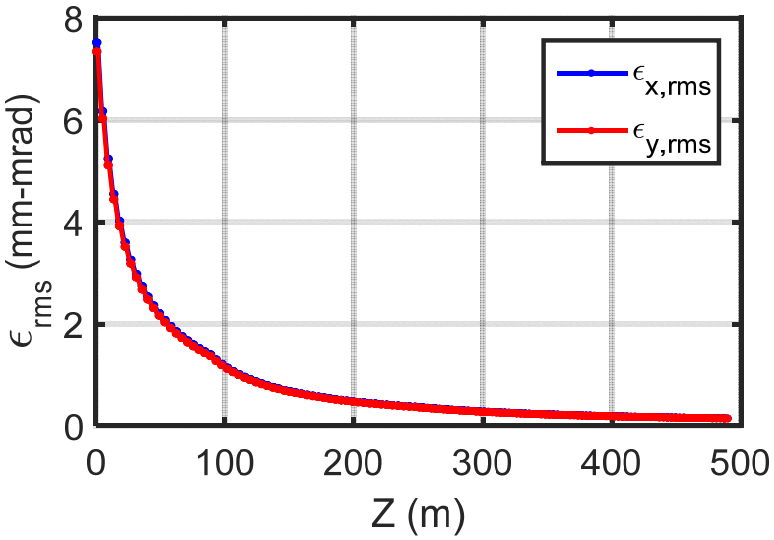

Figure4.4.9: Emittance of the positron beam along linac.

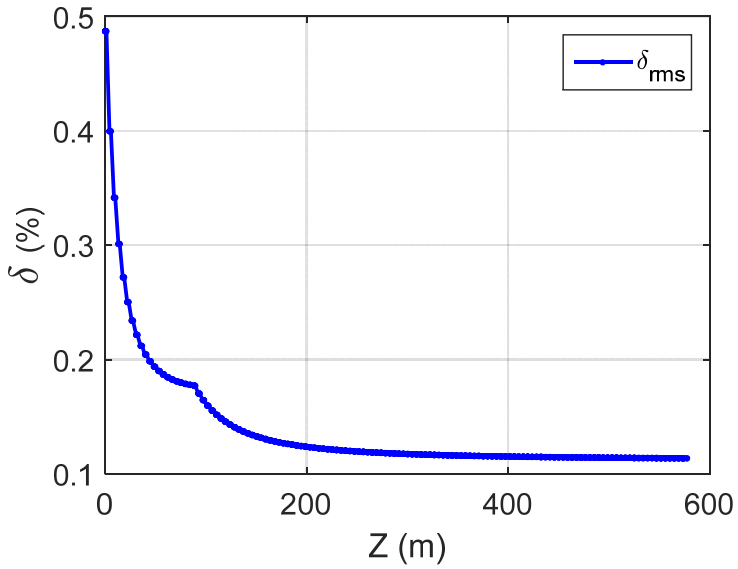

Figure 4.4.10: Energy spread in the positron beam along linac.

4.4.2 References

1. K. Yokoya, "The longitudinal high–frequency impedance of a periodic accelerating structure," Proceedings of the 1999 Particle Accelerator Conference, New York, 1999.

4.5 Bunching System

After leaving the electron guns, the electron bunches go into the bunching system, which consists of the following components: the first sub-harmonic buncher (SHB1), operating at 142.8375 MHz (20th subharmonic), the second sub-harmonic buncher (SHB2) operating at 571.35 MHz (5th subharmonic), and a constant-impedance travelling-wave buncher operating in 2π/3 mode at 2856.75 MHz.

4.5.1 SHB1

4.5.1.1 General Description

A resonant cavity has the following parameters:

1) Resonant frequency f
   The resonant frequency is the most important parameter, and is always the first parameter that needs to be decided on in the design. The resonant frequency is inversely proportional to the cavity size – the higher the frequency, the smaller the cavity. In order to let the microwave power go into the cavity without reflection, the resonant frequency of cavity needs to be the same as the power supply system.
2) Quality factor Q
   The Quality Factor Q is also called the Q value. The unloaded Q is the measurement of the quality of a resonant cavity defined as the ratio of the storage energy inside cavity to the microwave loss within one radian RF period,

$$\boldsymbol{Q = \frac{\omega U}{P}} \tag{4.5.1}$$

where ω is the resonant radian frequency of the cavity. When the microwave loss is fixed, the higher the Q value, the more storage energy inside cavity, and the higher electric field we can obtain. Or the storage energy is fixed, the higher the Q value, the less microwave loss. However, a higher Q value can lead to other problems such as a larger phase shift caused by the frequency error of cavity. The Q value is related to the material and fabrication quality.

3) Shunt impedance R
The shunt impedance R is defined as the ratio of the square of the maximal voltage over the cavity to the total microwave consumed by the cavity,

$$\boldsymbol{R = \frac{[\int_0^L E_z(z)dz]^2}{P} = \frac{V^2}{P}} \tag{4.5.2}$$

where P is the total microwave power consumed by the cavity, Ez(z) is the electric field value along the axis of the cavity, V is the maximum voltage overall in the cavity. R is a very important cavity parameter. It represents the efficiency of a structure and measured in MΩ. R/L is the shunt impedance per unit length and is measured in MΩ/m. R is determined only by the geometric shape and has no relationship with the fabricating quality or material.

4) Transit time factor T
The time an electron needs to pass through a cavity is called the transit time. The field is always changing within the transit time, so it is impossible for an electron to see the maximum field value at all time. So the maximum energy change an electron can have after going through a cavity (Δε) is always smaller than the product of the line integral of the electric field along the axial line V and the electron charge e.Tthe ratio is defined as the Transit Time Factor,

$$\boldsymbol{T = \frac{\Delta \varepsilon}{eV}} \tag{4.5.3}$$

T is always less than 1, and the higher the T, the more efficient use of the cavity electric field. T is related to the field distribution of *Ez(z)*.

5) Effective shunt impedance Reff
R_{eff} is the most relevant parameter to represent the cavity accelerating efficiency, and it is also measured in *MΩ*.

$$\boldsymbol{R_{eff} = RT^2} \tag{4.5.4}$$

6) Maximum electric field factor on the wall of cavity, Emax
This is equal to the ratio of the maximum electric field on the wall to the average field along the axis. The maximum average accelerating field along the cavity axis depends on *Emax*, which is limited by the maximum input power that would result in sparking.

4.5.1.2 Design of SHB1

The resonant frequency of SHB1 is 142.8375 MHz, and considering the material used OFC (oxygen free copper), the Q value is about 8175. To retain a margin, the bunching

voltage is chosen to be 105 kV. The shunt impedance is 1.4 MΩ considering that the power from the power supply system at 142.8375 MHz is about 10 kW.

According to the Kilpatrick Criterion, the breakdown electrical field is 12.9 MV/m at 142.8375 MHz. To retain some operating margin, we set the design goal of a maximum surface field of 7 MV/m for 10 kW input power.

The frequency tuning range is 400 kHz, where we use the KEKB linear accelerator as a reference [1].

The length of the short drift tube is carefully chosen taking into account the shunt impedance and cavity volume as well as the field distribution along the accelerating gap, Figure 4.5.1 shows the shunt impedance and cavity length when the length of the short drift tube is changed. Figure 4.5.2 shows the axial electric field distribution along the accelerating gap for different lengths of the short drift tube.

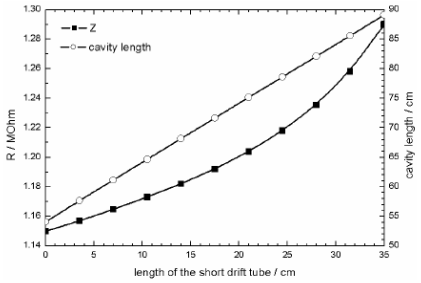

Figure 4.5.1： Shunt impedance and cavity length vs. length of the short drift tube.

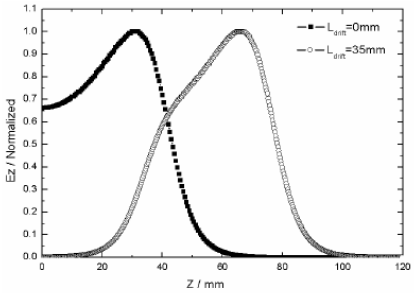

Figure 4.5.2: The axial electric field distribution along the accelerating gap for different lengths of the short drift tube

The outer diameter of the drift tube *a* and the inner diameter of the cavity *b* need to be optimized considering the shunt impedance and the *Q* value. The larger the value of *a* (the smaller the *b*), the smaller the shunt impedance and the *Q* value. So based on wanting the shunt impedance to be 1.4 MΩ, the *Q* value should be as small as possible. Figure 4.5.3 shows the relationship between the shunt impedance, *Q* value and *a*, *b*.

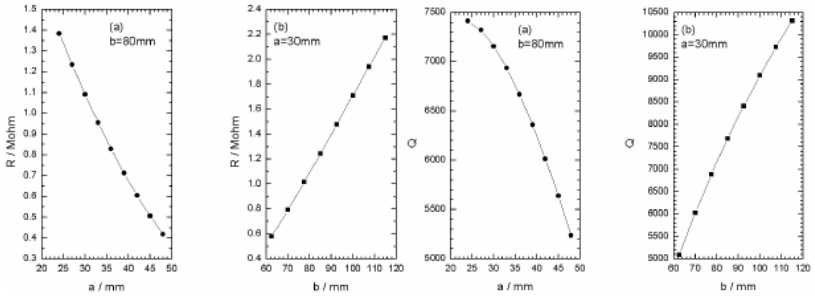

Figure 4.5.3: The relationship between the shunt impedance, *Q* value and *a*, *b*.

The length of the accelerating gap should be chosen taking into account the shunt impedance *R* and the maximum surface electric field E_{max}. Figure 4.5.4 shows the relationship between these factors: the larger the gap distance, the smaller the *R* and E_{max}.

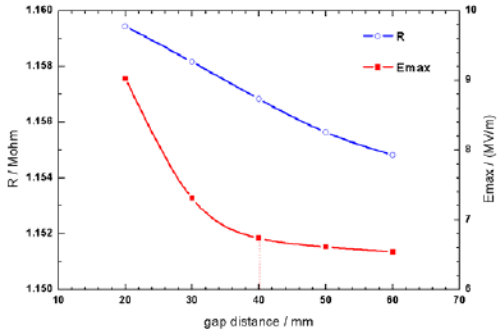

Figure 4.5.4: The relationship between the shunt impedance R, the maximal surface electrical field E_{max} and the gap distance.

The maximum surface electrical field E_{max} is usually at the nose. The value of E_{max} mainly depends on the thickness of the drift tube and the shape of the nose. The thicker the drift tube, the smaller the E_{max}. Figure 4.5.5 shows the relationship between the E_{max} and the nose outer radius.

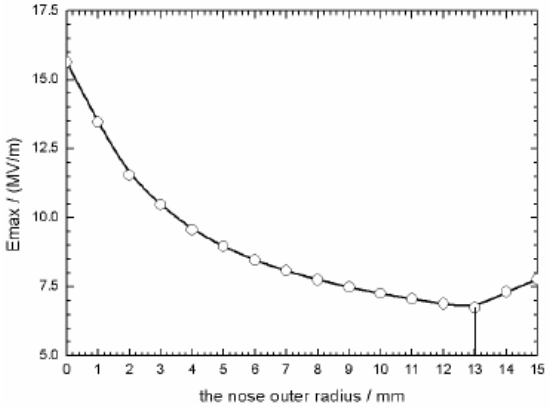

Figure 4.5.5: The relationship between the maximal surface electric field E_{max} and the nose outer radius.

By considering the capacity of the power supply system and the size of the sub-harmonic bunching system, using Superfish [1], MAFIA [2], HFSS [3] and ANSYS[4]

software, the design of microwave structure and water cooling plan for SHB1 can be optimized. A photograph of SHB1 designed for BEPCII is shown in Figure 4.5.6. The electric field distribution of SHB1 is shown in Figure 4.5.7.

Figure 4.5.6: SHB1 designed for BEPCII.

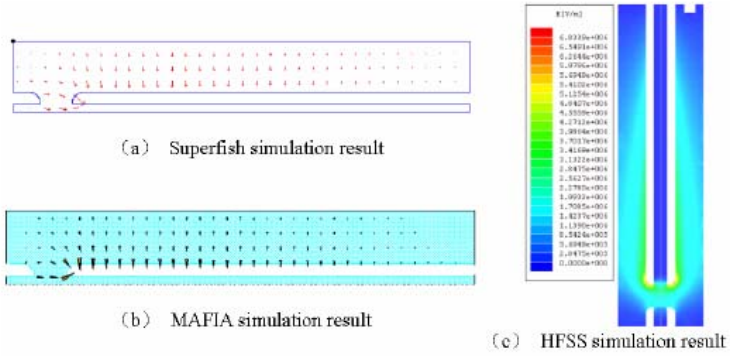

Figure 4.5.7: The electric field distribution of SHB1.

4.5.2 SHB2

The design procedure for SHB2 is similar to SHB1, The resonant frequency of SHB2 is 571.35 MHz. The material is OFC and the Q value is about 13,000. To retain a margin, the designed bunching voltage is chosen as 145 kV. The shunt impedance is 3.7 MΩ and the power from the power supply system at 571.35 MHz is about 7 kW.

According to the Kilpatrick Criterion, the breakdown electrical field is 22.5 MV/m at 571.35 MHz. To retain operating margin, our design goal is a maximum surface field of 11 MV/m for 7 kW input power.

The relationship between the shunt impedance, Q value, the outer diameter of the drift tube a and the inner diameter of the cavity b is shown in Figure 4.5.8. The relationship of the shunt impedance, the cavity length and the length of the short drift tube is shown in Figure 4.5.9. The relationship between the maximum surface electric field E_{max} and the nose outer radius is shown in Figure 4.5.10. The electrical field distribution of SHB2 is shown in Figure 4.5.11. The photograph of SHB2 designed for BEPCII is shown in Figure 4.5.12.

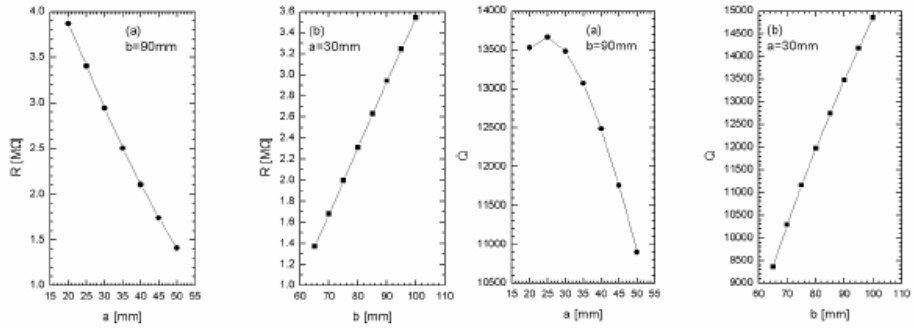

Figure 4.5.8: The relationship between the shunt impedance, *Q* value and *a*, *b.*

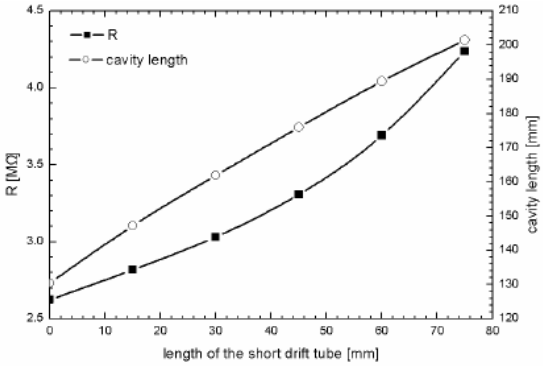

Figure 4.5.9: Shunt impedance and cavity length vs. length of the short drift tube.

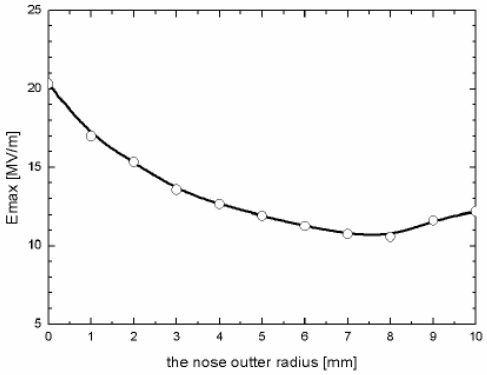

Figure 4.5.10: The relationship between the maximum surface electric field E_{max} and the nose outer radius.

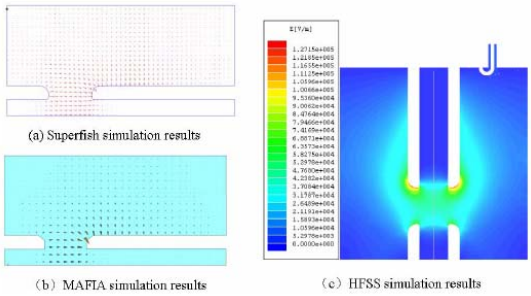

Figure 4.5.11: The electrical field distribution of SHB2.

Figure 4.5.12: SHB2 designed for BEPCII.

4.5.3 Buncher

The buncher is a 6-cavity (including 2 coupling cavities) traveling-wave structure operating in 2π/3 mode at 2856.75 MHz, the relative phase velocity is 0.75.

The beam bunches from the SHBs go into the input coupler of the buncher at correct phase. They are then focused by the microwave field and accelerated at the same time. The input power of the buncher is 3 MW.

The two sub-harmonic pre-bunchers and the one S-band buncher act to velocity modulate the non-relativistic electron beam emerging from the gun, and compress the pulse before it passes into the buncher. A beam pulse of 1.0 ns FWHM length from the gun is compressed into a single bunch of 10 ps (FWHM) by an RF bunching section with two sub-harmonic bunchers of 142.8375 MHz and 571.35 MHz and an S-band (2856.75 MHz) buncher cavity. The main parameters of the sub-harmonic pre-bunchers and S-band buncher are shown in Table 4.5.1.

Table 4.5.1

Table 4.5.1: The main parameters of the sub-harmonic pre-buncher and S-band buncher.

First sub-harmonic pre-buncher		
Type	Re-entrant	
Frequency	MHz	142.8375
Unloaded Q		8175
Shunt impedance	MΩ	1.4
$E_{surface,\ max}/E_{gap,\ max}$		2.53
Second sub-harmonic pre-buncher		

Frequency	MHz	571.35
Unloaded Q		13000
Shunt impedance	MΩ	3.7
$E_{surface,\ max}/E_{gap,\ max}$		2.44
S-Band Buncher		
Type	Constant impedance ,TW, 2π/3-mode	
Frequency	MHz	2856.75
Operating temperature	°C	40±0.1
Input and output VSWR		≤1.2
Bandwidth (VSWR ≤ 1.2)	MHz	≥4.0
Peak RF input power	MW	3
Phase velocity (V_p/c)/group velocity (V_g/c)		0.75 / 0.0119
Shunt impedance	MΩ/m	36
Unloaded Q		11000
RF attenuation parameter	Neper/m	0.228
Number of cavities		4＋2×0.5

4.5.4 References

1. S. Yamaguchi, S. Ohsawa et al. Development of a 114.24 MHz sub-harmonic buncher for the KEKB injector linac. Proc of LINAC 1998. Chicago, 1998.
2. J. H. Billen, L. M. Young et al. Possion Superfish: LA-UR-96-1834. Los Alamos National Laboratory, 2002.
3. The MAFIA Collaboration. MAFIA User Manual (Version 4.106). Germanny: CST Inc, 2000.
4. The Ansoft High Frequency Simulator. Copyright Ansoft Corporation.
5. ANSYS Corporation. Manual of Electromagnetic Field Anasysis in ANSYS. America: ANSYS Inc, 2000.

4.6 Main Linac RF System

The 10 GeV linac operates at 50 Hz, is approximately 1000 m long and is powered by klystrons. The klystrons produce 65 MW power at 2856.75 MHz. The power is then evenly divided among four 3-m constant gradient accelerating sections on a support girder. At 22 MV/m accelerating gradient, each klystron is thus capable of providing 264 MeV to each particle at a repetition rate of 50 Hz. Figure 4.6.1 shows one unit power supply system for the accelerating structures.

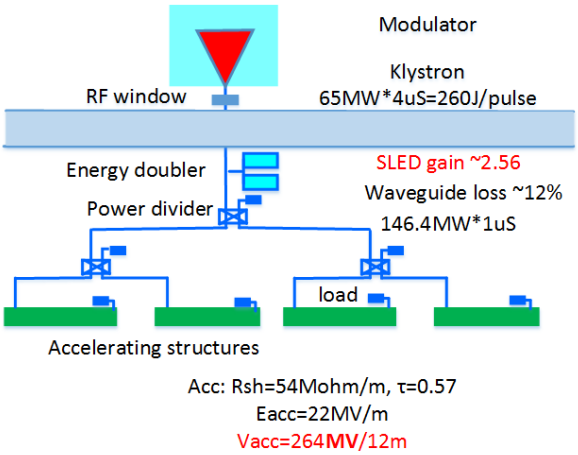

Figure 4.6.1: The layout of one unit of the RF system.

4.6.1 RF Transmission System and Measurement System

The RF transmission and measurement system is a microwave path between the klystron and the accelerating sections which is composed of a waveguide and other microwave components. The required microwave devices include straight waveguide, E-band waveguide, H-band waveguide, directional coupler, power divider, high power waveguide phase shifter and attenuator, dry load, microwave monitoring unit, and peak power meter.

The waveguide model is R32, the section size is 72.14 mm by 34.04 mm, the material is oxygen-free copper, and the flange is made of stainless steel. The microwave signal can be phase-shifted or attenuated by a high power waveguide phase shifter and attenuator. The microwave signal coupled from the directional coupler can be tested not only to observe waveform, but also for power measurement. In order to absorb the excess microwave power from the accelerating structure, a high power SiC dry load is required. It uses brazing rod β-phase SiC ceramics as a peak microwave energy absorber and incorporates indirect water cooling. The SiC dry load withstands peak power up to 60 MW in high-power testing. Its performance has reached the international advanced level for similar products.

Table 4.6.1: High power SiC dry load parameters.

Parameters		Unit
Frequency	2856	MHz
VSWR	<1.1	
Maximum peak power	30 (with SLED) 10 (without SLED)	MW
Repetition frequency	50	Hz
Pulse width	4	μs

The modular microwave monitoring unit will be redesigned and will contain several independent parts, such as the attenuation unit, filter unit, detection unit and virtual

oscilloscope unit. The modular multi-unit design not only facilitates maintenance, but also reduces the space required to avoid electromagnetic interference. The microwave monitoring unit realizes three functions at the same time and provides three kinds of signals, signals for power measurement, signals for observing the waveform on a oscilloscope, and virtual oscilloscope signals for input into the local computer.

4.6.2 RF Pulse Compressor

In order to achieve beam acceleration to 10 GeV we adopt the experience from operation of the Stanford Linear Accelerator Energy Doubler (SLED) at the maximum klystron output peak power of 80 MW, with a pulse length of 4 μs. The S-band SLED, which is an RF pulse compression system using high-Q resonant cavities, is one of the most important RF components in the S-band high-power RF station. The S-band SLED consists of a 3-dB power hybrid and two identical over-coupled cylindrical cavities resonant at the 2856 MHz. A fast-acting triggered phase-shift-keying (PSK) π-phase-shifter, which reverses the RF phase of the klystron output power, is inserted into the klystron drive line. The cavities begin by storing klystron output power during a large fraction of the time duration of each pulse. Then the phase of the klystron output is reversed, and the cavities emit the stored power rapidly into the accelerating section, adding to the klystron output power during the remaining pulse length. This means that the peak power is enhanced at the expense of the pulse length without increasing the average input power consumption.

The specifications of the S-band SLED are listed in Table 4.6.2. Two coupling slots are located between the waveguide and the cavity to decrease the peak surface field, and thus to increase the operating stability in high power conditions. The input pulse length is 4 us with a 180°phase reverse at time of 3.17 us. The energy multiplication factor can be larger than 1.6 from the operations experience of the BEPC-II Linac.

Table 4.6.2: The main parameters of the pulse compressor.

Parameters		Unit
Operation frequency	2856.75	MHz
Resonant mode	$TE_{0,1,5}$	
Coupling coefficient	5	
Peak power gain	> 5	
Unload Q factor	~100,000	
Energy multiplication factor	~1.6	
Max. input peak power	80	MW
Input pulse length	4	us
Output pulse length	0.83	us
Repetition rate	100	Hz

4.6.3 Accelerating Structures

S-band constant-gradient copper accelerating structures operating in 2π/3 mode at 2856.75 MHz will be used to accelerate the bunched electron and positron beams up to the final energy. The accelerating structure parameters are shown in Table 4.6.3. A dual-feed racetrack symmetry coupler design will be used to reduce emittance growth from the asymmetry coupler. The accelerating structure operation temperature is 30℃, which is

maintained within 0.1˚so that the phase shift along the entire length of an accelerator section is kept within 2˚.

Table 4.6.3: Accelerating structure parameters.

Parameters		Unit
Operation frequency	2856.75	MHz
Operation temperature	30.0 ± 0.1	°C
Number of cells	84 +2 coupler cells	
Section length	3048	mm
Phase advance per cell	2π/3 - mode	
Cell length	35.0012	mm
Disk thickness (t)	5.84	mm
Iris diameter (2a)	26.231～19.243	mm
Cell diameter (2b)	83.460～81.781	mm
Shunt impedance (r_0)	54.6～63.9	MΩ/m
Q factor	13990～13836	
Group velocity (v_g/c)	0.0208～0.0070	
Filling time	830	ns
Attenuation factor	0.57	Neper

4.6.4 Low Level RF

The 10 GeV linac accelerates electron and positron beams and is the injector into the Booster. It is composed of warm temperature bunching systems and hundreds of S-band acceleration structures with HLRF S-band signals are modulated by 50 Hz short pulses with power levels of dozens of MW and lengths on the order of a few μs. The pulse-to-pulse amplitude fluctuation and phase drift must be compensated by the LLRF system. The intra-pulse control method is also considered and will be investigated as a way to ensure beam quality and stability.

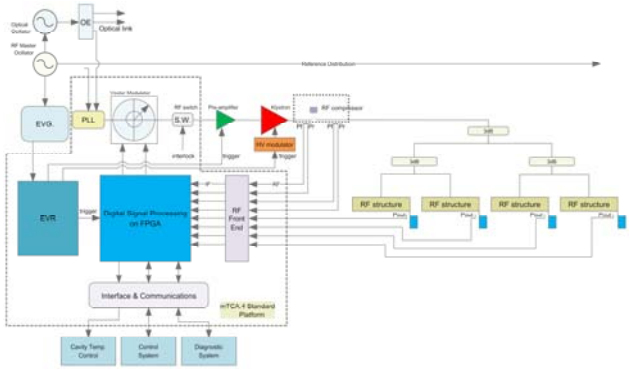

Figure 4.6.2: The LLRF system layout for the injector accelerating structures.

The LLRF systems are synchronized to the phase reference system and control the RF fields in the accelerating structures to the tolerance requirements, which are based on beam-dynamics considerations of energy stability, luminosity loss, and emittance growth. In the CEPC injector, the 2 sub-harmonic bunchers and the first accelerating tube with S-band buncher structure are fed by one separate RF power source, a single klystron and an

RF pulse compressor delivers RF power to two S-band structures at the low energy part of electron and positron sections. This is in contrast to those sections where a single klystron delivers RF power to two S-band structures without a pulse compressor. A layout of a typical RF station in the main linac is given in Figure 4.6.2. The controller will regulate amplitude and phase of the vector sum of a string of those accelerating structures.

Since the RF pulse duration is short, pulse-to-pulse feedback and adaptive feed-forward techniques are used to correct slow drifts and to correct repetitive distortions respectively. We also provide an interface for the implementation of beam-based feedback. The phase reference distribution, the phase-locked loops, the vector modulator, the pre-amplifier and the high-voltage modulator, together with the klystron determine the pulse-to-pulse stability. Each of these components has to meet the required short-term stability.

In addition to control of the local RF stations, the LLRF system interfaces to other systems. These also need to be carefully considered: the phase reference system, the global timing system, the local protection system and Machine Protection System.

4.6.5 References

1. CEPC-SPPC Preliminary Conceptual Design Report Volume II – Accelerator
2. THE INTERNATIONAL LINEAR COLLIDER Technical Design Report | Volume 3.ii: Accelerator Baseline Design
3. SwissFEL Conceptual Design Report
4. LHC Design Report Volume I, Chapter 6, The RF systems and beam feedback.
5. Architecture and Performance of the PEP-II Low-Level RF System
6. http://mtca.desy.de/

5 SPPC

5.1 Introduction

5.1.1 The SPPC Complex

SPPC is a complex accelerator facility able to support research in different fields of physics, similar to the multiuse accelerator complex at CERN. Besides the energy frontier physics program in the collider, the beams from each of the four accelerators in the injector chain can also support their own physics programs. The four stages, shown in Figure 5.1.1, are a proton linac (p-Linac), a rapid cycling synchrotron (p-RCS), a medium-stage synchrotron (MSS) and the final stage synchrotron (SS). This research can occur during periods when beam is not required by the next-stage accelerator. For example, the high-power proton beam of about 1.6 MW from the p-Linac can be used for production of intense beams of neutrons, muons and rare isotopes for a wide range of research. The high-power beams of 10 GeV from the p-RCS and 180 GeV from the MSS can be used to produce very intense neutrino beams for neutrino oscillation experiments and the high energy beam from the SS can be used for hadron physics research.

The option of heavy ion collisions also expands the SPPC program into a deeper level of nuclear matter studies. There would also be the possibility of electron-proton and electron ion interactions.

In summary, SPPC will play a central role in experimental particle physics in this post-Higgs discovery world. It is the natural next stage of the circular collider physics program after CEPC. Combining these two world class machines will be a significant milestone in our pursuit of the fundamental laws of nature.

5.1.2 Design Goals

SPPC is a proton-proton collider, a discovery machine at the energy frontier. Given the 100 km circumference tunnel predefined by CEPC, we will try to achieve the highest possible collision energy in p-p collisions with the anticipated accelerator technology in the 2030's. This, of course, depends on the magnetic field that bends the protons around the ring. Taking into account the expected evolution in detector technology we can expect that the peak luminosity of 1.6×10^{35} cm-2s-1 will be usable. At least two IPs will be available for experiments.

Table 5.1.1: Key SPPC parameters

Parameter	Value	Unit
Collision energy (C. of M.)	100	TeV
Nominal luminosity	1.6×10^{35}	$cm^{-2}s^{-1}$
Number of IPs	2	
Circumference	100	km
Injection energy	2.8	TeV
Overall cycle time	9-14	hours
Dipole field	16	T

This chapter describes what the SPPC will look like, basic design parameters, and its major challenges in accelerator physics and technology. It also explores compatibility in the same tunnel with a previously built CEPC and different operating modes such as electron-proton, proton-ion, and electron-ion. Key parameters are shown in Table 5.1.1.

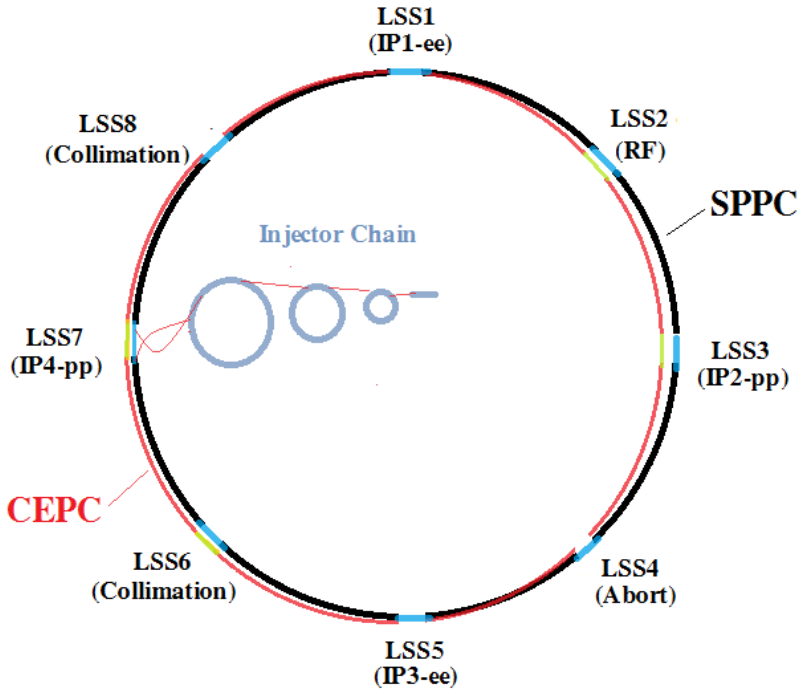

Fig. 5.1.1: SPPC accelerator complex

5.1.3 Overview of the SPPC Design

The collider will coexist with the previously built CEPC, housed in the same tunnel, of circumference 100 km. The shape and symmetry of the tunnel is a compromise between the two colliders. The SPPC requires relatively longer straight sections which will be described later. This means eight identical arcs, and eight long straight sections for two large detectors, injection and extraction, RF stations and a complicated collimator system. Based on expected progress in high-field magnet technology in the next fifteen to twenty years, we expect that a field of 16 T will be attainable for the main dipole magnets. A hybrid structure of Nb-Ti and high-temperature superconducting (HTS) conductors or a pure HTS conductor structure with two beam apertures is foreseen. A filling factor of 79% in the arcs (similar to LHC) is assumed. The SPPC will potentially provide beams at a center of mass collision energy of about 100 TeV.

With a circulating beam current of about 0.9 A and small beta functions (β*) of 0.75 m at the collision points, the peak luminosity can reach 1.6×10^{35} $cm^{-2}s^{-1}$. The high beam energy, high beam current and high magnetic field will produce very strong synchrotron radiation which will impose critical requirements on the vacuum system which is based on cryogenic pumping. We expect that this technical challenge will be solved in the next two decades by developing efficient beam screens to extract the heavy heat load from the

synchrotron radiation and reduce the electron cloud density within the beam apertures. If forced to lower the synchrotron radiation power, we would have to reduce the bunch population or the number of bunches and try to achieve a smaller β*.

As in other proton colliders using superconducting magnets, the injection energy is mainly defined by the field quality of the magnets at the bottom of their range. Persistent currents in the coils (magnetization) distort the field distribution at injection energy. Other factors favoring relatively higher injection energy are the coupling impedance, which is important in collective beam instabilities; the small emittance required to reduce apertures of beam screen and magnet, and the requirement on the good-field-region of the magnets. If we use the LHC ratio of 15 for top to bottom fields the injection energy would be 3.3 TeV. A larger ratio of 20 could be considered, which would mean an injection energy of 2.5 TeV. This would make the injector chain cheaper. In this report, we have adopted a compromise with an injection energy of 2.8 TeV.

The injector chain pre-accelerates the beam to injection energy with the required bunch current, bunch structure, and emittance. The injection chain determines the beam fill period. To reach 2.8 TeV, a four-stage injector chain is proposed: the p-Linac to 1.2 GeV, the p-RCS to 10 GeV,the MSS to 180 GeV and the SS to 2.8 TeV. High repetition rates for the lower energy stages help reduce the SS cycling period. This is important because the SS uses superconducting magnets. The high repetition rate beams can also be used for other research applications when the accelerators are not preparing beam for injection into the SPPC.

If not controlled, synchrotron radiation cooling would rapidly reduce the beam emittances and cause excessive beam-beam tune shifts. Noise in transverse deflecting cavities must be used to limit the minimum transverse emittances, and thus tune shifts. Without leveling, and with constant beam-beam tune shift, the luminosity decays exponentially from its peak with a lifetime of approximately 10 hours. To maximize the integrated luminosity, the turnaround time (defined as the period in a machine cycle excluding the collision period) should be made as short as possible, preferably short compared to the beam decay time. The initially assumed average 3-hour is acceptable, giving an optimized complete cycle time of about 10 hours, but a turnaround time of as little as 1.0 hour would certainly be preferred.

The peak and average luminosities could be raised by allowing the synchrotron damping to lower the transverse emittance and allowing higher but acceptable tune shifts (0.02-0.03). But, if not leveled, the peak luminosities and thus the numbers of interactions per beam crossing could become excessive. Limiting the peak luminosity (leveling) would limit this number, yet still allow an increase in the average luminosity. Using more and closer spaced bunches could reduce the number of interactions per bunch crossing, without lowering the peak luminosities. However, if the beam current is not to be raised, the numbers of protons per bunch must be proportionally reduced, and, if luminosity is to be preserved, the synchrotron damping must be allowed to further lower the emittances, while not increasing the tune shifts. Whether closer bunch spacing is consistent with electron cloud considerations is yet to be determined.

Lowering the beta functions at the collision points could further increase luminosities without increasing the tune shift. If this was done after the emittances have been damped, then larger aperture final triplet magnets, or requiring them to be closer to the IP, are not required. This option will be studied.

There are many technical challenges in designing and building the collider, including its injector chain. The two most difficult are the development and production of 16-T

magnets, and the beam screen associated with the very strong synchrotron radiation. Significant R&D efforts in the coming decade are needed to find solutions to these problems.

5.1.4 SPPC Parameter Choice

The energy goal of the SPPC is to reach collision energies of 70 to 100 TeV, using the same tunnel as the CEPC [1,2,3]. This will require superconducting magnets 12 to 20 T [4]. We develop a systematic way to calculate the SPPC parameters beginning from the maximum beam-beam tune shift and the design goals as the input parameters, including: luminosity L, beam energy E_0, ring circumference C_0 and IP numbers N_{IP}.

The luminosity of a pp collider can be expressed as a function of the beam current I_b, the beam-beam tune shift ξ_y , the beta-function at the IP β^*, the classical proton radius r_p, its charge e, and the luminosity reduction factor due to the crossing angle and hourglass effect [2]:

$$L = \frac{I_b}{e}\frac{\xi_y}{\beta^*}\frac{\gamma}{r_p}F_{ca}F_h = L_0 F_{ca}F_h$$

where F_{ca} F_h can be expressed as [3,5]:

$$F_{ca} = 1/\sqrt{1+(\frac{\sigma_z\theta_c}{2\sigma^*})^2}$$

$$F_h = \frac{\beta^*}{\sqrt{\pi}\sigma_z}\exp(\frac{\beta^{*2}}{2{\sigma_z}^2})\ K_0(\frac{\beta^{*2}}{2{\sigma_z}^2})$$

From the following equations,

$$\xi_{y,max,pp} = \frac{2845\gamma}{f(\mathrm{x})\mathrm{F}}\sqrt{\frac{r_p}{6\pi R N_{IP}}} = \frac{2845}{f(\mathrm{x})2\pi}\sqrt{\frac{T_0}{\tau_y\gamma N_{IP}}}$$

$$f(\mathrm{x}) = 1 - \frac{2}{\sqrt{2\pi}}\int_0^x e^{-\frac{t^2}{2}}\,dt$$

$$x^2 = \frac{4f(x)}{\pi\xi_{y,max,pp}N_{IP}} = \frac{4f(x)^2}{2845\pi}\sqrt{\frac{6\pi R}{r_p N_{IP}}}$$

We find a limit for the luminosity:

$$L_0 = \frac{I_b}{e}\frac{\xi_{y,max,pp}}{\beta^*}\frac{\gamma}{r_p} = \frac{2845}{2\pi r_p e\, f(x)}\frac{1}{\beta^*}\sqrt{\frac{I_b U_0\gamma}{2E_0 N_{IP}}}$$

$$L_{max} = L_0 F_{ca}F_h$$

The beta function at an IP can then be written as:

$$\beta^* = \frac{2845}{2\pi r_p e\, f(x)}\frac{1}{L_0}\sqrt{\frac{I_b U_0\gamma}{2E_0 N_{IP}}}$$

where P_{SR} is the synchrotron radiation power per ring:

$$P_{SR} = U_0 I_b$$

U_0 is the energy loss per turn [5]:

$$U_0 = 0.00778[\mathrm{MeV}]\frac{(E_0[TeV])^4}{\rho[m]}$$

and the critical photon energy is [5]:

$$E_c[KeV] = 1.077 * 10^{-4}(E_0[TeV])^2 B[T]$$

The proton beam is round (σ_x=σ_y=σ), so the rms IP spot size is:

$$\sigma^* = \sqrt{\beta^* \varepsilon} = \sqrt{\beta^* \frac{\varepsilon_n}{\gamma}}$$

The beta function at the 1st parasitic encounter with bunch separation Dt is:

$$\beta_1 = \beta^* + \frac{(l_1/2)^2}{\beta^*}$$

$$l_1 = \mathrm{c}\times\Delta\mathrm{t}$$

The rms spot size at the 1st parasitic encounter is:

$$\sigma_1 = \sqrt{\beta_1 \varepsilon} = \sqrt{\beta_1 \frac{\varepsilon_n}{\gamma}}$$

Many circular colliders are designed to reach high luminosity by using a large number of closely spaced bunches. This introduces the problem of parasitic encounters near the interaction point. To avoid unwanted parasitic encounters, we use a crossing angle scheme. However, before the two beams enter separate beam pipes, they travel in the same vacuum chamber where parasitic `long range' collisions can occur. Although these are rather weak due to the separation of the bunches, their large number makes their effect important and will lower the luminosity. In LHC the two beams share an approximately 130 m long common beam pipe in the interaction regions (IRs). The exact length is 126 m in IR2 and IR8, which use superconducting separation dipole magnets next to the triplet assemblies, and 140 m in IR1 and IR5, which have normal conducting separation dipoles and are therefore somewhat longer next to the triplets. With large number of bunches (2808 for each proton beam), and a nominal bunch spacing of 25 ns, this implies 34 parasitic collision points for each experimental insertion region in the long common beam pipe. So for the four experimental IRs this is a total of 136 unwanted collision points [5]. In the SPPC the length of the common beam pipe, where both beams share a common vacuum tube, is determined by the IR optics design. In the preliminary SPPC design, there are 2 common beam pipes, each about 300 m long. As we use the same bunch spacing (25 ns) as the LHC, the number of parasitic collision points in the machine is about 160. These long range collisions may cause a tune shift spread. The spread must be limited to those values that avoid crossing dangerous resonances in the machine tune space. These crossings may also produce instabilities in the beam, limiting beam lifetime and luminosity and creating radiation problems in the detectors from beam-halo [6,7]. To obtain a large beam-beam parameter with small effect on the luminosity, and considering the experience gained from experiments at the LHC and the Tevatron [8-10], the full crossing angle θ_c is chosen to provide a beam-beam separation of n_s=*10-12* rms beam sizes for the parasitic crossings [2,11]:

$$\theta_c = \frac{2\times\frac{n_s}{2}\sigma_1}{l_1/2} = \frac{2n_s\sigma_1}{l_1}$$

Then we can rewrite Fca as:

$$F_{ca} = \frac{1}{\sqrt{1+\Phi^2}}$$

where,

$$\Phi = \frac{\sigma_z \theta_c}{2\sigma^*} = \frac{n_s \sigma_z \sigma_1}{l_1 \sigma^*} = \frac{n_s \sigma_z \sqrt{\beta_1 \frac{\varepsilon_n}{\gamma}}}{l_1 \sqrt{\beta^* \frac{\varepsilon_n}{\gamma}}} = \frac{n_s \sigma_z}{l_1} \sqrt{\frac{\beta_1}{\beta^*}} = n_s \sqrt{\frac{{\sigma_z}^2}{(c\Delta t)^2} + \frac{1}{4(\beta^*/\sigma_z)^2}}$$

F is the Piwinski angle, β^* is the beta function at the IP, σ_z is the bunch length and Δt is the bunch separation.

When the luminosity is reduced by less than 10% due to the crossing angle effect, we have $F_{ca} \geq 0.9$. From Eq. (19) we get: $F \leq 0.484322(rad)$.

We know the number of bunches:

$$n_b = \frac{T_0 f_2}{\Delta t}$$

and the bunch population:

$$N_p = \frac{I}{n_b \ f_{rev} \ e}$$

Combining Equations (10), (20), (21), (22) and (23), we can get reasonable values of $\beta^*, I_b, Dt, n_b, N_p$ and the ratio of β^*/σ_z. We also need to consider the influence of these choices on beam instability and technical constraints.

From the definition of the beam-beam tune shift [5]:

$$\xi_y = \frac{N_p r_p}{4\pi\varepsilon_n}$$

we can obtain the normalized emittance:

$$\varepsilon_n = \frac{N_p r_p}{4\pi\xi_{y,max,pp}}$$

We can then calculate $\sigma^*, \beta_1, \sigma_1, \theta_c$ F_{ca} and F_h. Finally, we obtain the luminosity:

$$L = L_0 F_{ca} F_h$$

From this we can now generate sets of parameters for SPPC. In these sets of parameters, the full crossing angle θc is kept to a separation of 12 rms beam sizes for the parasitic crossings. The luminosity reduction factor due to the crossing angle is larger than 0.9 and the ratio of β^* and σ_z is about 15.

In Table 5.1.2 are presented parameter lists for SPPC with different circumferences and at different beam energies. If we choose the dipole field as 20 T, then with a 61 km circumference we can reach 70 TeV. Since we want to go higher, we need a larger circumference ring. So to explore the physics at a center-of-mass energy of 100 TeV while keeping the dipole field at 20 T, the circumference should be at least 80 km. With this size, there is hardly any room for an upgrade. So a 100 km SPPC is preferable because the dipole field is then only 15.26 T, a more reasonable number. If the dipole field is 20 T, then in a 100 km SPPC we can get a center-of-mass energy as high as 130 TeV [12,14].

Table 5.1.2: SPPC Parameter List.

	SPPC Pre-CDR	***SPPC 61 km***	***SPPC 100 km***	***SPPC 100 km***	***SPPC 82 km***
Main parameters and geometrical aspects					
Beam energy[E_0]/TeV	35.6	35.0	50.0	64.0	50.0
Circumference[C_0]/km	54.7	61.0	100.0	100.0	82.0
Dipole field[B]/T	20	19.81	15.62	19.98	19.74
Dipole curvature radius[ρ]/m	5928	5889.64	10676.1	10676.1	8441.6
Bunch filling factor[f_2]	0.8	0.8	0.8	0.8	0.8
Arc filling factor[f_1]	0.79	0.78	0.78	0.78	0.78
Total dipole length [L_{Dipole}]/m	37246	37006	67080	67080	53040
Arc length[L_{ARC}]/m	47146	47443	86000	86000	68000
Straight section length[Lss]/m	7554	13557	14000	14000	14000
Physics performance and beam parameters					
Peak luminosity per IP[L]/ $cm^{-2}s^{-1}$	1.1×10^{35}	1.20×10^{35}	1.52×10^{35}	1.02×10^{36}	1.52×10^{35}
Beta function at collision[β*]/m	0.75	0.85	0.99	0.22	1.06
Max beam-beam tune shift [ξy]/IP	0.006	0.0065	0.0068	0.0079	0.0073
Number of IPs contribut to Δ Q	2	2	2	2	2
Max total beam-beam tune shift	0.012	0.0130	0.0136	0.0158	0.0146
Circulating beam current[I_b]/A	1.0	1.024	1.024	1.024	1.024
Bunch separation[Δ t]/ns	25	25	25	25	25
Number of bunches[n_b]	5835	6506	10667	10667	8747
Bunch population[N_p] (10^{11})	2.0	2.0	2.0	2.0	2.0
Normalized RMS transverse emittance[ε]/μm	4.10	3.72	3.59	3.11	3.35
RMS IP spot size[σ*]/μm	9.0	8.85	7.86	3.04	7.86
Beta at the 1st parasitic encounter[β_1]/m	19.5	18.67	16.26	69.35	15.31
RMS spot size at the 1st parasitic encounter[σ_1]/μm	45.9	43.13	33.10	56.19	31.03
RMS bunch length[σ_z]/mm	75.5	56.69	66.13	14.62	70.89
Full crossing angle[θc]/μrad	146	138.03	105.93	179.82	99.29
Reduction factor according to cross angle[Fca]	0.8514	0.9257	0.9247	0.9283	0.9241
Reduction factor according to hour glass effect[F_h]	0.9975	0.9989	0.9989	0.9989	0.9989
Energy loss per turn[U_0]/MeV	2.10	1.98	4.55	12.23	5.76
Critical photon energy[Ec]/keV	2.73	2.61	4.20	8.81	5.32
SR power per ring[P_0]/MW	2.1	2.03	4.66	12.52	5.90
Transverse damping time [τ_x]/h	1.71	1.994	2.032	0.969	1.32
Longitudinal damping time [τ_ε]/h	0.85	0.997	1.016	0.4845	0.66

5.1.5 References

1. J. Y. Tang, J. ScottBerg, W. Chai et al, arXiv: 1507.03224v1
2. https://tlep.web.cern.ch/sites/tlep.web.cern.ch/files/Hadron ColliderParameters_V1.0.pdf#overlay-context=content/fcc-hh, retrieved 5th March 2015
3. D. Wang, J. Gao, M. Xiao et al, Optimization Parameter Design of a Circular e+e- Higgs Factory, IHEP-AC-LC-Note2013-005
4. J. Gao, M. Xiao, F. Su et al. Analytical Estimation of Maximum Beam-beam Tune Shifts for Electron-Positron and Hadron Circular Colliders. Proceedings of HF2014. p.114-121.
5. O. Bruning, P. Coller, S. Myers et al, LHC Design Report (CERN Scientific Information Service-1300-June 2004), Vol. 1, p21-22
6. L. F. Wang, C. Zhang, S. H. Wang et al, Tune Shifts and Spreads Due to Short and Long Range Beam-beam Interaction, in Proceedings of PAC2001, edited by P. Lucas, S. Webber, p.2011-2013
7. G. Lopez, Head-On and Long-Range Beam-Beam Tune Shift Spread in the SSC, in Proceedings of PAC1993, p.3467-3469
8. W. Herr, Tune Spreads and Shifts Due to the Long Range Beam-Beam Effect in the LHC, in Proceedings of EPAC1990, p.1630-1632
9. V. Shiltsev et al, Phys. Rev. ST Accel. Beams, \textbf{8}:101001 (2005)
10. D. Sagan, R. Siemann S. Krishnagopal et al, in Proceedings of the 2nd EPAC (1990), p.1649
11. T. J. Bian, J. Gao, F. Su et al, Horizontal Seperation at the Parasitic Crossing Points of CEPC, IHEP-AC-LC-Note2015-006
12. F. Su, J. Gao et al, "SPPC Parameter Choice and Lattice Design", TUPMW001, Proceedings of IPAC2016.
13. F. Su, J. Gao et al, "CEPC Partial Double Ring Lattice Design", THPOR009, Proceedings of IPAC2016.
14. F. Su, J. Gao, etc., "CEPC partial double ring lattice design and SPPC lattice design", International Journal of Modern Physics A (SCI), Vol. 31, p. 1644017, 2016.

5.2 Key Accelerator Physics Issues

5.2.1 Electron Cloud Effects

The electron cloud (EC) can cause beam instability. The build-up of accumulated photon electrons and secondary electrons has proved to be one of the most serious restrictions on collider luminosity in PEP II, KEKB, LHC, and BEPC [1, 2]. The EC links together the motion of subsequent bunches and induces coupled bunch instability. It also leads to emittance blow-up and luminosity degradation [3, 4]. For next-generation super proton colliders such as SPPC, a bunch population higher than 10^{11} and a bunch spacing less than or equal to 25 ns, the EC effect will be a critical factor in the ability to reach a luminosity level of 1×10^{35} $cm^{-2}s^{-1}$.

There are three sources for the electron cloud, photon electrons, residual gas ionization and secondary electron emission. At a vacuum of about 1.0 nTorr, the residual gas density is about 2×10^{13} $1/m^3$. With an ionization cross section of 2.0 Mb, the electrons produced by gas ionization can be ignored. The necessary condition for electron amplification is that the average secondary electron emission yield (SEY) exceeds one. Electron multipacting occurs if the electrons emitted from the vacuum chamber wall reach the opposite side wall just prior to the arrival of the next bunch. The criterion $n = \frac{r^2}{n_b r_e L_{sep}}$

can be used to estimate which kind of electrons are the dominant component in the electron cloud. In the formula, r is the radius of the vacuum pipe, n_b the number of particles in the bunch, L_{sep} is the bunch spacing and r_e=2.8×10^{-15} m, the classical electron radius. If n<1, part of the primary electrons are lost before the next bunch arrives and secondary electrons dominate the electron cloud; if n>1, the primary electrons interact with more than one bunch and photon electrons compose most of the electron cloud. The estimated parameter n for different pp colliders are listed in Table 5.2.1. The EC build-up saturates when the attractive beam field at the chamber wall is compensated on the average by the electron space charge field. The line density of the electron cloud in the vacuum chamber is $\lambda_e = n_b/L_{sep}$, which corresponds to the volume density $\rho_{e,neutr} \approx \frac{\lambda_e}{\pi ab}$, where a and b are half sizes of the elliptical vacuum pipe. According to the estimated neutralization density shown in Table 5.2.1, the EC density in the SPPC rings will be comparable to those at LHC and FCC-hh.

The EC links oscillation between subsequent bunches and may lead to coupled bunch instability. The action propagated by the EC between subsequent bunches can be presented as a wake field expressed as $W_{ec,x,y}/L = 4\pi\rho_{e,neutr}/n_b$, which gives the dipole component per unit length of the wake field. Based on the wake field, the growth rate for the coupled bunch instability is shown as $\frac{1}{\tau_{e,CB}} = \frac{2r_p n_b c^2}{\gamma\omega_\beta ab L_{sep}}$. The coupled bunch instability can be damped by a feedback system. The EC also drives transverse emittance blow-up, which is very important at lower energy when the synchrotron radiation damping is very weak. The single bunch instability caused by the short-range wakefield can be analysed with the two-particle model where head and tail particles each carry a charge of $n_b e/2$. The head particles disturb the EC distribution and the oscillation in the bunch head will be transferred to the bunch tail. For sufficiently long bunches, $\omega_e\sigma_z > c\pi/2$, the wake field felt by the tail particle is $W_{0,SB} \approx 8\pi\rho_e C/n_b$, where C is the circumference of the ring and ρ_e is the volume density of the accumulated electron cloud. The single bunch instability manifests itself as a strong-tail or transverse mode coupling instability (TMCI). With the strong head-tail model, the dimensionless parameter $\Gamma = \frac{N_b r_p W_{0,SB}\bar{\beta}}{16\gamma\nu_s} < 1$, is used to give the wakefield threshold. The EC threshold density for the instability is expressed as $\rho_{e,threhold} < \frac{2\gamma\nu_s}{r_p\pi C\bar{\beta}}$. Rough estimates on TMCI and the density threshold for SPPC are summarized in Table 5.2.1. Some measures such as solenoid magnetic fields, clearing electrodes, or pipe coating should be taken to diminish the electron cloud.

Table 5.2.1: Estimates on electron cloud instability for some super pp colliders [5]

	LHC	FCC-hh	SPPC
Circumference(km)	26.7	100	100
Bunch particles (10^{11})	1.15	1.0	1.8
Bunch spacing (ns)	25	25	25
Beam energy (TeV)	7	50	50
Pipe radius (mm)	20	13	13
Parameter *n*	0.165	0.189	0.105
Neutralization line density (10^{10}/m)	1.53	1.33	2.394
Neutralization volume density (10^{13}/m^3)	1.22	2.51	4.518
Wake field *W/L* (10^3/m^3)	1.33	3.15	3.154
Betatron tune	43.3	-	60.3
Synchrotron tune	0.006	0.002	0.005
Growth time (ms)	4.31	-	2.437
Threshold electron density (10^{13}/m^3)	0.66	0.147	0.360

With the above parameters, the primary simulation for electron cloud density in different region are shown in Fig 5.2.1. It is clear that the electron cloud will be serious in the drift region of the ring. Because of the magnetic field, the distribution of electron cloud will be reconstructed and the central density will be restricted to a lower level.

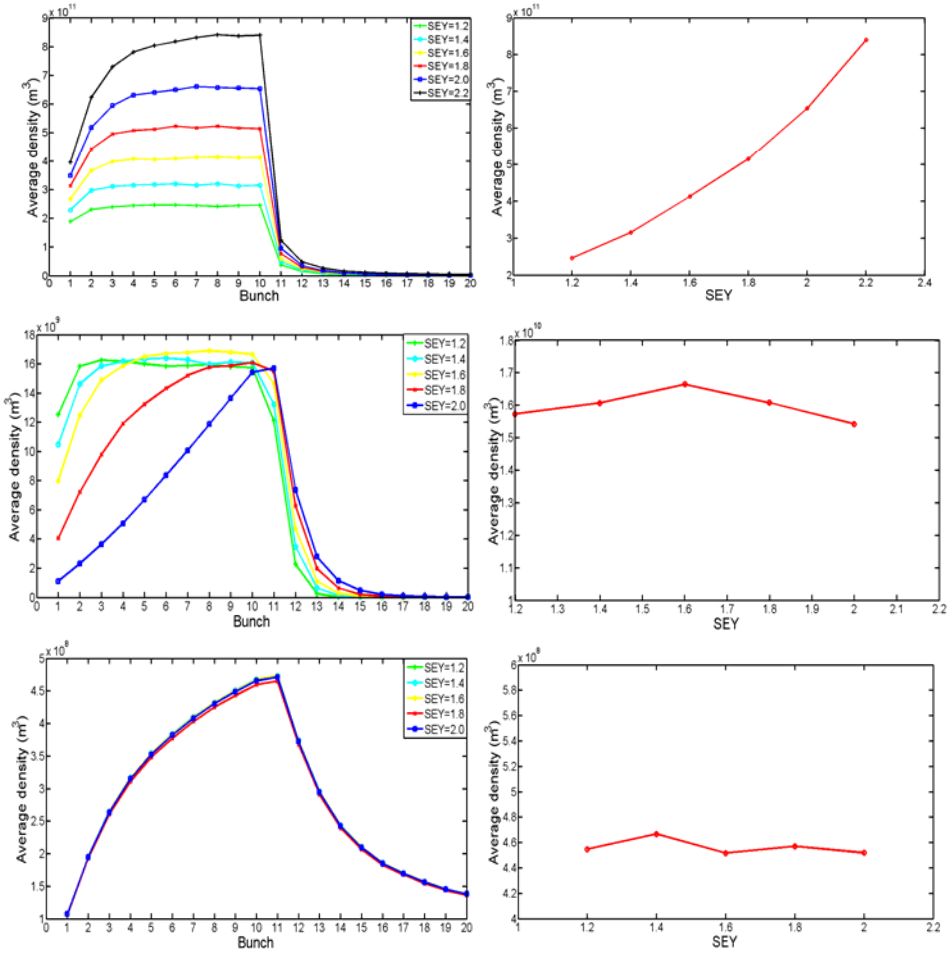

Fig 5.2.1 Electron cloud density in different region of the ring

(upper: drift region; middle: dipole region; bottom: quadrupole region)

The accumulated electron cloud as a focusing force on the proton beam will cause an incoherent tune shift. Assume the EC is transversely uniform around the beam, the tune shift is given by the formula [2] $\Delta\nu = \frac{r_p}{\gamma}\bar{\beta}\rho_{ec}C$. A larger tune shift can lead to a severe drop in luminosity. For SPPC, with an average betatron function of about 100 m, the tune shift is estimated to be about 0.00263 which cannot be ignored when the EC density is about 1.0×10^{13} m^{-3}. Therefore, in the future lattice design, it is necessary to consider the tune shift caused by the EC.

Because of very high synchrotron radiation power and low-temperature beam pipes for the superconducting magnets, the deposited power on the beam screen from the secondary electron multipacting may be a serious issue. The measured deposited power in the dipole magnets of LHC has proven to increase exponentially to about 10 W/m, when SEY is larger than 1.4. Therefore, SEY at SPPC should be controlled to stay below 1.4 or even 1.2 by coating TiN or NEG on the internal walls of the vacuum chamber and devices inside the vacuum.

5.2.2 Injection and Extraction

5.2.2.1 Injection

Injection into SPPC is performed in a 1250-merters-long straight section. A series of Lambertson type septum magnets and kicker magnets inserted in the drift section of a FODO cell deflect the beam onto the ring closed orbit. The defocusing quadrupole between septum magnets and kicker magnets provides part of the required total deflection for eccentric beam injection, thereby reducing the required strength of kicker magnets. The half-cell length of the FODO structure is determined by the deflection angle and energy of the injected beam. At nominal beam energy of 2.8 TeV, the half-cell length should be more than 100 meters for achievable filed strengths of 1.6 T for normal conducting septum magnets and 0.6 T for kicker magnets.

The extremely high stored energy makes machine protection a major issue, and imposes constraints on the injection scenario. In order to prevent damage caused by asynchronous triggering of kicker magnets, passive protective insertions are necessary in front of superconducting magnets downstream from the kicker magnets. Each bunch contains 1.8×10^{11} particles at an injection energy level of 2.8 TeV and delivers 80.6 KJ beam energy into SPPC. A staged injection of batches with limited number of bunches is a feasible solution to keep structure stresses and thermal load in absorbers below their damage level. The number of bunches per batch is 112 and the delivered beam energy in one injection cycle is about 9 MJ.

The staged injection scenario establishes the dependence of the bunch filling factor on the kicker magnet rise time. In order to ensure a filling factor of 76% in SPPC, the time interval between the injected batches should be less than 1 μs, which imposes high requirements on the design of high strength kicker magnets and switches. The switches of SS extraction kickers and SPPC injection kickers have to be synchronized and have a common repetition rate.

5.2.2.2 Extraction

Extraction from SPPC is performed in a 4300-merters-long straight section. The extraction system of SPPC adopts a scenario of single turn extraction, which means all the beam bunches are extracted in one turn and transported towards an external dump block. The extraction system design addresses two key issues, the layout design, and the dump system design.

Due to the extremely high energy of the extracted beam, asynchronous triggering of extraction kicker magnets would cause serious localized machine element damage. Necessary protection against all failure modes and the limited length of the straight section are the main challenges in the layout design. There are several different schemes for layout design. Extraction kicker magnets and septum magnets which deflect the beam out of the ring orbit are indispensable elements in all layout designs. Other elements in the extraction insertion such as quadrupoles, bending magnets and specially designed septum magnets are being studied. Defocusing quadrupoles after extraction kicker magnets would decrease the required strength of the kicker magnets. A local bump formed by four bending magnets or two bending magnets with a series of special septum magnets would further decrease the kicker magnet strength and accommodate to the limited

straight section length. In order to improve kicker magnet stability, there are several possible solutions, e.g. using a solid-state switch of better stability, or improving synchronization of triggering for all kicker magnets. If one of the kicker magnets is pre-triggered, all the other kicker magnets must be triggered in a very short time to avoid possible serious machine damage. Use of a number of small strength kicker magnets is an attractive possibility. The orbit oscillation caused by the pre-triggering of one kicker magnet is restricted to one sigma of beam size with a specially designed optics, thus ensuring the safety of the machine. Passive protective insertions are also necessary in front of septum magnets and superconducting magnets downstream of the kickers to protect these elements.

The 14.5 GJ of stored energy in the beam poses a great challenge to the dump system design. There are several absorber materials commonly used in accelerators, e.g. laminated graphite, pressurized water, pressurized gas, solids with low melting point like lead and ice. For simplicity and stability, the absorber at SPPC will be made up of graphite interlayers of different densities, surrounded by iron and concrete blocks to shield the radiation. Since the transverse dimension of the extracted beam is small, the beam must be sufficiently diluted to ensure that the energy density deposited in the graphite absorber is below a safe level. A set of horizontally and vertically deflecting dilution kicker magnets are required to sweep the bunch impact positions impinging on the absorber. Superconducting insertion quadrupoles can be added in the beam dump line to reduce the strength of the dilution kicker magnets. A beam sweep trajectory of an Archimedes spiral makes the distribution of energy deposition more uniform, thus making full use of the absorber capability. Detailed studies on sweep patterns and curves are needed to find ways to absorb beam energy up to 14.5GJ safely.

5.2.3 References

1. Miguel A. Furman, "The Electron-Cloud Effect in the Arcs of the LHC," LHC Project Report 180,1998.
2. F. Zimmermann, G. Rumolo, "Two-stream Problems in Accelerators," CERN SL-2001-057(AP),2001.
3. G. Arduini,V. Baglin,et,.al, "Present Understanding of Electron Cloud Effects in the Large Hadron Collider," PAC 2003, Portland, Rregon, USA, 12-16, May,2003.
4. E.Benedetto, D.Schulte and F.Zimmermann, "Simulation study of electron cloud induced instabilities and emittance growth for the CERN Large Hadron Collider proton beam", PRST-AB,8,124402(2205).
5. A.Ball, M.Benedikt, et al,, "Future Circular Collider Study Hadron Collider parameters," FCC-1401101315-DSC.

5.3 Preliminary Accelerator Physics Design

5.3.1 Preliminary Lattice Design

5.3.1.1 General Layout and Lattice Consideration

Different lattice designs are under study, especially for the arcs. Typically, there are three kinds of arc designs for such a proton-proton collider, with the differences in the dispersion suppression methods. One uses full bend suppressors which incorporate the same dipole magnets as in the regular arc cells; another uses half bend suppressors which

have half dipole strength as in the regular arc cells; and the third one uses the LHC-like suppressors which have less dipole strength but shorter cell length. The latter appears to be more compatible with an electron-positron collider in the same tunnel, which is the case for CEPC-SPPC. In this report, two lattice designs, one with the LHC-like suppressors and the other with half-bend suppressors, are presented.

For both designs, there are basic requirements: 1) Long straight sections, one long straight section (LSS) of least 4.3 km for collimation, six long straight sections of at least 1.25 km each for the two main IPs, RF stations, injection, one reserved for e-p and A-A IPs. 2) Magnetic fields and apertures, dipole magnet strength is limited to 16 T, dipole magnet length to 15 m, quadrupole magnet pole tip field limited to 16 T. Figs. 5.3.1 and 5.3.2 are the layout of SPPC and the complex arrangement with CEPC in the same tunnel.

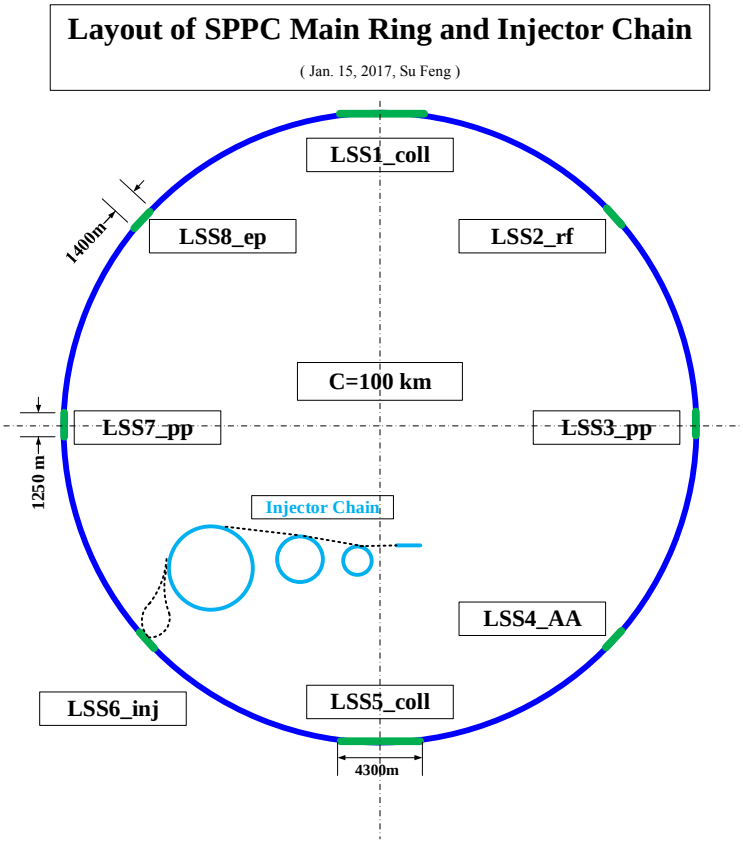

Figure 5.3.1: Layout of SPPC

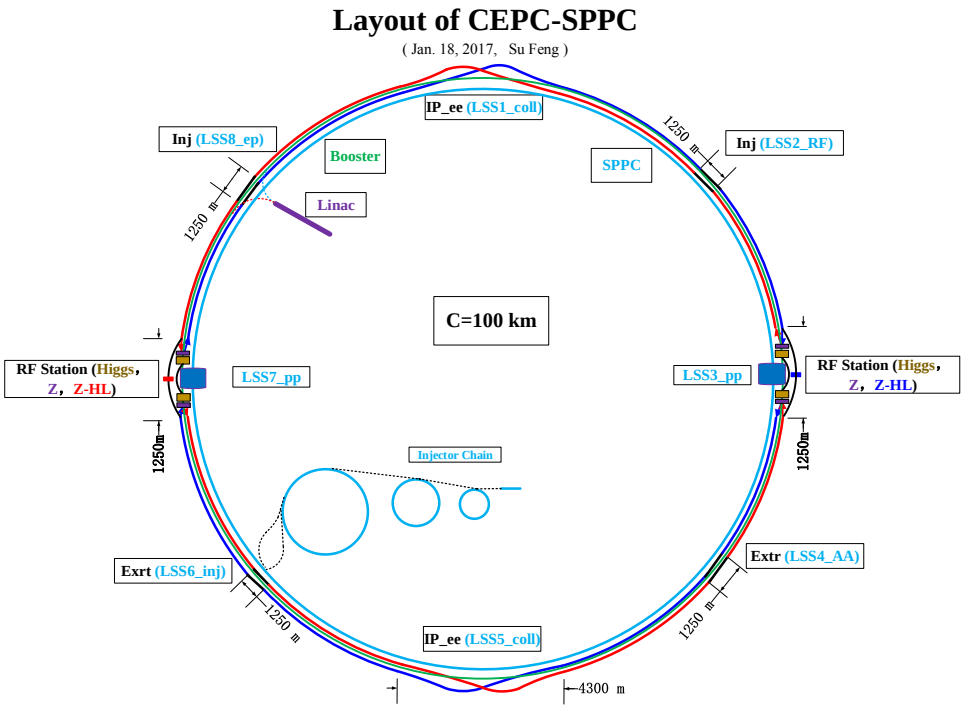

Figure 5.3.2: Layout of SPPC-CEPC.

5.3.1.2 Lattice Design with LHC-like Suppressors

5.3.1.2.1 The Arcs

The arcs are composed of standard FODO cells. The basic phase advance chosen for one FODO cell is 90 degrees in both transverse planes. But the phase advance may be changed slightly in practice in order to adjust betatron tunes. To decide the length of FODO cells, we make a balance between the dipole filling factor and beam optics. Generally speaking, the longer the FODO cell, the larger dipole filling factor attainable, but the beta functions and dispersion function will be larger at the same time. Larger beta functions and dispersions will require larger magnet apertures, which is critical to the magnet cost. What's more, the dispersion function also influences the momentum collimation design; details will be described in Section 5.3.2.

The magnets arrangement and beam optics of one standard FODO cell in the present design are shown as Fig. 5.3.1. The horizontal beta function and dispersion function have their maximum values in the middle quadrupole, which are 362 m and 2.36 m, respectively. There are 12 bending magnets in the cell, with a length of 14.45 m and magnetic strength of 15.725 T. The quadrupole length is 6 m. The distance between dipoles is 1.4 m to provide installation clearance, and the distance between dipole and quadrupole is 3.5 m to allow room for multipole and corrector magnets. A sextupole is placed on the right side of each quadrupole for chromatic correction. The space on the left side of each quadrupole can be used to install beam diagnostics equipment such as BPMs. The length of a standard FODO cell is 213.4 m, and there are 46 such cells in each arc.

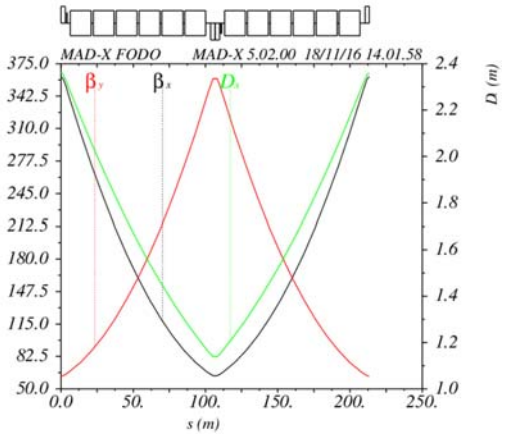

Figure 5.3.1: Lattice functions of a standard arc FODO cell

5.3.1.2.2 The Dispersion Suppressor

The dispersion suppressor (DS) matches the dispersion and beta functions between adjacent arc and long straight section. Besides matching the optics, the dispersion suppressor is designed to reserve the ability to slightly adjust the SPPC layout to meet the compatibility requirements between the CEPC and SPPC. The present design of the dispersion suppressor is showed in Fig. 5.3.2. This is similar to the LHC design. It is composed of two FODO cells, which are shorter than a standard arc cell, with only 4 dipoles or empty in each half cell. There is a drift in the first half DS cell designed to be flexible, from 30 m to 80 m. The last half cell is not filled with dipoles to make the betatron function matching easier.

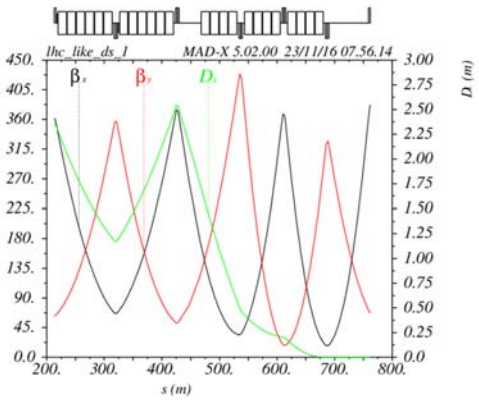

Figure 5.3.2: LHC-like dispersion suppressor of SPPC

5.3.1.2.3 The High Luminosity Insertions

LSS3 and LSS7 are for p-p collisions. The identical lattice structures of LSS3 and LSS7 are anti-symmetrical, so a crossing angle at the IPs can be produced and the beams go from outer ring to inner ring or reverse. The preliminary lattice designs of LSS3 and LSS7 are shown in Fig. 5.3.3. They are composed of the following sections listed in order beginning from the interaction point.

1) Free space for hosting a large detector: L*=45 m, from the interaction point to the first triplet quadrupole.

2) Inner quadrupole triplet: This is critical to produce very small beta functions (β*) at the IP. With the nominal design goal of β*=0.75 m, the maximum beta function at the inner triplets quadrupoles is very large, about 18 km.
3) Pair of separation dipoles: These make the required beam separation between the two beams from the nominal 0.3 m at the arcs to almost zero at the IP. The bending magnet D1 close to the inner triplet is a single aperture dipole, and the bending magnet D2 close to the outer triplet is a twin-aperture dipole, with an aperture separation of 300 mm. The D1 and D2 magnets are 10 m long. The strengths of both D1 and D2 are 15.725 T, but with opposite bending directions. The distance between D1 and D2 is 149 m.
4) Outer quadrupole triplet: This matches the beta functions and dispersion function into the arc together with the dispersion suppressor. The dispersion function is matched to be near zero at the interaction point.

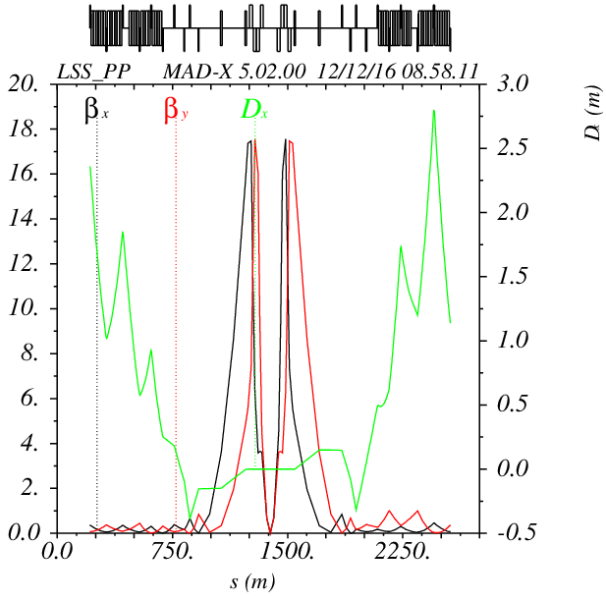

Figure 5.3.3: Lattice of LSS3 and LSS7

5.3.1.2.4 Dynamic Aperture

To carry out a preliminary study of dynamic aperture or multiple particle simulations of the collimation system, an integrated lattice is required. Thus we use two simple FODO lattices for the insertions that are not yet designed, such as RF stations, injection, e-p and A-A IPs, as shown in Figs. 5.3.4 and 5.3.5.

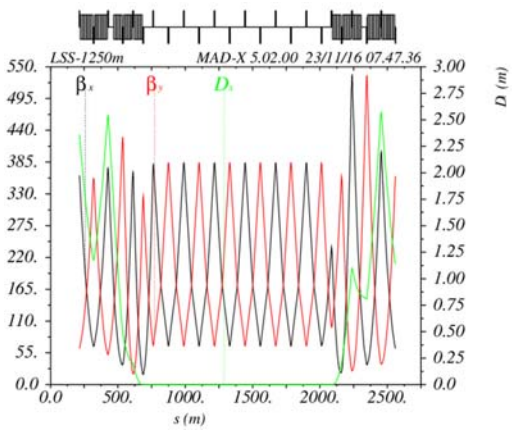

Figure 5.3.4: Long straight section 1250 m

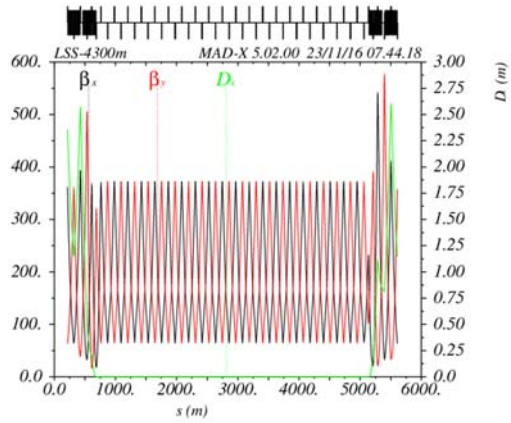

Figure 5.3.5: Long straight section 4300 m

Using the first lattice version, a preliminary study of dynamic aperture was performed with the code SIXTRACK. The only nonlinear elements included in the tracking are chromaticity correction magnets. The dynamic aperture at the collision energy seems to be acceptable, as shown in Fig. 5.3.6, about 160 σ in the horizontal plane and about 120 σ in the vertical plane. The simulation at the injection energy is under way; it will be worse due to poor magnetic field quality.

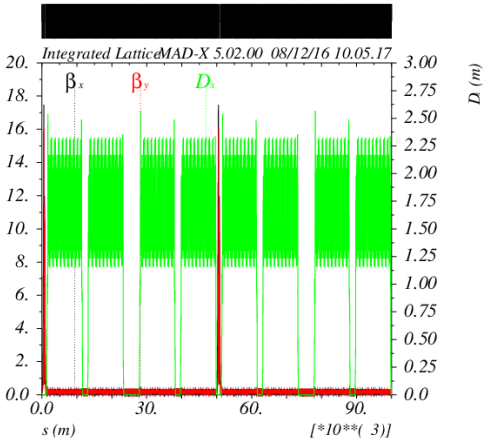

Fig. 5.3.6: Lattice functions of the integrated lattice

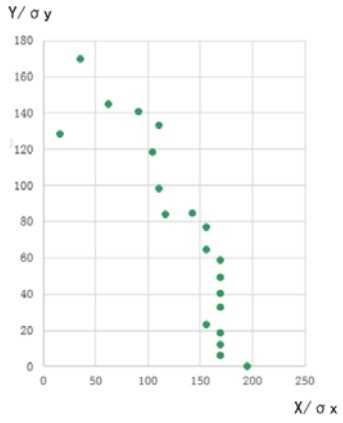

Fig. 5.3.7: Dynamic aperture at top-energy

5.3.1.3 Lattice Design with Half-bend Suppressors

5.3.1.3.1 Arc and FODO Cell

Here we introduce a preliminary lattice design. There are 8 arcs and 8 long straight sections. We use FODO in the ARC. Each cell has 8 dipoles of length 14.8 m and strength 20 T. The total cell length is 215.6 m, maximum beta function is 366.426 m, minimum beta function is 63.424 m and phase advance is 90 degree in both horizontal and vertical planes. The quadrupole gradient and dipole parameter are reasonable according to the Pre-CDR choices. The aperture of the quadrupole is also reasonable at both injection and collision energy. Figs. 5.3.8 and 5.3.9 show the optics of the FODO cell and the arc.

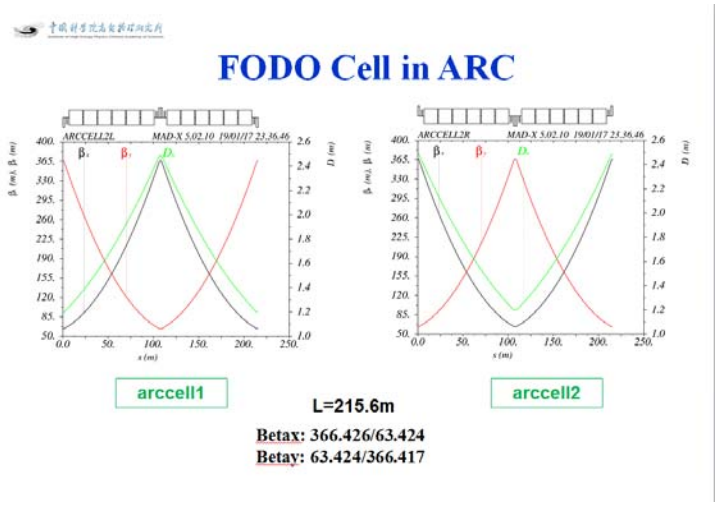

Fig. 5.3.8: SPPC FODO cell optics.

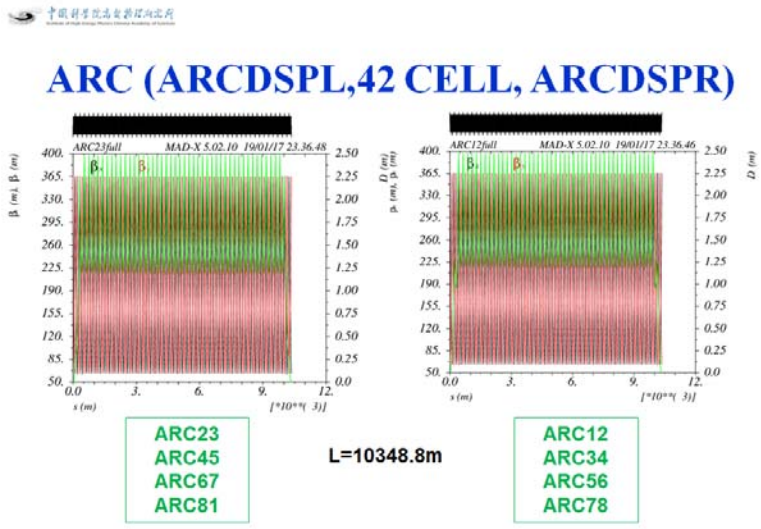

Fig. 5.3.9: SPPC arc optics.

5.3.1.3.2 Dispersion Suppressor

For 90 degree phase advance FODO cell, the dispersion suppressor section has three schemes, called full-bend scheme, half-bend scheme and missing-dipole scheme. In this design we choose the half-bend scheme as it's the simplest. Fig. 5.3.10 is the optics of dispersion suppressor section.

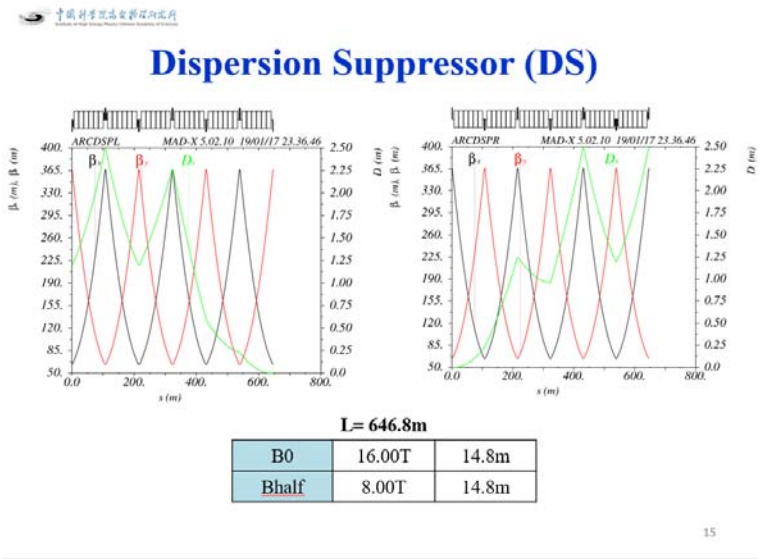

Fig. 5.3.10: The optics of the dispersion suppressor section.

5.3.1.3.3 Long Straight Section and Interaction Region

There are 8 long straight sections in the SPPC lattice: LSS1_coll, LSS2_inj, LSS3_pp, LSS4_RF, LSS5_coll, LSS6_RF, LSS7_pp and LSS8_extr. Long straight sections 3 and 7 are for low β pp collision. Long straight section 1 and 5 are for collimation using the 4.3 km space. Long straight section 4 and 6 are for RF stations. Long straight section 2 and 8 are for injection and extraction. Figs. 5.3.11-5.3.14 show the optics of these long straight sections.

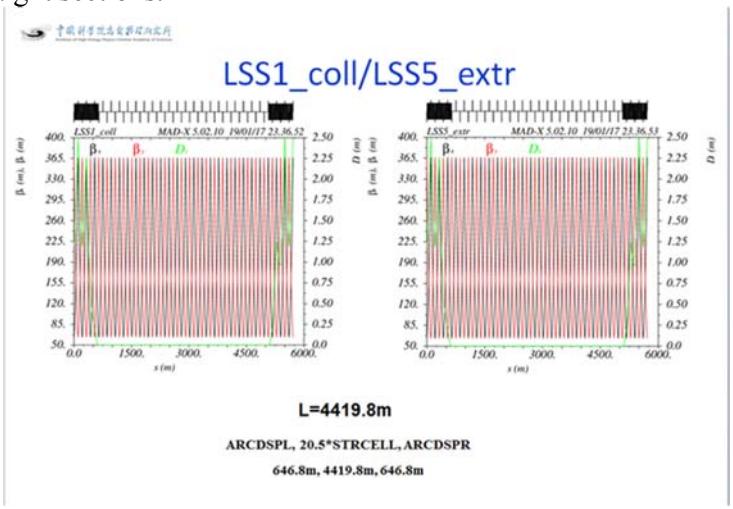

Fig. 5.3.11: Optics of LSS1 and LSS5.

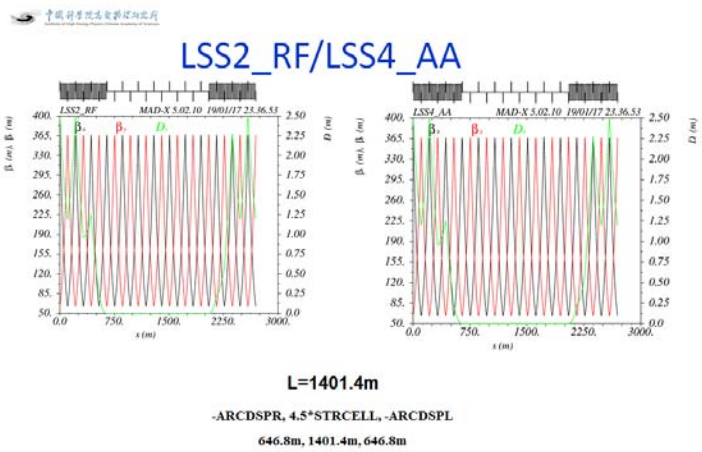

Fig. 5.3.12: Optics of LSS2 and LSS4.

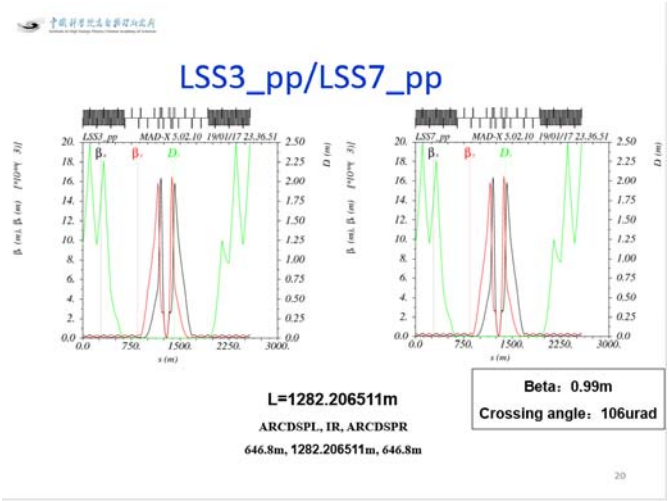

Fig. 5.3.13: Optics of LSS3 and LSS7.

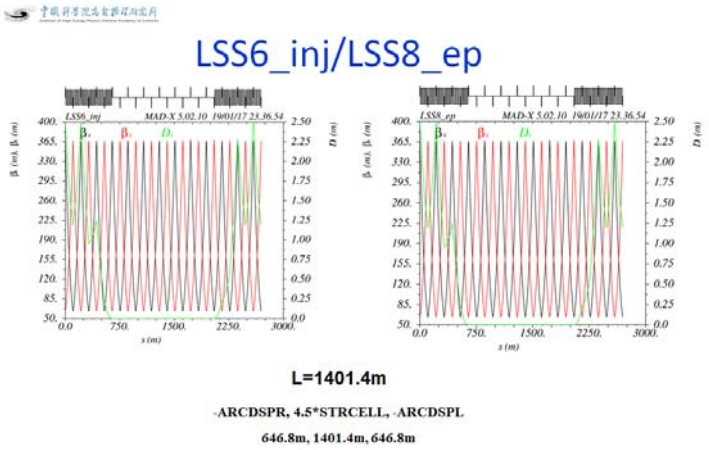

Fig. 5.3.14: Optics of LSS6 and LSS8.

5.3.1.3.4 Dynamic Aperture Study and Beam Dynamics

Dynamic aperture is a very important and interesting issue in pp colliders. The Dynamic aperture is divided into 2 kinds. One is called Real-World-Dynamic-Aperture (RW-DA) defined as the largest amplitude at which particles remain in the accelerator over the time range of interest. The other is called Potential-Dynamic-Aperture (PO-DA) defined as the onset of global chaos, which also means the largest amplitude with mainly regular motion. Insignificant chaotic layers within the regular regime will be ignored. However considerable wide "chaotic spikes" have to be taken into account. It turns out that the PO-DA is typically smaller than the RW-DA estimate. The chaotic motion is measured by the evolution of initially close-by particles. The Lyapunov exponent is a sensitive signal for DA tracking.

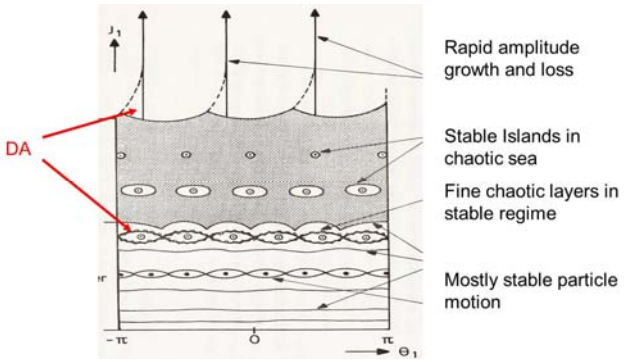

Figure 5.3.15: Dynamic aperture scheme

A. Dynamic Aperture without an Interaction Region

First, we studied the dynamic aperture without an interaction region. There are 8 arcs in the main ring and 8 long straight sections. We use simple FODO in the long straight section, later we can optimize the long straight section design for different uses like RF stations, injection, extraction and collimation.

Following is the dynamic aperture obtained from Sixtrack. Fig. 5.3.16 shows 4-D phase space for regular and chaotic motion. Fig. 5.3.17 shows the evolution of the distance of phase space for regular (left) and chaotic (right) motion. Figs. 5.3.18 and 5.3.19 show the horizontal and vertical phase space projections for the regular (left) and the chaotic (right) cases. Fig. 5.3.20 shows the physical phase space projections for the regular (left) and the chaotic (right) cases. We can deduce from these figures that the dynamic aperture is about 38.39 mm (200 σ_x) in the horizontal plane and 13.56 mm (200 σ_y) in the vertical plane.

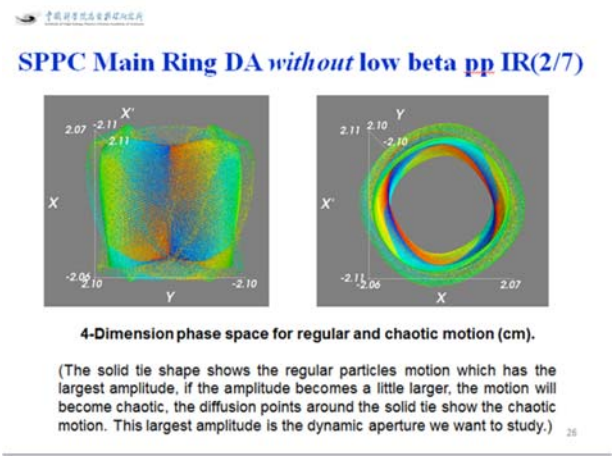

Fig. 5.3.16: 4-D phase space for regular and chaotic motion (cm).

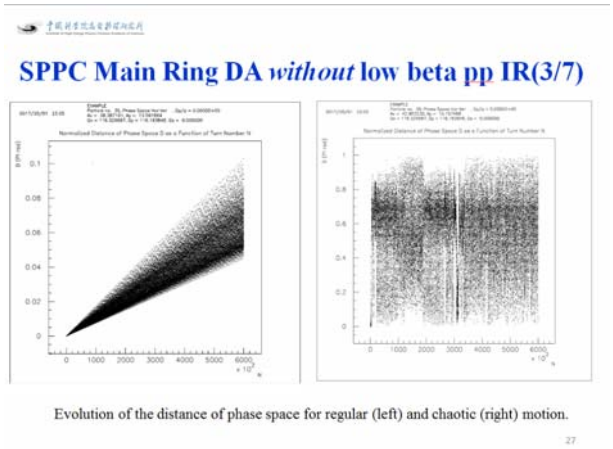

Fig. 5.3.17: Evolution of the distance of phase space for regular (left) and chaotic (right) motion.

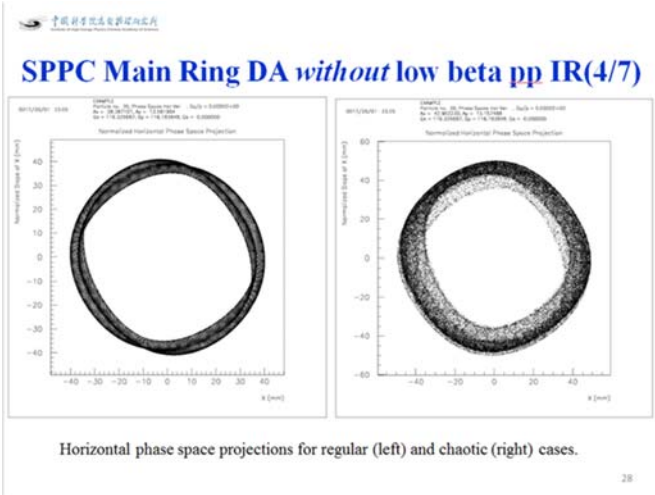

Fig. 5.3.18: Horizontal phase space projections for regular (left) and chaotic (right) cases.

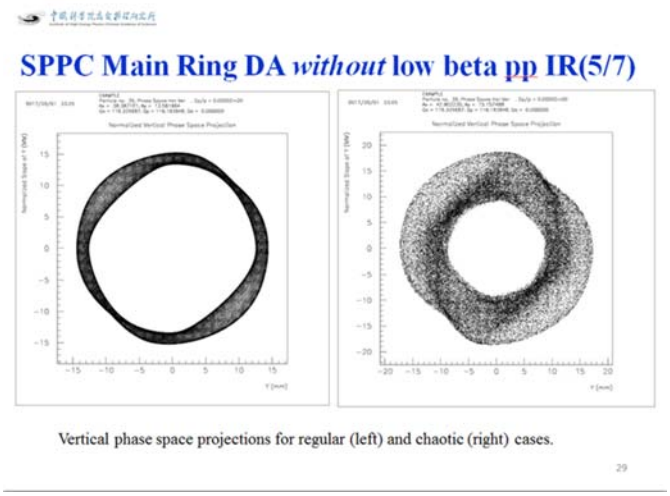

Fig. 5.3.19: Vertical phase space projections for regular (left) and chaotic (right) cases.

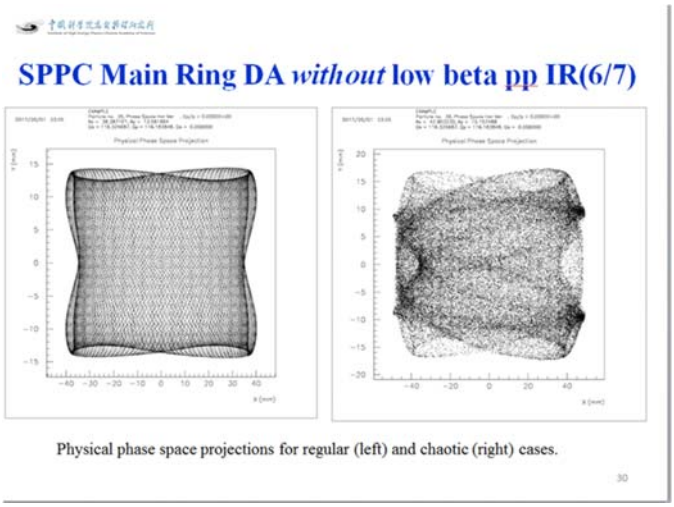

Fig. 5.3.20: Physical phase space projections for regular (left) and chaotic (right) cases.

B. Dynamic Aperture with an Interaction Region

Following is the dynamic aperture with a low beta pp interaction region included. The beta function at the IP is 0.99 m. The maximum beta function in this region is about 15.9 km. The dynamic aperture becomes smaller. At the low beta pp IP, the dynamic aperture is only 1.22 mm (140 σ) in both horizontal and vertical planes because the beam size is very small (8.17 μm).

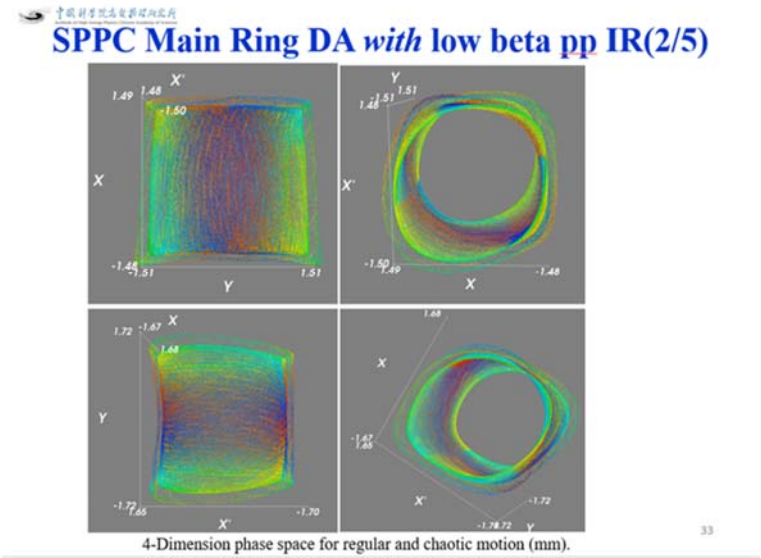

Fig. 5.3.21: 4-D phase space for regular and chaotic motion (cm).

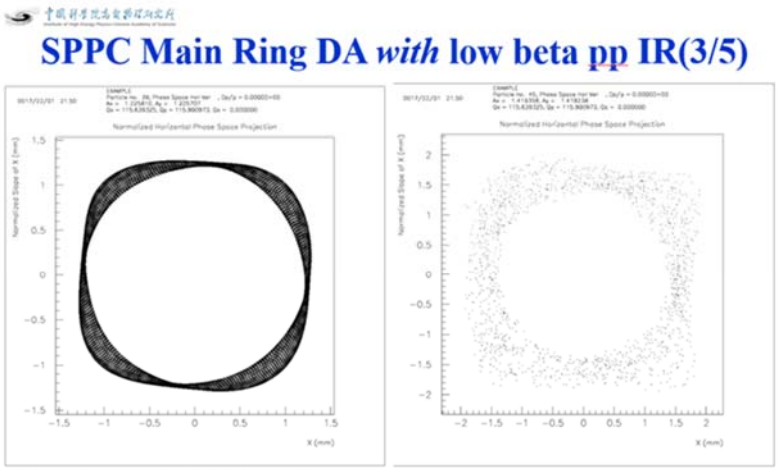

Fig. 5.3.22: Horizontal phase space projections for regular (left) and chaotic (right) cases.

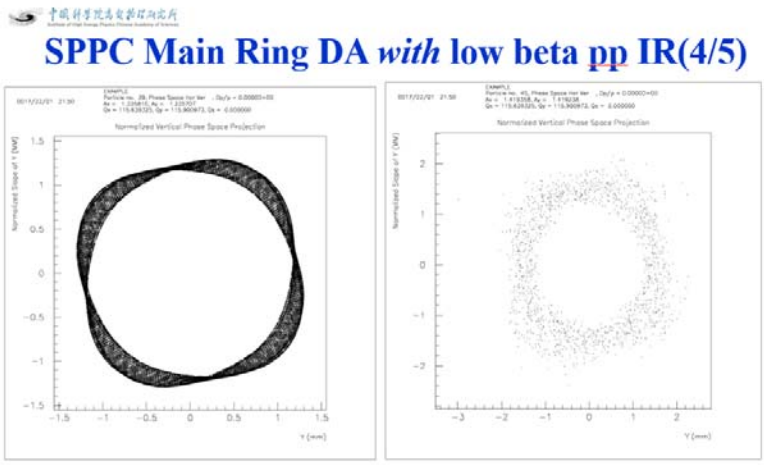

Vertical phase space projections for regular (left) and chaotic (right) cases.

Fig. 5.3.23: Vertical phase space projections for regular (left) and chaotic (right) cases.

5.3.1.3.5 Summary

We have shown the SPPC lattice including the arc, half-bend scheme dispersion suppressor section and long straight sections. We also have shown the first dynamic aperture and beam dynamic studies with and without a low beta pp interaction region although there remains a considerable amount of work to be done to optimize these lattices.

5.3.2 Preliminary Collimation Design

5.3.2.1 Introduction

For SPPC [1], the stored energy per beam is extremely high up to 14.5 GJ (1.8×10^{15} protons at 50 TeV), so the beams can be highly destructive. Even a tiny fractional loss of the full beam (on the level of 30 mJ/cm^{-3}) in a superconducting magnet could lead to a quench, and large beam losses could cause serious damage to accelerator components. However, beam losses are unavoidable in a collider where beam-beam collisions are the leading loss source. Therefore, besides strictly controlling beam losses and having an extremely reliable beam abort system, to prevent the unavoidable beam losses around the ring circumference, a collimation system is necessary. The collimation system must be sophisticated, robust and extremely-efficient to safely dispose of beam losses and have at least the following functionality [2]:

1) Very efficient cleaning of the beam halo during the full SPPC beam cycle in order to avoid beam-induced quenches of the superconducting magnets.
2) Passive protection of the machine aperture against abnormal beam loss.
3) Minimization of halo-induced backgrounds in the physics experiments.
4) Abort the gap cleaning to avoid spurious quenches after normal beam dumps.

To quantify the performance of the collimation system, the local cleaning inefficiency is defined as:

$$\tilde{\eta}_c = \frac{N_{lost}^{\Delta s}}{\Delta s \cdot N_{abs}}, \tag{5.3.1}$$

where $N_{lost}^{\Delta s}$ is the number of particles lost locally over a length of Δs = 10 cm, and N_{abs} is the total number of particles absorbed in the collimation system.

The required cleaning inefficiency or in other words the maximum leakage rates can be specified from the quench limit, the minimum beam lifetime, and the total intensity. The quench limit R_q is related to the limit of heat transmission capability and the maximum energy density deposition. The total intensity N_{tot}^{q} at the quench limit R_q and the minimum lifetime τ_{min} is given by:

$$N_{\mathrm{tot}}^{q} = \frac{\tau_{\mathrm{min}} \cdot R_q}{\tilde{\eta}_c}. \tag{5.3.2}$$

Fig. 5.3.24 shows the maximum total intensity at the quench limit as a function of the local cleaning inefficiency. We assumed that a minimum beam lifetime of 0.1 hours at injection energy and 0.2 hours at top energy must be satisfied just like in the LHC. From the figure, it is noted that the SPPC at top energy has the most stringent requirements for cleaning inefficiency. The designed intensity of 1.8×10^{15} protons per beam requires a cleaning inefficiency of 5×10^{-7} m^{-1}, which is more stringent by about an order of magnitude than the LHC.

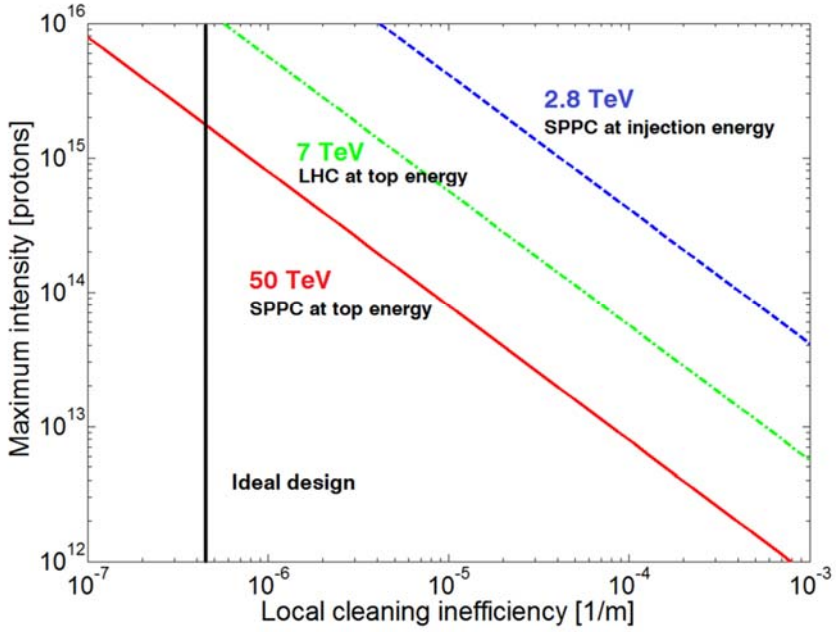

Fig. 5.3.24. The maximum total intensity is shown as a function of the local cleaning inefficiency for SPPC injection, top energy, and the LHC top energy. A beam lifetime of 0.2 hours at top energy and 0.1 hours at injection is assumed.

To date, the LHC collimation system is state-of-the-art performance. The cleaning efficiency can reach up to 99.993% with stored energy of 360 MJ and it ensures there is only about 10^{-5} local inefficiency in superconducting magnets [3]. However, even this performance is considered insufficient to prevent the superconducting magnets from quenching when upgraded to HL-LHC [4, 5] with stored energy up to 700 MJ. The problem arises from beam loss at the downstream dispersion suppression (DS) section of

the betatron collimation insertion which becomes more important due to single diffractive (SD) effect [6]. The situation will become much more serious at the SPPC energy level, as the SD effect will become the most critical factor preventing further improvement in the collimation efficiency, which means much larger potential cold losses in the DS could cause a quench.

To solve this key issue, a more efficient collimation method for SPPC is required to make sure the unavoidable cold losses due to SD effect could be intercepted to avoid quenches.

5.3.2.2 Preliminary Collimation Design

The proposed collimation method at SPPC is to arrange both the betatron and momentum collimation systems in the same insertion to clean the particles that have significant energy loss due to the SD effect. These particles, which would be otherwise lost in the downstream cold region, will be cleaned by the momentum collimation system. Our studies show that this method is a very efficient way to solve the issue and could greatly improve the cleaning efficiency. Preliminary collimation design and multi-particle simulations for this cleaning method will be introduced below.

In the general case, a particle reaches the primary collimator with a mixing of betatron amplitude and momentum offset. The largest momentum offset δ_{max} which can pass the primary momentum collimator is defined by [7]

$$\delta_{\max} = \frac{n_1\sqrt{\varepsilon}}{\chi_1}, \tag{5.3.3}$$

where n_1 denotes the primary momentum collimator aperture, ε denotes the geometric emittance, while χ_1 denotes the normalized dispersion at the collimator. If the maximum normalized dispersion in the primary momentum collimation section is larger than the one at DS or the whole arc section, in principle there will be very little cold losses at DS in the downstream or even all the arc sections, based on the fact that the arc aperture is larger or not less than n_1.

More specifically, the normalized dispersion at the primary momentum collimator must satisfy [8]

$$\chi_{D,\mathrm{prim}}(n_1) \geq \frac{n_1\chi_{D,\mathrm{arc}}}{A_{\mathrm{arc,inj}}(\delta_p=0)-(n_2^2-n_1^2)^{1/2}}, \tag{5.3.4}$$

to avoid the cold losses at DS or in the arc, where $A_{\mathrm{arc,inj}}$ ($\delta_p = 0$) denotes the arc aperture for on-momentum particles; $\chi_{D,\mathrm{arc}}$ is the normalized dispersion with errors in the focusing quadrupole magnets; n_1, n_2 denote the apertures of primary and secondary momentum collimators. As an example, $A_{\mathrm{arc,inj}}$ ($\delta_p = 0$) = 22.3, $\chi_{\mathrm{D,arc}}$ = 0.246 $\mathrm{m}^{1/2}$, n_1 = 5.5, n_2 = 7.5, one obtains that the required absolute value of the minimum normalized dispersion is 0.079 $\mathrm{m}^{1/2}$.

How to produce the required dispersion for the momentum collimation is a key issue, with the betatron and momentum collimation system in the same long straight section. This is different than the momentum collimation section at the LHC where dispersion is intentionally designed non-zero between the two adjacent DS sections. Here it is required to have an achromatic end at the junction between the momentum collimation and the transverse collimation sections. This means that we need to produce the required

dispersion by cold dipole magnets for the momentum collimation and suppress the dispersion at the end of the section.

Necessary protection from beam loss and radiation for the cold dipole and quadrupole magnets is also indispensable. Some protective collimators are needed to intercept particles with very large momentum deviation. Another limitation is that this collimation method requires significantly longer space for multi-stage collimation system and the two proton beams running in opposite directions than the normal method. One can envision a chicane structure for the momentum collimation, as shown in Fig. 5.3.25.

Fig. 5.3.26 illustrates the betatron and dispersion functions of the whole cleaning insertion. Warm groups of quadrupoles are fixed in the betatron collimation section with maximum β-function of about 1800 m, while superconducting groups of dipoles and quadrupoles are fixed in the momentum collimation section to produce the required dispersion and suppress the betatron function, and also to make sure the final orbit is on the same line with the betatron collimation section. The cryostats for the superconducting magnets are connected by warm vacuum tubes, and some local shielding is provided to protect the superconducting magnets. The first-version parameters are listed in Table 5.3.1.

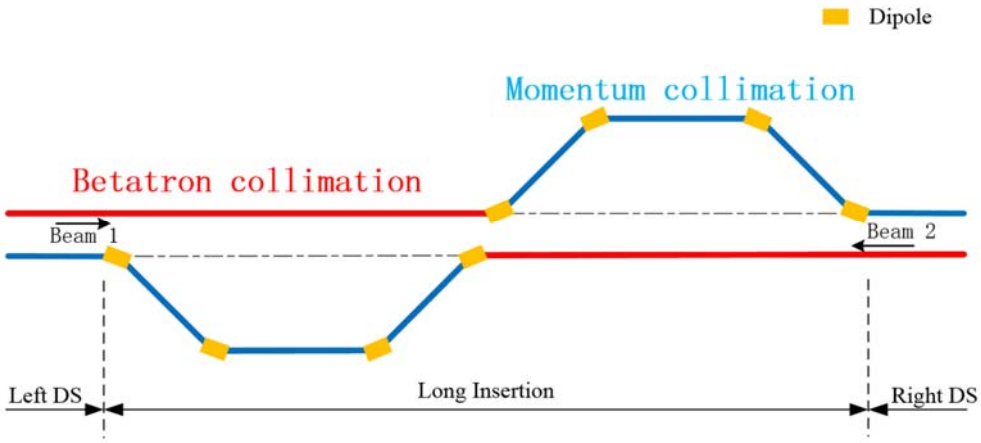

Fig. 5.3.25. Layout of the novel collimation method

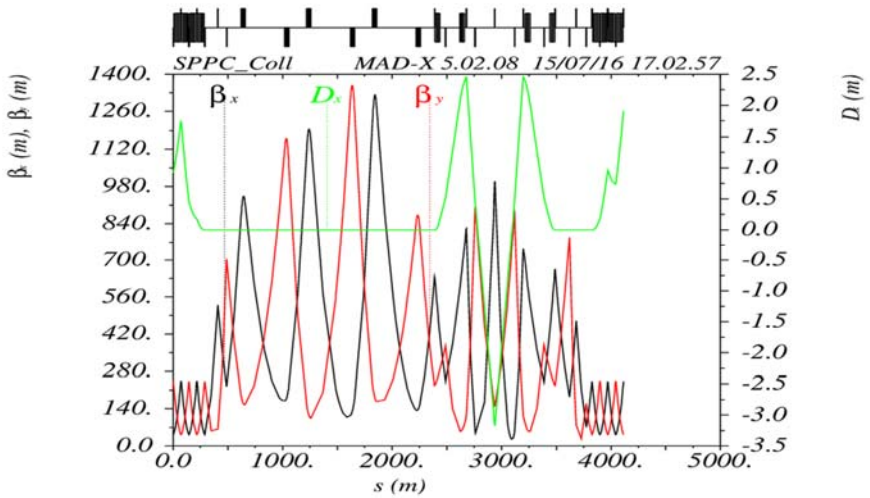

Fig. 5.3.26. The betatron and dispersive functions of the cleaning insertion

Table 5.3.1. Basic parameters of the collimation insertion at the SPPC

Parameter	value	Unit
Total cleaning insertion length	4.2	km
Length of betatron / momentum collimation section	2.6 / 1.6	km
Horizontal phase advance of betatron / momentum collimation section	1.87π /2.25π	rad
Warm/cold quadrupole length	3.3/4.62	m
Warm quadrupole strength	0.00014	m^{-2}
Dipole length in the momentum cleaning section	14.62	m
Number of dipoles per group	4	
Number of dipole groups	4	
Dipole field	16	T
Maximum beta function (β_x / β_y)	1819/1896	m

5.3.2.3 Preliminary Multi-Particle Simulation

Multi-particle simulations using the lattice parameters and collimator settings have been carried out with the code Merlin [9]. As the first approach for the betatron collimator settings, similar physical gaps and phase advances as the LHC have been chosen just for verifying the effectiveness of the novel collimation method, especially in cleaning particles related to the SD effect. The primary momentum collimator is placed at the middle quadrupole between the second and third groups of dipoles, where the normalized dispersion is close to the maximum absolute value. The other momentum collimators are placed downstream with the same phase advances as in the current LHC. One can find the collimator positions in Fig. 5.3.27. For simplicity, the IRs are replaced by simple FODO periods in the simulations. To increase the simulation efficiency with a huge number of particles of 10^8, the initial beam distributions are chosen as a ring type distribution in the horizontal plane and a Gaussian distribution in the vertical plane. In order to protect the cold magnets at the start of the momentum collimation section, protective collimators (used as absorbers) are needed. This is different than placing protective collimators in the DS region where the lattice structure is strictly fixed and tight. It is much easier to provide the space for the collimators at room temperature in the momentum collimation section. According to the positions of the lost particles, three protective collimators of tungsten with aperture the same as the primary momentum collimator are placed there to intercept the particles. The specific locations are as follows: one protective collimator is placed between the second and third dipole magnets of the first dipole group to intercept particles with very large momentum deviation, and the cryostat for the dipole group is split into two parts to allow the insertion of the collimator in room temperature; another one is placed before the quadrupole between the first and

second groups of dipoles to protect the quadrupole; the third one is placed in front of the second group of dipole magnets.

Figs. 5.3.27 and 5.3.28 show the beam loss distributions in the cleaning insertion and the full ring with the protective collimators, respectively. From these two figures, one can see that with suitable protective collimators, nearly all the beam losses in the DS regions due to the SD effect disappear. Almost all the lost particles are in the collimators which are in warm regions. For the present design, only considering the linear condition, the maximum energy spread of particles which can pass through the primary collimator is about 0.1 %. The situation with energy spread is also simulated, as illustrated in Figs. 5.3.29 and 5.3.30. From this two figures, one can see that even with the maximum energy spread, this novel collimation method also has extremely high cleaning inefficiency in the downstream DS regions, at least better than 5×10^{-7}, which meets the SPPC requirement.

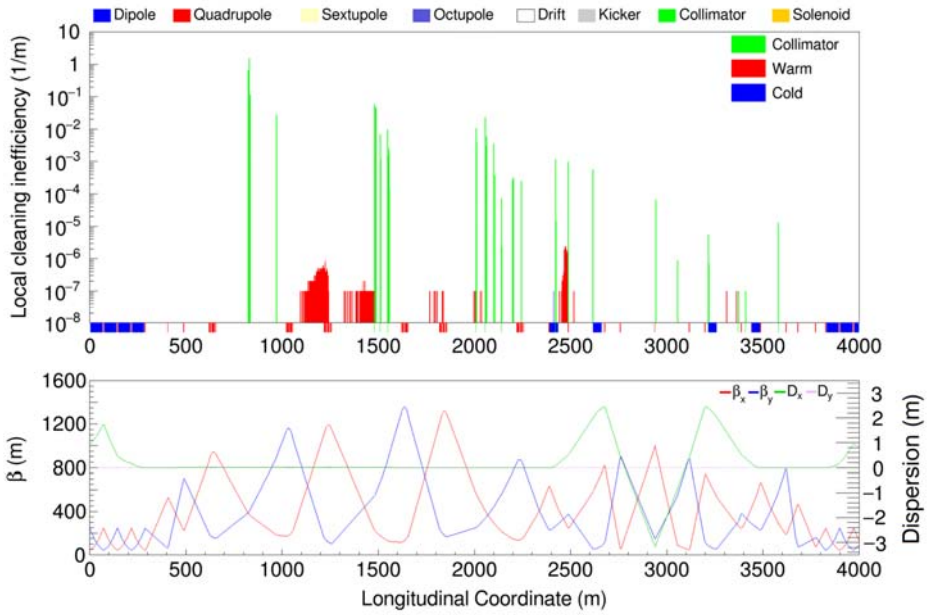

Fig. 5.3.27. The beam loss distribution of the cleaning insertion with protective collimators

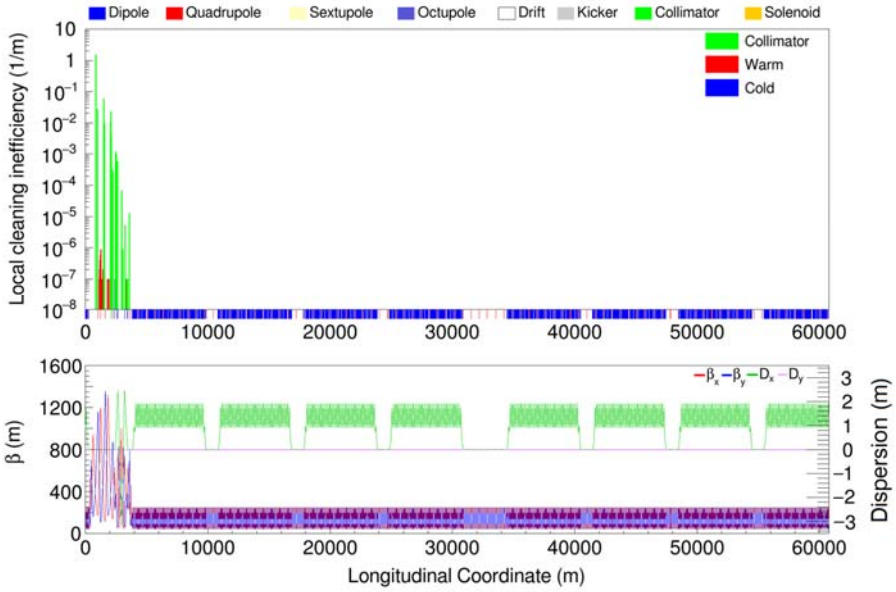

Fig. 5.3.28. The beam loss distribution along the full ring with protective collimators

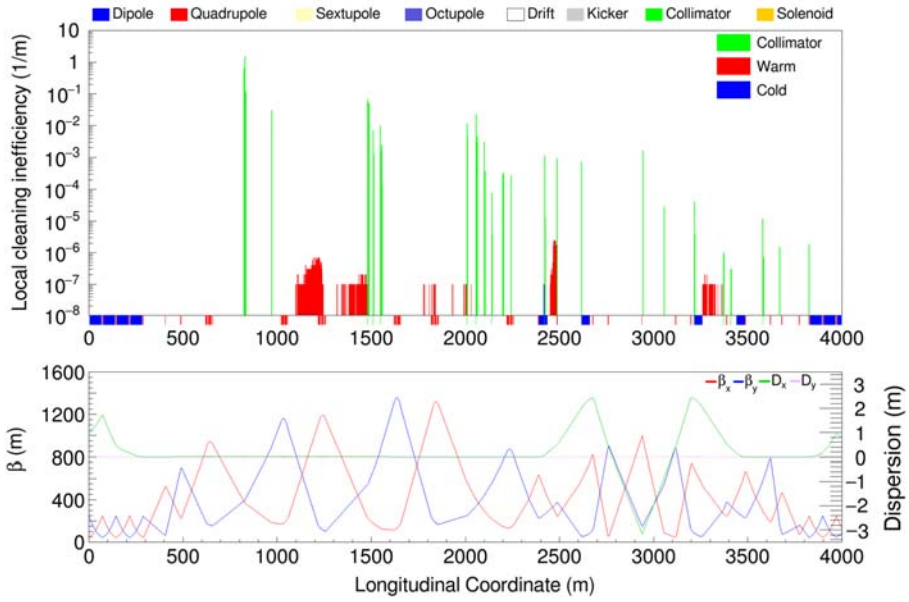

Fig. 5.3.29: The beam loss distribution of the cleaning insertion with energy spread $\delta = 0.1$ %

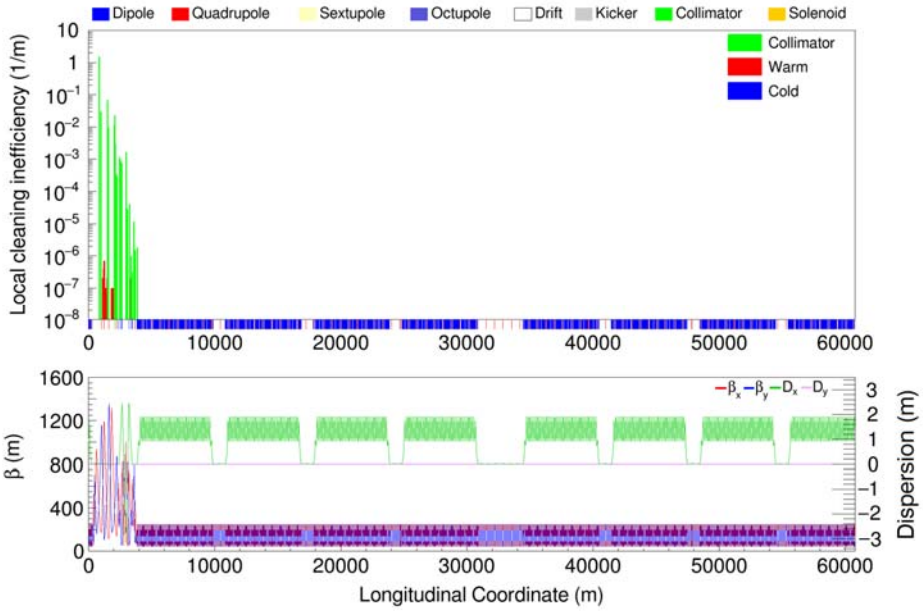

Fig. 5.3.30. The beam loss distribution along the full ring with energy spread $\delta = 0.1$

5.3.3 References

1. The CEPC-SPPC Study Group, CEPC-SPPC Preliminary Conceptual Design Report, Volume II: Accelerator, IHEP-CEPC-DR-2015-01 (2015)
2. O. S. Bruning, P. Collier, P. Lebrun, S. Myers, R. Ostojic, J. Poole, and P. Proudlock (editors), LHC Design Report Volume I: The LHC Main Ring, CERN-2004-003-V1, 2004
3. B. Salvachua, et al., Cleaning performance of the LHC collimation system up to 4 TeV, Proceedings of IPAC13, Shanghai, China (2013), p. 1002
4. G. Apollinari, et al., High-Luminosity Large Hadron Collider (HL-LHC) preliminary design report: Chapter 5. CERN-2015-005, 2015
5. R. Bruce et al., Cleaning performance with 11T dipoles and local dispersion suppressor collimation at the LHC, Proceedings of IPAC14, Dresden, Germany (2014), p. 170
6. K. Goulianos, Diffractive interactions of hadrons at high energies, Physics Reports, 101(3):169-219, 1983
7. T. Trenkler and J.B. Jeanneret, The principles of two-stage betatron and momentum collimation in circular accelerators, Part.Acc., 50 , (1995) 287, January 1995.
8. J.B. Jeanneret, Optics of a two-stage collimation system, Phys. Rev. ST-AB, 1,081001 (1998)
9. Merlin, https://sourceforge.net/projects/merlin-pt/
10. R. Appleby et al., The practical Pomeron for high energy proton collimation, Eur. Phys. J. C (2016) 76:520

5.4 High Field Superconducting Magnets

SPPC needs thousands of 20-T level dipole and quadrupole magnets to bend and focus proton beams. The nominal aperture in these magnets is 40~50 mm. A field uniformity of 10^{-4} should be attained in up to 2/3 of the aperture radius. The magnets will have two beam apertures of opposite magnetic polarity within the same yoke to save space and cost.

The currently assumed distance between the two apertures in the main dipoles is around 330 mm, but this could be changed based on the detailed design optimization to control cross-talk between the two apertures, and with considerations on the overall magnet size. The outer diameter of the main dipole and quadrupole magnets should not be larger than 900 mm, so that they can be placed inside cryostats having an outer diameter of 1500 mm. The total magnetic length of the main dipole magnets is about 39 km out of the total circumference of 54.4 km. If the length of each dipole magnet is 15 m, then about 2500 dipole magnets are required [2].

R&D of the high field superconducting magnets is the most challenging and crucial activity for realization of the SPPC project. All the superconducting magnets used in present accelerators are based on NbTi technology. These magnets work at significantly lower field than the required 20 T, e.g., 3.5 T at 4.2 K at RHIC and 8.3 T at 1.9 K at LHC [3, 4]. It appears reasonable to build dipoles with fields of 20 T by using NbTi and Nb_3Sn coils combined or Nb_3Sn coils alone to provide a field of 15 T, together with 5 T provided by HTS (High Temperature Superconductor, mainly Bi-2212 or ReBCO) insert coils. There are a total of 4 coil configurations which can provide dipole magnetic field for accelerators: cos-theta type [5], common coil type [6], block type [7] and canted cos-theta type [8]. Among these the common coil type is the simplest structure. The coils have much larger bending radius and there is much less strain level in the coils. Since both Nb_3Sn and HTS superconducting materials are strain-sensitive, which means the critical current density J_c of superconductors will be largely reduced by the high strain level, the common coil configuration has been chosen as the first option for the design study of the SPPC 20-T dipole magnets. The magnetic analysis, mechanical analysis, preliminary design study of the straight section and coil ends have been completed for a 20-T common coil dipole magnet.

5.4.1 Coil Layout and Main Design Parameters

There is a preliminary magnetic design study for the 20-T common coil dipole magnet [9]. Some important updates have been applied: a) Instead of using flared ends to make space for beam pipes, all the coils in the latest design are flat race-track configuration as shown in Fig. 5.4.1 left. One of the most inner coil blocks in each quadrant bends to the top (or bottom for another aperture) of the iron yoke to make space for beam pipes. This design will simplify the coil fabrication procedures and lower the strain level in the coils. A tradeoff is that a little more superconductor is needed to go through the top and bottom of the magnet without any positive contribution to the main field in the aperture. b) The coil layout in the straight section is re-optimized to further increase the main field and decrease the stress level. The ratio of the coil height to the coil width is increased, in other words, the coil blocks become thinner to make them more efficient to generate high field with a fixed quantity of superconductors, as shown in Fig. 5.4.1 right. One more benefit of this "thinner" design is that the stress level in the coil is reduced due to the increased area perpendicular to the Lorentz force direction. c) By carefully re-optimizing the position and size of each coil block, the ratio of the peak field in the coil to the main field in the aperture is reduced from 20.71 T / 20.06 T = 1.032 to 20.42 T / 20.09 T = 1.016. The operating load line is reduced from 90% to 89% at 4.2 K.

The main design parameters of the magnet are listed in Table 5.4.1. The 50 mm aperture is a privional assumption. The final diameter should be around 40~50 mm, determined by the design study results of the SPPC accelerator physics. The operating

margin is 11% at 4.2 K, ~ 20% at 1.9 K. The outer diameter of the iron yoke is assumed to be 800 mm, subject to possible reduction to make space for a thicker mechanical support structure. We are trying to limit the whole size of the 20-T magnet to 900 mm, to reduce the tunnel size and the cost of civil construction for the CEPC-SPPC project. The magnet is made up of 12 superconducting coils: 2 Nb3Sn outer coils, 2 Nb3Sn inner coils, 2 HTS outer coils, 4 HTS inner-b coils and 2 HTS inner-c coils, as shown in Fig. 5.4.1 left. The 12 coils are wound with 3 different types of superconducting cables: 15 mm width Nb3Sn outer cable (38 strands), 22 mm width Nb3Sn inner cable (56 strands) and 20 mm width HTS cable (50 strands). The 3 superconducting cables are fabricated with 2 types of strands: high Jc Nb3Sn strand and HTS Bi-2212 strand (ReBCO is also an option). The Jc of these strands is assumed to be the same as the current level [10], but we are aware of the real probability that the Jc of these conductors will be largely increased in the next several years [11, 12].

The coil layout in the ends has been optimized to reduce the integrated high order multipoles to be less than 10^{-4} of the main field. To make the structure the simplest, we assume each coil block bends with the same radius as the ends, in other words, the shape of each coil is always a "semicircle" in the ends, as shown in Fig.5.4.1 left. The length of straight section in each coil block is the main variable for optimizing the integrated field quality. Fig. 5.4.2 shows the distribution of high order multipoles along axis for an optimized coil ends shown in Fig. 5.4.1 left, with the reference radius of 15 mm. The integrated multipoles (from 0 mm to 1500 mm in Fig. 5.4.2) are listed in Table 5.4.2. All of them are less than 1 unit. The bending radius of each coil is listed in Table 5.4.1, varying from 100.9 mm to 135.7 mm.

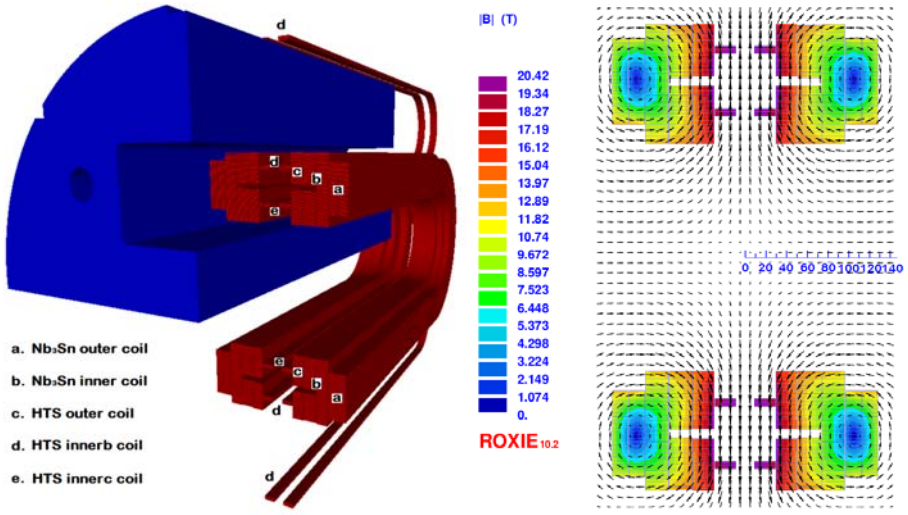

Fig. 5.4.1. Latest design of the 20-T dipole magnet with common coil configuration. Left: coil layout and iron; Right: Magnetic flux in the straight section.

5.4.2 Mechanical Support

Fig. 5.4.3 shows the direction of magnetic force in the coils. The total force per aperture is 23.5 MN/m in the horizontal direction and 4.4 MN/m in the vertical direction. The coils tend to move outward in both directions after excitation. If we divide the horizontal magnetic force by the area perpendicular to its direction, i.e., the coil height in

Fig. 5.4.3, we can get a rough estimate of the stress level in coils: 23.5/0.121=194 MPa. FEM simulation results show that the peak stress in the coil is around 249 MPa. Such stress level may reduce the critical current density of Nb_3Sn and Bi-2212 superconductors [13, 14]; Effective methods for stress management need to be investigated. The other type of HTS superconductor, ReBCO, can tolerate much higher stress and strain without showing any degradation, but the magnetization effect in the tape conductor is more severe than multi-filament round wires like Bi-2212 and Nb_3Sn, which will make it difficult to achieve 10^{-4} field quality.

Different than in other coil configurations like cos-theta type or block type, the two apertures of the common coil configuration are located vertically, which doubles the requirement of mechanical support strength in the horizontal direction, i.e., for each aperture the magnetic force is 23.5 MN per meter, and for the whole magnet it becomes 47 MN per meter. If the shell based structure is adopted to provide support for the magnet [15], to constrain such level of stress, the thickness of the aluminum shell would be 75 mm, assuming the stress level in the shell is limited to less than 300 MPa [16]. To reduce the shell thickness and whole size of the magnet, aluminum alloys with higher yield strength will be tested in the future.

Table 5.4.I. Main Parameters of a 20-T Common Coil Dipole Magnet

Item			Value
Magnet		Number of apertures	2
		Aperture diameter (mm)	50
		Inter-aperture spacing (mm)	333
		Operating current (A)	14700
		Operating temperature (K)	4.2
		Operating field (T)	20
		Peak field (T)	20.4
		Margin along the load line (%)	11
		Stored magnetic energy (MJ/m)	7.8
		Inductance (mH/m)	72.1
		Yoke ID (mm)	260
		Yoke OD (mm)	800
		Weight per unit length (kg/m)	3200
		Energy density (coil volume) (MJ/m^3)	738
		Force per aperture – X / Y (MN/m)	23.5/4.4
		Peak stress in coil (MPa)	240
		Fringe Field @ r = 750 mm (T)	0.02
Coil	Nb_3Sn outer	Number of layers	2
		Number of turns per layer	46
(2 Nb_3Sn outer + 2 Nb_3Sn inner +		Bending radius (mm)	127.8
2 HTS outer +4 HTS inner-b +	Nb_3Sn inner	Number of layers	2
2 HTS inner-c)		Number of turns per layer	59/64
		Bending radius (mm)	109.1
	HTS outer	Number of layers	1
		Number of turns per layer	59
		Bending radius (mm)	109.0
	HTS inner-b	Number of layers	1
		Number of turns per layer	4
		Bending radius (mm)	135.7
	HTS inner-c	Number of layers	1
		Number of turns per layer	4
		Bending radius (mm)	100.9
Cable	Nb_3Sn outer	Number of strands	38
		Cable dimension (mm^2)	15*1.5
(Nb_3Sn outer+ Nb_3Sn inner		Insulation thickness (mm)	0.15
+ HTS cable)	Nb_3Sn inner	Number of strands	56
		Cable dimension (mm^2)	22*1.5
		Insulation thickness (mm)	0.15
	HTS	Number of strands	50
		Cable dimension (mm^2)	20*1.5
		Insulation thickness (mm)	0.15
Strand	Nb_3Sn	Diameter (mm)	0.82
		Copper/Superconductor ratio	1
(Nb_3Sn + HTS)		Non-Cu J_c (A/mm^2 @15 T, 4.2 K)	1500
		dJ_c/dB (A/T)	350
	HTS	Diameter (mm)	0.82
		Copper/Superconductor ratio	1
		Non-Cu J_c (A/mm^2 @20 T, 4.2 K)	1300
		dJ_c/dB (A/T)	13

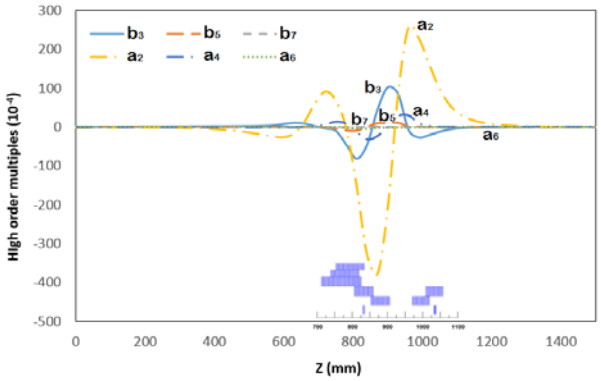

Fig. 5.4.2. High order multipoles along the axis for optimized coil ends shown in Fig. 5.4.1 left (with a reference radius of 15 mm).

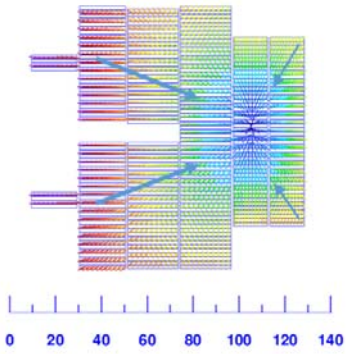

Fig. 5.4.3. Direction of magnetic force in the coils.

Table 5.4.2. Integrated field quality along the axis with a reference radius of 15 mm

Integrated b_n/a_n along axis	Value (10^{-4})
b3	0.24
b5	0.78
b7	-0.48
b9	-0.70
a2	0.37
a4	0.00
a6	0.17

5.4.3 Challenges for Fabrication and R&D Steps

The above design study is carried out based on the present J_c level of available superconductors. To fabricate such a 20-T dipole magnet, there are several main challenges listed below:

a) *Stress management in coils*: The stress in superconducting coils is above 200 MPa at 20-T operation. As both Nb_3Sn and Bi-2212 superconducting materials are strain sensitive (J_c going down quickly with increasing strain), effective methods need to be investigated to reduce the stress to a more acceptable level.

b) *Achieving 10^{-4} field quality with HTS coils*: The current distribution within a conductor is related to the history of the fields it has seen. This 'magnetization' depends on the dimensions of the conductor. Finer strands give much less

magnetization. LTS (Low Temperature Superconductor) conductors such as NbTi are made of thousands of small filaments with diameter of only a few microns. The filaments in current Bi-2212 conductors are larger than those in NbTi, and the ReBCO tape is a single 'filament' and is orders of magnitude larger. This will make it difficult for the magnets with the HTS coils to reach the field uniformity level of 10^{-4}. Some innovative solutions are being studied.

c) *Achieving quench protection of HTS coils*: The quench propagation speed in HTS coils is hundreds of times slower than in LTS coils. This makes the present quench detection and protection methods unsuitable for HTS coils. Innovative solutions need to be investigated.

To realize a 20-T dipole magnet in the next 10~15 years, a 3-step R&D plan was proposed, as shown in Fig. 5.4.4. A 15-T subscale magnet will be first fabricated with Nb_3Sn and HTS superconductors, to test the stress management method for Nb_3Sn & HTS coils and the quench protection method for HTS coils. Then a 15-T operational field dipole magnet will be fabricated with Nb_3Sn and HTS superconductors, which will have two Φ50 mm beam pipes and 10^{-4} field quality, to test the field optimization method for HTS coils; The final step is fabricating the 20-T magnet with Nb_3Sn and HTS superconductors, or only one of them if we can get significant progress on the performance of Nb_3Sn or HTS superconductors, i.e., their J_c level 3~6 times increased or even more, and the cost significantly reduced.

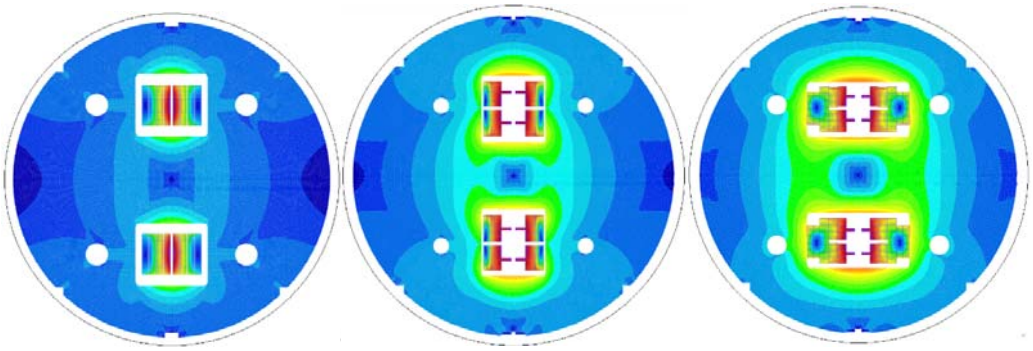

Fig. 5.4.4. R&D steps for fabrication of the 20-T dipole magnet with common coil configuration: Left: Development of a 15-T sub-scale magnet (Nb_3Sn + HTS); Middle: Development of a 15-T operational field dipole magnet with 2 * Φ50 mm beam pipes and 10^{-4} field quality (Nb_3Sn, Nb_3Sn + HTS); Right: Development of a 20-T operational field dipole magnet with 2 * Φ50 mm beam pipes and 10^{-4} field quality (Nb_3Sn + HTS or only one of them).

5.4.4 References

1. Q. Xu et. al., 20-T Dipole Magnet with Common Coil Configuration: Main Characteristics and Challenges, IEEE Trans. Appl. Supercond., VOL. 26, NO. 4, 2016，4000404
2. CEPC-SPPC Preliminary Conceptual Design Report [Online]. Available: http://cepc.ihep.ac.cn/preCDR/volume.html
3. A. Greene et al., "The Magnet System of the Relativistic Heavy Ion Collider (RHIC)", IEEE Trans. Mag., VOL. 32, NO. 4, JULY 1996, pp 2041-2046
4. LHC design report: The LHC Main Ring, Chapter 7: Main Magnets in the Arcs, [Online]. Available: http://ab-div.web.cern.ch/ab-div/Publications/LHC-DesignReport.html

5. Alvin Tollestrup, Ezio Todesco, “The Development of Superconducting Magnets for Use in Particle Accelerators: From the Tevatron to the LHC,” Reviews of Accelerator Science and Technology 04/2012; 01(01). DOI: 10.1142/S1793626808000101
6. R. Gupta, “A Common Coil Design for High Field 2-in-1 Accelerator Magnets,” Proceedings of the 1997 Particle Accelerator Conference, Vol. 3, May 1997, pp. 3344-3346.
7. Sabbi G et al., “Design of HD2: a 15 Tesla Nb3Sn dipole with a 35 mm bore,” IEEE Trans. on Appl. Supercond. 15, 2005, pp 1128-1131.
8. S. Caspi et al., “Canted–Cosine–Theta Magnet (CCT)—A Concept for High Field Accelerator Magnets”, IEEE Trans. on Appl. Supercond., VOL. 24, NO. 3, JUNE 2014 4001804
9. Q. Xu et al., “Magnetic Design Study of the High-Field Common-Coil Dipole Magnet for High-Energy Accelerators,” IEEE Trans. on Appl. Supercond., VOL. 25, NO. 3, JUNE 2015, 4000905.
10. P. Lee, “A comparison of superconductor critical currents.” [Online]. Available: https://nationalmaglab.org/magnet-development/applied-superconductivity-center/plots
11. X. Xu, M. Sumption, X. Peng, and E. W. Collings, “Refinement of Nb3Sn grain size by the generation of ZrO2 precipitates in Nb3Sn wires,” Appl. Phys. Lett. 104, 082602 (2014).
12. D. C. Larbalestier, J. Jiang, U. P. Trociewitz, F. Kametani, C. Scheuerlein, M. Dalban-Canassy, M. Matras, P. Chen, N. C. Craig, P. J. Lee, and E. E. Hellstrom, “Isotropic round-wire multifilament cuprate superconductor for generation of magnetic fields above 30 T,” Nature Materials, Vol. 13, (2014) pp. 375-381.
13. D. R. Dietderich and A. Godeke, “Nb3Sn research and development in the USA – Wires and cables,” Cryogenics, 48 (2008) 331–340.
14. D. R. Dietderich, T. Hasegawa, Y. Aoki, and R. M. Scanlan, “Critical current variation of Rutherford cable of Bi-2212 in high magnetic fields with transverse stress,” Physica C, vol. 341-348, no. 4, p. 2599, 2000.
15. P. A. Bish, S. Caspi, D. R. Dietderich, S. A. Gourlay, R. R. Hafalia, and R. Hannaford et al., “A new support structure for high field magnets,” IEEE Trans. Appl. Supercond., vol. 12, no. 1, pp. 47–50, 2002.
16. K. Zhang, Q. Xu et. al., “Mechanical Study of a 20-T Common-coil Dipole Magnet for High-Energy Accelerators,” IEEE Trans. Appl. Supercond., VOL. 26, NO. 4, 2016, 4003705

6 R&D Program

6.1 Superconducting RF

CEPC will require two large Superconducting RF (SRF) systems: 336 cavities operating at 650 MHz in 56 cryomodules for the collider and 128 cavities operating at 1300 MHz in 16 cryomodules for the Booster. This would be one of the largest SRF installations in the world. To succeed with designing, fabricating, commissioning and installation of such a system, a very significant investment in R&D, infrastructure and personnel is necessary.

6.1.1 Initial SRF Technology R&D (2017-2020)

The initial R&D goals would be to develop with industry the prototypes of all the components and demonstrate that they meet the required performance.

6.1.1.1 Initial Technology R&D

1. Develop an SRF cavity of each type; order several prototypes from industry; perform a series of tests to optimize the cavity surface treatment; build vertical test stands and perform tests to demonstrate the cavity performance goals. Weld helium jackets on the cavities, re-test and demonstrate the performance goals.
2. Design fundamental RF power couplers (FPCs a.k.a. RF input couplers); order at least two couplers of each type from industry; build FPC test stands; test the FPCs and demonstrate that their performance meets the CEPC requirements.
3. Design HOM dampers; fabricate one or two prototypes of each design; design and build test set ups; test the HOM dampers.
4. Design and fabricate frequency tuners and a LLRF control system.
5. Design and build a short (one or two cavities) horizontal cryomodule for each cavity type; build a test stand; demonstrate performance of all components integrated together into a cryomodule.

6.1.1.2 Infrastructure and Personnel Development

For the initial R&D, most of the infrastructure (clean rooms, HPR system, vertical and horizontal test stands) is available on-site or can be accommodated in the new SRF Lab in Huairou in northern suburb Beijing, about 50 km from the city center. Some existing facilities will have to be upgraded; additional project-specific equipment will be purchased and some additional space is needed. These needs can be estimated as soon as a detailed R&D plan is developed.

At this stage, it is very important to begin the hiring and development of personnel. The core project personnel must be in place by the middle of this 2017-2020 phase of the project. It will take at least 4 years with two teams working in parallel: one working on the collider SRF and the other on the Booster SRF. Each core team should consist of about 10 people (physicists, engineers, technicians). Support from other technical groups will be required when necessary. Collaboration with other laboratories (BNL, DESY, Fermilab, JLab, KEK, …) will help shorten this stage of the project.

6.1.2 Pre-production R&D (2021-2023)

The goal during this pre-production phase is to demonstrate robustness of fabrication and assembly processes of the cryomodule and its components. We will establish procedures, quality control steps, test set ups, assembly sequences, etc. for the production phase.

6.1.2.1 Pre-production R&D

During the pre-production phase, we plan to build and test two Booster cryomodules and three collider cryomodules. To accomplish this, the following will be necessary:

1. Build and test twenty 1.3 GHz Booster cavities and thirty 650 MHz collider cavities. This will allow pre-qualification of vendors for future cavity mass production, establish treatment processes and debug all procedures. This will demonstrate that the cavity fabrication and treatment approaches are adequately robust to produce cavities meeting requirements with high acceptance (~90 %). Several cavities of each type should be chosen for horizontal testing. Two to three cavity fabrication and treatment vendors should be pre-qualified by the end of this phase.
2. Build and test twenty FPCs for the Booster cavities and twenty FPCs for the collider cavities.
3. Build and test a sufficient number of tuners and other ancillary components.
4. Build and test cryomodules and demonstrate cryomodule performance. A cryomodule beam test is recommended especially for the HOM damping and heat load performance of the collider cryomodule.

6.1.2.2 Infrastructure and Personnel Development

A large scale SRF R&D and production facility (at least 10,000 m^2) must be built on the CEPC site. Before this, a superconducting RF Laboratory of 4,000 m^2 will be built in 2017-2019 with facilities and assembly lines sufficient for pre-production. The CEPC SRF team should make site visits at the beginning of the initial R&D phase and study facilities used at JLab, FNAL, KEK and Euro-XFEL (DESY, Saclay, LAL) as well as industries for SRF system production and scale them as appropriate to the size of the CEPC SRF system.

The final facility (on the CEPC site and in industry) should include: cavity inspection and local repair facilities, RF laboratory and tuning set ups, BCP and EP treatment facilities, annealing furnaces, 4 vertical test stands, clean rooms, HPR systems, FPC preparation and conditioning facilities, cryomodule assembly lines, 4 cryomodule horizontal test stations, high power RF equipment and a cryogenic plant.

To build and install the Booster SRF system in three years (2024-2026), the production facility should have the capacity to assemble about 1 cryomodule per two months. To build and install the collider SRF system in four years (2024-2027), the assembly lines should manufacture about one cryomodule each month. To sustain this rate, the vertical test stands should be able to test 2 Booster cavities per week and 2 collider cavities each week.

Commissioning and operation of the pre-production facility should begin during the last two years of the initial R&D phase (2018-2019). The pre-production stage will take 4 years, two of which will be for equipment installation and commissioning. The pre-

production capacity of the off-site facility should be one fifth to one quarter of the eventual production facility.

Beginning in the last year of the initial R&D (2019), the core SRF teams should begin hiring and training more personnel (~ 200 FTEs, mostly engineers and technicians), who will then work first in the pre-production and then in the production facility.

6.2 RF Power Source

6.2.1 650 MHz High Efficiency Klystron

6.2.1.1 Introduction

Thanks to the discovery of the low mass Higgs boson, and stimulated by ideas of Circular Higgs Factories in the world, the CEPC and SPPC configuration was proposed in September 2012. As the CEPC beam power is more than 100 MW [1], it needs high efficiency RF sources to reduce power loss and cost and also facilitate project implementation. The most popular RF source for an accelerator is a klystron, which has the advantages of operating at high power with a reasonably high efficiency. The high power klystron is the more attractive as an RF source because of its potential for higher efficiency than a solid state amplifier and more stable operation than an IOT. There are 384 RF stations in the CEPC SRF system and each RF station includes a 5-cell 650 MHz accelerating superconducting cavity. A minimum transmitter power of 280 kW is required to meet the sum of the radiated, HOM, and reflected power demands. With one klystron powered for two cavities, the specified saturation power of the klystron should be in the range 600 to 700 kW. This takes into an account klystron operation in a linear region, and the losses in the circulator and waveguide. Considering the klystron operation lifetime and power redundancy, a single 800 kW klystron amplifier will drive two of the collider cavities through a magic tee and two appropriately rated circulators and loads. The choice of klystron for two cavities is justified technically by better control of microphonic noise and minimum perturbation in the case of a klystron trip. Table 6.2.1 shows the RF power requirements for the CEPC collider SRF system.

Table 6.2.1: CEPC collider SRF system parameters

Frequency	MHz	650
Cavity type	5-cell	5-Cell
Cavity No.		384
Klystron No.		192
Klystron power	kW	800

6.2.1.2 Design Consideration

The klystron, with its gun and collector, will be more than 4 m in length. It could be manufactured in industry by a partnership between IHEP and an industrial company. Computer simulation tools are used to design the klystron including the electron gun, electromagnet, cavities and RF output structure [2]. However, design and simulation are not sufficient and mature enough. Therefore, we need to follow with a series of experimental steps. The first step is to set up a beam test stand to verify the gun and collector design, then to connect the cavity components to form a classical klystron

prototype, and finally to change from classical cavities to high efficiency ones to verify the peformance.

Increasing the efficiency of RF power generation is considered a high priority issue. The vast majority of existing commercial high power pulsed klystrons operate with an efficiency from 40% to 55%. Only a few continuous wave and multi-beam klystrons available on the market are capable of operating with 65% efficiency or higher. A new method to achieve 90% RF power conversion efficiency in a klystron amplifier is presented in A. Y. Baikov's paper [3]. Considering this recent high efficiency approach, our efficiency goal is 80%. One klystron prototype will be manufactured to achieve this efficiency. The design parameters for a 650 MHz klystron are shown in Table 6.2.2.

Table 6.2.2: CEPC Klystron Key Design Parameters

	First step	Boal
Frequency(MHz)	650	650
Output Power(kW)	800	800
Beam Voltage(kV)	82	70
Beam Current(A)	16	15
Efficiency	65%	80%

6.2.1.3 Electron Gun

Though the future tube employs a diode gun, in our initial design we used an electron gun with a modulating anode (MA) using DGUN software [4]. Uniform beam trajectories, with a beam perveance of 0.64 $\mu A/V^{3/2}$ are in this design. Also is a Ba-dispenser cathode of radius 35 mm with Φ10 hole at the center. A current density on the cathode of less than 0.45 A/cm^2 is obtained. The beam trajectories were also simulated over the entire tube length with a magnetic field of 180 Gauss [5]. The design parameters of the klystron gun are shown in Table 6.2.3. Simulation results using DGUN code are shown in Figure 6.2.1. Left (a) shows the beam trajectory with maximum electric field on the electrodes. Right (b) shows the current density on the cathode.

Table 6.2.3: CEPC Klystron Gun Parameters

Cathode voltage.	kV	-81.5
MA voltage.	kV	-48.0
Beam waste diameter	mm	35.6
Beam/Gun perveance.	$\mu A/V^{3/2}$	0.64/1.45
Average cathode density.	A/cm^2	0.45
Cathode uniformity		1.24

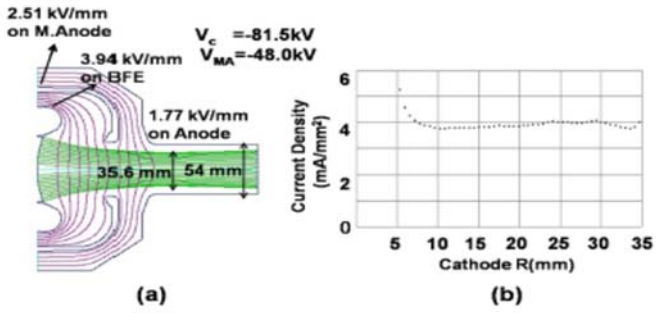

Figure 6.2.1: DGUN simulation results.

HV ceramic seal design is important for reliable operation. Layout of the ceramics is based on an outside layout of a socket tank and a magnet design (with an extra coil in the gun region). However, we choose the solution with no extra coil near the gun region in the oil tank. Average/maximum field on the ceramic was 0.32/0.52 kV/mm (C-MA) and 0.25/0.47 kV/mm (MA-A) along the length (about 150 mm) of the ceramic. The HV simulation result is shown in Figure 6.2.2.

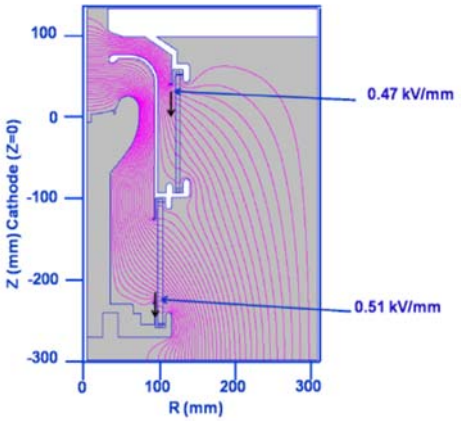

Figure 6.2.2: HV simulation result

6.2.1.4 RF Interaction and Cavities

The RF section plays an important role in the klystron gain, bandwidth and overall efficiency. The collider requires more than 100 MW RF power, so the klystron efficiency is the most important figure of merit for reduction of the operation cost. The klystron efficiency depends largely on the quality of electron bunching. High fundamental beam current and low velocity spread are prerequisites for obtaining high efficiency. After decades of development, the theory and technology of high efficiency klystron have made great progress. Some techniques are mature such as perveance reduction, high order harmonic cavity application and multi-beam klystrons, and some methods are speculative such as adiabatically bunching, COM, BAC and depressed collector [6-11]. In order to obtaining experience, initially the traditional mature methods will be used to obtain moderate efficiency of 65%. Then the newer less established methods will be applied to raise the efficiency to 80%. These two design approaches were optimized using AJDISK [12] as shown in Figure 6.2.3 and the parameters are summarized in Table 6.2.4.

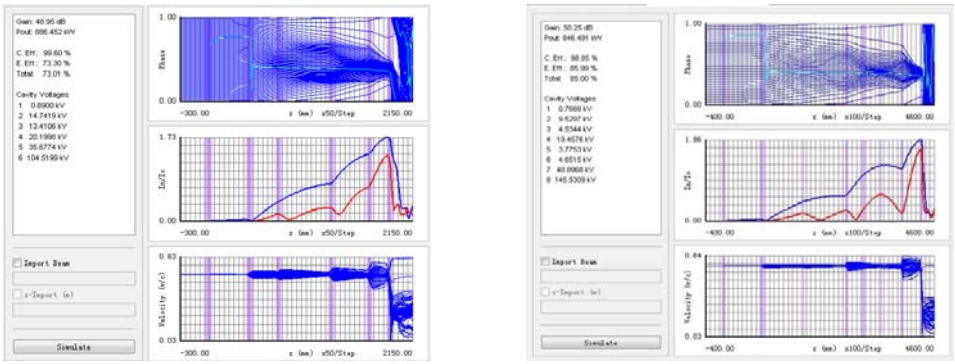

(a) (b)

Figure 6.2.3: Results of AJDISK (a) Traditional klystron (b) Klystron with BAC

Table 6.2.4. Summary of klystron parameters

Parameters	Traditional klystron	Klystron with BAC
Operating frequency	650 MHz	650 MHz
Beam Voltage	81.5 kV	110 kV
Beam Current	15.1 A	9.1A
Beam Perveance	0.65 μA/V$^{3/2}$	0.25 μA/V$^{3/2}$
Efficiency at rated Output Power	73%	85%
Saturation Gain	48.95 dB	50.25 dB
Output power	886 kW	846kW
Brillouin field	106	76
Reduced Plasma Wavelength	3.47 m	6.89 m
Number of Cavities	6	8
Normalized Drift Tube Radius	0.63	0.53
Normalized Beam Radius	0.41	0.34
Beam Fill Factor	0.65	0.65
Length	2 m	4.4 m

With the aid of electromagnetic simulation tools such as SUPERFISH [13], CST Microwave Studio [14] and High Frequency Structure Simulator (HFSS) [15], all six cavities of traditional klystron have been optimized to meet the RF section requirement [16]. The electromagnetic field pattern of the input and output cavity are shown in Figures 6.2.4 and 6.2.5.

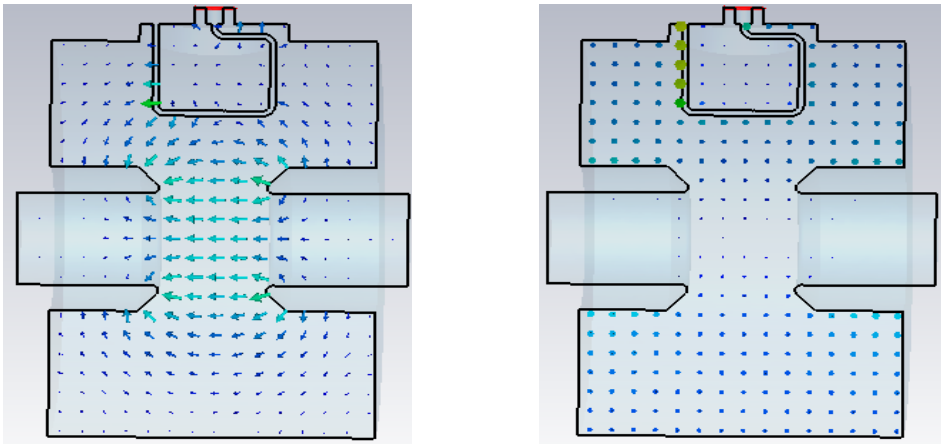

Figure 6.2.4: Input cavity field pattern

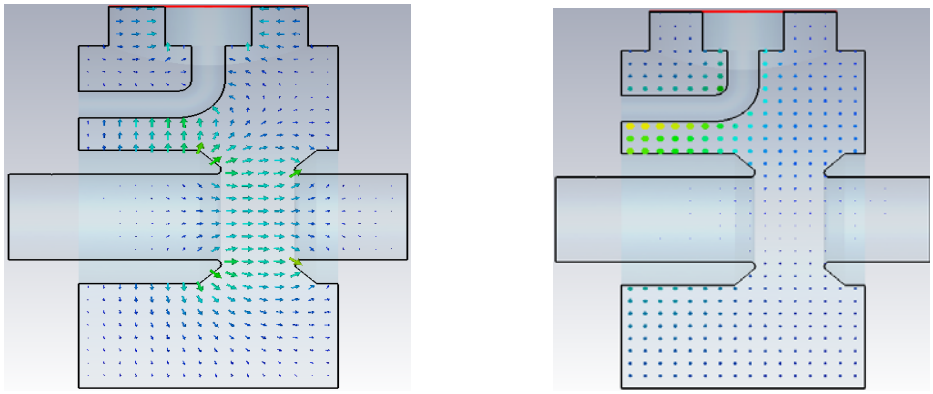

Figure 6.2.5: Output cavity field pattern

6.2.1.5 Window Design

The coaxial output window is one of the important issues for developing the high-power klystrons. For designing the windows, an average power capability and multipacting analysis for both fundamental and harmonic frequencies are important. The electromagnetic simulation of an output window was carried out using the CST Microwave Studio Code. We have optimized the return loss, not only at the desired frequency but also over the entire range of the desired bandwidths. Figure 6.2.6 show the parameter optimized reflection coefficient in the desired frequency range.

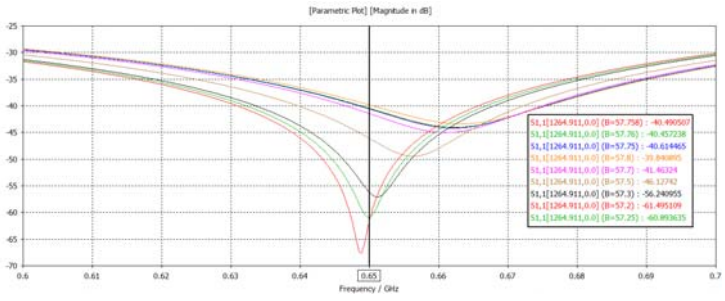

Figure 6.2.6: The parameter optimized of reflection coefficient

The magnitude of the S-parameter for operation with 800kW of power at 650MHz can reach -60dB, and the S-parameter is well below -30dB throughout the 600MHz ~700MHz range.

Multipacting is a phenomenon of resonant electron multiplication in which a large number of electrons build up an electron avalanche. This avalanche absorbs the RF energy, leading to a significant amount of power loss and wall heating. Multipacting is one of the serious problems for high power RF components and may cause ceramic window breakdown in high power klystrons operation. It is necessary to understand the process and prevent the loss of ceramic windows. So multipacting simulations and experiments are needed. Codes such as the CST Particle Studio and Multipac is used to do multipacting simulations. Results are shown and compared in Figures 6.2.7 and 6.2.8.

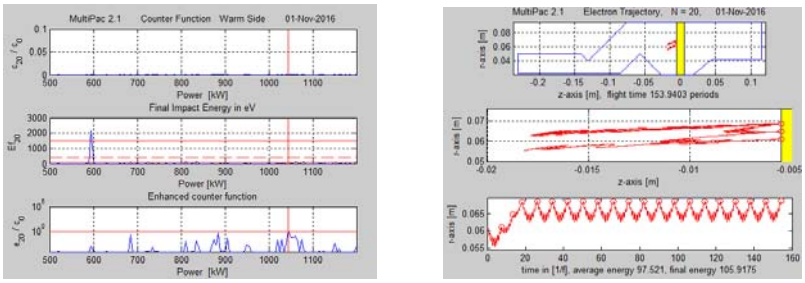

Figure 6.2.7: Multipacting simulation results from the Multipac code

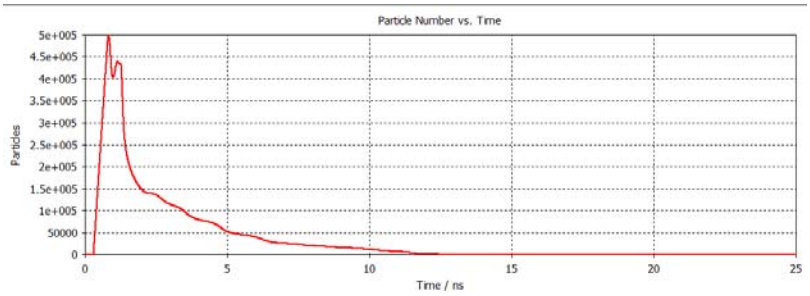

Figure 6.2.8: Multipacting simulation resulst from the CST code

From the top to the bottom of the right-hand figure in Figure 6.2.7 are presented the electron counter function, the average impact energy of the last impact in eV and the enhanced electron counter. The horizontal axis gives the average incident power in kW. The enhanced counter function e20/C0 is the ratio of the total number of secondary electrons after 20 impacts to the initial number of electrons, so if the relative enhanced counter function exceeds unity or the final impact energy of the electron after 20 impacts is in the range of which the secondary emission coefficient is larger than 1, then multipacting probably would occur. Even though the simulation results shown in the left-hand figure indicate that multipacting may exist, the right-hand figure shows that the e20/c0 are much lower than one and the average energy is not in the range for secondary emission coefficient larger than 1. So we may deduce that multipacting does not exist from the Multipac code result. The results shown in Figure 6.2.8 strengthen the result that multipacting does not exist form the CST simulation result. It is seen that the number of particles rapidly decreases with increasing time.

6.2.1.6 Collector

The capability of collector beam dissipation is an issue. If all the beam power is dissipated without RF drive, it could reach up to 1.2 MW. The dissipated power is limited while klystron input power is switched on; it is less than 400 kW. Initially, water cooling was chosen to deal with this problem. In order to investigate the collector design and its feasibility, a gun-collector test module is planned to be manufactured and tested before fabrication of a klystron prototype [17]. Due to a possible furnace size problem in China, we need to reduce the collector size so that the full length of a gun-collector test module is less than 2 m. A beam test module employing a modulated anode (MA) gun will be manufactured and tested. The pulsed operation of the MA gun gives different pulsed power to the structure, and it is especially important to evaluate the performance of a collector. Figure 6.2.9 shows a profile of the collector. The beam trajectory in the collector was cross-checked with the EGUN and MAGIC 2D codes. Figure 6.2.10 shows the beam trajectory simulation for the gun-collector test module.

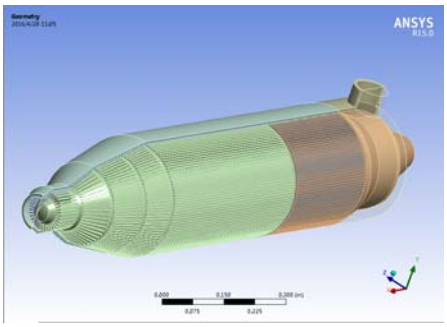

Figure 6.2.9: Collector profile.

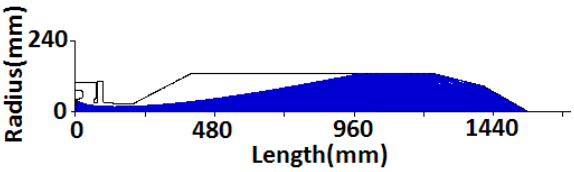

Figure 6.2.10: Trajectory simulation for the gun-collector test module

The collector outer surface is grooved to enhance cooling efficiency. The number of grooves, the water flow rate and other parameters are optimized by a fluid flow and coupled heat transfer simulation. The maximum peak power dissipation density for the full beam power exceeds 500 W/cm^2 for this reduced size collector. We have been tentatively assuming that the limit of the thermal interface temperature is 100 ℃ in this simulation. However, when the pulsed duty cycle reaches 0.6, the thermal interface temperature exceeds 100 ℃. The collector thermal analysis is shown in Figure 6.2.11.

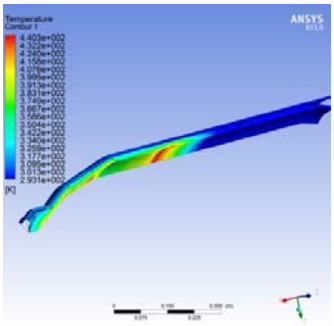

Figure 6.2.11: Collector thermal analysis

6.2.1.7 Beam Tester

Considering the manufacturing restriction, we plan to start the work with the beam test stand including gun and collector and then add the interaction region between gun and collector. The beam test stand includes gun, collector and short focusing magnets to verify design of gun and collector. The beam trajectories are simulated for a beam test tube length of about 2 m with a magnetic field of 213 Gauss using the DGUN code as shown in Figure 6.2.12.

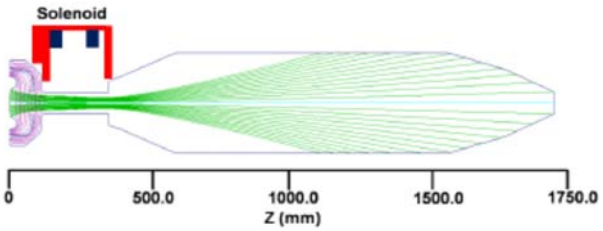

Figure 6.2.12: Simulation results for the beam tester.

We will begin manufacture of a beam tester within 3-4 months to evaluate the basic parameters. The mechanical design of the beam tester is shown in Figure 6.2.13. The next step will be to introduce a larger furnace and replace the interaction region with the current short drift tube.

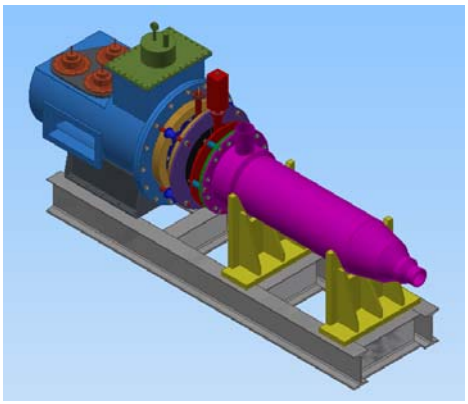

Figure 6.2.13: Mechanical design of the beam tester

6.2.1.8 Summary

The development of CEPC high efficiency klystrons has been summarized. Preliminary simulation shows that the klystron efficiency is more than 80%. The klystron will be manufactured by a Chinese company. The gun, cavities, collector and output window are designed to meet the required specifications and capacities. The beam tester will be built soon and the test stand will also be prepared in the near future.

6.3 Cryogenic System

The basis for the success of large scale scientific construction projects is research and development of the relevant technologies. The key technologies of CEPC cryogenic system are the large helium refrigerator and the study of 2K superfluid helium. R&D subjects mainly include:

(1) Design of a refrigerator of 4.5K equivalent capacity of about 12kW.
(2) Large helium turbine expander and its test bench.
(3) Research and prototype development of a large helium screw compressor
(4) Research and design of a large helium centrifugal cold compressor with high pressure ratio and its associated test stand.
(5) Sub-cooled 2K Joule-Thomson counter flow heat exchanger.

6.3.1 Large Helium Refrigerator

With the development of larger and larger accelerator projects, refrigerator technology has also developed to larger scale, higher reliability, better efficiency and lower cost. The 12kW at 4.5K refrigerators have been successfully used in the LHC project at CERN and all refrigerator components are available from industry. Design work on the large helium refrigerator for CEPC is being carried out by the Technical Institute of Physics and Chemistry (IPC) of the Chinese Academy of Science (CAS).

The refrigerator has the equivalent cooling capacity of 12 kW at 4.5K or 3 kW at 2K, and consists of the following subsystems: cold-box, main compressor station with oil removal system, vacuum pump group, gas management panel (GMP) with buffer tank and control system. There are five pressure levels in the cryo-plant: 20 bara, 4 bara, 1.05 bara, 0.4 bara and 3 kPa. These are obtained with the high pressure screw compressor group, middle pressure screw compressor group, vacuum pumps and cold compressors. There are 6 temperature levels in the system, which are formed with LN2 precooling, 5-class turbine expansions and a throttle valve. During the cool-down, LN2 will be used to increase the cooling power, whereas the LN2 precooling will be replaced by the 1st stage turbine string during normal operation. In the cold box, there are 9 heat exchangers, 8 turbo-expanders, 3 cold compressors in series, an inner purifier working at 80 K and dozens of cryogenic control valves. The cryo-plant can supply 4 K supercritical helium at 3bara and 50 K helium gas at 18bara to users as well as receive 2 K superfluid helium at 3kPa, 4 K saturated helium vapor at 1.3bara and 70 K helium gas back from the users.

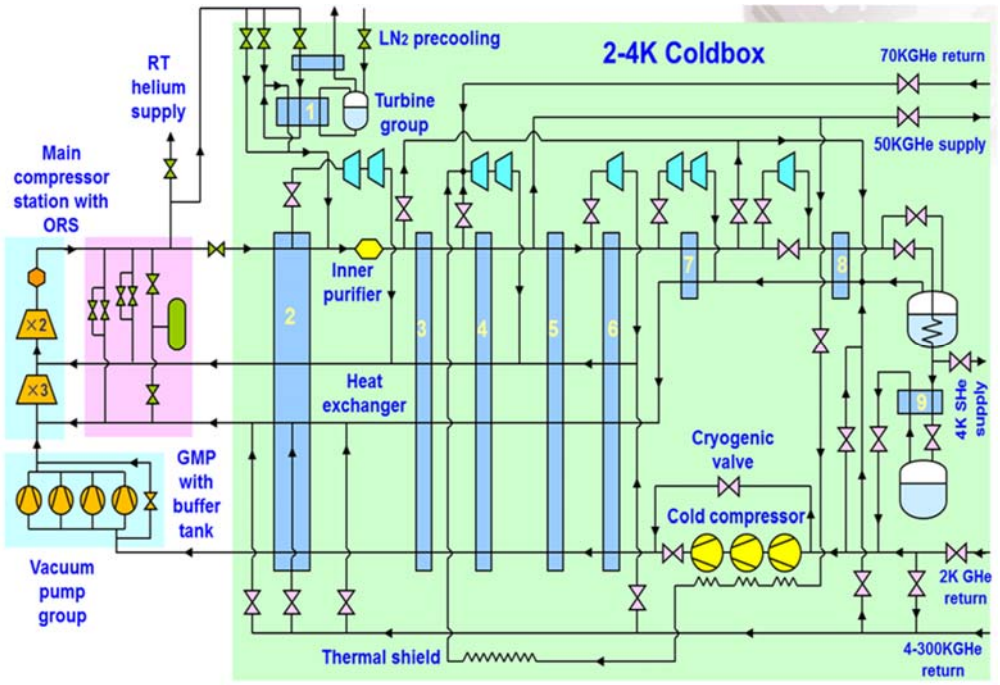

Fig.6.3.1 Flow diagram of the refrigerator design for CEPC

6.3.2 Turbine Expander

The turbine expander is a key component of the refrigerator. There are different kinds of turbine expanders in the large helium refrigerator. At high temperature, a large scale turbine expander is required to meet the need for large flow rate. At low temperature, a small turbine expander is required This has high speed and small flow rate. In order to solve this problem, a comprehensive optimization program needs to be developed. Much efforts should be devoted to theoretical analysis of the dynamic properties of high speed rotor bearing systems, the experimental study of the aerodynamic performance of the flow section, and the structural design to improve the reliability of the cold quantity adjusting mechanism. This detailed study includes:

(1) The design and development of high stability radial bearing.
(2) The design and development of high capacity thrust bearing.
(3) The development of large refrigeration capacity helium turbine expander.
(4) The development of a test bench with large stable flow rate.

The helium turbine expander is the core element of a large helium cryogenic system. Stability and good thermodynamic performance are very important. The target is to guarantee the stability of the high-speed helium gas bearing of the turbine expander rotor bearing system, as well as to improve the thermodynamic efficiency.

6.3.3 Screw Compressor

The main study of the helium compressor group for the cryogenic system is the plan design, and performance simulation at different pressure levels (1/4/20bar) linked to regulation performance. Following the theory of similarity modeling, an experimental prototype will be developed. The key problem of the design of the large helium flow injection screw compressor is to improve the efficiency of the host screw compressor. This includes optimization of rotor type line, reducing the leakage triangle area, reducing the contact line length, the optimization of meshing clearance, spray atomization cooling technology, and high efficient oil separation technology.

The main research content is as follows:

(1) Optimization design of the rotor type line.
(2) Design and experimental study of the special seal structure of the power transmission shaft in the screw compressor.
(3) Design and test of the mechanical oil and gas separation system with the basic principle being mechanical centrifugal force and speed control.
(4) The prototype of the oil injection type helium screw compressor.

The oil injection type helium screw compressor will be proposed and developed in collaboration with domestic manufacturers. Determined by the characteristics of high leakage rate and compression heat, the dynamic characteristics of large screw compressor, helium screw rotor type line and assembly processes will be studied. Then helium compression experiment and compressor performance tests will be carried out to improve the structure and processing technology. The main technical parameters are as follows:

(1) Oil injection type helium screw compressor:
    Volumetric efficiency ≥ 75%
    Shaft seal leakage rate ≤ 10-3Pa·m3/s
(2) Precision oil separation system:
    Oil content ≤ 0.01ppm (W)

6.3.4 Centrifugal Cold Compressor

The major R&D work on the centrifugal cold compressor is focused on the thermodynamic and mechanical performance as well as the system reliability. As the literature has indicated, the adiabatic efficiency of the cold compressor will be reduced to 1% with 20W heat leakage. Therefore, under the condition of less than the critical speed, the length of the shaft will be increased and the overall sealing performance will be investigated. The stability of the cold compressor embodied in two aspects, one is the stable working area of the cold compressor, the other is the stability of magnetic bearing.

The centrifugal cold compressor will be developed with retention of intellectual property rights. The experimental study to be carried out includes thermodynamic characteristics, sealing insulation characteristics, internal flow instability characteristics, surge recovery features and many sets of cold compressor cascade working characteristics. The electromagnetic bearing, high-speed motor performance test platform will be developed to meet the requirements of the centrifugal cold compressor.

The main technical parameters of the centrifugal cold compressor are as follows:

(1) Adiabatic efficiency: ≥60%

(2) Compression ratio: ≥2
(3) Leakage rate: 10^{-9} Pa·m^3/s
(4) A high-speed motor output power: ≥1 kW
(5) High speed motor speed: ≥36krpm

6.3.5 2K Joule-Thomson Heat Exchanger

The Joule-Thomson heat exchanger is one of the key components of the 2K cryogenic system. The 4.4K saturated helium is sub-cooled to about 2.2K in the Joule-Thomson counter flow heat exchanger and enters at 2.2K the forward tube of the cryomodules. The helium is expanded to 31mbar via a JT valve, resulting in more than 80% helium Ⅱ liquid at 2K. The evaporation of 2K helium with a pressure of 31mbar is superheated to about 3.5K in the heat exchanger. The Joule-Thomson counter flow heat exchanger can improve the efficiency of the JT valve.

The sub-atmospheric pressure and low temperature heat exchanger has the characteristics of small volume, light quality, small fluid resistance and large heat transfer area. A finned tube is proposed to enhance the heat transfer and improve efficiency. In order to balance the heat transfer and pressure drop for the JT heat exchanger, the diameter of the tube and fin height will be optimized.

A compact and efficient heat exchanger, the Hampson type is widely used in the field of natural gas liquefaction and cryogenics. The design parameters of the JT heat exchanger is shown in Table 6.3.1.

Table 6.3.1: Design parameters of the JT heat exchanger

Flow rate (g/s)	Temperature range (K)	Pressure drop (Pa)	Efficiency
5	2~4.5	<300	>80%

6.4 Magnets

During the R&D phase of the CEPC project, four prototype magnets will be developed to study the key technical issues of magnet design and production. The specifications of the magnets are listed in Table 6.4.1.

Table 6.4.1: Prototype magnets specifications

	Magnet name	Specification
1	Low field dipole magnet	1) Magnetic length: 4m 2) Gap: 40mm 3) Working field: from 31Gs to 614Gs 4) Good field region: 52mm 5) Field uniformity: 3E-4
2	Dual-aperture dipole magnet (DAB)	1) Working field：B0=0.07T 2) Gap：gap=66mm 3) Good field region：+-40mm 4) Field uniformity: <3E-4 5) Magnetic length：Leff=9m
3	Dual-aperture quadrupole magnet (DAQ)	1) Gradient：G0=10T/m 2) Aperture diameter：Apert.=66mm 3) Good field region：R0=26.4mm 4) Harmonic errors：η<3E-4 5) Magnetic length：Leff=2m
4	Dual-aperture sextupole magnet (DAS)	1) Sextupole field：S0=180T/m^2 2) Aperture diameter：Apert.=66mm 3) Good field region：R0=26.4mm 4) Harmonic errors：η<2E-3 5) Magnetic length：Leff=400mm

The first prototype magnet to be built will be the low field dipole magnet for the Booster. The key characteristics are:

1) The 4m long core has a H-type frame for better shielding of the earth field.
2) The core is made of silicon steel laminations. The coil (one turn per pole) is solid aluminum bars without water cooling.
3) By using the supporters in the magnet gap to compensate for the core weight and magnetic forces, the return yoke of the core will be made as thin as possible.
4) In the upper and lower pole areas of the laminations, 8 rectangular holes and 2 round holes will be stamped to reduce the weight of the cores in addition increasing the field in the laminations.
5) In order to install the vacuum chamber, the core can be divided into upper and lower half cores.
6) Around the outside of each half core, four long bars are used to weld the laminations of the half core together. In the round hole of each pole, there is a long bar to pressure the laminations together.

The cross section and flux distribution of the low field prototype dipole magnet for the Booster is shown in Figure 6.4.1

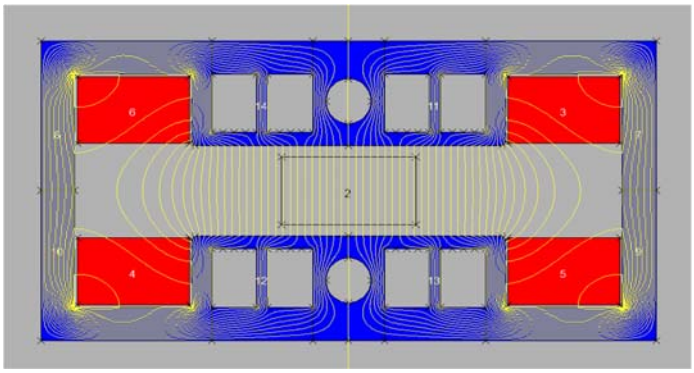

Fig. 6.4.1: The cross section and flux distribution of the Booster dipole magnet

The second prototype magnet is the dual-aperture bend (DAB) magnet for the collider. The key characteristics are:

1) The core of the DAB magnet is composed of two C-type dipole magnets placed back to back.
2) The two apertures share one return yoke and one coil.
3) For safety considerations (production, lift and delivery), the length of each core is kept to less than 4.5m. These units then are assembled into the magnets of the required length in the tunnel.
4) A sub-scale magnet will be first developed initially to study the low field properties, such as the effects of coercivity and remnant field.

The cross section and flux distribution of the dual-aperture prototype dipole magnet for the Main Ring is shown in Figure 6.4.2.

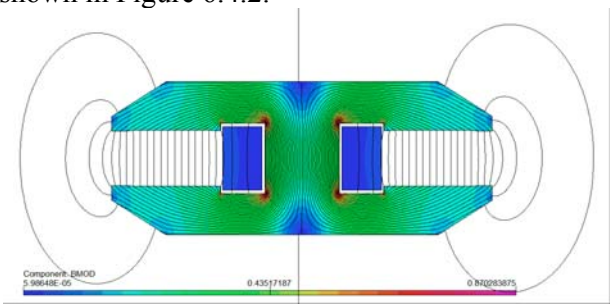

Fig. 6.4.2: The cross section and flux distribution of the DAB magnet

The third prototype magnet is the dual-aperture quadrupole (DAQ) magnet for the Main Ring. The key characteristics are:

1) The magnets are composed of two single quadrupole magnets with shared return yoke. Saturation in some areas of the cores will be avoided by optimizing the magnet design.
2) The core of the DAQ magnet consists of six parts made of silicon steel laminations with thickness 0.5mm.
3) To install the vacuum chamber, the magnets can be split into upper and lower parts.
4) The coils will be hollow copper or aluminum conductors.
5) By using end chamfering, harmonic errors can be suppressed down to the required values.

6) The distance between the two apertures will be less than 350mm.

The cross section and flux distribution of the dual-aperture prototype quadrupole magnet for the Main Ring is shown in Figure 6.4.3.

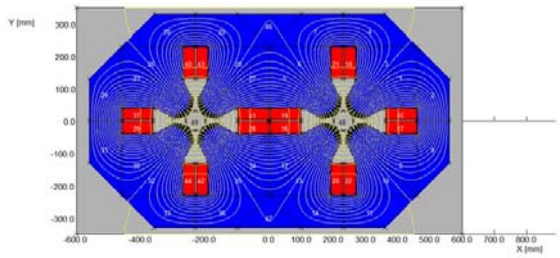

Fig. 6.4.3: The cross section and flux distribution of the DAQ magnet

The fourth prototype magnet is the dual-aperture sextupole (DAS) magnet for the Main Ring. The key characteristics are:

1) The DAS magnet is composed of two single sextupole magnets with shared return yoke. Saturation in some areas of the cores will be avoided by optimizing the magnet design.
2) The core of the DAS magnet consists of ten parts made of silicon steel laminations with thickness 0.5mm.
3) To install the vacuum chamber, the magnets can be split into upper and lower parts.
4) The coils will be wound of hollow copper or aluminum conductors.
5) By using technology of end chamfering, harmonic errors can be suppressed down to the required values.
6) The distance between two apertures will be less than 350mm.

The cross section and flux distribution of the dual-aperture prototype sextupole magnet for the Main Ring is shown in Figure 6.4.4.

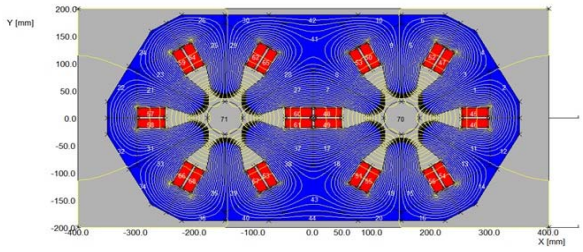

Fig. 6.4.4: The cross section and flux distribution of the DAS magnet

6.5 Magnet Power Supplies

All magnet power supplies for CEPC will be produced in China. So a very significant investment in R&D for critical equipment or sub systems is necessary.

6.5.1 5000 A/10 V High-Precision Power Converter

The CEPC accelerator requires high currents (~5kA) and relatively low voltages (~10 V) for its superconducting magnets and requires a very high level of performance from the power converters, particularly in terms of DC stability. To meet these requirements we will develop a 5000 A/10 V high-precision power converter. The main design parameters of the power converter is given in Table 6.5.1.

Table 6.5.1: Power supply design parameters

Output Current – Imax (A)	5000
Output Voltage (V)	10
Stability(8h-10s) – referred to Imax (ppm)	50
Stability (10s-0s) – referred to Imax (ppm)	20
Reproducibility - referred to Imax (ppm)	100
Absolute accuracy - referred to Imax (ppm)	100
Current ripple - referred to Imax (ppm, 50 Hz and greater)	20

The power supply will use soft-switching techniques, The chosen topology for the converter is to split it into three modules:

- Module 1: a diode rectifier on the AC mains with a damped L-C passive filter.
- Module 2: Full-bridge Zero Voltage Switching Phase Shift Inverter (FB-ZVS-PS).
- Module 3: high frequency transformers, rectifier stage and output filter. Combining these in one module will fulfil the weight constraints.

The converter will be split into n + 1 modules, whose outputs are connected in parallel. N modules supply the nominal current, and one module will work in case of trip. The modules can automatically “hot” switch between each other.

Radiation tolerance tests will be performed during the converter design, in case the power converter will be operated near a radioactive environment for reducing volume and to gain high efficiency.

6.5.2 Digital Power Supply Control Module

All CEPC power supplies are fully-digitally controlled. The Digital Power Supply Control Module (DPSCM) controls and monitors the high precision current loop and communicates with the CEPC control room. IHEP will have full responsibility for this critical high precision component and ensure that the software upgrades required from operations are made. The control module principle block diagram is shown below.

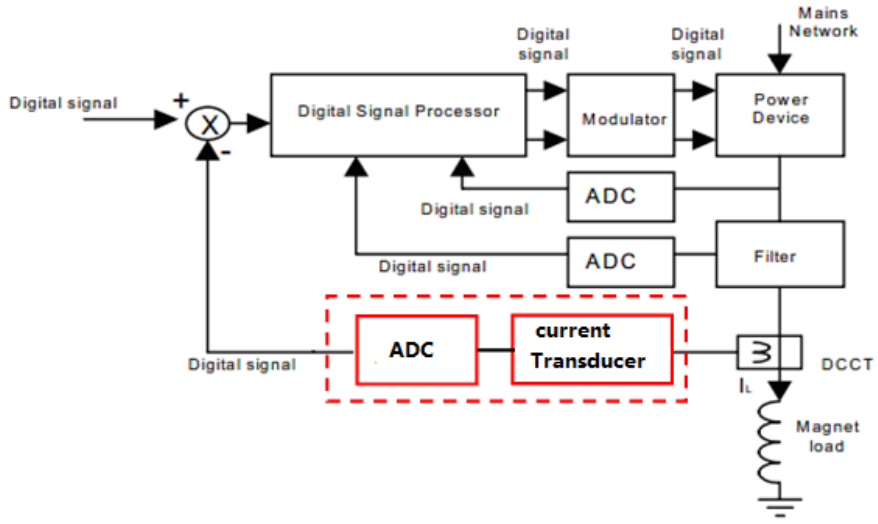

Figure 6.5.1: Digital controller for CEPC magnet power supplies.

To meet the high performance requirements of the magnet power supplies, the following issues must be considered during DPSCM development.

- Chip choice of digital signal processing: based on the system-on-chip of FPGA (Altera)
- ADC design: low noise design on the PCB; constant temperature protection for ADC; anti-dithering circuit design
- Implementation of the digital control algorithm on the FPGA: embedded fuzzy logic and expert system into the digital control platform (DCP) for better diagnostics, faults analysis, auto-detection and self-calibration

6.5.3 High-Precision DC Current Transducers

A dc current transducer is required to measure the converter output current in order to control it accurately. Some domestic accelerator laboratories have been developing their own DCCT products, and some have already been used in convertors. But the rated current of these DCCTs are below ±200A, and the precision specifications (e.g. linearity error, offset stability, temperature coefficient) are not good enough compared to some foreign products. To have available a high rated current DCCT up to 600A, we still need to do development.

A DCCT operating according to the zero-flux principle measures direct current, as shown in figure 6.5.2. The primary current is passed through a toroidal transducer core of special high-μ magnetic material creating a one-turn transformer.

In the first stage the current is divided with a fixed ratio to a low level. Its bandwidth is extended down to dc through a feedback loop, measuring the dc flux in the core and producing a compensation current, which will balance the flux to zero at all times. The ratio can be established to the ppm level.

In the second stage the low-level compensation current is passed through a high-precision load resistor. The voltage chosen is a compromise between power dissipation and producing enough voltage to overcome noise and thermal emf effects. This voltage is

then amplified in a high precision amplifier providing 10 V output at the nominal primary current.

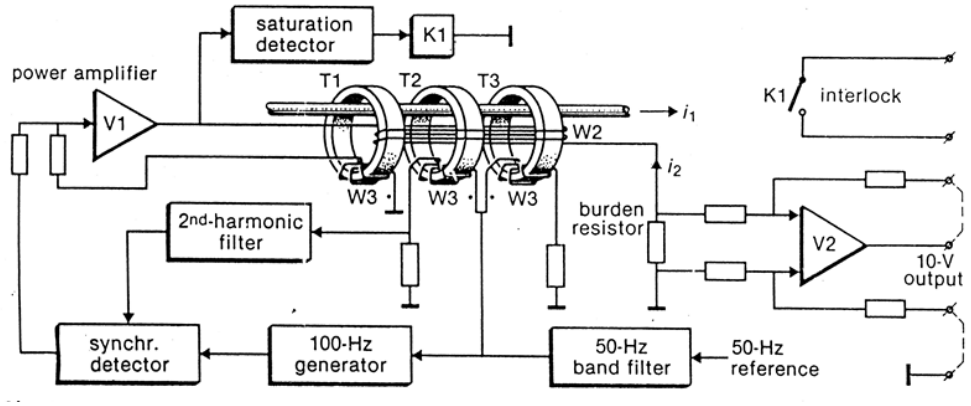

Figure 6.5.2: Zero flux DCCT principle

A DCCT consists of a measuring head and an electronics module.

The resolution of the DCCT mainly depends on sensitivity and zero deviation of the magnetic modulator, so we use a four-toroid magnetic modulator as the measuring head and choose ultrafine crystalline magnetic materials and non-magnetic annealing processse to make the DCCT core.

During the design of the electronics module, we choose 50 Hz square-waves and use synchronous sampling, band-pass filter to detect the second harmonic. We use an analog proportional integral (PI) circuit in the feedback loop and a four-wire load resistor and a very stable differential amplifier for current-to-voltage (I/V) conversion.

6.6 Vacuum System

6.6.1 Vacuum Chamber

There are types of dipole chambers to consider for the CEPC vacuum system. One is an aluminum chamber similar to the one used at LEP, with a beam channel, three cooling water channels, a pumping channel used to install NEG strips, and lead shielding covered outside the dipole chamber with a thickness of 3 to 8 mm. Another choice is a copper chamber with a beam channel and a cooling water channel, coated with NEG films inside the dipole chamber. These two types of dipole chambers will be fabricated and tested. The final choice will be decided based on the R & D results on the prototypes.

The aluminum chamber manufacturing process follows these steps:

- Extrusion of the chambers,
- Machining of the pumping slots,
- Machining of the components to be welded,
- Chemical cleaning,
- Welding of the side ports,
- Mounting of the NEG strips,
- Welding of the covers of the pumping channel, water connections and flanges,

- Leak detections,
- Lead coating of the outside of the chamber.

The copper chamber manufacturing process is:

- Extrusion of the beam pipe and cooling channel,
- Machining of the components to be welded,
- Chemical cleaning,
- Electron-beam welding,
- Welding of the end flanges and water connections,
- Leak checks,
- NEG coating of the inside chamber.

The copper chamber will be fabricated from an extruded copper chamber and cooling channel with two conflate-type end flanges. The chamber will be extruded to full length from UNS C10100 copper, and the cooling channel will be extruded from UNS C10300 copper. These are both drawn to achieve their final shape and to produce a minimum half-hard temper. The pieces are then cleaned and joined by electron-beam welding. After welding, the subassembly is stretch-formed to its correct radius, then the ends are machined and the parts cleaned. Finally, the end flanges are TIG-brazed onto the ends of the chamber. A one-piece chamber extrusion eliminates all longitudinal vacuum welds, which thus produces a more accurate and reliable chamber. Figure 6.6.1 is a schematic drawing of the copper dipole chamber.

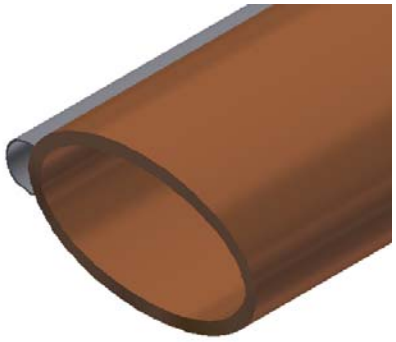

Figure 6.6.1: Schematic drawing of the copper dipole chamber

6.6.2 NEG Coating

The NEG coating is a titanium, zirconium, vanadium alloy, deposited on the inner surface of the chamber by sputtering. The NEG-coated chamber is first inspected for gross contamination or surface defects, which could cause poor film adhesion. Each dipole chamber will be fitted with three cathodes (made by twisting together Ti, Zr and V metal wires) mounted along the chamber axis to achieve uniform thickness distribution along the perimeter. Each TiZrV cathode is made of three 0.5 mm wires. To keep the cathode close to the chamber's axis, several ceramic spacers are spaced along the chamber length, plus two adaptors at the extremities. Chambers are then evacuated to the 10^{-9} mbar range

by a turbomolecular pump group and before coating baked overnight and leak tested with helium. A Residual Gas Analyzer (RGA) is also used to monitor partial pressure. The process gas and pressure are krypton at ~0.1 mbar, and the chamber temperature around 110 °C.

The sputtering process for NEG film deposition needs to be optimized to avoid instability and lack of reproducibility which can significantly change the gas sorption and surface properties (e.g. secondary electron yield, ion-induced gas desorption). During coating, all related parameters (plasma gas pressure, substrate temperature, plasma current, and magnetic field value) will be recorded and suitably adjusted to ensure the stability of the deposition process. After coating, the chambers will be cooled down to room temperature, exposed to air and left to age for a couple of days before being visually inspected again. Aging is a recommended procedure, since it helps in identifying areas where the film adhesion is poor.

6.6.3 RF Shielding Bellows Module

Typical RF-shielding has many narrow Be-Cu fingers that slide along the inside of the beam passage as the bellows is compressed, as shown in Figure 6.6.2. For CEPC, the fingers maintain a relatively high contact pressure of 150±10 g/finger, and the slit length between fingers is 20 mm. The RF-shielding can accommodate a maximum expansion of 10 mm and contraction of 20 mm, allowing for a 2 mm offset. The step at the contact point is limited to less than 1 mm. The cooling water channel takes care of synchrotron radiation power, Joule loss and HOM heat load on the inner surface, and leaked HOM power inside the bellows.

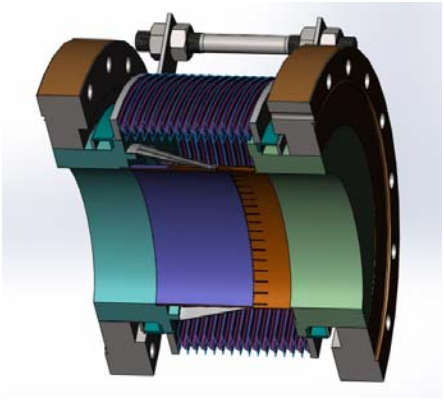

Figure 6.6.2: Bellows module with RF shielding

6.7 Instrumentation

Beam instrumentation (BI) is an essential part of CEPC. This system must provide precise and sufficient information on the beam and machine so that accelerator physicists and machine operators can improve injection efficiency, optimize the lattice parameters, monitor beam behaviour and increase the luminosity. Beam position monitors (BPMs) measure beam orbit in the ring and are especially important to measure precisely the beam orbit and crossing angle at the interaction points (IPs). Beam loss monitors (BLMs) help study the mechanism of beam loss and prevent damage to the machine. The tune monitor

is useful to study beam behaviour and optimize the working point, and the feedback system is employed to suppress beam instability. BI system R&D consists of work on the BPM and BLM electronics, beam diagnostic at the IP, the tune measurement system and feedback systems.

6.7.1 Pre-processing Eelectronics of Beam Signal

There are three methods for beam signal distribution as listed below.

6.7.1.1 Pickup Signal Waveform

The pickup signal from the e+ and e- bunches are both picked up from one group cable as shown Figure 6.7.1.

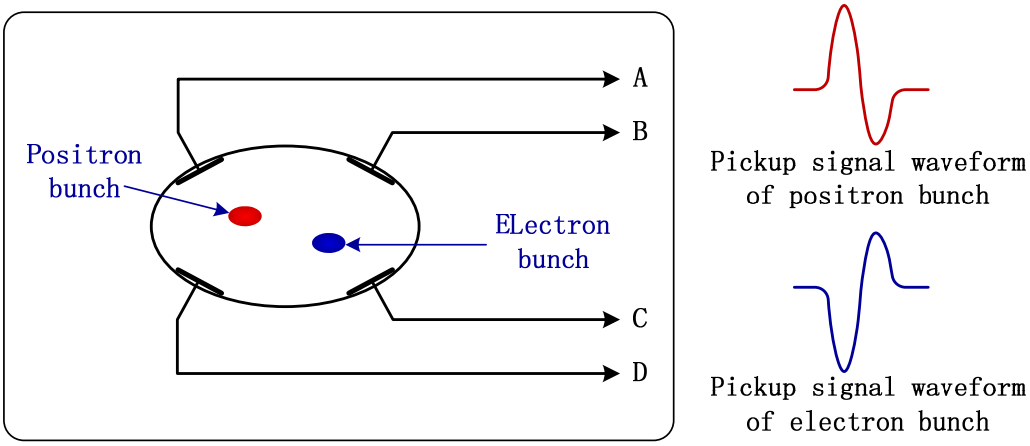

Figure 6.7.1: Pickup signal waveform from BPM detector

6.7.1.2 Working Principle

The signal from the BPM detector is split into 2 parts. One part is connected to a discriminator and control logic to generate the strobe pulse for a gating switch, the other part is sent to the SPDT switch input port via a "fixed delay line." After the switch, the signal is processed by different logics as shown in Figure 6.7.2.

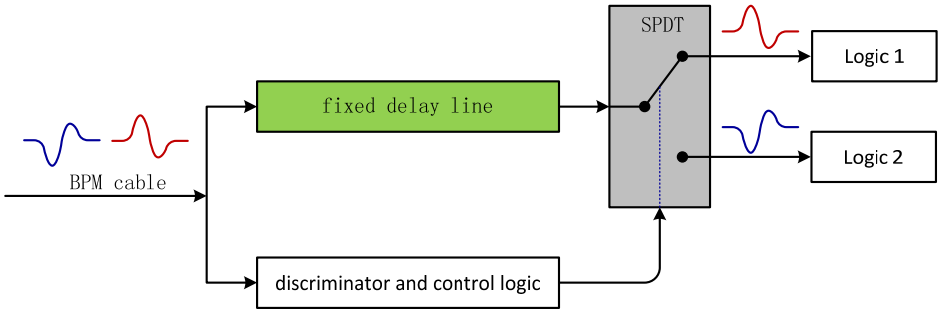

Figure 6.7.2: Working principle

The "discriminator and control logic" is used to check the e+ and e- pickup up signal, and furthermore, to generate a control signal to switch the SPDT gate

6.7.1.3 Discrimination Technique Study

Amplitude and discriminator method

As shown in Figure 6.7.3, in the "discriminator and control logic", the signal from the BPM detector is first amplitude checked, and then discriminated by high and low standard voltage, which shape a couple of earlier and later pulses according the BPM signal. If the pulse generated by high threshold is earlier, the positron BPM signal is picked. Otherwise, the electron BPM signal is picked.

The logic above is used to control the SPDT gating switch.

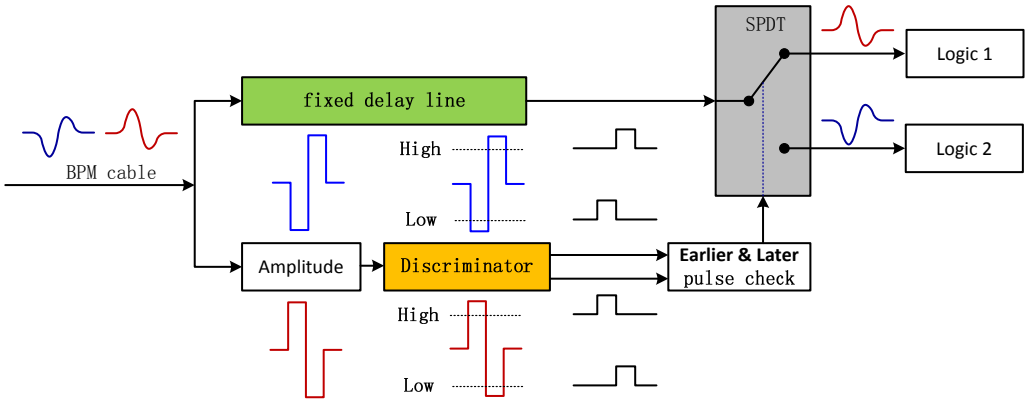

Figure 6.7.3: Amplitude and discriminator method

Amplitude and high speed ADC method

This method is different from the former. After the amplitude of the BPM signal is checked, a high-speed ADC is adopted to process the signal, as shown in Figure 6.7.4, and a switch control logic controls the SPDT according to the ADC result.

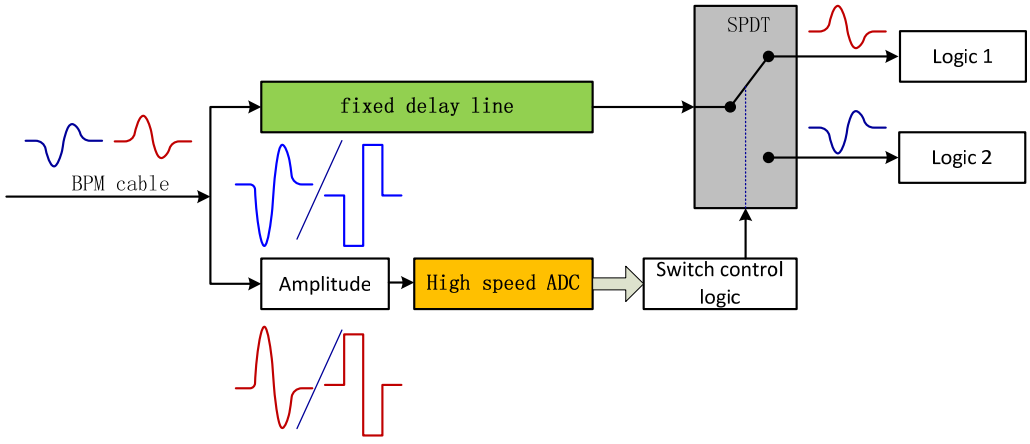

Figure 6.7.4: Amplitude and high speed ADC method

The ADC chip used operates at 125 MHz and 8-bit resolution, and the ADC is triggered to a series of samples. The sampling ADC block diagram is shown in Figure 6.7.5.

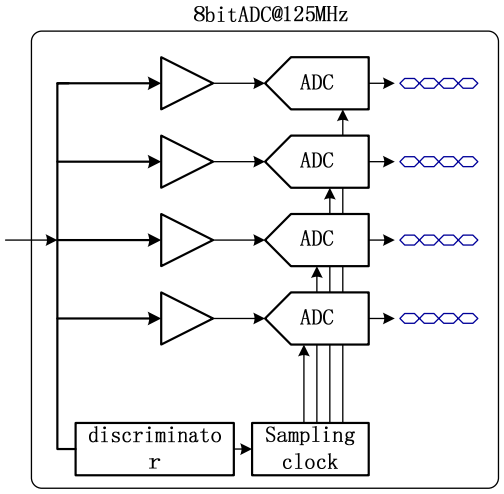

Figure 6.7.5: Sampling ADC block diagram

6.7.1.4 System Clock and System Trigger Method

The system trigger and the beam bunch arrive at the BPM detector at a fixed and known time. So the system clock and system trigger can be used in a timer logic to monitor different BPM bunch signals as shown in Figure 6.7.6.

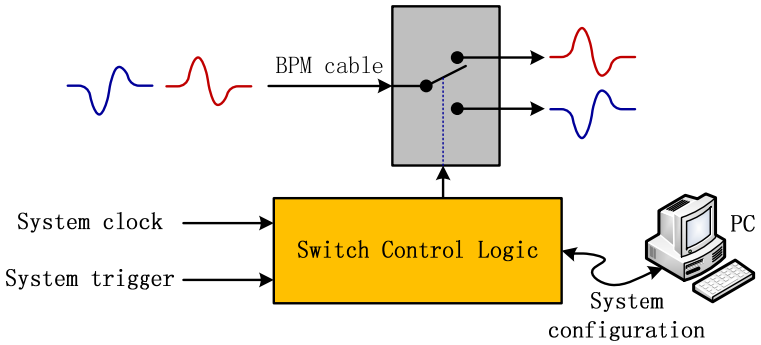

Figure 6.7.6: Using the system clock and system trigger to distribute the different signal

6.7.2 Beam Position Monitor Electronics

The digital BPM hardware function block shown in Figure 6.7.7 includes Rear Transition Module (RTM) boards, an Advanced Mezzanine Card (AMC), and the data acquisition and display system in computer. The front-end RTM boards pick up the BPM analog signal, and the RTM feeds the processed signal to the AMC board; In the AMC board, the analog signal is converted to a digital signal, and then processed with a special algorithm in the FPGA, and the results are transferred to the back-end computer.

An open standard MTCA will be used in the BPM system. The PICMG ratified the MTCA specification in 2005. This includes mechanical infrastructure, shelf management, power infrastructure, cooling and connector, and a simplified power interface solution. MTCA architecture is compatible with AMC and Advanced Telecom Computing

Architecture (ATCA), and is equipped with standardized function modules, configurable business module, expandable backplane, compact hardware structure and flexible application modes, low cost of development and application, less product development time and distribution clock for trigger system. MTCA devices are widely used in high energy physics equipments. MTCA BPM module and other hardware devices are under development at SLAC and DESY. The Libera products also have adopted the MTCA technique.

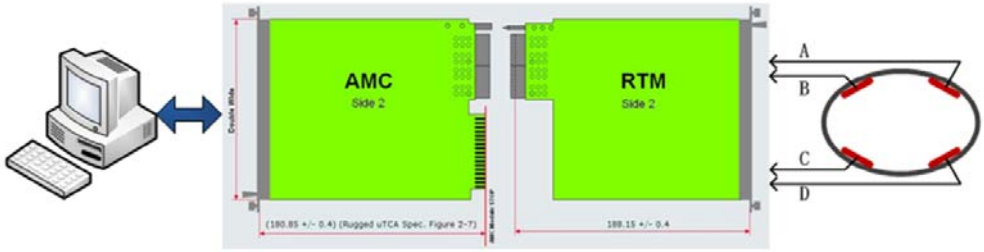

Figure 6.7.7: Digital BPM system function block

Electronics development is divided into three parts: RTM, AMC and signal processing and algorithm. For the RTM electronics, two version of PCBs have been developed and tested in the laboratory last year. The performance of the electronics are shown in Fig. 6.7.8.

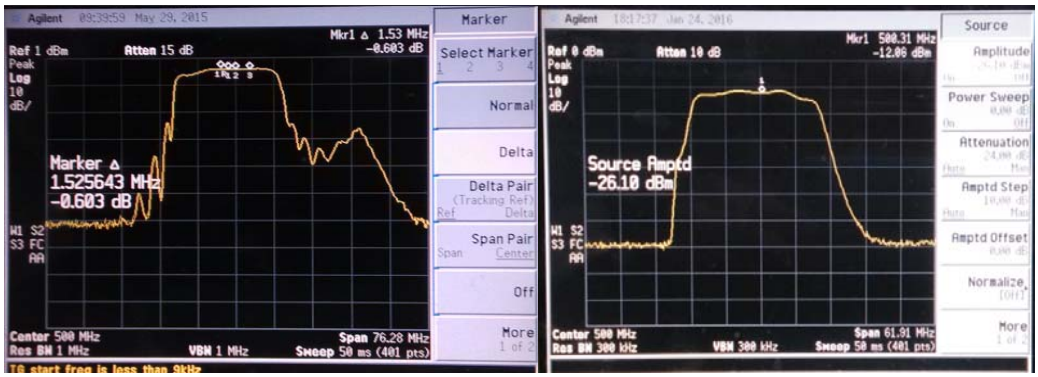

Fig. 6.7.8: the performance of PCBs the left is V1.0, the right is V2.0

6.7.3 Other R&D

The other systems where R&D is needed are: beam tune measurement, the feedback system, beam loss monitors and the beam diagnostic required at the IP. The R&D for the next five years is planned as follows:

- 1st year: determine the system structure and complete the physical design and simulation of the system.
- 2nd year: optimization of simulation results, and on this basis, complete the development and fabrication of equipment; complete equipment tests and related software development.
- 3rd and 4th year: complete equipment and commissioning; test the instruments in existing accelerators to verify equipment performance; analysis

experimental results, improve and optimize the initial design, finish test reports.

- 5th year: continue to optimize designs and improve the system performance to meet the needs of CEPC.

The Design specifications are summarized in Table 6.7.1.

Table 6.7.1: Specifications of the other beam instrumentation systems

Devices	Specifications
Beam loss monitor	Radio resistance >100 Mrad Maximum counting rate >10MHz， False counting rate <1Hz Minimum ionization particle detection efficiency >30%
Tune measurement system	Sensitivity: >100db Nosie: ＜120db
Beam diagnostics at the interaction point (IP)	Position resolution: 20um Time resolution: 200ps
Feedback system	System bandwidth: 350MHz Damping time: 0.2ms

6.8 Mechanical System

6.8.1 Development of the Collider Dipole Support System

For the dipole support systems in the collider, the R&D goals are:

- Develop simple and reliable mechanical solutions for safe mounting and easy alignment;
- Design the alignment method for dipole magnets;
- The systems must be stable over long time periods, avoiding creep and fatigue deformation;
- Reduce the cost through structural optimization and experimentation.

The technical paths for achieving these goals are:

- Design the support structure.
- Optimize the structure and the position of the supports to reduce the deformation, stress and vibration using Finite Elements Analyses (FEA).
- Investigate methods to make the support system stable.
- Design the alignment method based on the support and magnet structure.
- Develop a support system prototype, either one or a half support unit.
- Conduct experiments on installation, alignment and vibration.
- Summarize the work and confirm the final design for CEPC.

6.8.2 Development of Booster Dipole Support System

For the dipole support systems in the Booster, the R&D goals are:

- Develop simple and reliable mechanical solutions for safe mounting and easy alignment;
- Design installation and replacement methods and necessary tools for Booster dipole magnets and supports;
- Design alignment method for the dipole magnets;
- The systems must be stable over long time periods and avoid creep and fatigue deformation;
- Reduce the cost through structural optimization and experiments.

The technical paths for achieving these goals are:

- Design of the support structure, especially the location for hanging the dipoles and the support scheme.
- Optimization of the structure and the position of the supports to reduce deformation, stress and vibration using FEA. Topologic optimization may be used in this job. The optimized steel frame should be optimized for both static and dynamic stability.
- Design of the installation and replacement methods of the supports. This job will include creation of the necessary tools and fixtures.
- Design of the alignment method for the magnet support and magnets themselves.
- Build one support system prototype.
- Conduct experiments on installation, alignment and vibration.
- Summarize the work and confirm the final design for CEPC.

6.8.3 Development of Mockup of the Tunnel

For the mockup of the tunnel, the R&D goals are:

- Design a tunnel layout with all the devices in the tunnel cross section.
- Develop a support system to support all the prototypes needed to be installed in the mockup.
- Develop some necessary tools for the mockup.

Technically this will include:

- Design and development of the mechanical structure of an 8-meter long tunnel prototype including all the support systems defined in the mockup.
- Design the transportation and installation methods for all the devices in the tunnel cross section and develop the necessary tools and fixtures.
- Assemble all the devices in the mockup tunnel. The dipole magnets and their supports will be available by then, and one can use wooden prototypes for all the other devices. Test the transportation and installation methods.
- Test the magnet alignment methods.
- Summarize the work and confirm the final design for CEPC.

6.8.4 Development of Movable Collimators

For the movable collimators, the R&D goals are:

- Design a movable collimator with low impedance and with simple and flexible mechanical structure.
- Develop one prototype with required performance.

The technical routes are:

- Design the inner section of the collimator according to the physical requirements. Optimize the profile to obtain low impedance.
- Calculate the thermal and mechanical status using FEA. Optimization maybe needed depending on the results.
- Design and develop a collimator prototype with a simple and flexible structure.
- Test the mechanical and other performance.
- Summarize the work and confirm the final design for CEPC.

6.9 Survey and Alignment

6.9.1 High Precision Alignment Photogrammetry Research

The circumference of CEPC is about 61km and it is not possible to compromise between construction precision and efficiency. Commonly used equipment such as laser trackers, levels, and the total stations cannot simultaneously meet the requirements for precision and efficiency. So a special high precision alignment photogrammetry instrument will be designed to meet our alignment and maintenance requirements. The coordinate precision needed is 0.15 mm within 10 m range, and level measurement precision is 4". Photogrammetry has not been used in accelerator alignment up until now.

The critical R&D techniques are:

1) 0.005 micron omnibearing reflection target.
2) Large capability coded target.
3) High precision calibration field.
4) New measurement model and adjustment scheme.
5) High precision measurement camera with leveling function.

The CEPC project will need at least 30 photogrammetry instruments. There is a great application opportunity to replace the CMM, with a much more flexible method. The annual sales of this CEPC "spin-off" will be about 1000 units with a value of about 150 million RMB.

6.9.2 Domestication of the Laser Tracker

The laser tracker is the main measuring instrument used in many different kinds of fields, all depending on import. The design objective is to achieve 3 micron distance measurement precision, 2" angle measurement precision, and 2" leveling precision.

The critical R&D techniques are:

1) Precise bearing system.
2) Error compensation and software development.
3) Orientation adjustment methods and software development.

The CEPC project will need about 50 laser trackers. The domestic annual demand is for about 300 units. So, it is promising that there will be a market for the CEPC laser

trackers with an estimated value of about 225 million RMB.

Figure 6.9.1: Laser tracker

6.9.3 Domestication of the Total Station

The total station (Fig. 6.9.2) is the main instrument used in geodetic network measurement. They are imported from foreign countries. The design objective is to achieve 0.7mm/m distance measurement precision and 0.5" angle measurement precision and to make it in China.

The critical R&D techniques for us to work on are:

1) Precise bearing system.
2) Error compensation methods and software development.
3) Orientation adjustment and software development
4) High precision instrument accessories.

The CEPC project will need about 20 total stations, the domestic annual demand is about 500 stations with an estimated value of 150 million RMB.

Figure 6.9.2: Total station

6.9.4 Domestication of the Digital Level

The high precision level (Fig. 6.9.3) is the main instrument used in alignment leveling network. They are imported. The design objective is to achieve 0.2 mm/km closure error and make it in China.

The critical R&D techniques are:

1) Precise bearing system.
2) Error compensation methods and software development.
3) Orientation adjustment and software development

4) High precision instrument accessories.

CEPC will need about 20 digital levels. The domestic annual demand is about 600 levels with an estimated value of about 100 million RMB.

Figure 6.9.3: Digital level

6.9.5 High Precision Beidou GPS Receiver R&D

The Beidou satellite navigation system has been a great technological breakthrough and the CEPC geodetic network is going to use it. But there is no high precision Beidou GPS receiver yet. So this will be a great spin-off product for our country.

The design objectives: phase center precision better than 1 mm, phase center repeatability better than 1 mm, zenith axis ratio <1.2, confidence coefficient better than 99.99%.

The critical R&D techniques to work on are:

1) Precise satellite antenna design.
2) Error compensation methods and software development.
3) Phase center and mechanical center to coincide.
4) High precision instrument accessories.

The CEPC project will need 15 receivers, the domestic annual demand is about 1500 receivers with an estimated value of 100 million RMB.

6.9.6 Accelerator Local Geoid Refinement

The alignment challenge presented by the CEPC project requires us to look closely at the gravity field, because the earth can't be simply taken as an ellipsoid. We have two main datum plane schemes, but these surfaces are not accurate enough to take into account the anomalies of the vertical gravitational effects of mountains, lakes or geomagnetic variations. An equipotential gravity surface, called a geoid, to which the force of gravity is perpendicular everywhere must be defined.

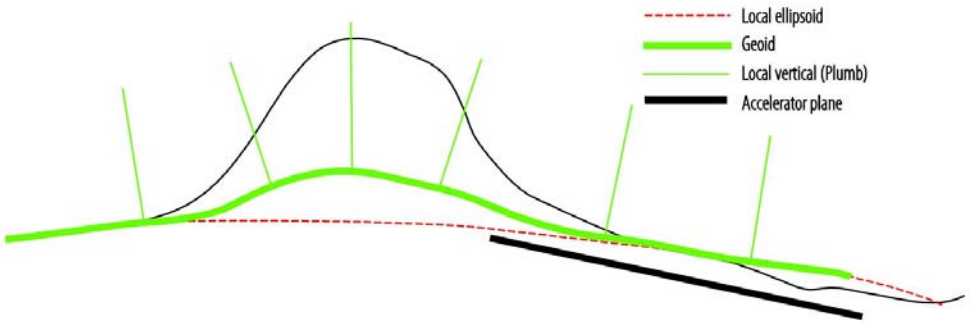

Figure 6.9.4: The Geoid

The refinement objective is 0.05 mm/100 m, or about 5 mm within the whole CEPC circle. Here too is a great application spin-off prospect for the high speed rail construction field.

6.10 Injector

6.10.1 Polarized Electron Gun

For the future prospect of having collisions between a polarized electron beam and an unpolarized positron beam, a photocathode dc-gun type electron source using a specially prepared GaAs/GaAsP superlattice will be considered as an option. This polarized electron gun will enable the Linac to produce a high-intensity and low-emittance beam with high polarization. The proposed polarized electron beam routinely yields at least 85% polarization with a maximum QE of ~1%. The high voltage between cathode and anode is 150 - 200 kV. This is a rather new technology and there is no successful experience in developing this in China. So an R&D program on polarized electron guns is necessary for this future development of CEPC Linac. Table **6.10.1** shows the design parameters of a polarized electron gun for CEPC Linac.

Table 6.10.1: Design parameters of a CEPC polarized electron source.

Gun type	Photocathode DC Gun
Cathode	Super-lattice GaAs/GaAsP photocathode
HV	150-200 kV
QE	0.5%
Polarization	>80%
Electrons per bunch	2×10^{10}
Repetition rate	50 Hz
Drive laser	790 nm（±20nm），10 μJ at 1 ns

The key and challenging technologies to work on for a polarized electron source involve advanced photocathode materials, high intensity pulsed laser, high energy beam polarization measurements and ultra-high vacuum. There are several crucial problems to be solved during the R&D oo a polarized electron gun.

- A super-lattice GaAs/GaAsP photocathode which is able to emit a very high polarization (>80%) electron beam is the most ideal photocathode for a polarized electron source worldwide. There is no local experience on using a super-lattice GaAs/GaAsP photocathode up to now, so international cooperation is necessary.
- Research on a 790 nm wavelength high intensity pulsed laser will be part of the effort. In order to obtain high polarization of the electron beam, a drive laser with a wavelength at 790 nm is selected. A single bunch in CEPC has 2×10^{10} electrons, which requires the drive laser to have a 10 μJ pulse energy of 1 ns pulse length (peak power 10kW).
- Design and development of a Mott polarimeter and a Wien filter system for a 200 keV electron beam.
- Optimization of 200 kV DC-Gun and its ultra-high vacuum system which is very important to maintain the QE and lifetime of photocathode.

6.10.2 High Intensity Positron Source

The technology of conventional positron sources is mature and can satisfy the requirements for the CEPC Linac. However, the CEPC positron source requires a bunch charge of 3.2 nC, two orders of magnitude greater than in BEPC-II, which had difficulty with positron source at high intensity. Therefore, R&D on a high intensity positron source is necessary. This R&D will be focused on the following aspects.

- Use Geant4/FLUKA code to do a simulation study on the generation of a positron beam from a high-energy electron beam incident on a converter target. Simulate the positron yield by optimizing target material, thickness and capture efficiency.
- Use ANSYS to complete the thermal analysis of converter target and determine its structure and cooling system.
- Complete the design of a Flux Concentrator system which has a 6 Tesla peak magnetic field output by using Opera code. Develop a 15 kV/15 kA/5 μs pulsed power supply and set up a Flux Concentrator test platform, and finally achieve 6Tesla peak magnetic field output through full HV conditioning.

The parameters of the CEPC positron source is similar to the positron source of Super-KEKB in Japan, so an international collaboration between IHEP and KEK about high intensity positron source design and beam tests will be carried out in the future.

6.10.3 S-Band Accelerator Structure Related R&D

S-Band accelerating structure is a mature technology. Usually the RF power feed is through a single coupling-hole which results in a field asymmetry. The time dependent multipole fields in the coupler induce a transverse kick along the bunch and cause an increase in beam emittance. An S-Band accelerator structure adopting a dual-feed racetrack design instead of the single-feed couplers will be developed to minimize the multipole field effects and improve beam quality. A symmetry coupler will be designed, manufactured, tested and welded with the cavities.

The iris and cavity shape will also be optimized, for an elliptical iris size can decrease the peak surface electric field. A round shape of the cavity can improve quality factor more than 10%. At the same time increase the whole tube shunt impedance.

After simulation design, processing technology of the symmetry coupler and the new cavity shape will be studied. An entire tube will be produced, adjustment, and cold test.

To measure the high power performance of the accelerating structure, the high power test bench needs to be improved. A dark current analysis system should be established. Finally, the test results of accelerator tube will be obtained.

6.11 High Field Superconducting Magnet

6.11.1 A Subscale Magnet Fabricated with Nb3Sn and NbTi Superconductors

First a 12-T sub-scale magnet will be fabricated with Nb_3Sn and NbTi superconductors. The cross section of this magnet is shown in Fig. 6.11.1. The red section in the figure represents the iron yoke of the magnet, with an outer diameter of 600 mm. The blue section represents the superconducting coils. The coil cross section in the first quadrant is shown in Fig. 6.11.2. The whole coil width is 52 mm, and the height is 36 mm. Two types of cables are used to fabricate the superconducting coils, called IHEPW1 and IHEPW2. The cables have the same width and thickness. The parameters of the cables are shown in Table 6.11.1. IHEPW1 is made up of IHEPWCJC Nb_3Sn strands, and IHEPW2 is made up of IHEPWNJC NbTi strands; Table 6.11.2 shows the parameters of these strands. A total of 8 such double-pancake coils are needed (4 Nb_3Sn + 4 NbTi) to reach 12-T peak field in the coil at 82% load line or 14.6-T peak field in the coil at 100% load line at 4.2 K. For each layer of coil, there are 20 turns of cables. The bending radius of the coil is 60 mm. Table 6.11.3 shows the required amount of superconductor per meter. The required length of the IHEPWCJC strand (Nb_3Sn) and IHEPWNJC strand (NbTi) are 4.5 km for each.

The maximum coil field with 100% load line ratio at 4.2 K is 14.6 T, corresponding to an operating current of 5000 A, located at the center of the Nb_3Sn coil, as shown in Fig. 6.11.3; the peak field of the NbTi coil is around 6.7 T. Or we can get a maximum coil field of 12 T with an operating margin of 18.4% at 4.2 K. corresponding to an operating current of 3970 A; the peak field of the NbTi coil is around 5.6 T.

Table 6.11.1. Main parameters of the cables

Cable	Width	Thickness-I	Thickness-o	Ns	Strand	Filament	Insulation
IHEPW1	5.8	1.5	1.5	14	IHEPWCJC	Nb_3Sn	0.15
IHEPW2	5.8	1.5	1.5	14	IHEPWNJC	NbTi	0.15

Table 6.11.2. Main parameters of the strands

Strand	diam.	cu/sc	RRR	Tref	Bref	Jc@BrTr	dJc/dB
IHEPWCJC	0.82	1	100	4.2	12	2400	400
IHEPWNJC	0.82	1	100	4.2	7.2	1500	550

Table 6.11.3. The required amount of superconductor per meter

Cable	Cable turns (1/4)	Cable turns (all)	Strand length (km)
IHEPW1	80	320	4.5
IHEPW2	80	320	4.5

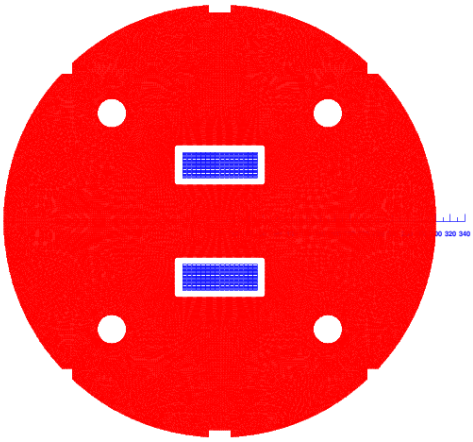

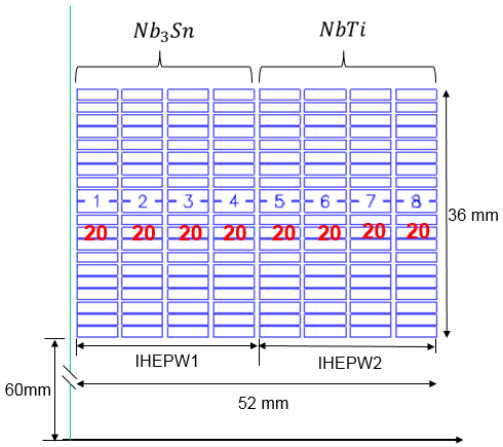

Fig.6.11.1. Cross section of the 12 T subscale magnet **Fig.6.11.2.** Coil cross section 1st quadrant

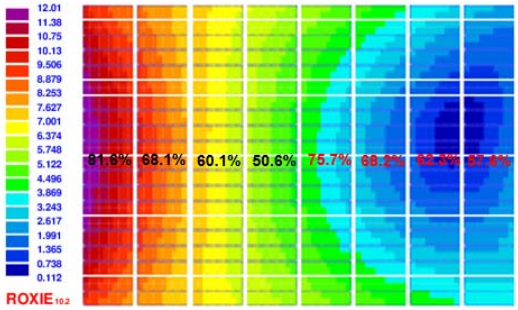

Fig.6.11.3. Field distribution of the coil in the 1st quadrant with the operating current of 3970 A

6.11.2 A Subscale Magnet Fabricated with only Nb3Sn Superconductor

After the above step, a 12-T subscale magnet will be fabricated with only Nb_3Sn superconductors, to test the stress management method for Nb_3Sn coils. The cross section of this magnet is shown in Fig. 6.11.4. The outer diameter of the iron yoke is 600 mm. The coil cross section in the first quadrant is shown in Fig. 6.11.5. The coil width is 51.6 mm, and the coil height is 36 mm. Two types of cables are used to fabricate the superconducting coils: IHEPW1 and IHEPW3. The cables have the different width. The main parameters are shown in Table 6.11.4. A total of 6 such double-pancake coils are needed (4 narrow + 2 broad) to reach the 12.4-T peak field in the coil at 80% load line or 15.4-T peak field in coil at 100% load line at 4.2 K. For each layer of coil, there are 20 turns of cables. The bending radius of the coil is 60 mm. Table 6.11.5 shows the required amount of superconductor per meter. The required length of the IHEPWCJC strand (Nb_3Sn) is 9.12 km total.

The maximum coil field with 100% load line ratio at 4.2 K is 15.4 T, corresponding to an operating current of 8050 A, located at the center of the coil, as shown in Fig. 6.11.6; Or we can get a maximum coil field of 12.4 T with an operating margin of 20% at 4.2 K, corresponding to an operating current of 6250 A. Fig. 6.11.6 shows the field distribution with the operating current of 6250 A.

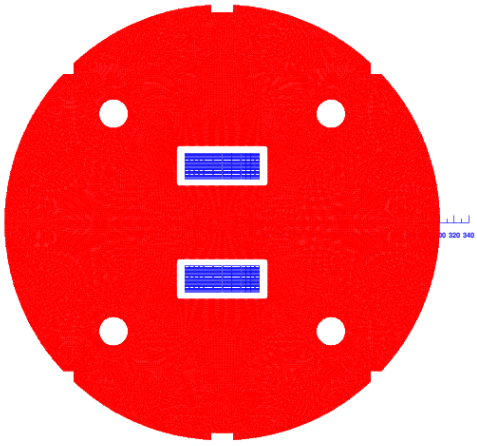

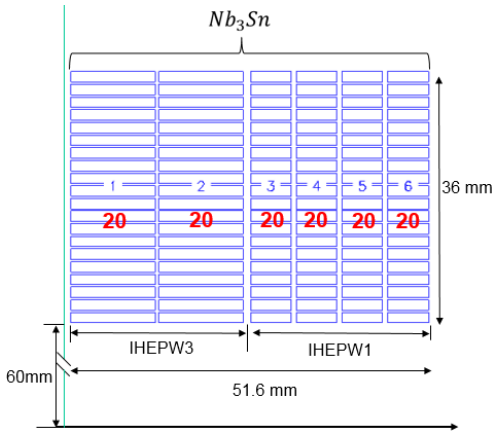

Fig.6.11.4. Cross section of 12-T common-coil dipole **Fig.6.11.5.** Coil configuration first quadrant

Table 6.11.4. The main parameters of the cables

Cable	Height	Width-I	Width-o	Ns	Strand	Filament	Insulation
IHEPW1	5.8	1.5	1.5	14	IHEPWCJC	Nb_3Sn	0.15
IHEPW3	1 2	1.5	1.5	29	IHEPWCJC	Nb_3Sn	0.15

Table 6.11.5. The required amount of superconductor per meter

Cable	Cable turns (1/4)	Cable turns (all)	Strand length (Km)
IHEPW1	80	320	4.48
IHEPW3	40	160	4.64

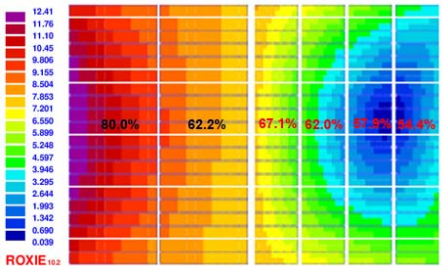

Fig.6.11.6. Field distribution in the coil (in 1st quadrant) (I=6250A)

6.11.3 A Common Coil Magnet with HTS and Nb_3Sn Superconductors

Finally, a 12-T common-coil dipole magnet with two apertures will be fabricated with HTS (YBCO) and Nb_3Sn superconductors, to test the field optimization method for HTS coils. The cross section of this magnet is shown in Fig. 6.11.7. There are two apertures in this dipole magnet. The clear bore diameter is temporarily set at 15 mm and the inter-aperture spacing is 156 mm. The outer diameter of the iron yoke is 600 mm. The coil cross section in the 1st quadrant is shown in Fig. 6.11.8. The whole coil width is 60.6 mm, and the height is 36 mm. The outer Nb_3Sn coils are with the same parameters as the subscale magnet at step 2. The field quality has been optimized at the main field of 12 T. All the high order multipoles are less than 1 unit. The YBCO insert coils are fabricated

with 4-mm width and 0.2-mm thickness YBCO tape. The main parameters are listed in Table 6.11.6. Table 6.11.7 shows the required amount of superconductor per meter. The required length of the IHEPWCJC strand (Nb_3Sn) is 9.12 km, and the YBCO tape is 0.6 km.

The main field with 100% load line ratio at 4.2 K is 14.6 T at 4.2 K, corresponding to an operating current of 358 A in the YBCO tapes and 9930 A in the Nb_3Sn cables. The peak field is 14.7 T in the YBCO coil and 14.5 T in the Nb_3Sn coils. Or we can get a main field of 12 T with an operating margin of 19% at 4.2 K, corresponding to an operating current of 280 A in the YBCO tapes and 7900 A in the Nb_3Sn cables. The peak field is 12.2 T in the YBCO coil and 12 T in the Nb_3Sn coils. Fig. 6.11.9 shows the field distribution in coils with an operating margin of 19% at 4.2 K.

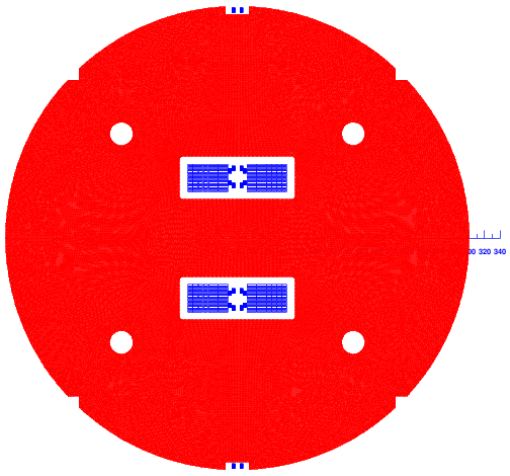

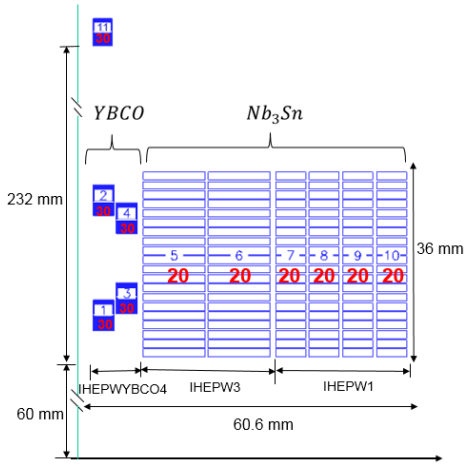

Fig. 6.11.7. Cross section of 12-T common-coil dipole **Fig.6.11.8.** Coil cross section 1st quadrant

Table 6.11.6. The main parameters of the YBCO tape

Strand	Size	cu/sc	RRR	Tref	Bref	Ic@BrTr	dIc/dB
YBCO4	4*0.2 mm^2	---	---	4.2	12	400	15

Table 6.11.7. The required amount of superconductor per meter

Cable	Cable turns (1/4)	Cable turns (all)	Strand length per 1m coil (Km)
IHEPW1	80	320	4.48
IHEPW3	40	160	4.64
IHEPWYBCO4	150	600	0.6

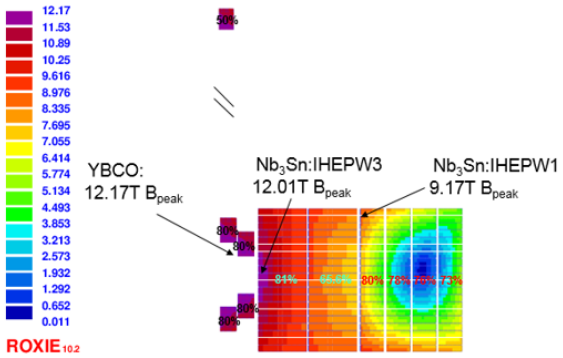

Fig. 6.11.9. Field distribution in the coil (in first quadrant)

6.11.4 References

1. Chengtao Wang, Kai Zhang, and Qingjin Xu, R&D STEPS OF A 12-T COMMON COIL DIPOLE MAGNET FOR SPPC PRE-STUDY, International Journal of Modern Physics A 31(33):1644018, November 2016